

In Situ Magnetic Domain Imaging at the Spin-Reorientation Transition of Ultrathin Ni- and Fe/Ni-Films

Von der Fakultät für Naturwissenschaften
der Universität Duisburg-Essen
(Campus Duisburg)
zur Erlangung des akademischen Grades eines
Doktors der Naturwissenschaften
genehmigte Dissertation

von

Robert Ramchal

aus

Celle

Referent: Prof. Dr. Michael Farle

Korreferent: Prof. Dr. Werner Keune

Tag der mündlichen Prüfung: 07. Dezember 2004

Dedicated to my parents

Abstract

In this thesis the spin-reorientation transition (SRT) of ultrathin $\text{Ni}_x/\text{Cu}(100)$ and $\text{Fe}_y/\text{Ni}/\text{Cu}(100)$ films is investigated as a function of the film thickness x and y , respectively, at 300 K in ultrahigh vacuum (UHV). By imaging the magnetic domain microstructure by means of spin-polarized low energy electron microscopy (SPLEEM), it is shown that the SRT of ultrathin $\text{Ni}/\text{Cu}(100)$ films is a phase transition of second order, i. e. the magnetization reorients *continuously* within the domains. A transition of first order, i. e. a discontinuous SRT, in which in-plane and out-of-plane magnetized stripe domains coexist, was not observed in $\text{Ni}/\text{Cu}(100)$ films. The detection of the three components of the magnetization during the SRT shows, that the magnetization turns from the orientation in the film plane and parallel to the step edges of the Cu substrate to the orientation perpendicular to the film plane and perpendicular to the step edges with increasing layer thickness. The SRT occurs as a *spiral-like* motion of the magnetization. The size of the in-plane magnetized domains of some $10 \mu\text{m}$ for films of 5 – 9 monolayers (ML) thickness decreases at the SRT (9 – 11 ML) to $>1 \mu\text{m}$. The size of the perpendicularly magnetized domains (>11 ML) is about 3 – 5 μm .

Ultrathin $\text{Fe}/\text{Ni}/\text{Cu}(100)$ films represent the prototype of a ferromagnetic double layer system, whose individual layers exhibit an opposite SRT. The investigation of the SRT of this double layer system is therefore of fundamental interest, and it is studied in the framework of this thesis *for the first time in detail*. The evaporation of 2.5 – 2.9 ML Fe on top of a perpendicularly magnetized $\text{Ni}/\text{Cu}(100)$ film results in a reorientation of the magnetization into the film plane. The reason for this SRT is the increased shape anisotropy due to the Fe coverage and the large negative Fe-Ni-interface anisotropy. Also in $\text{Fe}/\text{Ni}/\text{Cu}(100)$ films a *continuous spiral-like* reorientation of the magnetization, i. e. an SRT of second order is found, while the magnetic domains *simultaneously* break up into approx. 180 nm wide stripe domains along the Cu step edges. At the SRT a transformation of the domain walls from the Bloch mode into the Néel mode takes place.

Moreover, a UHV-SQUID-magnetometer was built up, which allows for *in situ* measurements of the magnetic stray field of an ultrathin ferromagnetic film, such as for instance $\text{Ni}/\text{Cu}(100)$. From the stray field measurement the absolute value of the magnetization of the film can be determined.

Kurzfassung

In dieser Arbeit wird der Spinreorientierungsübergang (SRT) von ultradünnen $\text{Ni}_x/\text{Cu}(100)$ - und $\text{Fe}_y/\text{Ni}/\text{Cu}(100)$ -Filmen als Funktion der Schichtdicke x bzw. y bei 300 K im Ultrahochvakuum (UHV) untersucht. Über die Abbildung der magnetischen Domänenstruktur mittels spin-polarisierter Niederenergie-Elektronenmikroskopie (SPLEEM) wird gezeigt, dass der SRT von $\text{Ni}/\text{Cu}(100)$ ein Phasenübergang *zweiter* Ordnung ist, bei dem sich die Magnetisierung *kontinuierlich* innerhalb der Domänen dreht. Ein SRT erster Ordnung, d. h. ein diskontinuierlicher Übergang, bei dem in der Filmebene und senkrecht zur Filmebene magnetisierte Streifendomänen koexistieren, wurde in $\text{Ni}/\text{Cu}(100)$ -Filmen nicht beobachtet. Die Abbildung der drei Komponenten der Magnetisierung während des SRT zeigt, dass sich die Magnetisierung mit zunehmender Schichtdicke von der Orientierung in der Filmebene und parallel zu den Stufenkanten des Cu-Substrates zu der Orientierung senkrecht zur Filmebene und senkrecht zu den Substratstufen dreht. Der SRT erfolgt also *spiralförmig*. Die Größe der in der Ebene magnetisierten Domänen von einigen $10 \mu\text{m}$ für Filme der Schichtdicke 5 – 9 Monolagen (ML) nimmt am SRT (9 – 11 ML) auf $>1 \mu\text{m}$ ab. Für senkrecht magnetisierte Ni-Filme (>11 ML) beträgt die Domänengröße circa 3 – 5 μm .

Ultradünne $\text{Fe}/\text{Ni}/\text{Cu}(100)$ -Filme stellen den Prototyp eines ferromagnetischen Doppelschichtsystems dar, dessen einzelne Schichten einen entgegengesetzten SRT aufweisen. Die Untersuchung des SRT dieses Doppelschichtsystems ist daher von fundamentalem Interesse und wird im Rahmen dieser Arbeit *erstmalig im Detail* untersucht. Das Aufdampfen von 2.5 – 2.9 ML Fe auf einen senkrecht magnetisierten $\text{Ni}/\text{Cu}(100)$ -Film hat eine Reorientierung der Magnetisierung in die Filmebene zur Folge. Die Ursache dafür ist die durch das Fe erhöhte Formanisotropie und die große negative Fe-Ni-Grenzflächenanisotropie. Auch in $\text{Fe}/\text{Ni}/\text{Cu}(100)$ Filmen wird eine *kontinuierliche spiralförmige* Reorientierung der Magnetisierung, d. h. ein SRT zweiter Ordnung beobachtet, während die Domänen *gleichzeitig* in ca. 180 nm breite Streifendomänen entlang der Stufenkanten aufbrechen. Am SRT findet eine Transformation der Domänenwände aus dem Bloch-Modus in den Néel-Modus statt.

Es wurde außerdem ein UHV-SQUID-Magnetometer aufgebaut, mit dem das magnetische Streufeld eines ultradünnen ferromagnetischen Films, wie beispielsweise $\text{Ni}/\text{Cu}(100)$, *in situ* gemessen werden kann. Aus einer solchen Messung läßt sich die Magnetisierung des Films in absoluten Einheiten bestimmen.

Acronyms and abbreviations

AES	Auger Electron Spectroscopy
AFM	Atomic Force Microscopy
bcc	Body-centered cubic
CMA	Cylindrical Mirror Analyser
d_c	Critical thickness
fcc	Face-centered cubic
fmt	Face-centered tetragonal
FMR	Ferromagnetic Resonance
LEED	Low Energy Electron Diffraction
LEEM	Low Energy Electron Microscopy
LT	Low Temperature
MAE	Magnetic Anisotropy Energy
MC	Magnetic Contrast
MFM	Magnetic Force Microscopy
ML	Monolayer
MOKE	Magneto-Optical Kerr Effect
M-SNOM	Magneto-Optical Scanning Near-Field Microscopy
PND	Polarized Neutron Diffraction
QMS	Quadrupole Mass Spectrometer
RF	Radio Frequency
RT	Room Temperature
SEMPA	Secondary Electron Microscopy with Polarization Analysis
SPLEEM	Spin-Polarized Low Energy Electron Microscopy
SP-STM	Spin-Polarized Scanning Tunnelling Microscopy
SQUID	Superconducting QUantum Interference Device
SRT	Spin-Reorientation Transition
STM	Scanning Tunnelling Microscopy
T_c	Critical temperature
T_C	Curie-temperature
TEM	Transmission Electron Microscopy
UHV	Ultrahigh Vacuum
XAS	X-ray Absorption Spectroscopy
XMCD	X-ray Magnetic Circular Dichroism
X-PEEM	X-ray Photo Emission Electron Microscopy

Contents

Abstract	i
Kurzfassung	iii
Introduction	1
1 Fundamentals	5
1.1 Ferromagnetism in ultrathin 3d bilayer films	5
1.1.1 Exchange coupling in bilayer systems	6
1.1.2 Magnetic moments at interfaces and in alloys	6
1.2 Spin-reorientation transition (SRT)	10
1.2.1 The role of magnetic anisotropies	10
1.2.2 Spin-reorientation transition of Ni/Cu(100) and Fe/Cu(100) films	13
1.3 Magnetic domains	21
1.3.1 The thermodynamic ground state of magnetic domains	21
1.3.2 Domain walls in ultrathin films	21
1.3.3 The stripe domain state	25
2 Experimental details	29
2.1 SPLEEM	29
2.1.1 Mode of operation	29
2.1.2 Comparison with other domain imaging methods	34
2.2 XMCD	37
2.2.1 Determination of magnetic moments using “sum rules”	39
2.2.2 Element-specific determination of the magnetization direction in bilayers	41
2.3 SQUID magnetometry	42
2.3.1 Operation of an rf-SQUID	42
2.3.2 Determination of magnetic moments from the stray field	43

3	Substrate preparation and ultrathin film growth	47
3.1	Preparation of the Cu(100) and GaAs(001) substrates	47
3.2	Growth of ultrathin Ni, Fe and Fe/Ni films on Cu(100) and GaAs(001)	49
4	Design of the UHV-SQUID system	53
4.1	Construction of the UHV chamber	53
4.2	The SQUID sensor	55
4.3	Cryostat and magnetic shielding	55
4.4	The sample holder	56
4.5	Calibration of the SQUID	57
4.6	Data acquisition	59
4.7	Measurements of the stray field of a 12.5 ML Fe/GaAs(001) film	59
5	Magnetic domains	61
5.1	5 to 8 ML Ni on Cu(100)	61
5.1.1	Comparison of domains at 100 K and 300 K	61
5.1.2	Analysis of a domain wall of an 8 ML Ni/Cu(100) film	65
5.2	Evolution of magnetic stripe domains in Fe/Cu(100) films	69
5.3	Fe monolayers on 7 to 11 ML Ni/Cu(100)	72
5.3.1	Out-of-plane magnetized domains (0 to 2.5 ML Fe)	73
5.3.2	In-plane magnetized domains (> 2.8 ML Fe)	78
6	Magnetic domains near the spin-reorientation transition	79
6.1	Continuous reorientation of the magnetization in Ni/Cu(100) films	79
6.2	Spin-reorientation transition of Fe/Ni bilayers on Cu(100)	84
6.2.1	Coupling between Fe and Ni layers	84
6.2.2	Magnetic moments per Fe and Ni atom	87
6.2.3	Continuous SRT as a function of the Fe layer thickness	89
6.2.4	Determination of the Fe-Ni interface magnetic anisotropy from the critical Fe layer thickness	96
6.2.5	Domain wall evolution near the SRT	100
6.2.6	SRT of $\text{Fe}_x/\text{Ni}_{1.5}/\text{Cu}(100)$	104
7	Conclusion	107
A	Appendix	111
A.1	Conversion of properties and units	111
A.2	Drawings of the UHV-components	112
A.3	Motor control and data acquisition program	116

A.4	Technical data of the SQUID sensor	118
A.5	Calibration of the Fe evaporator	118
A.6	Determination of the canting angle from XMCD measurements	119
	List of Figures	121
	List of Tables	125
	References	127
	List of publications	139
	Acknowledgment	143
	Zusammenfassung	145

Introduction

The investigation of magnetic ultrathin films has made great progress over the last decades [1,2]. Of particular importance for both the basic research and with regard to possible applications in magnetic recording techniques is the influence of the temperature, the film thickness or the film composition on the direction of the magnetization. Spin-reorientation transitions (SRT), i. e. changes of the magnetization direction as a function of the above mentioned parameters have both theoretically [3–6] and experimentally [7–10] been investigated also to answer the question, if they are continuous or discontinuous phase transitions¹, or if they proceed via a breakup into a multi domain state, in which in-plane and out-of-plane magnetized domains co-exist [4,11–14]. The orientation of the magnetization is determined by the magnetic anisotropy energy, which includes spin-orbit (magnetocrystalline and magnetostrictive anisotropy) and dipolar (shape anisotropy) induced interactions [15]. The so-called easy axis of the magnetization is given by the minimum of the sum of these contributions. In the case of an ultrathin film the magnetostatic energy (strayfield energy) is minimum for an alignment of the magnetization parallel to the surface [16]. Thereby, the magnetostatic energy competes with the magnetocrystalline anisotropy energy, which may comprise contributions, that favor an orientation of the magnetization perpendicular to the surface. Due to the high surface to volume ratio of ultrathin films (1 – 10 ML), the increased surface influence as well as the lattice distortion caused by the lattice mismatch to the substrate, give rise to large intrinsic anisotropies, which are otherwise small compared to the magnetostatic energy in the respective bulk materials. The different dependencies of the individual anisotropy contributions on the temperature T and the film thickness d implicate a relative change of the contributions upon varying the parameters T or d , which may cause a change of the direction of the magnetization and thus give rise to a spin-reorientation transition.

In general, the ground state of a ferromagnetic system is a domain state, which arises from the coexistence of the short-range exchange interaction and the long-range dipolar interaction. Due to the competition of these interactions the magnetic moments of a ferromagnet are aligned parallel to each other at a short distance and antiparallel at a large distance. Depending on the

¹Although the SRT is generally accepted to represent a phase transition, the order parameter, which must vanish above the critical thickness or temperature, is not uniquely defined.

energy, which is needed to form domain boundaries, different sizes and various kinds of domain shapes such as stripes, bubbles or meanders occur [17]. Since the extensions of the magnetic domains and the domain walls vary with the thickness dependent anisotropies [18,19], a magnetic imaging technique is required, which provides the opportunity to resolve magnetic structures on the submicrometer scale *in situ* during the film growth with a high image acquisition rate, in order to study the formation of magnetic domains during the thickness-driven SRT. Simultaneously, all three components of the magnetization have to be detected to determine the magnetization direction during the SRT. All these requirements are achieved by spin-polarized low energy electron microscopy (SPLEEM) [20,21], which was used in this thesis to study the SRT of ultrathin Ni/Cu(100) [5,8,10,22–24] and Fe/Ni/Cu(100) [25,26] as a function of the thickness. Due to the energy of the electrons below 10 eV this method is surface sensitive and affords the correlation of magnetic structures to topographic features, such as atomic step edges and defects at the same time. The lateral resolution of ≈ 10 nm is suited for the investigation of domain walls, which typically have widths of 1 – 1000 nm in thin films.

The spin-reorientation transition of ultrathin Ni/Cu(100) films proceeds from an orientation of the magnetization in the film plane to an orientation perpendicular to the plane as a function of increasing temperature or thickness. The reason for the reversed SRT of Ni/Cu(100) in comparison to other film systems, such as e. g. Fe/Cu(100) [27–32], is the negative surface anisotropy of Ni, which favors a magnetization orientation in the film plane and has the largest influence at low thicknesses. The positive thickness independent volume anisotropy, which arises from the tetragonal distortion of the lattice, is responsible for the orientation of the magnetization perpendicular to the surface above 11 ML [33]. The system Fe/Ni/Cu(100) represents the prototype of a ferromagnetically coupled bilayer system, in which the individual layers deposited on Cu(100) show an opposite SRT. Previous investigations revealed interesting magnetic properties of Fe/Ni/Cu(100) films of various thicknesses, such as a ferromagnetic Fe layer at the Fe/Ni interface beneath an antiferromagnetic Fe film in the thickness range of 5 to 10 monolayers (ML) Fe [25,26,34]. Recently, an exchange coupling between a ferromagnetic surface layer of the Fe film and the Ni film was observed [35]. The influence of the concentration x of $\text{Fe}_x\text{Ni}_{1-x}$ alloy films on the spin-reorientation transition was investigated lately [36].

The SRT of ultrathin Ni/Cu(100) films has been investigated so far by different techniques, i. e. x-ray magnetic circular dichroism [7], ferromagnetic resonance [37], magneto-optical Kerr effect [9] and second harmonic generation [10]. In all these techniques an external magnetic field is applied to saturate the magnetization of the film in different directions. Furthermore, the respective measured signal originates either from the whole sample or at least from a millimeter-sized region of the film. In this work, the micromagnetic domain structure of ultrathin Ni/Cu(100) and Fe/Ni/Cu(100) films is imaged during the SRT as a function of the thickness. These measurements provide an insight into the change of magnetic domains at the

reorientation of the magnetization in the absence of an external magnetic field for the first time. The aim of this thesis is the clarification of the following main questions: (i) Is there a continuous SRT [10,22] or a breakup into a multi domain state at the SRT of Ni/Cu(100) films? (ii) Is the reorientation of the magnetization at the SRT affected by the step edges of the Cu(100) crystal? (iii) What are the typical scales of the domains and the domain walls of in-plane magnetized ultrathin Ni/Cu(100) films, and how do their sizes change at the SRT? (iv) Is the SRT of Fe/Ni/Cu(100) as a function of the Fe thickness a continuous one or does the SRT proceed via a breakup into stripe domains like in Fe/Cu(100) [12,38]? (v) How does the SRT take place in the individual Fe and Ni layers, and how does the Fe-Ni interface affect the magnetic moments per Fe and Ni atom? (vi) What are the dominant anisotropy contributions to the SRT?

A second aim of this thesis is the construction of a UHV-chamber and the setup of a high- T_c -SQUID magnetometer [39] in order to determine the absolute value of the magnetization of an ultrathin film *in situ*. The chamber should also allow for measurements of the ferromagnetic resonance (FMR) [40] of the *same* sample *in situ*.

The present work is organized as follows: In chapter 1 the fundamentals of ferromagnetism in coupled ultrathin films and both theoretical and experimental aspects of the spin-reorientation transitions of Ni/Cu(100) and Fe/Cu(100) films are introduced. Moreover, the occurrence of magnetic domains in ultrathin films is elucidated. Experimental details of the applied techniques, i. e. spin-polarized low energy electron microscopy (SPLEEM), x-ray magnetic circular dichroism (XMCD) and superconducting quantum interference device (SQUID), are presented in chapter 2. The substrate preparation and the growth of ultrathin films is summarized in chapter 3. The design of the UHV-SQUID is described in chapter 4. More technical details, drawings of the system and the computer program used for the data acquisition can be found in the appendix. In chapter 5 the analysis of the magnetic domain structure of Ni/Cu(100), Fe/Cu(100) and Fe/Ni/Cu(100) films is given. Finally, a detailed investigation of the spin-reorientation transitions of Ni/Cu(100) and Fe/Ni bilayers on Cu(100) is presented in chapter 6.

1 Fundamentals

This chapter gives an introduction of the fundamental aspects of magnetic phenomena, which are relevant to describe the spin-reorientation transition of ultrathin ferromagnetic single and double layers. Since ferromagnetic bilayers have been studied in detail, the direct exchange coupling and the role of local magnetic moments per atom at the interface of two ferromagnetic layers are considered. In order to explain the mechanism of the spin-reorientation transition, the role of magnetic anisotropies and their dependence on both the film thickness and the temperature is discussed. The opposite spin-reorientation transition of ultrathin Ni/Cu(100) and Fe/Cu(100) films and its manipulation by different conditions of the film growth is reviewed. The principles of how magnetic domains and domain walls are formed in ultrathin films being in the thermodynamical ground state and near the spin-reorientation transition is outlined.

1.1 Ferromagnetism in ultrathin 3d bilayer films

The ferromagnetic properties of a solid are correlated with its dimensionality. The spontaneous magnetization, which arises from the parallel alignment of the magnetic moments of atoms due to the exchange interaction is one characteristic observable of a ferromagnet. In contrast to a bulk *3d* ferromagnet, like Fe, Co or Ni, in which the orbital magnetic moment is almost quenched due to the high symmetry of the arrangement of the surrounding atoms within the crystal, in ultrathin films this quenching is partly lifted due to both the broken symmetry at the surface and the strain as resulting from the epitaxial growth on the substrate [41]. The reduced dimensionality also affects the Curie-temperature, which decreases with decreasing layer thickness of an ultrathin film (finite size effect) [15]. Moreover, thickness and temperature dependent surface and interface magnetocrystalline anisotropies largely contribute to the orientation of the magnetization in ultrathin films [2]. In bilayers, consisting of two different ferromagnetic layers, an additional contribution arises from the interface between the coupled single layers. At this interface the two types of atoms exchange electrons and form the band structure of an alloy. The individual magnetic moments will change, depending on the degree of alloying [42].

1.1.1 Exchange coupling in bilayer systems

In two ultrathin ferromagnetic layers A and B, which are in direct contact, the exchange coupling J^{AB} is strong and orients the magnetic moments of the single layers into a common direction. The exchange energy is based on pair interaction at the interface and yields:

$$E_{ex} = -2J^{AB} S^A \cdot S^B \quad (1.1)$$

where S^A and S^B are nearest neighbor spins. From the exchange coupling constant J_{AB} , an interface exchange stiffness parameter $A^{AB} = 2J^{AB} S^A S^B / a^{AB}$ results, where $a^{AB} = \sqrt{a^A a^B}$, with a^A and a^B being the lattice spacings of the layers A and B, respectively. A^{AB} can be estimated from the bulk values for Fe and Ni [43]. The total magnetization of the bilayer is the sum $M^A + M^B$ of the individual magnetizations, whereby the average saturation magnetization is given by $M_S^{av} = (d^A M^A + d^B M^B) / (d^A + d^B)$ where d^A and d^B are the thicknesses of the two layers [44]. The ferromagnetic coupling will decrease if the magnetic layers are separated by a non-magnetic interlayer of increasing thickness. An oscillation between a ferromagnetic and an antiferromagnetic coupling as a function of the spacer layer thickness was observed [45].

1.1.2 Magnetic moments at interfaces and in alloys

For the discussion of local magnetic moments at the interface of a ferromagnetic bilayer, like Fe/Ni/Cu(100), it has to be taken into account that even for a perfectly flat Fe/Ni interface there already exists an overlap of the $3d$ -bands of the adjacent Fe and Ni layers. For such flat surfaces the coordination number of both the fcc Fe(100) and the fcc Ni(100) layer is reduced from 12 to 8. This reduction is lifted when both surfaces are touching each other. At each atomic site of Fe (Ni), 4 Ni (Fe) atoms supplement the coordination number up to 12. On average, for each interface atom the number of nearest neighbors is 6 Fe atoms and 6 Ni atoms (see Fig. 1.3 (b)). The resulting band structure corresponds to that of an $Fe_{0.5}Ni_{0.5}$ alloy, i. e. Fe and Ni atoms exchange their electrons. The average magnetic moment of the interface may be obtained from the Slater-Pauling curve, which gives the magnetic moment of an alloy as a function of the number of valence electrons per atom (e/a).

The Slater-Pauling curve

The Slater-Pauling curve describes that the average magnetic moment of an Fe_xNi_{1-x} alloy increases with increasing Fe concentration starting from $x = 0$. Due to the fact that variations of the magnetic moment depend only on the relative number of occupied or unoccupied states in the spin-up and spin-down d -bands, and not on the shape of the density of states $Z(E)$ or the state density at the Fermi-level E_F [46], the basic understanding of the Slater-Pauling curve is

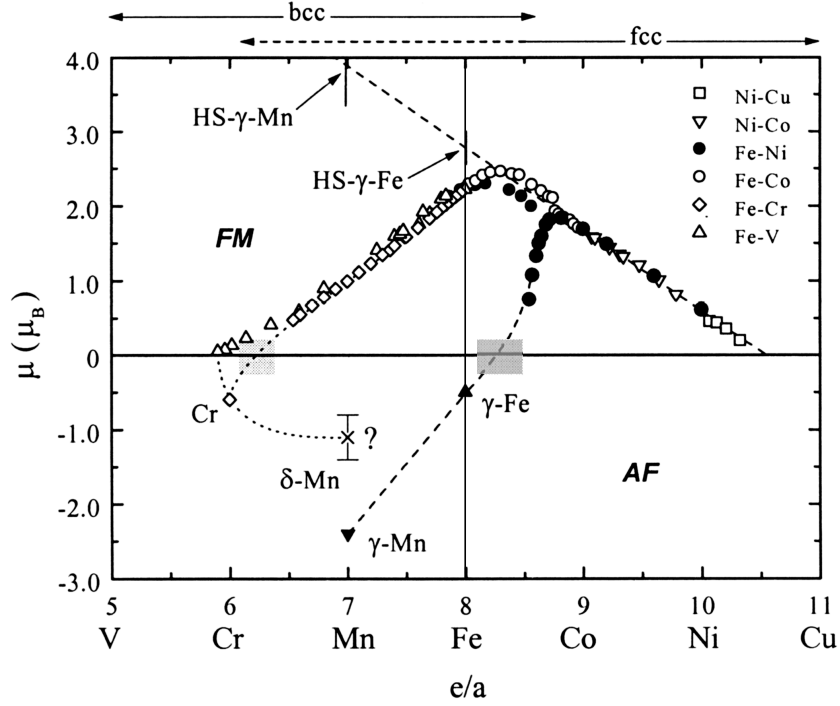


Figure 1.1: The Slater-Pauling curve for an $\text{Fe}_x\text{Ni}_{1-x}$ alloy (\bullet) shows the average magnetic moment ($\mu > 0$) versus the number of valence electrons per atom (e/a). Extrapolation to the ferromagnetic high-spin state of γ -Fe yields $\mu_{\text{Fe}} \approx 2.7 \mu_{\text{B}}$. The sharp decline around $8.5 e/a$ is due to a fcc-bcc-phase transformation. The antiferromagnetic ground state ($\mu < 0$) of γ -Fe is indicated by the symbol \blacktriangle . (From [47]).

usually given within the rigid-band-model, which assumes that the s - and d -bands are rigid in shape as the atomic number changes.

The spin magnetic moment¹ μ_S per atom of a transition metal alloy is given by the spin imbalance of particularly the d -electrons:

$$\mu_S \approx (n_d^\uparrow - n_d^\downarrow) \mu_{\text{B}} \quad (1.2)$$

where n_d^\uparrow and n_d^\downarrow are the d -subband populations. Generally both n_d^\uparrow and n_d^\downarrow may vary upon alloying. Starting at $x = 0$, i. e. with pure fcc Ni, one finds the well known magnetic moment of $0.6 \mu_{\text{B}}$. Since Ni is a strong ferromagnet, for which E_F lies above the top of the spin-up (majority) band, the magnetic moment per atom can be simply calculated as:

$$\mu_S = (5 - n_d^\downarrow) \mu_{\text{B}}. \quad (1.3)$$

Because $n_d^\downarrow = n_d - 5$ and $n_d = n_d^\uparrow + n_d^\downarrow$ it follows that:

$$\mu_S = (10 - n_d) \mu_{\text{B}}. \quad (1.4)$$

¹Only the spin moment is considered; the small orbital contribution to the total magnetic moment is not included in this model.

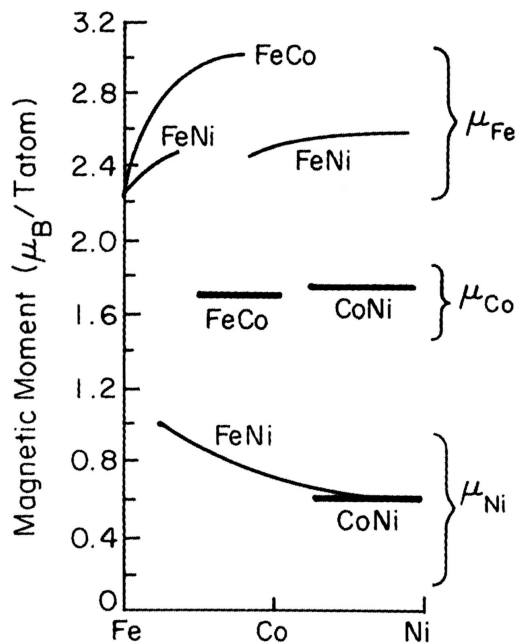


Figure 1.2: Local magnetic moments on Fe and Ni sites for an Fe-Ni alloy determined by neutron scattering measurements. Upon alloying Ni progressively with Fe the magnetic moment of Ni increases while the magnetic moment of Fe declines. (From [46]).

For strong ferromagnets this equation is a straight line with slope -1 , meaning a change of $1 \mu_B$ per valence electron, which is found in the right hand branch of the Slater-Pauling curve in Fig. 1.1. Equation (1.4) also explains, why the average moment of Co should be so close to that of $\text{Fe}_{0.5}\text{Ni}_{0.5}$, since they both have the same number of valence electrons and thus the same value of n_d . For higher Fe concentrations in fcc Ni, the Fermi-level is continuously lowered, because the number n_d of d -electrons decreases and hence the average magnetic moment increases according to Eq. (1.4). As long as the binary alloy remains in an fcc structure, there is no change in the slope of the Slater-Pauling curve as the Fe concentration is increased. Finally, alloying would end up with pure fcc γ -Fe in the high-spin state. In this state the magnetic moment of γ -Fe, which arises from a large atomic volume, is $\approx 2.7 \mu_B$ (see Fig. 1.1).

The average magnetic moment of Fe-Ni alloys with $(e/a) < 8.7$ strongly deviates from the Slater-Pauling curve towards $\mu = 0$ because of a transition to antiferromagnetism in the Fe-rich concentration range. The shaded area in Fig. 1.1 around $\mu = 0$ shows the concentration region where ferromagnetic and antiferromagnetic interactions compete. Such coexisting interactions lead to interesting magnetic states such as spin-glasses [47]. However, before the concentration of the system can reach a composition corresponding to that of a spin-glass state, which occurs at $(e/a) \approx 8.5$,² the structure becomes bcc, and the average magnetic moment jumps up to about $2 \mu_B$. Upon further increase of the Fe concentration, the magnetic moment increases up to the well known bulk value of $2.2 \mu_B$ for pure bcc α -Fe. The change of the site-resolved magnetic moments per Fe and Ni atom in Fe-Ni alloys determined by neutron scattering measurements

²At $(e/a) \approx 8.5$ i. e. for an $\text{Fe}_{0.75}\text{Ni}_{0.25}$ alloy, the individual magnetic moments have been calculated to be $\mu_{\text{Fe}} = 0.0008 \mu_B$ and $\mu_{\text{Ni}} = -0.0023 \mu_B$ [48]

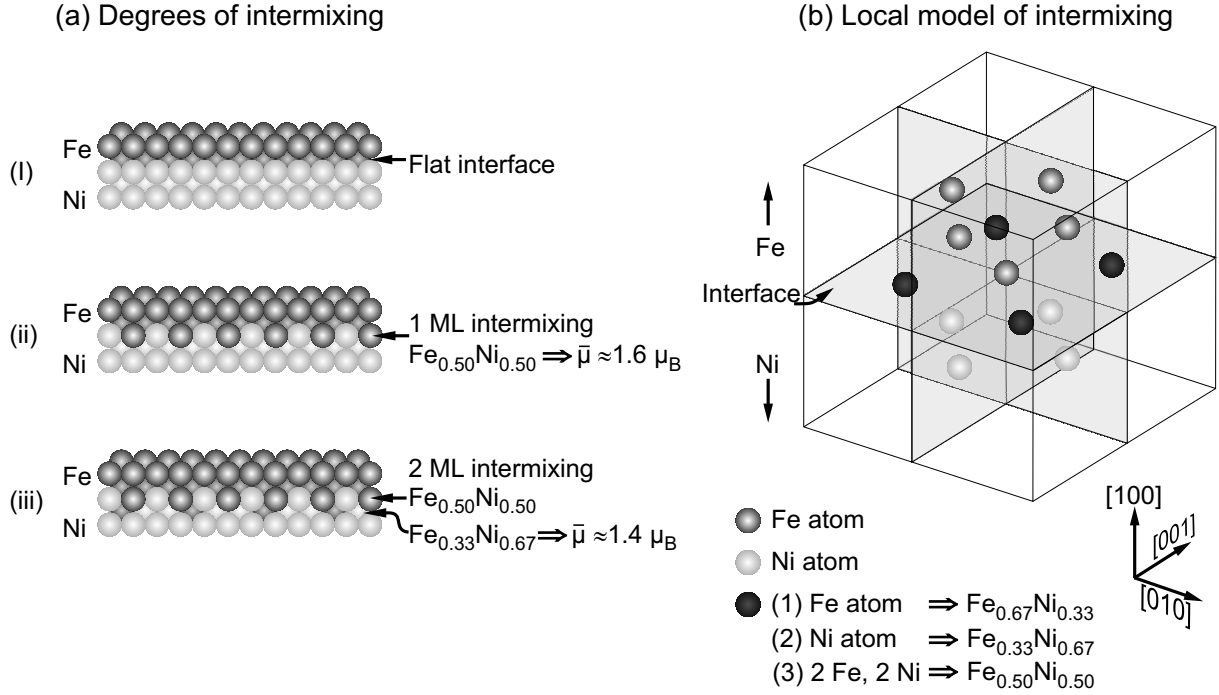


Figure 1.3: The possible degrees of intermixing (a) and the different nearest neighbors at the Fe/Ni interface –assuming fcc growth– of Fe/Ni/Cu(100) (b) give rise to different average magnetic moments according to the Slater-Pauling curve. The centered Fe atom in (b) is located at the interface. Three special cases for the 12 nearest neighbors are sketched by the black spheres: 4 Fe atoms at the interface lead to the Invar-concentration $\text{Fe}_{0.67}\text{Ni}_{0.33}$ (1), 4 Ni atoms yield an $\text{Fe}_{0.33}\text{Ni}_{0.67}$ alloy which is near the Permalloy concentration (2) and an equal number of Fe and Ni atoms results in $\text{Fe}_{0.50}\text{Ni}_{0.50}$ (3).

is presented in Fig. 1.2. It shows that the Ni magnetic moment continuously increases from $0.6 \mu_B$ (bulk value) up to $1.0 \mu_B$, when the Fe concentration increases, while the moment per Fe atom decreases from $2.6 \mu_B$ to the bulk value $2.2 \mu_B$.

At the concentration of $\text{Fe}_{0.65}\text{Ni}_{0.35}$ the alloy shows the Invar effect [48,49], which is correlated with a nearly vanishing thermal expansion coefficient within a broad temperature interval around 300 K. Fe-Ni alloys in the Invar composition range have a ferromagnetic ground state with a high magnetic moment and a large volume [47]. The underlying principle of this effect is a moment-volume instability [50].

For any deviation from the ideal flat interface due to intermixing of Fe and Ni atoms, the band structure of the interface will be different, leading to a variation in the local magnetic moment of both types of atoms. In Fig. 1.3 three special cases are pointed out, which may result in a strong deviation of local magnetic moments, contributing to an average moment of the bilayer. An intermixing within one monolayer, assuming an equal number of Fe and Ni atoms, gives rise to an $\text{Fe}_{0.50}\text{Ni}_{0.50}$ alloy as sketched in Fig. 1.3 (a,ii) with an average magnetic moment of $1.6 \mu_B$ according to the Slater-Pauling curve. If the alloy ranges over two layers as reported in [51], hypothesizing an Fe concentration gradient towards the Ni film, the second layer may

result in an $\text{Fe}_{0.33}\text{Ni}_{0.67}$ alloy, which is near the Permalloy concentration. The associated average magnetic moment is about $1.4 \mu_{\text{B}}$. Fig. 1.3 (b) illustrates the 12 nearest neighbors of an Fe atom at the Fe/Ni interface within a three dimensional fcc lattice. The Fe atom in the center is surrounded by four Fe atoms (gray spheres) of the top layer and four Ni atoms (bright spheres) of the bottom layer. Moreover, there are four atoms (dark spheres) within the interface plane, each of them being either Fe or Ni atoms. Depending on whether these four atoms are Fe or Ni atoms, different local magnetic moments of the centered Fe atom are expected. Three special cases are singled out in the figure, which correspond to local magnetic moments per Fe atom at (1) the Invar concentration, (2) the Permalloy concentration and (3) in an $\text{Fe}_{0.50}\text{Ni}_{0.50}$ alloy.

1.2 Spin-reorientation transition (SRT)

A *spin-reorientation transition* describes how the direction of the easy axis of the magnetization changes upon variation of e. g. the film thickness or the temperature. The modification of the magnetic anisotropy, which determines the orientation of the magnetization, and corresponding changes of the magnetic domains during an SRT are elucidated in the following.

1.2.1 The role of magnetic anisotropies

The magnetocrystalline anisotropy energy (MAE) is the difference in the free energy density associated with different directions of the magnetization with respect to the crystallographic axes of a crystal. The origin of the MAE is the long range dipole-dipole-interaction and the spin-orbit-interaction. The dipolar interaction gives rise to the shape anisotropy, which for a homogeneously magnetized rotational ellipsoid is given by $K_d = \frac{1}{2}\mu_0(N_x M_x^2 + N_y M_y^2 + N_z M_z^2)$, where $N_x + N_y + N_z = 1$ is the trace of the diagonalized demagnetizing tensor. Ultrathin films of a few atomic layers thickness and a lateral size of some millimeters may be described by an ultrathin disc with infinite lateral size, for which $N_x = N_y = N_{\parallel} = 0$ and $N_z = N_{\perp} = 1$. The shape anisotropy is then given by $K_d = \frac{1}{2}\mu_0(N_{\perp} - N_{\parallel})M^2$, and it always favors an in-plane orientation of the magnetization for ultrathin films. The spin-orbit-interaction causes the magnetocrystalline (intrinsic) anisotropy, which may lead to either an in-plane or an out-of-plane direction of the magnetization. In ultrathin films, the orientation of the magnetization is determined by the balance between the intrinsic and the shape anisotropy. This balance changes as a function of both temperature and film thickness. We use the generally accepted sign convention, i. e. a positive anisotropy constant favors a perpendicular easy axis. A spin-reorientation transition from an out-of-plane to an in-plane orientation of the magnetization will occur, when the shape anisotropy dominates over a large positive magnetocrystalline anisotropy. The easy axis of the magnetization is determined from the minimum of the free energy density F , which for an ultrathin film with a uniaxial magnetic anisotropy along the surface normal may

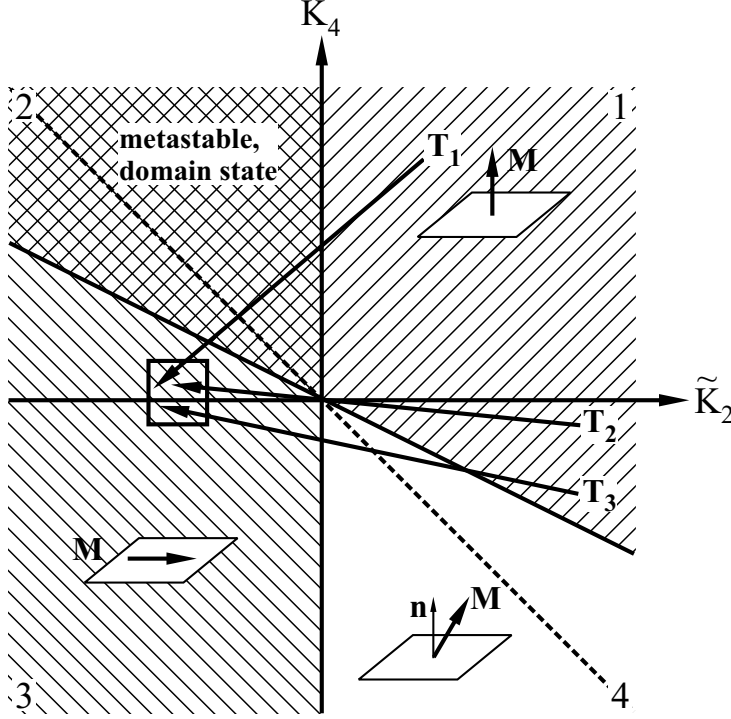


Figure 1.4: Stability diagram of the easy axis of the magnetization without an external magnetic field. Areas of various hatching mean different phases. Three cases of the thickness-driven SRT from out-of-plane to in-plane are illustrated: through the metastable phase (T_1), via the origin (T_2) and through the canted phase (T_3). The dashed line indicates equally deep energy minima. $\tilde{K}_2 = K_2 - \frac{1}{2}\mu_0 M^2$. (After [4,11]).

be written as [11]:

$$F = \left(\frac{1}{2}(N_{\perp} - N_{\parallel})\mu_0 M^2 - K_2 \right) \cos^2 \theta - K_4 \cos^4 \theta \quad (1.5)$$

where θ is the angle of the magnetization M with respect to the surface normal. The effective magnetocrystalline anisotropy constants K_i are commonly separated into a thickness-independent volume coefficient K^V and a thickness-dependent contribution $2K^S/d$ that includes the surface and interface anisotropy constants [52]:

$$K_i = K_i^V + \frac{2K_i^S}{d} \quad (1.6)$$

with $i = 2, 4$ according to the second- and fourth-order constants, respectively, where d is the film thickness.

A consideration of second-order contributions to the anisotropy only ($K_4 = 0$) does not allow for a canted magnetization vector. Instead, a discontinuous reorientation of the magnetization, which is a first-order SRT, takes place as K_2 changes. The first-order SRT is indicated in Fig. 1.4 [4], ³ which displays K_4 versus $\tilde{K}_2 = K_2 - \frac{1}{2}\mu_0 M^2$, by tracing a trajectory from the perpendicular orientation of the magnetization (first quadrant) to the in-plane oriented magnetization (third quadrant) along the \tilde{K}_2 -axis ($K_4 = 0$). The critical thickness d_c for the SRT,

³The diagram has been modified with respect to the notation used for the free energy density given by Eq. (1.5), i. e. the canted and the metastable phase appear in opposite quadrants as compared to the original work, where the free energy density is given by $F = K_1 \sin^2 \theta + K_2 \sin^4 \theta + \frac{1}{2}\mu_0 M^2 \cos^2 \theta$.

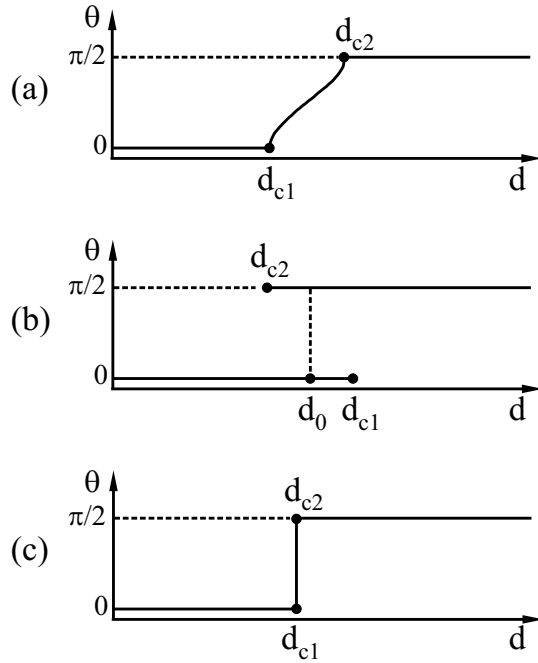


Figure 1.5: Different types of spin-reorientation transitions. The ranges of stability (metastability) are indicated for perpendicular magnetization ($\theta = 0$) and in-plane magnetization ($\theta = \frac{\pi}{2}$). (a) Continuous SRT with a gap between both ranges. (b) Discontinuous SRT with an overlap of the ranges. (c) Special transition. (From [3]).

which arises from the balance $K_2 = \frac{1}{2}\mu_0 M^2$, is given by

$$d_c = \frac{2K_2^S}{\frac{1}{2}\mu_0 M^2 - K_2^V} \quad (1.7)$$

A discontinuous reorientation also occurs if both \tilde{K}_2 and K_4 change during the SRT, such that any trajectory T_2 from the in-plane magnetized state to the perpendicularly magnetized state or vice versa passes the origin in Fig. 1.4. The occurrence of a canted magnetization within a continuous SRT is possible, if the fourth-order anisotropy coefficient $K_4 < 0$. In Fig. 1.4, the trajectory T_3 , which passes through the fourth quadrant, represents such kind of an SRT. If K_4 becomes positive, the trajectory T_1 passes the hatched area of the second quadrant between in-plane and out-of-plane magnetization states, which describes a metastable configuration of the magnetization. In this case a multi domain state of coexisting out-of-plane and in-plane magnetized domains is possible [11].

In general, if K_4 is non-zero, two critical thicknesses arise, i. e. d_{c1} and d_{c2} corresponding to the onset and the completion of the reorientation process, respectively:

$$d_{c1} = d_c = \frac{2K_2^S}{\frac{1}{2}\mu_0 M^2 - K_2^V} \quad (1.8)$$

$$d_{c2} = \frac{2(K_2^S + 2K_4^S)}{\frac{1}{2}\mu_0 M^2 - (K_2^V + 2K_4^V)} \quad (1.9)$$

Three types of spin-reorientation transitions can be distinguished [3]:

1. *Continuous transition* for $d_{c1} < d_{c2}$, see Fig. 1.5(a). Within an interval $d_{c1} < d < d_{c2}$, both the perpendicularly and the in-plane oriented magnetization represent energetic max-

ima with a minimum in between. The magnetization rotates continuously from $\theta(d_{c1}) = 0$ to $\theta(d_{c2}) = \frac{\pi}{2}$ with increasing d . The anisotropy does not disappear.

2. *Discontinuous transition* for $d_{c1} > d_{c2}$, see Fig. 1.5(b). Within an interval $d_{c2} < d < d_{c1}$, both the perpendicularly and the in-plane oriented magnetization represent energetic minima with a maximum in between. The magnetization switches between both minima at the thickness d_0 (between d_{c2} and d_{c1}), where the depths of both energetic minima become equal. The anisotropy does not totally vanish.
3. *Special transition* for $d_{c1} = d_{c2}$, see Fig. 1.5(c). For this transition the anisotropy vanishes. In a real system this transition can hardly be expected.

For a tetragonally distorted film like e. g. Ni/Cu(100) the anisotropic part of the free energy density is given by [33]:

$$F = \left(\frac{1}{2} \mu_0 M^2 - K_2 \right) \cos^2 \theta - \frac{1}{2} K_{4\perp} \cos^4 \theta - \frac{1}{8} K_{4\parallel} (3 + \cos 4\Phi) \sin^4 \theta \quad (1.10)$$

where θ is defined as in Eq. (1.5), and Φ is the azimuthal angle measured against the easy in-plane axis of the magnetization. $K_{4\perp}$ and $K_{4\parallel}$ are the fourth-order terms of the MAE, which account for the disparity of the directions perpendicular and parallel to the plane due to the lattice distortion. In consideration of $K_{4\perp}$ and $K_{4\parallel}$ and under the assumption, that the in-plane easy axis of the magnetization does not change during the SRT, i. e. $\Phi = 0^\circ$, the critical thicknesses of the SRT are determined by:

$$d_{c1} = \frac{2(K_2^S - K_{4\parallel}^S)}{\frac{1}{2}\mu_0 M^2 - K_2^V + K_{4\parallel}^V} \quad (1.11)$$

$$d_{c2} = \frac{2(K_2^S + K_{4\perp}^S)}{\frac{1}{2}\mu_0 M^2 - (K_2^V + K_{4\perp}^V)} \quad (1.12)$$

1.2.2 Spin-reorientation transition of Ni/Cu(100) and Fe/Cu(100) films

The spin-reorientation transition of ultrathin Fe/Cu(100) films as a function of temperature and film thickness shows a behavior, which can be regarded as prototypical for ferromagnetic films on most substrates. This thin film system has a large positive surface magnetic anisotropy at low temperatures and thicknesses, which forces the magnetization perpendicular to the film plane. Upon increasing the temperature or Fe layer thickness the magnetization reorients into the plane. Ultrathin Ni/Cu(100) films on the other hand exhibit a reversed SRT from an in-plane direction at low temperatures and thicknesses to a perpendicular orientation of the magnetization at sufficiently high temperatures and layer thicknesses. In the following two subsections the fundamental microscopic phenomena, which on the one hand lead to the SRT in Fe/Cu(100)

and on the other hand to the anomalous SRT in Ni/Cu(100) films are described separately, in detail.

Fe/Cu(100)

In Fe/Cu(100) films the switching of the magnetization from out-of-plane to in-plane, as the Fe thickness or the temperature is increased, is accompanied by structural changes in the ultrathin film, which have a crucial influence on the magnetic properties. Bulk Fe is known to crystallize in the body-centered-cubic (bcc) phase (α -Fe). The face-centered-cubic (fcc) phase (γ -Fe) is thermodynamically unstable at 300 K [53]. It occurs in the temperature range of 1184 K to 1665 K, and no ordered magnetic structure is found in this high-temperature range [54].

When Fe is deposited on Cu(100), however, a ferromagnetic order exists with a perpendicular magnetic anisotropy between 2 ML and 4 – 5 ML Fe [55,56]. The lattice mismatch between fcc Cu ($a_{\text{Cu}} = 0.361$ nm) and fcc Fe ($a_{\text{Fe}} = 0.359$ nm) is about 1%. At room temperature (RT), ultrathin Fe films have been observed to exhibit a layer-by-layer growth [57–59]. Below 1.6 ML interdiffusion of Fe and Cu occurs due to the relatively higher surface energy of Fe as compared to Cu(100), such that Fe clusters form, which are embedded in the Cu surface [58]. In the subsequent thickness interval up to 4 – 5 ML, Fe films grow in a shear-distorted face-centered-cubic structure as revealed by scanning tunneling microscopy (STM) [60]. It was shown that a few atoms wide bcc-like stripes were formed, which in order to compensate the lattice mismatch lead to a zigzag deformation of the original straight atom rows. The shear angle was found to be $\pm 14^\circ$ [60,61]. The ferromagnetism was earlier explained by a large atomic volume ($V = 0.0121$ nm³) of Fe, which arises from an expansion of both the in-plane and the vertical interlayer distance (tetragonally distorted fcc lattice) [62]. Also the shear-distorted fcc lattice observed by STM is accompanied by an enhancement of the atomic volume, giving rise to the ferromagnetism [60].

Upon increasing the Fe layer thickness, a structural transformation to the fcc phase takes place above 4 ML Fe, which is stable in the range of 5 ML to 10 ML [63]. A good layer-by-layer growth is observed in this thickness range. The Fe layers consist of large islands, having a relaxed fcc structure, and showing a smaller lattice constant of $a = 0.357$ nm ($V = 0.0114$ nm³). This has been predicted theoretically to be associated with an antiferromagnetic order [64] (see Fig. 1.1.2). Elongated bcc phase inclusions are responsible for the observed relaxation [54,65].

Two ferromagnetic “live layers” ($T_C = 280$ K) with a perpendicular anisotropy have been detected in Fe/Cu(100) films between 5 ML and 10 ML thickness by polar magneto-optical Kerr effect (MOKE) measurements [57]. By utilizing Mössbauer spectroscopy the interior layers are found to be paramagnetic at 300 K, and they are in an antiferromagnetic ground state, exhibiting a low magnetic moment of $\mu_{\text{Fe}} < 0.7 \mu_B$, below the Néel-temperature $T_N = 65$ K [66,67]. In

contradiction, one ferromagnetic surface layer in the fct structure with a $T_C = 250$ K, and a $T_N = 200$ K for the interior layers in the fcc structure was reported by Li et al. [29]. Two different spin configurations in the interior layers of a 6 ML Fe/Cu(001) film, namely a stable ground state and a metastable state, respectively, have been determined [68]. In the stable state, pairwise ferromagnetically coupled layers were joined, which couple antiferromagnetically to each other, whereas in the metastable state each layer was found to couple antiferromagnetically to the adjacent one. A recent investigation of an 8 ML Fe/Cu(100) film by means of depth-resolved x-ray magnetic circular dichroism (XMCD) confirmed the existence of two ferromagnetically coupled surface layers. Moreover, strong evidence was found that the inner layers were in a spin density wave (SDW) state, where the amplitude of the SDW was comparable to the magnetic moment in the ferromagnetic (FM) Fe layers. Furthermore, the FM/SDW interface coupling was discovered to be antiferromagnetic [69].

As the Fe thickness exceeds 11 ML, a structural transformation from fcc to bcc occurs, and the magnetization rotates into the film plane with the easy axis along the [110] direction of the Cu-crystal, which in turn is aligned parallel to the [100] axis of Fe. In this state the film is homogeneously magnetized, but it exhibits a rough surface, since it is difficult for the bcc Fe phase to adopt the fcc structure of the underlying Cu-substrate [54]. The structural transformation from γ -Fe to α -Fe, and hence the SRT can be retarded in the presence of oxygen to a thickness of up to 45 ML on top of the Cu. The surfactant effect of oxygen gives rise to an improved layer-by-layer growth of γ -Fe due to a Cu(001)-O($2\sqrt{2} \times \sqrt{2}$)R45° reconstruction. A fully developed bcc structure with an in-plane orientation of the magnetization is achieved around 53 ML Fe [70].

In low temperature-(LT)-grown Fe/Cu(100) interdiffusion between Fe and Cu is reduced, and the films are rougher as compared to RT-grown films. Below 0.9 ML a growth of double-layered islands is observed, followed by a layer-by-layer growth up to 4 – 6 ML, where the SRT occurs [71]. In LT-grown Fe/Cu(001) films, which have been annealed to 300 K, an extremely high value of $K^V = 1.8 \times 10^6$ J/m³ was found, which arises from strain as resulting from a 6% vertical expansion of the distorted fcc Fe layers as compared to the fcc phase. This value of K^V is two orders of magnitude larger than that for bcc Fe films. Both K_2^V and $2K_2^S$ represent large perpendicular anisotropy energies, and they determine the perpendicular easy axis of the magnetization of the distorted fcc Fe film. The SRT toward an in-plane direction of the easy axis of the magnetization around 10 ML was attributed to the reduction of K^S with increasing Fe layer thickness, whereas it was not directly attributed to the structural transformation from fcc to bcc as reported generally [72].

The temperature-driven SRT in ultrathin films of 2.5 – 3.5 ML is found to be a reversible process [27]. The observation of a temperature dependent SRT is based on the temperature dependence of the anisotropy constants. This leads to the conclusion, that the surface anisotropy

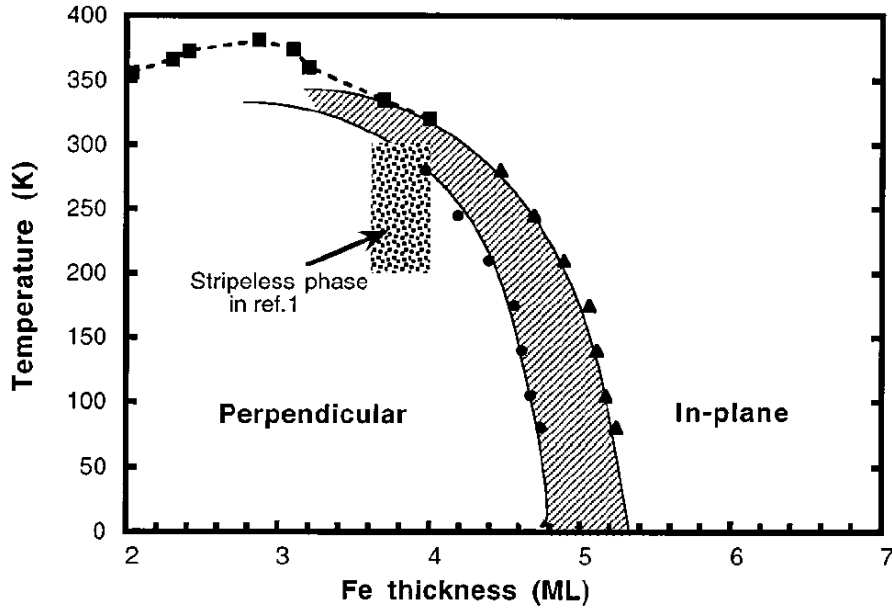


Figure 1.6: Magnetic phase diagram of fct Fe on Cu(100) taken from Ref. [73]. The hatched area is the transition regime in which the magnetization is either canted, or composed of both perpendicular and in-plane magnetic domains. The rectangular shaded area identifies the temperature and thickness regime, in which an fct-to-fcc structural transformation occurs, and where a stripeless phase was found [12].

energy decreases faster than the shape and volume anisotropy energy, when the temperature is increased [74]. Furthermore, the temperature dependence of the magnetocrystalline surface and volume anisotropy constants has been discussed using a spin fluctuation model [75]. The results demonstrate that thermal fluctuations have a much weaker effect on the surface anisotropy as compared to the bulk anisotropy of a cubic material, because for the surface case the next closest energy minimum is 180° away, as opposed to only 90° in the case of the bulk [74].

Across the SRT, the evolution of stripe domains with a preferential orientation along the [001] direction being stable against thermal fluctuations, was theoretically predicted [76]. Such an occurrence of stripe domains was confirmed by spin-polarized scanning electron microscopy [28].

The adsorption of atoms and molecules can affect the SRT decisively. The SRT at 293 K was found to occur under a hydrogen atmosphere of 5×10^{-6} Pa around 6 ML Fe/Cu(001) [77], which is the critical thickness of the magnetization reorientation observed earlier in Fe/Cu(100) films grown and measured at 100 K [78]. Moreover, the fcc phase, which is known to form within the thickness range of about 4 – 10 ML in RT-grown Fe films, did not occur during the film growth under the hydrogen atmosphere at 293 K. Hence, there is strong evidence, that the known different structural phase transitions and the according magnetic properties between LT- and RT-grown and measured Fe/Cu(100) films are due to the adsorption of hydrogen when the film is cooled during growth. In a recent study it was found, that CO on top of an Fe/Cu(100)

film shifts the critical thickness d_c to smaller Fe thicknesses by at most 0.7 ML. This is explained by a reduction of the surface anisotropy term from $K^S = 0.89 \text{ mJ/m}^2$ to $K^S = 0.63 \text{ mJ/m}^2$. Upon oxygen adsorption a complete reorientation of the easy axis into the film plane was observed for all thicknesses down to 2 ML Fe [55].

The coverage of Fe/Cu(100) films with fractions of a Co layer can help to determine the “real” critical thickness $d_c = 3.5 \text{ ML}$ (LT-grown) and $d_c = 4.8 \text{ ML}$ (RT-grown) [31]. Using this method the SRT of Fe is induced by the negative effective anisotropy of the Co coverage, *before* the structural transformation of the Fe film from fct to fcc occurs. The amount of Co, which is necessary for the SRT, decreases linearly with increasing Fe layer thickness. Finally, the extrapolation to an evanescent Co thickness yields the “real” critical thickness of the SRT of Fe/Cu(100). A critical thickness of $d_c = 4.3 \text{ ML}$ (LT-grown) was discovered by using Ni adatoms [79], as if there was no structural phase transition. The reorientation of the easy axis from perpendicular to in-plane results from the in-plane anisotropy of the Fe-Co and Fe-Ni interface, respectively. Using this method with Co-adatoms, Pierce et al. [73] developed the magnetic phase diagram for fct Fe/Cu(100) as depicted in Fig. 1.6. Moreover, it was found that the SRT induced by Co-capping, proceeds via a multi domain formation [80]. By changing the spatial arrangement of the Co atoms on top of the Fe layers as a function of the annealing temperature two opposite SRT directions can be obtained. (i) A temperature of $150 \text{ K} < T_{\text{anneal}} < 250 \text{ K}$ firstly leads to a rotation of the easy axis of the magnetization from out-of-plane to in-plane, and (ii) upon further annealing up to 300 K, the magnetization rotates back into the out-of-plane direction [32].

Investigations of Fe/Cu(100) films by photoelectron spectroscopy revealed that films close to 2 ML Fe thickness have a unique electronic structure, which is not predicted by calculations of bulk fcc Fe, nor do they correspond to bulk bcc Fe. The Fermi-surface exhibits significant changes at the SRT around 4 ML to 5 ML thickness [30].

A reversed SRT from an in-plane to an out-of-plane magnetization orientation, as found for Ni/Cu(100) ultrathin films, is also observed in pulsed-laser-deposited ultrathin Fe/Cu(100) films. Within the thickness range of 2 ML to 5 ML the magnetization lies in the plane, followed by a region where the direction of the magnetization is perpendicular to the surface (6 ML to 10 ML). At a thickness of around 11 ML, the magnetization reorients into the plane again, which is associated with the well known fcc-to-bcc transformation. Observation of this behavior was only possible because of an improved layer-by-layer growth, achieved by the high deposition rate of 1 ML/min [81].

Ni/Cu(100)

The first 15 Ni layers grow pseudomorphically on Cu(100) [82]. Due to the lattice mismatch between fcc Ni ($a_{\text{bulk}} = 0.352 \text{ nm}$) and fcc Cu ($a_{\text{bulk}} = 0.361 \text{ nm}$) the Ni layers grow in the

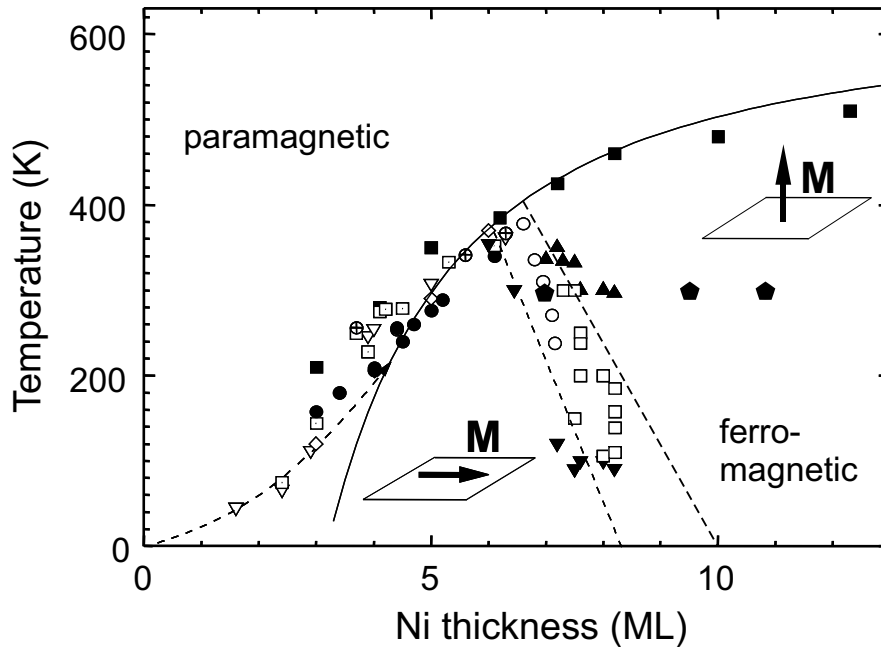


Figure 1.7: Magnetic phase diagram of Ni/Cu(001) as a function of the film thickness d . The solid line indicates the finite size scaling, the straight dashed lines are guides to the eye. Details for the various symbols are given elsewhere [37,84]. The pentagons indicate the SRT thickness at 300 K determined by SPLEEM (this work). In the area between in-plane and out-of-plane orientation of the magnetization solid triangles up (down) indicate out-of-plane (in-plane), open circles and squares mean $0^\circ < \theta < 90^\circ$ orientation of the magnetization. (From [85]).

fect structure on Cu(100). Thereby, the in-plane lattice constant of Ni is expanded by 2.5%, and the vertical interlayer spacing is compressed by 3.2% as compared to the bulk values. This tetragonal distortion is the reason for the large positive volume anisotropy constant $K_2^V = 30 \mu\text{eV}/\text{atom}$ at 300 K [37], which favors an out-of-plane orientation of the magnetization. The positive sign of K_2^V results from the negative magnetostriction constant of Ni [15,33]. Both the Cu-Ni interface anisotropy constant $K_2^{\text{Cu-Ni}} = -59 \mu\text{eV}/\text{atom}$ and the Ni surface-to-vacuum anisotropy constant $K_2^{\text{Ni-vac}} = -107 \mu\text{eV}/\text{atom}$ [83] are negative, and they therefore favor an in-plane orientation of the magnetization. The shape anisotropy $\frac{1}{2}\mu_0 M^2 = 7.5 \mu\text{eV}/\text{atom}$ [9] also favors an in-plane magnetization direction. The only contribution, which favors a perpendicular magnetization direction arises from the magnetocrystalline volume anisotropy, which is the key to understand the anomalous SRT of Ni/Cu(100). Fig. 1.7 shows the magnetic phase diagram of Ni/Cu(001) as a function of the temperature and the layer thickness. Below 5 ML the film is in the paramagnetic state at 300 K. According to a finite size fit (solid line) it becomes visible, how the Curie-temperature T_C of this system depends on the Ni layer thickness. At 5 ML the Curie-temperature reaches room temperature. Between 5 ML and 7 ML the magnetization is oriented in the plane, which means that in this thickness regime the sum of the shape anisotropy

and the negative surface and interface anisotropy overcomes the positive volume anisotropy contribution. Since the sum of the surface and the interface contribution is thickness dependent, according to Eq. (1.6) their influence decreases upon increasing the thickness.

At an initial critical thickness $d_c = 7 - 10$ ML [7,37,86,87], the anisotropies, which favor an in-plane and a perpendicular orientation of the magnetization, respectively, are balanced such that this marks the onset of the SRT to an out-of-plane magnetization orientation. This thickness is given by Eq. (1.7), if higher-order anisotropies are ignored. A more detailed consideration, which accounts also for the data points ranging in the thickness interval between the dotted lines in Fig. 1.7, yields two critical thicknesses d_{c1} and d_{c2} , which are given by Eq. (1.11) and (1.12). The data points between the dotted lines in the figure represent canted magnetization configurations, i. e. the magnetization continuously reorients from an in-plane orientation to an orientation perpendicular to the surface with increasing layer thickness.

In a narrow thickness interval around 7 ML the SRT may also be observed as a function of the temperature. The magnetocrystalline anisotropy coefficients K_2 and K_4 were determined by angular dependent FMR measurements [8,85]. The magnetization angle was found to change continuously, indicating a second-order SRT with an upper and a lower critical thickness d_{c1} and d_{c2} , respectively. The SRT is explained by the temperature dependence of the interface and the volume contributions of the anisotropy [88]. The anomalous SRT via a canted magnetization is also confirmed by theoretical calculations [5], which are in good agreement with the experimental data of Ref. [8,85].

There are a number of conditions, which have been proven to influence the SRT of Ni/Cu(100) films. Studies of the influence of the growth temperature on the SRT reveal, that the critical thickness of LT-grown (170 K) films, which have been annealed to 300 K, is about 1 ML smaller than that of an RT-grown film. A higher density of small rectangular islands is observed in the LT-grown film of 8.5 ML thickness as compared to the RT-grown film, whereas the crystalline structure is fct in both cases. By calculating the difference in SRT thicknesses, $d_c^{RT} - d_c^{LT}$, a reduced surface anisotropy in the LT-grown Ni film is found to be the main reason for the smaller critical thickness [89].

Ni films grown on a stepped Cu-surface, for instance, with a (1 1 32) orientation show nearly the same critical thickness of the SRT (5.5 ML to 7 ML) at 300 K as compared to Ni films grown on a flat Cu(100) substrate. However, a canted magnetization with angles of $20^\circ - 30^\circ$ with respect to the surface normal is observed. In addition, a 90° in-plane rotation of the magnetization is observed, resulting in an orientation perpendicular to the step edges [90]. A spiral-like rotation of the magnetization vector from an in-plane orientation parallel to the step edges, to an out-of-plane orientation perpendicular to the steps has been discovered, which is explained by an extra anisotropy originating from steps at the Cu(001) surface [10]. A systematic investigation of the SRT thickness was performed by Bovensiepen *et al.*, who grew

Ni films on curved Cu(001) substrates. These measurements indicated that the SRT thickness is invariant in a range of $0^\circ - 7^\circ$ of the vicinal angle [24]. Calculations ($T = 0$) of a Ni film with a (1 1 13) stepped surface predicted an additional SRT, in which the magnetization turns from parallel to perpendicular to the step alignment with increasing Ni film thickness. This should originate from the presence of a uniaxial magnetoelastic volume anisotropy contribution, caused by tetragonal strain in the film due to film/substrate lattice mismatch, however, at a thickness of about 16 ML [91].

The SRT has also been studied on planar Cu-substrates with different crystallographic orientations such as Cu(100) in comparison to Cu(110) and Cu(111). Qualitatively, the same SRT as compared to Ni/Cu(100) films was reported by Wu *et al.* [92], however, at a much larger re-orientation thickness of $d_c = 16$ ML at 300 K. In contradiction to this result, no easy axis of the magnetization perpendicular to the surface was found in Ni/Cu(110) films up to 28 ML thickness in a recent study at 300 K [93]. No perpendicular magnetization is detected in Ni/Cu(111) films down to 3 ML [92].

Capping of an ultrathin Ni/Cu(100) film with a non-magnetic layer like Cu, reduces the critical thickness of the SRT, because the Ni-Cu interface anisotropy –although negative– is smaller than that of the Ni surface of the respective uncapped film. 1 nm of Cu reduces the critical thickness by 1 ML [23]. Using a cap of the same element as for the substrate like in Cu/Ni/Cu allows one to differentiate between the interface anisotropy $K_2^{\text{Cu-Ni}}$ and the surface anisotropy $K_2^{\text{Ni-vac}}$, by comparison with the $2K_2^S$ of the uncapped Ni/Cu(100) film⁴. On the other hand, capping ultrathin Ni/Cu(100) with 2 ML of Co increases the magnitude of the surface anisotropy, which forces the magnetization of the Ni film in-plane, at least for thicknesses up to 18 ML [94].

Another procedure, which leads to an SRT from perpendicular to in-plane, has recently been investigated for 6 nm and 9 nm Cu-capped Ni/Cu/Si(001) films without changing the film thickness or temperature. Irradiation of the film with 1 MeV C⁺-ions reduced the in-plane strain, such that the magnetization reoriented into the film plane [95].

Growth temperature as well as the exposure of adsorbates can significantly shift the critical thickness d_c of the SRT. A complete hydrogen coverage for example reduces d_c by about 4 ML with respect to a clean Ni surface [9], which in turn is in good agreement with a theoretical analysis [67]. Also adsorption of CO decreases d_c due to a decrease of the surface anisotropy [96]. Besides, an improved layer-by-layer growth after oxygen preadsorption onto the Cu(001) surface is observed, the SRT is shifted from about 10 – 11 ML (without preoxidation) to about 5 ML Ni thicknesses. Additionally, an in-plane rotation of the magnetization from the [110] to the [100] direction is obtained, when the Ni film is grown on the oxygen-pre-covered Cu(001) [83,97].

⁴ $2K_2^S = K_2^{\text{Cu-Ni}} + K_2^{\text{Ni-vac}}$

1.3 Magnetic domains

This chapter addresses the nature of magnetic domains in ultrathin ferromagnetic films. In section 1.3.1 the formation of magnetic domains in the thermodynamic equilibrium as a consequence of the long-range magnetic dipole-dipole interaction is outlined. Typical types of domain walls separating both perpendicularly and in-plane magnetized domains are described in section 1.3.2. An extensive review about various types and the formation of magnetic domains can be found in the textbook of Hubert and Schäfer [17].

1.3.1 The thermodynamic ground state of magnetic domains

In its thermodynamic ground state a ferromagnet usually consists of differently oriented magnetic domains, i. e. regions in which the magnetic moments are aligned parallel. The exchange interaction is responsible for this parallel alignment of magnetic moments, and it is restricted to short-range interaction among adjacent spins. Magnetic domains are formed, in order to reduce the energetically unfavorable magnetic stray field outside of the sample, which originates from the long-range dipole-dipole interaction. However, energy is consumed in order to configure the domain walls, i. e. the transition regions between the domains. Within a domain wall, the magnetization rotates continuously from its direction within one domain into the direction within an adjacent domain. This results in energetically unfavorable orientations of the magnetic moments with respect to the easy axes determined by the magnetic anisotropy. The two simplest types of domain walls are Bloch walls and Néel walls, which are described in section 1.3.2. The total free energy density of a domain configuration is given by the sum of the exchange energy, the magnetocrystalline anisotropy, the dipolar energy, the magneto-elastic energy and the Zeeman energy (if an external magnetic field is applied). By minimizing the total free energy density the most stable domain configuration is then attained.

1.3.2 Domain walls in ultrathin films

The width of a domain wall is determined by the competition between the exchange energy, which is lowest for a large number of magnetic moments including small canting angles between each other, and the anisotropy energy, which favors a low number of magnetic moments oriented off the easy direction of the magnetization. The exchange contribution to the surface energy density σ (J/m²) of a 180°-domain wall is given by [46]:

$$\sigma_{ex} \approx J S^2 \frac{\pi^2}{N a^2} \quad (1.13)$$

where J is the exchange integral, S the spin quantum number, N the number of atomic magnetic moments and a the lattice constant. An increase of N denotes an increased number of magnetic

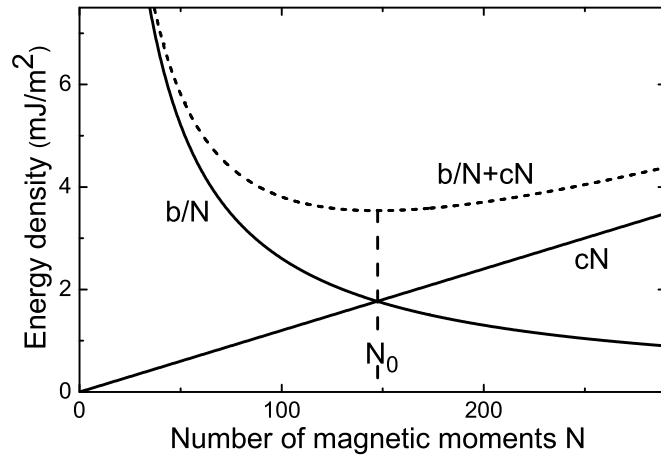


Figure 1.8: Determination of the equilibrium number N_0 of magnetic moments involved in the reorientation transition within a domain wall of a bulk-like Fe/Cu(100) film by minimization of the sum of exchange b/N and anisotropy energy density cN (Eq. (1.15)). The minimum of the sum (dotted curve) occurs for $b/N = cN$, i. e. $N_0 = \sqrt{b/c} = 147$ using $J = 2.16 \times 10^{-21}$ J, $K_2^{\text{eff}} = 4.2 \times 10^4$ J/m³ and $a = 2.86 \times 10^{-10}$ m.

moments oriented in directions of higher anisotropy energy density according to:

$$\sigma_{an} \approx K_2 N a \quad (1.14)$$

K_2 being the uniaxial anisotropy. The equilibrium wall thickness results from the minimization of the sum

$$\sigma_{ex} + \sigma_{an} \approx J S^2 \frac{\pi^2}{N a^2} + K_2 N a \quad (1.15)$$

with respect to N .

In Fig. 1.8 the dependence of the total energy density $b/N + cN$ (b and c are the abbreviations of the prefactors of N) on N for a bulk-like Fe/Cu(100) film is depicted. The minimum of the energy density yields the equilibrium number of spins $N_0 = \sqrt{b/c} = \sqrt{J S^2 \pi^2 / K_2^{\text{eff}} a^3} = 147$, which contribute to the rotation within the domain wall of the width $w = N_0 a \approx \pi \sqrt{A / K_2^{\text{eff}}}$. The according surface energy density is given by $\sigma_{dw} \approx 2\pi \sqrt{A K_2^{\text{eff}}}$, where $A = J S^2 / a = 1 \times 10^{-11}$ J/m is the exchange stiffness constant. The parameters⁵ used to determine N_0 are $J = 2.16 \times 10^{-21}$ J, $K_2^{\text{eff}} = 4.2 \times 10^4$ J/m³, $S = 1$ and $a = 2.86 \times 10^{-10}$ m (values taken from Ref. [16], p.408 and 413). The wall width corresponding to $N_0 = 147$ is about 42 nm. Since domain walls form a *continuous* transition between two domains, there is no unique definition of the domain width. The classical definition is based on the slope of the magnetization angle, and it is consistent with the wall width determined by the minimization of the total energy density. However, for domain imaging methods using electrons, which detect the projection of the magnetization within a domain wall, the width of a 180°-wall is given by $w = 2\sqrt{A / K_2^{\text{eff}}}$ (p. 219 of Ref. [17]).

Fig. 1.9 illustrates the rotation of the magnetization vector from one domain to the other through the two simplest cases of a 180°-domain wall, i. e. a Bloch wall (a) and a Néel wall

⁵The value of the exchange integral is determined from $J = 0.15 k_B T_C$ [16] using $T_C = 1043$ K for bulk bcc Fe

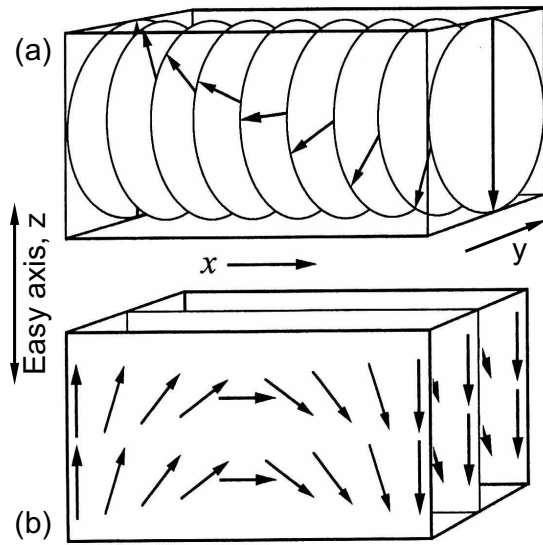


Figure 1.9: Rotation of the magnetization between two domains of a uniaxial material through a 180° -wall. Two different rotation modes are shown: The Bloch wall (a) is the optimum mode, whereas the Néel wall (b) is less favorable here but can be preferred in ultrathin films and in applied fields. The opposite reorientation direction is possible for both modes. (From [17]).

(b). The magnetic moments in a Bloch wall rotate in the y - z -plane, whereas the x - z -plane is the plane of rotation in a Néel wall with z being the easy axis of the magnetization. If the thickness of a thin film with an in-plane anisotropy becomes comparable to the Bloch wall width, a transition between two domains via an in-plane rotation like in Néel walls has a lower energy than a Bloch wall. Fig. 1.10 shows the model for a Bloch and a Néel wall approximated by an elliptical cylinder of width W and height D . The demagnetizing factor of this cylinder along the perpendicular magnetization direction is $N_{\text{Bloch}} = W/(W + D)$ for a Bloch wall and $N_{\text{Néel}} = D/(W + D)$ for a Néel wall, which is smaller than N_{Bloch} for $W > D$. A transition between the two wall modes, which is connected with a minimum in wall width and a maximum in the specific wall energy, was predicted by Néel [17]. The right hand side of Fig. 1.10 illustrates that the reduction of the magnetic charges due to an in-plane oriented external magnetic field, applied perpendicular to the easy axis of the magnetization, is much more pronounced in Néel walls as compared to Bloch walls. In complex composite walls, termed cross-tie walls [98], the energy is even lower than in a 180° -Néel wall because they consist mainly of energetically favorable 90° -walls. However, this kind of walls generally do not occur in ultrathin films. In the center of ultrathin films with perpendicular anisotropy domain walls are generally considered to be Bloch walls. At the surface the stray field of the domains acts on the wall, which may result in a rotation of the surface near magnetic moments into the Néel wall mode, in order to avoid energetically unfavorable stray fields reaching into the vacuum.

Whereas domain walls in bulk materials generally scale with the exchange length of the anisotropy energy $\xi = \sqrt{A/K_2}$, walls in thin films scale with the exchange length of the stray field $\xi_d = \sqrt{A/K_d}$, which becomes important in Néel walls. A completely analytic

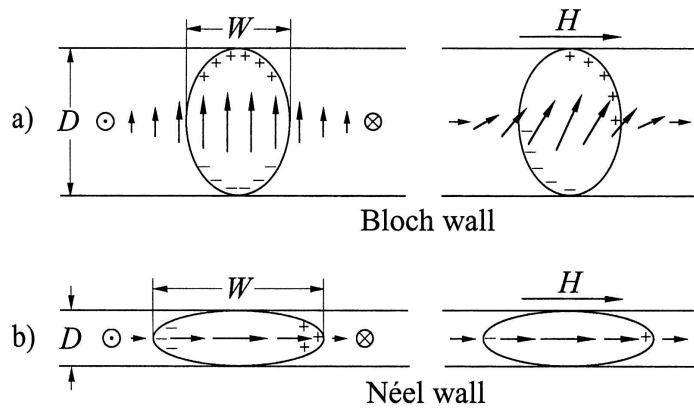


Figure 1.10: Cross section through a Bloch and a Néel wall in thin films of different thickness D and wall width W . The magnetic charges are indicated with and without applied field. (From [17]).

computation like for walls in the bulk is not possible in ultrathin films, where the wall profile needs to be explored by variational procedures or numerical test functions [17]. In particular, the problem of computing symmetric Néel walls is due to the decomposition of these walls into three parts of different scale: a sharply localized core interacts with two widely spread tails, in which a large part of the total rotation takes place. Riedel and Seeger [99] found an approach to solve this issue by separating the mathematical description into a differential equation for the core and an integral equation for the tail. The analytic solution for the core yields:

$$W_{core} = 2\sqrt{A(1-h^2)/[(K_2 + K_d)(1-c_0)^2]} \quad (1.16)$$

where c_0 is the so-called core-tail boundary value which can range from $h = \frac{H M_s}{2 K_2}$ to 1, H being an in-plane magnetic field perpendicular to the easy axis, and M_s is the saturation magnetization. The tail width, which is determined by the balance of the stray field energy (K_d) and the anisotropy energy density (K_2), reads:

$$W_{tail} = e^{-\gamma} D K_d / K_2 \quad (1.17)$$

where $\gamma \approx 0.577$ is Euler's constant and D is the film thickness. The opposite effect of the stray field energy on the core width and the tail width is apparent: As K_d increases, the core width decreases while the tail width increases.

A consequence of the extended tails of a Néel wall is the interaction between them in an ultrathin film. Depending on the direction of rotation, i. e. the chirality, Néel walls can attract each other in the case of opposite chirality, 'because they generate opposite charges in their overlapping tails' [17]. If they are not pinned they can annihilate each other or can form double walls as observed for a Mo-Permalloy film of 14.7 nm thickness [15,100]. In the case of equal chirality the walls repel each other, which results in large in-plane magnetized domains. Again, domain wall pinning at defect sites or substrate step edges can limit the domain size. The interaction of Néel walls was found to extent over distances on the order of 100 μm in 50 nm thick Permalloy films [17].

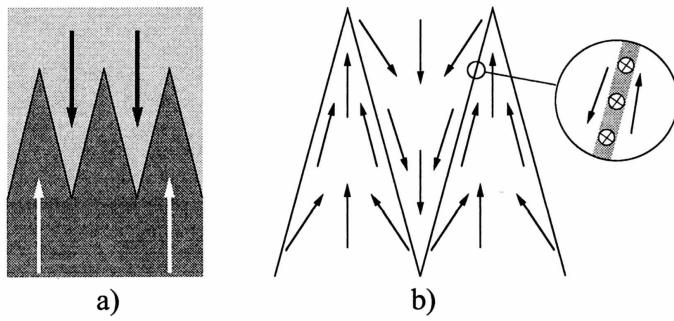


Figure 1.11: Zigzag-shaped charged domain wall separating two domains meeting “head-on” (a) and the formation of an uncharged Bloch type core within a zigzag wall. (From [17]).

Contrary to bulk materials, charged walls can be frequently observed in thin films. One typical situation of a charged wall is depicted in Fig. 1.11 (a) where two domains meet “head-on”. In this situation the separating domain wall develops a sawtooth shape to reduce the charge density, which would be highest for a straight wall. As the zigzag angle is decreased the charge density is decreased at the expense of wall surface. In order to reduce the stray field energy in the vicinity of the core, long-range tails are formed comparable to the tails of Néel walls. The core remains almost uncharged at an alignment of the magnetization as shown in Fig. 1.11 (b). This concept was introduced by Finzi and Hartmann [101], and it was experimentally confirmed for materials used as magnetic storage media [102–104]. Depending on the film thickness, the core which is sketched to be of Bloch type in Fig. 1.11 (b) can also be that of a Néel or cross-tie wall [17].

Considering the size Δ of perpendicularly magnetized domains as a function of the layer thickness d , the theory of Kittel [18] predicts an increase of the domains according to $\Delta \propto \sqrt{d}$. However, experimentally a linear increase of the domain size with increasing thickness was found for ultrathin Co/Au(111) films below the thickness of the spin-reorientation transition [105]. This linear increase as a function of the thickness can be understood, if the thickness dependent surface anisotropy part $2K_2^S/d$ makes the major contribution to the effective anisotropy, i. e. for ultrathin films. If the volume contribution K_2^V is neglected, the domain width Δ may be written as $\Delta = \sqrt{\sigma/2K_2^S} d$, σ being the energy density per unit area of a 180° -domain wall between two domains [106]. In in-plane magnetized ultrathin layers, where the stray field lies in the film, the size of the domains can be orders of magnitude larger. This can be understood in terms of a repulsive interaction of Néel walls, which are energetically favorable in ultrathin in-plane magnetized films [17].

1.3.3 The stripe domain state

At the onset of ferromagnetic order as a function of the thickness in an ultrathin film with perpendicular anisotropy, as well as in the vicinity of the spin-reorientation transition or magnetization reversal at the SRT by an in-plane oriented external field (e. g. [107]), a perpendicular single

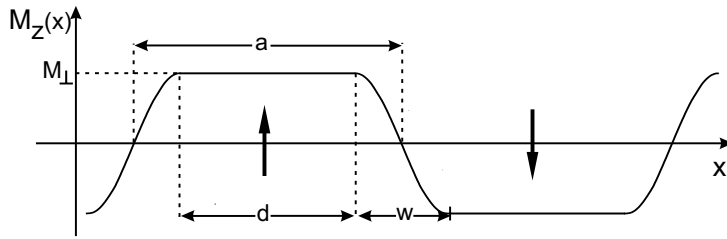


Figure 1.12: Profile of a perpendicularly magnetized stripe domain state of a monolayer. $M_z(x)$ varies as $\cos(\pi x/w)$. The arrows indicate the orientation of the magnetization. After [108].

domain state is unstable. This is due to the fact that the surface contribution of the magnetocrystalline anisotropy $2K_2^S > 0$ becomes weaker compared to the long-range dipolar interaction, which favors an in-plane orientation of the magnetization. At a still sufficiently large $2K_2^S$ the magnetization does not reorient into the plane, but the domains break up into alternating up and down magnetized stripe domains, whereby the stray field energy is reduced. The reduction of the stray field energy, however, is accompanied by an increase of domain wall energy, leading to a spatially modulated magnetic structure near the spin-reorientation transition, which in the simplest case is a stripe pattern.

Yafet and Gyorgy [108] calculated the profile of a stripe domain pattern of a monolayer with perpendicular anisotropy at $T = 0$. They assumed a simple domain configuration of a film lying in the x - y -plane as illustrated in Fig. 1.12. The profile of the magnetization varies along the x -axis with the period $2a$ and is constant in y -direction. The stripes are separated by domain walls, in which the magnetization rotates in the y - z -plane according to a Bloch wall which has a lower energy than a Néel wall for perpendicularly magnetized films. In the regions of the width $d = a - w$ the perpendicular component of the magnetization is constant and equals the saturation magnetization M_0 :

$$M_z(x) = \pm M_0 \quad (1.18)$$

In the regions w the z - and the y -component of the magnetization are given by:

$$M_z(x) = \pm M_0 \cos\left(\frac{\pi x}{w}\right) \quad (1.19)$$

$$M_y(x) = \pm \sqrt{M_0^2 - M_z^2}. \quad (1.20)$$

Minimization of the total energy, which is the sum of the dipolar stray field energy, the anisotropy energy and the exchange energy, with respect to $\delta = \frac{w}{a}$ leads to the energetic description of the domain pattern of a ferromagnetic monolayer. The domain configuration turns out to be very sensitive to the dimensionless quantity

$$f = \frac{K_2^S}{\frac{1}{2}\mu_0 M_0^2 a_0 c} \quad (1.21)$$

in which K_2^S is the positive surface anisotropy, $c = 1.0782$ is specific to the square lattice and reflects its discreteness, and a_0 is the lattice constant. The minimum value $f = f_{\min}$, for which

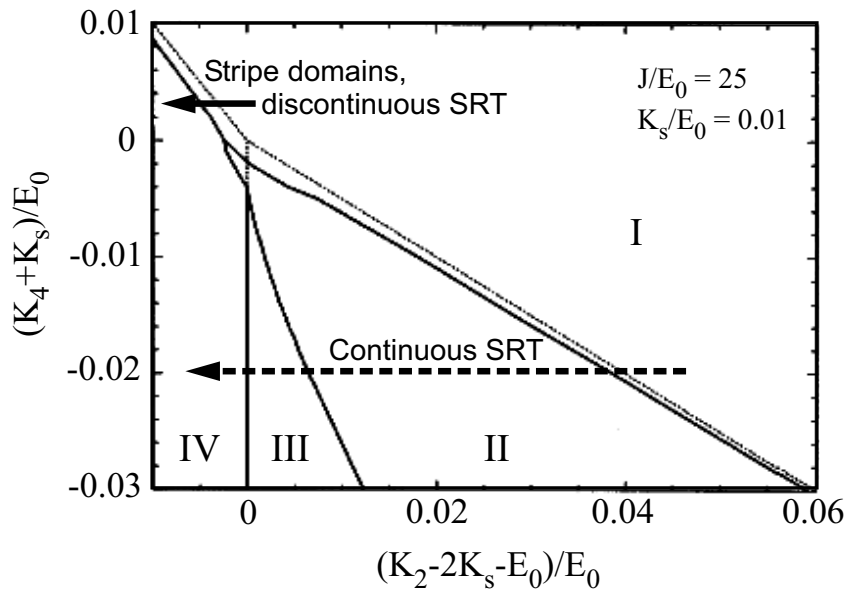


Figure 1.13: Magnetic phase diagram of a monolayer at $T = 0$ in the (K_2, K_4) plane. Assuming a periodic domain structure four different magnetic phases are separated by the solid lines: a domain phase with a perpendicular (I) and a canted (II) orientation of the magnetization within the domains, and uniform phases with a canted (III) and an in-plane (IV) magnetization. The dotted lines indicate the boundaries between magnetic phases if only uniform phases are considered. From [11].

domains occur corresponds to $\delta = 1$ and, as f increases from f_{\min} , the domain configuration becomes energetically stable. Moreover, at $\delta = \frac{w}{a} = 1$ the profile of the domain pattern is purely cosine-like, i. e. the flat part d in Fig. 1.12 has shrunk to zero. This occurs as a consequence of the strong exchange energy competing only with the weak dipolar energy. An increase of f of only 4% corresponds to a reduction of δ by two orders of magnitude and results in a drastic increase of the domain size. Typical values for which domains are stable are given by $1 < f < 1.4$.

Jensen *et al.* [11] calculated the magnetic phase diagram of a monolayer at $T = 0$ in the $(K_2 - K_4)$ plane as shown in Fig. 1.13. By taking second- and fourth-order uniaxial anisotropies into account, they point out the role of the domain formation, using ratios of the exchange coupling J , the demagnetizing energy E_0 and the quartic in-plane anisotropy of the (100) face K_s of $J/E_0 = 25$ and $K_s/E_0 = 0.01$ appropriate for 3d transition metals. In agreement with Ref. [108] ‘for $K_4 = K_s = 0$, a stripe domain phase with a perpendicular orientation of the domains is more favorable than the uniform perpendicular magnetization for large values of $K_2 > E_0$ ’ [11] (region I). Within this phase, for $(K_4 + K_s)/E_0 > 0$, the width of the stripe domains decreases almost exponentially with decreasing K_2 until a cosine-like profile of the stripe domain pattern is reached and a discontinuous SRT to the uniform in-plane magnetization (region IV) occurs. This is indicated by the solid arrow in Fig. 1.13. In contrast, for $(K_4 +$

$K_s)/E_0 < 0$, the domain width does not decrease any longer with decreasing K_2 , but it stays almost constant within the canted domain phase (region II), while the canting angle of the magnetization rises. The domain width increases again at the value of K_2 , where the canted uniform magnetization emerges (region III), and the canting angle further rises until finally, an in-plane magnetized single domain state occurs for $(K_2 - 2K_s - E_0)/E_0 < 0$ (region IV) [11,109]. This continuous SRT is indicated by the dotted arrow in Fig. 1.13. For comparison, the dotted lines in the figure indicate the boundaries between magnetic phases if only uniform phases are considered.

2 Experimental details

2.1 SPLEEM

The spin-polarized low energy electron microscopy (SPLEEM) measurements have been performed at the National Center of Electron Microscopy (NCEM [110]) at the Lawrence Berkeley National Laboratory in Berkeley, California, USA. Besides the principles of the interaction of spin-polarized low energy electrons with matter, the mode of operation of the SPLEEM instrument is described in section 2.1.1. A comparison with other magnetic domain imaging methods follows in section 2.1.2.

2.1.1 Mode of operation

Magnetic contrast (MC) in SPLEEM is based upon the exchange interaction $E_{ex} = \sum_{ij} J(\mathbf{r}_i - \mathbf{r}_j) \mathbf{s}_i \cdot \mathbf{s}_j$ between the incident electrons with spin \mathbf{s}_i and the target electrons with spin \mathbf{s}_j at their positions \mathbf{r}_i and \mathbf{r}_j , J being the exchange coupling constant. In regions with preferred spin alignment \mathbf{s}_j a non-zero magnetization $\mathbf{M} \propto \sum_j \mathbf{s}_j$ exists, which gives rise to a magnetic contribution proportional to $\mathbf{P} \cdot \mathbf{M}$ to the scattered signal if the incident beam is spin-polarized with a polarization $\mathbf{P} \propto \sum_i \mathbf{s}_i$ [21]. In a crystal the occurrence of magnetic contrast can also be explained in terms of the spin-dependent band structure in which spin-up and spin-down electrons have different energies. This is illustrated in Fig. 2.1 (a) where, as an example, the spin-down and spin-up bands above the vacuum energy, which are the relevant bands for the incident electrons, are shown for normal incidence on the [0001] surface of hcp Co (Ref. [111]). For energies of the incident electrons below ≈ 1 eV the incident beam is reflected because there are no allowed states in the crystal independent of the spin orientation of the electrons. The strongest effects on the reflectivity appear when states are unavailable for electrons with a certain polarization, while states are available for electrons with the same energy but opposite polarization. Spin-down electrons with an energy between 1 and 2 eV above the vacuum level, which corresponds to the gap between the spin subbands in Fig. 2.1 (a), cannot exist in the crystal and are therefore totally reflected, whereas the spin-up electrons are able to enter the crystal band structure and are poorly reflected [111]. When \mathbf{P} is adjusted by the illumination optics, the reflectivity depends on the orientation of \mathbf{M} with respect to \mathbf{P} and therefore, the magnetic domain structure can be imaged with high contrast in this energy range. Above the

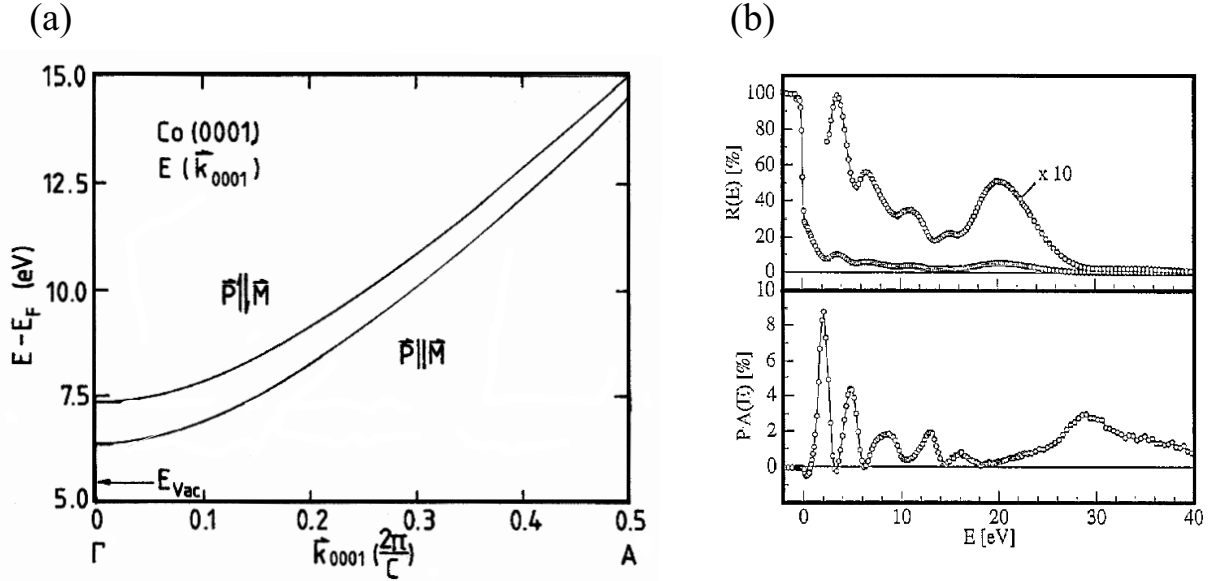


Figure 2.1: (a) Band structure of Co above the vacuum level in the [0001] direction (From [111]). (b) Oscillation of the measured reflectivity R (top) and asymmetry PA from a 6 ML Co/W(110) thin film as a function of the energy of the electrons. (From [112]).

upper band in Fig. 2.1, allowed states exist for both spin orientations and the magnetic contrast decreases with increasing energy until the next spin-dependent band discontinuity is reached. Some magnetic contrast, however, remains which can be enhanced by subtracting two images with opposite spin directions [113]. In the individual images also topographic contrast occurs. Since the topographic contrast is independent of \mathbf{P} and the magnetic contrast is proportional to $\mathbf{P} \cdot \mathbf{M}$ the resulting images reveal pure magnetic contrast. If I^\uparrow and I^\downarrow are the intensities at the same site in two images recorded with opposite \mathbf{P} , and the images are normalized by their sum, an image is obtained which is proportional to the reflectivity asymmetry A ,

$$P_0 A = \frac{I^\uparrow - I^\downarrow}{I^\uparrow + I^\downarrow} \quad (2.1)$$

P_0 being the polarization of the incident beam ($\approx 20 - 25\%$). Since spin-dependent magnetic contrast is determined by the spin-dependent band structure, the exchange asymmetry oscillates with energy. In ultrathin films, where the electron wavelength and penetration depth becomes comparable to the film thickness at very low energies, there is another important consequence of the fact that the k -values are different of the two bands at a given energy, namely the resonance conditions for standing waves which arise in such films are different. The resulting oscillations of the asymmetry due to this quantum size effect [114,115] is displayed in Fig. 2.1 (b). The quantum size oscillations vanish if the film thickness exceeds about 20 ML because their frequency increases rapidly with increasing thickness. The reflectivity oscillation due to the band structure, however, remains [21].

In order to maximize the magnetic contrast it is desirable to align \mathbf{P} parallel to any local

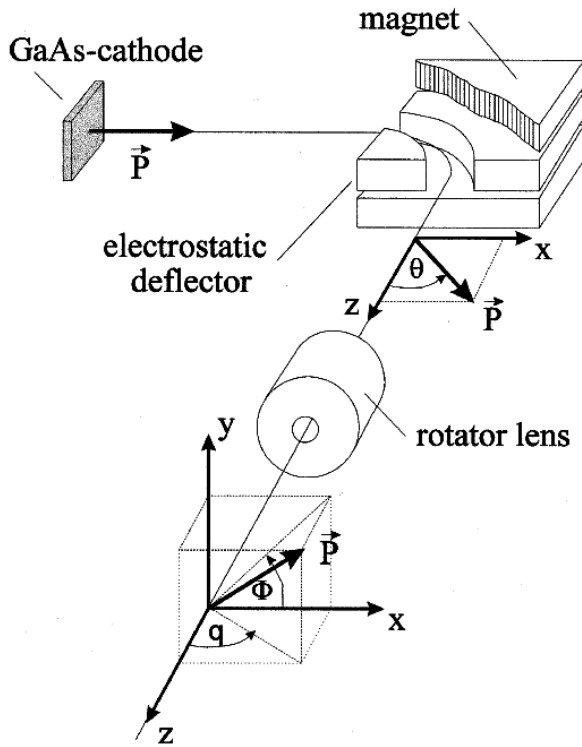


Figure 2.2: Schematic arrangement of the electrostatic and the magnetic deflectors of the SPLEEM instrument, which are used to bend the path of the laser excited electrons onto the microscope axis z . By means of the deflectors in combination with a magnetic rotator lens the direction of the polarization vector \mathbf{P} is adjusted with respect to the (x, y) sample plane. (From [20]).

magnetization \mathbf{M} , i. e. to rotate \mathbf{P} in any direction in space. The setup which allows this rotation of \mathbf{P} by electron optical means is the polarization manipulator shown schematically in Fig. 2.2 [20]. With the photon energy slightly larger than the bandgap of the GaAs-based semiconductor cathode, electrons are excited by circularly polarized light from the spin-split levels at the top of the valence band. Transition probabilities lead to an unequal population of the two spin states in the conduction band [116,117]. Normally, conduction electrons are not able to escape from the crystal due to the high electron affinity, but emission can be enhanced by lowering the vacuum level below the minimum of the bulk conduction band. This negative electron affinity condition is generated by depositing a caesium-oxide layer onto the crystal surface [118]. The excited electrons are polarized longitudinally by the circularly polarized laser beam. A 90° -deflection by the electrostatic sector field does not influence the polarization vector \mathbf{P} . Consequently, \mathbf{P} is oriented normal to the propagation directly after the sector field. If the electrostatic sector is turned off and the deflection is attained by the magnetic sector field, \mathbf{P} follows the trajectory of the electron as anticipated by the equation of motion for the polarization [119], resulting in a longitudinally polarized beam [111]. By superposition of the electric and the magnetic deflection fields, any orientation of \mathbf{P} can be obtained between $0^\circ < \theta < 90^\circ$ within the (x, z) -plane according to Fig. 2.2. After passing the 90° -deflector the electrons enter a magnetic lens, whose longitudinal magnetic field causes a precession of the transverse component of \mathbf{P} around the beam axis when the lens is excited. A combination of both the magnetic and the electric deflector as well as the magnetic rotator lens allows to rotate

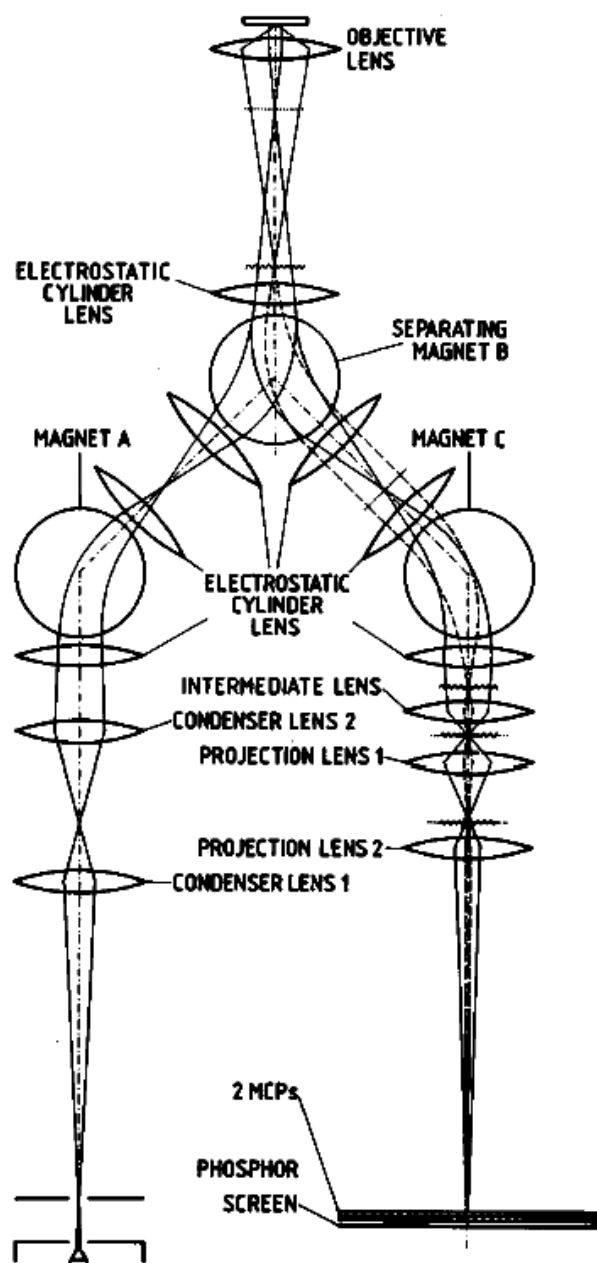


Figure 2.3: Electron optical schematic diagram showing the trajectories (dashed-dotted line) within the illumination column (left hand side) and the imaging column (right hand side). On the left hand side the solid lines shows optimum illumination, on the right hand side they represent rays in LEED mode, whereas the dashed lines stand for rays in LEEM mode. The sample resides in front of the objective lens. The low energy electrons are elastically backscattered into the direction of the imaging column. (From [120]).

P into any desired direction.

The trajectories of the electrons through the microscope after passing the spin manipulator is shown in Fig. 2.3. The spin-polarized electron source resides near the lower left part of the sketch, which is the entrance of the illumination column. Electrostatic lenses are used to focus the beam, and sector magnets deflect the beam twice before it passes the electrostatic tetrode objective lens [120]. Due to the variation in focal length with energy and the energy spread of the electron source, electron optical lenses focus electrons poorly at energies much less than a few keV [121]. Therefore, the electron optical columns are operated at a high energy of the electrons of 3 keV. To obtain low energy electrons at the sample, a strong, homogeneous retarding electric field between the objective lens and the sample, which is at ground potential,

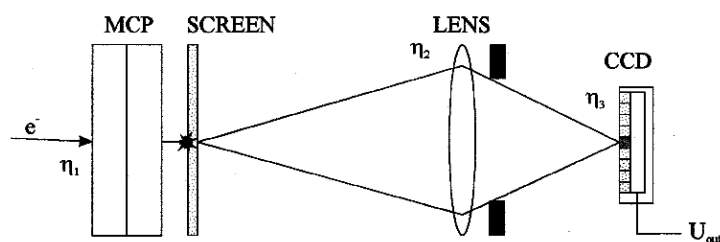


Figure 2.4: Simplified sketch of the detection system. The backscattered electrons are multiplied in two coupled multichannel plates (MCP) and the resulting image is displayed on a phosphorous screen, which is observed by a CCD camera. (From [111]).

decelerates the electrons to an energy of typically below 10 eV before they reach the sample at normal incidence. The distance between the sample surface and the objective lens is about 1.5 mm. The potentials of the first lens of the objective and of the rest of the instrument are 12.5 kV and 3 kV, respectively. Elastically backscattered electrons are accelerated again toward the imaging column, where electrostatic lenses and bending magnets finally guide the electron beam toward a multichannel plate (MCP). The specular beam finally forms a magnified real space image on a phosphorous screen, which is observed by a CCD camera, as sketched in Fig. 2.4. In order to prevent any disturbance of the electron beam by the magnetic field of the earth and electromagnetic radiation of the environment, the microscope resides within in a μ -metal shielding. At the site of the electron source the magnetic field is compensated by means of three pairs of Helmholtz coils. More details about the operating mode of the SPLEEM can be found elsewhere [20,21,111,120,122].

The contrast mechanism in low energy electron microscopy (LEEM) can be divided into two classes, i. e. diffraction and phase contrast. Diffraction contrast arises from local variations of the structure factor. In bright-field imaging at normal incidence it is due to geometric differences between different structural phases, for example, surface reconstructions of atoms on a clean crystalline substrate.

Two important mechanisms of the phase contrast are step contrast and quantum size contrast; both provide atomic resolution perpendicular to the surface. On surfaces with terraces separated by atomic steps the geometric step contrast arises from the interference of electron waves being reflected from opposite sides of a step. Due to the difference of the path lengths of these electrons, the interference arises from the acquired phase shift. At energies below 10 eV the wave length of the electrons is on the order of the atomic step height and thus small changes in the energy lead to a wide range of phase shifts, and consequently to various interference conditions [114]. The quantum size contrast is based on the quantum size effect (QSE), which results from the interference between the electron waves being reflected from the surface of a thin film and from the substrate, respectively. The two phase contrast mechanisms are depicted in Fig. 2.5. To find the optimum magnetic contrast for the Ni/Cu(100) films several series of

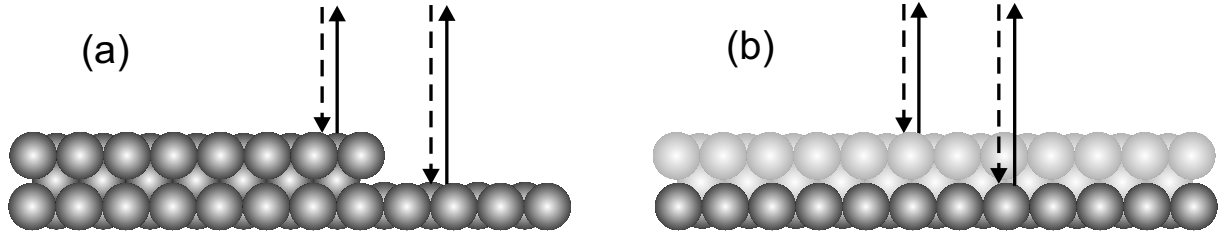


Figure 2.5: Mechanisms of the LEEM phase contrast. (a) step contrast, (b) quantum size contrast.

SPLLEEM images at different electron energies and different Ni thicknesses were taken. The exchange asymmetry oscillates between 4 and 11 eV with a maximum at about 9.2 eV. Note, that our energy scale is measured with respect to the Fermi level, i. e. to obtain the electron kinetic energy, the difference in the work functions of the sample and the cathode must be subtracted (about 3 eV). At about 4.5 eV the MC is reversed and much weaker than at 9.2 eV. Between 5 and 8 ML the maximum shifted only by a few tenth of 1 eV. All Ni domain images presented in this work were recorded at $E = 9.5$ eV. The same procedure was done for Fe/Cu(100) films with the result that optimum magnetic contrast was achieved at $E = 4.5$ eV. At this energy of the electrons, images of Fe domains were recorded. In order to image the step edges of the bare Cu crystal with high structural contrast with LEEM, an energy of the electrons of 4.9 eV turned out to be optimal for the used substrates.

2.1.2 Comparison with other domain imaging methods

Various approaches to magnetic microscopy have lead to different techniques to image magnetic domains. Since different physical phenomena are exploited, all methods presented in the following have advantages and disadvantages. Generally, there are two categories of imaging methods, some probing the far-field, and others scanning the near-field. Far-field techniques include electron-, magneto-optical-, and x-ray microscopy, whereas magnetic force microscopy (MFM) as well as magneto-optical scanning near-field (M-SNOM) and spin-polarized scanning tunnelling microscopy (SP-STM) belong to the near-field techniques. In the following the different features of the domain imaging methods are described and summarized in table 2.1.

Magneto-optical domain imaging in reflection and transmission, exploiting the magneto-optical Kerr effect (MOKE) [123] and the Faraday effect [124], respectively, is well established nowadays. Both effects are based on small rotations of the polarization plane of the light, and the domain pattern becomes viewable in the polarizing microscope. Since few samples are transparent, the Faraday effect can rarely be used, whereas the Kerr effect is applied in both its longitudinal and transverse mode to image the in-plane and out-of-plane components of the magnetization. In a calibrated computer-based Kerr microscope a quantitative determination of the magnetization direction and quantitative evaluation of domain wall parameters is possible

Table 2.1: Domain imaging methods classified into far-field (upper table) and near-field methods (lower table). (In part taken from [127]).

Imaging technique	Resolution	Special features
Lorentz microscopy	≤ 10 nm [17]	intermediate external magnetic fields H_{ex}
SEMPA	≥ 10 nm [128]	determination of magnetization direction
X-PEEM	≥ 20 nm [129]	element-specific imaging
SPLEEM	≥ 10 nm [130]	topography and determination of magnetization direction
Magneto-optical microscopy	≥ 300 nm [127]	strong external magnetic fields
MFM	≥ 10 nm [127]	H_{ex} , quantitative method
M-SNOM	≥ 50 nm [127]	topography and magnetic contrast
SP-STM	< 1 nm [131]	H_{ex} if antiferromagnetic tips used

[125]. The observation of domain wall dynamics in an applied magnetic field with up to 5000 frames per second on a 100 μm scale has been reported [126]. The possibility to apply high or low temperatures as well as mechanical stress and almost unlimited magnetic fields during the domain observation is a clear benefit of this method. As a drawback it should be mentioned that the lateral resolution is limited corresponding to an optical resolution of about 300 nm, and an electronic contrast enhancement may be necessary which is often associated with additional equipment [17].

In Lorentz microscopy a transmission electron microscope (TEM, 100-1000 keV) is used to image magnetic domains with high resolution better than 10 nm. This method is based on the deflection of transmitted electrons through a magnetic thin film due to the Lorentz force, which is proportional to the local magnetic induction. Domains can be imaged with high contrast and sensitivity even to small variations of the magnetization. The interaction between domain walls and lattice defects can be studied. However, a TEM equipment optimized for magnetic investigations is generally not optimal for other purposes. Manipulation of the sample by mechanical stresses or magnetic fields is difficult, and for measurements of the perpendicular component of the magnetization the sample must be tilted.

In secondary electron microscopy with polarization analysis (SEMPA) [132] the magnetic sample surface is scanned with a narrow electron beam, which excites secondary electrons of up to 50 eV near the surface of the sample. These electrons, which are spin-polarized parallel to the magnetization orientation of the site of their origin, are collected and accelerated toward a spin-detector, such as a Mott-detector. With a lateral resolution down to 10 nm [133] and the possibility to image the sample's topography and to simultaneously detect all three magnetiza-

tion components quantitatively [134,135] SEMPA is a powerful technique for domain imaging purposes. Due to the low efficiency of commonly used polarization detectors long exposure times up to several minutes are normally required. The sampling depth in metals is about 20 nm.

Magnetic force microscopy (MFM) is based on an atomic force microscope (AFM). Unlike AFM, in MFM a magnetized vertically vibrating cantilever tip is scanned in close proximity to the surface over the sample, detecting the magnetic dipole field. MFM images result from local frequency variations of the tip due to the presence of magnetic field gradients caused by the magnetic stray field of domain boundaries. The long range dipole-dipole-interaction limits the resolution to typically ≈ 50 nm, which can be improved by very small tip dimensions to ≈ 10 nm. A drawback is the difficulty of extracting quantitative information like the magnetization directly from MFM images, although there exist also various quantitative MFM methods to calibrate the tip, to calculate the stray field and to simulate MFM data [136–139]. Moreover, the magnetic stray field of the tip may modify the local domain structure of soft magnetic samples and the magnetization of the tip can change in the presence of an external magnetic field [127].

The basis of magnetic photoemission electron microscopy (X-PEEM) is x-ray magnetic circular dichroism (XMCD), which will be discussed in detail in section 2.2. Photoelectrons excited from core levels by circularly polarized x-rays are detected in the microscope. Pure magnetic contrast remains after subtracting two images taken with light of opposite helicity and an energy corresponding for example to the L_3 -edge of the sample material. The most striking advantage of X-PEEM is element-specific imaging, which is obtained from core-level selectivity by tuning the excitation to the absorption edge of the desired element in a heterogeneous sample [140]. Recent time-resolved X-PEEM measurements demonstrated the capability of taking a series of images in nanosecond-intervals after a high field pulse [141]. One drawback is that synchrotron based x-rays are needed for X-PEEM measurements.

Scanning near-field magneto-optical microscopy (M-SNOM) uses either linear magneto-optical effects (Kerr or Faraday effect) or nonlinear effects by scanning a near-field detector or, alternatively, a small-aperture light source of sub-wavelength size in close proximity to the surface of the sample. Besides the impressive resolution of ≈ 50 nm, a further advantage is that surface topography and optical image are recorded at the same time allowing for correlations between structure and magnetism.

The highest lateral resolution is achieved by spin-polarized scanning tunnelling microscopy (SP-STM). It is usually not better than 1 nm [142,143], however, recently an atomic-scale SP-STM has been demonstrated to resolve magnetic structure of the order of 0.5 nm [131]. In a SP-STM magnetic contrast is obtained through the spin-dependent tunnelling probability between a magnetic sample and a tip, which acts as a source of spin-polarized electrons. By using non-magnetic tips, which are coated with an antiferromagnetic material, e. g. Cr [144], an external

magnetic field can be applied during the measurement.

The mode of operation of SPLEEM has already been explained in the previous section. One benefit of this technique is the combination of topographic contrast, which is contained in every LEEM image due to the use of surface sensitive low energy electrons, and the pure magnetic contrast arising from the subtraction of two corresponding LEEM images as described above. By this virtue the origin of possible domain wall pinning or the correlation between magnetic domain formation and the substrate morphology can be clarified in every domain image. In addition, lateral resolution on the order of 10 nm for both LEEM and SPLEEM mode allows for the investigation of domain walls in ultrathin magnetic films, which have typical wall widths of 1-1000 nm. The possibility of real-time imaging, recording up to 10 images per second during thin film growth at low or high temperatures, makes SPLEEM a very flexible method to image the dynamics of domain formation. In addition, the application of external magnetic fields of $\approx 4 \text{ kA/m}^1$ perpendicular to the sample surface has been successfully performed without image distortion [145]. Another important advantage is that all three magnetization components can be detected within a few seconds, which was the decisive reason for this work to study the spin-reorientation transition in ultrathin Ni- and Fe/Ni-films on Cu(100) by the means of SPLEEM. A shortcoming of SPLEEM, however, is that the domain imaging is not element-specific, which would be desirable if multilayers or thin film alloys are to be studied.

2.2 XMCD

The x-ray magnetic circular dichroism (XMCD) technique is based on changes of the absorption cross section for left and right circularly polarized light, depending on the electronic band structure, which determines the magnetic properties of the absorbing material. XMCD is defined as the difference between the absorption spectra of left and right circularly polarized x-ray light for a static magnetic field along the incident axis of the photons. Following the definition in optics left (right) polarized light corresponds to a $+\hbar$ ($-\hbar$) helicity. For circularly polarized light the selection rules for an electric dipole transition from an atomic-like core state of the quantum numbers s , l , j and m according to the Wigner-Eckart theorem are given by:

$$\Delta s = 0, \quad \Delta l = \pm 1, \quad \Delta j = 0, \pm 1, \quad \Delta m = \begin{cases} +1, & \text{left circular} \\ -1, & \text{right circular} \end{cases} \quad (2.2)$$

where $\Delta s = 0$ means that a spin-flip during the transition is not allowed. This orbital-selective character of the x-ray absorption is sketched in Fig. 2.6 (a).

The basic principle of the XMCD effect at the L_3 and L_2 edges can be explained with the two-step model [146]. In the first step a circularly polarized photon excites a core electron from

¹4 kA/m \approx 50 Oe

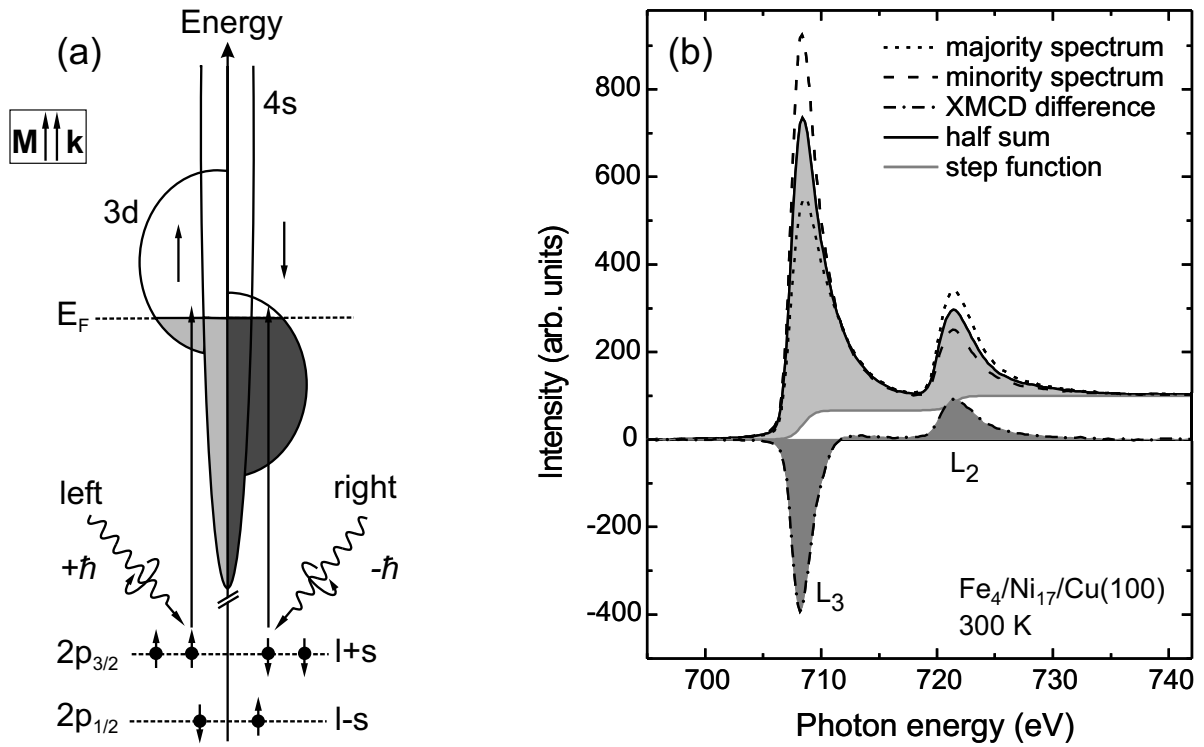


Figure 2.6: (a) Schematic of the x-ray magnetic circular dichroism at the $L_{2,3}$ edges of 3d transition metals. At the L_3 edge ($j = l + s$) the absorption of left (right) circularly polarized light causes a spin-selective excitation of photoelectrons from the spin-orbit split $2p_{3/2}$ core state to the exchange split 3d valence band which acts as a spin detector. Due to the imbalance of the unoccupied spin-up and spin-down states of the d band the absorption cross section for $+\hbar$ helicity is larger than for $-\hbar$. The effect reverses at the L_2 edge due to the opposite spin-orbit coupling ($j = l - s$). (b) The XMCD difference spectrum of an $\text{Fe}_4/\text{Ni}_{17}/\text{Cu}(100)$ film is obtained by subtracting the minority spectrum from the majority spectrum. The orbital (μ_L) and the spin (μ_S) moment can be determined by applying the magneto-optical sum rules after subtraction of the double step function from the half-sum spectrum.

the p -shell, which is split by the spin-orbit interaction into $2p_{3/2}$ (L_3) and $2p_{1/2}$ (L_2). At the L_3 and L_2 edges l and s are coupled parallel and antiparallel, respectively. The angular momentum of the photon is transferred to both the orbital and spin degree of freedom of the excited electron. At the L_3 -edge ($j = l + s$) the absorption of photons with the helicity $+\hbar$ will mainly excite spin-up photoelectrons, since the transition probability is maximum for a parallel alignment of l , s and $+\hbar$, whereas spin-down photoelectrons dominate the excitations with right circularly polarized light ($-\hbar$). Due to the opposite spin-orbit coupling ($j = l - s$) at the L_2 -edge the resulting spin-polarization of the photoelectrons reverses for excitations from the $2p_{1/2}$ states compared to those from the $2p_{3/2}$ states.

In the second step the spin-up (spin-down) photoelectrons are excited into unoccupied spin-up (spin-down) states of the 3d-valence band above the Fermi level. The 3d-band can thus be considered as a sensitive “spin-detector” for spin-polarized photoelectrons. Setting the mag-

netization of the d -band parallel to the direction of the wave vector \mathbf{k} , the occupation of the spin-down states is larger than that of the spin-up states.

Due to the spin conservation ($\Delta s = 0$) the photoelectrons excited from $2P_{3/2}$ ($2P_{1/2}$) by photons of $+\hbar$ helicity probe mostly the spin-up (spin-down) states above the Fermi level. Consequently, the absorption of left circularly polarized x-rays will be enhanced at the L_3 edge and reduced at the L_2 edge according to the exchange-split $3d$ -states. The absorption of right circularly polarized x-rays results in the opposite effect. This difference in absorption is the x-ray magnetic circular dichroism, which is conventionally defined as

$$\Delta\mu(E) = \mu^+(E) - \mu^-(E) \quad (2.3)$$

where μ^+ and μ^- indicate the absorption of right and left circular polarized light. Accordingly, the dichroism effect reflects the spin imbalance of the exchange-split $3d$ -band, and it is proportional to the difference in the unoccupied spin-up and spin-down states, i. e. to the spin magnetic moment. In order to obtain the XMCD spectra, one may also change the direction of the magnetization with respect to a fixed \mathbf{k} instead of changing the helicity of the x-ray beam.

Fig. 2.6 (b) shows the two absorption spectra according to μ^+ and μ^- , their half sum, which is the isotropic absorption cross section, the double step function and the resulting XMCD difference spectrum determined for the bilayer system $\text{Fe}_4/\text{Ni}_{17}/\text{Cu}(100)$ at normal incidence of the circularly polarized x-ray. The indices denote the layer thicknesses in monolayers.

2.2.1 Determination of magnetic moments using “sum rules”

In contrast to polarized neutron diffraction (PND) [147] or SQUID magnetometry [148] the total magnetic moment cannot be determined directly from XMCD measurements. The separate values of the spin μ_S and the orbital μ_L magnetic moment are determined by applying the XMCD sum rules. The magneto-optical sum rules, which yield directly the average expectation values of the ground state of the orbital angular momentum operator $\langle L_Z \rangle$, as well as the spin momentum operator $\langle S_Z \rangle$ and magnetic dipole operator $\langle T_Z \rangle$ acting on the shell which receives the photoelectron in the final state, were developed by Thole *et al.* [149] and Carra *et al.* [150], respectively. From these sum rules the magnetic moments are determined as follows:

- the orbital magnetic moment: $\mu_L = -\frac{\mu_B}{\hbar} \langle L_Z \rangle$
- the spin magnetic moment: $\mu_S = -\frac{2\mu_B}{\hbar} \langle S_Z \rangle$
- the magnetic dipole moment: $\mu_T = +\frac{\mu_B}{\hbar} \langle T_Z \rangle$

where $\langle T_Z \rangle$ provides a measure of the anisotropy of the spin density [150]. For atoms with cubic symmetry $\langle T_Z \rangle$ is negligible, but in a tetragonally distorted environment as well as at surfaces and interfaces $\langle T_Z \rangle$ becomes important. At the surface of $\text{Fe}(001)$ and $\text{Ni}(001)$ the value of

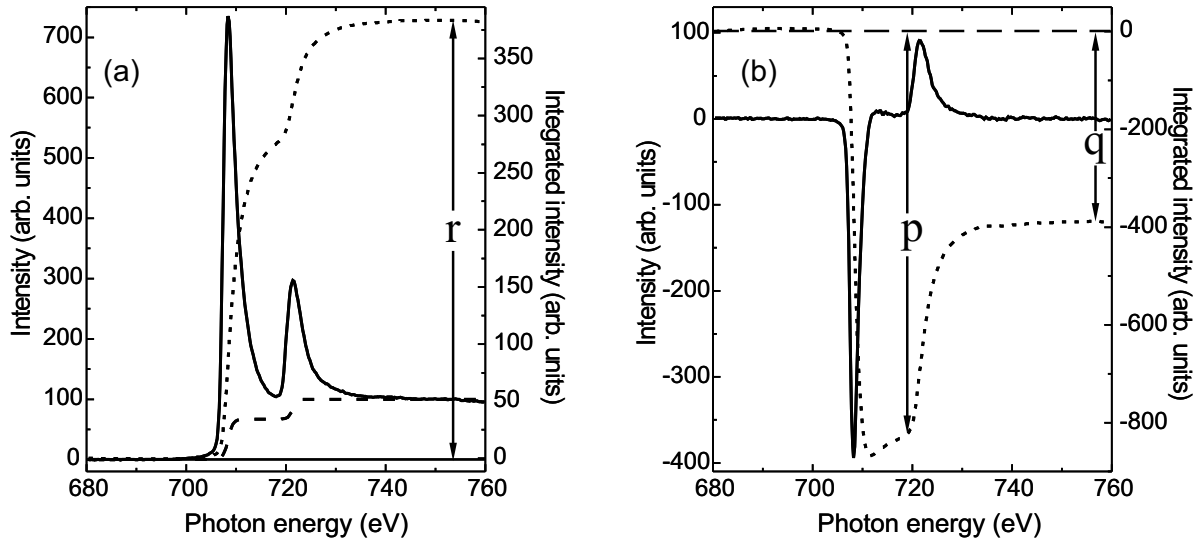


Figure 2.7: Isotropic absorption spectrum (a) and XMCD spectrum (b) (solid curves) and the corresponding integrals (dotted curves) of $\text{Fe}_4/\text{Ni}_{17}/\text{Cu}(100)$ at the Fe $L_{2,3}$ edges taken at 300 K. r equals the area between the isotropic spectrum and the step function (dashed curve) which simulates the contribution of photoelectrons being excited to continuum states.

$7\langle T_Z \rangle$ was calculated to equal $0.230 \mu_B$ and $-0.082 \mu_B$, respectively, compared to the values $0.028 \mu_B$ and $-0.027 \mu_B$ for Fe and Ni bulk-like layers [151].

The major source of errors on deriving the magnetic moments arises from the denominators of the sum rules, which correspond to the isotropic absorption cross section which is proportional to the number of holes n_h in the $3d$ -shell. To eliminate the contribution from the s - and p -continuum states a double step function is subtracted from the isotropic absorption spectrum. This procedure ensures the validity of the sum rules, but it adds some arbitrariness to the determination of n_h in the final state. Calculations based on a high precision local density approach reveal that the orbital sum rule is valid within 5 – 10%, the error being due to sd -hybridization. For the spin sum rule the error due to hybridization is 15% for Fe and 40 – 50% for Ni [151,152]. The ratio μ_L/μ_S is not affected by the error due to the uncertainty of n_h since both n_h and the isotropic absorption cross section are cancelled out. The determination of the single magnetic moments μ_L and μ_S requires a proper normalization of the absorption spectra as well as a correction of saturation effects, which occur if sampling of the electron yield is larger or comparable to the absorption depth of the incident x-rays [153]. Following the approach of [154] the magnetic moments μ_L and μ_S and their ratio are derived from experimental data by:

$$\mu_L = -\frac{2q}{3r} (10 - n_{3d}) \frac{1}{P_c \cos(\theta)} \quad (2.4)$$

$$\mu_S = -\frac{3p - 2q}{r} (10 - n_{3d}) \frac{1}{P_c \cos(\theta)} + 7\langle T_Z \rangle \quad (2.5)$$

$$\frac{\mu_L}{\mu_S} = \frac{2}{9 \left(\frac{p}{q} \right) - 6} \quad (2.6)$$

where p , q and r are the integrals denoting the area below the XMCD and the isotropic absorption spectra, respectively, as demonstrated in Fig. 2.7. P_c is the degree of circular polarization and θ indicates the polar angle measured between the wave vector \mathbf{k} and the sample's normal \mathbf{n} . The number of electrons in the $3d$ -band is given by n_{3d} , i. e. $(10 - n_{3d})$ is the number of unoccupied states in the $3d$ -band.

2.2.2 Element-specific determination of the magnetization direction in bilayers

The orientation of the magnetization of a bilayer system like Fe/Ni/Cu(100) can be determined by polar-angular dependent XMCD measurements performed at the element-specific $L_{2,3}$ edges of Fe and Ni, respectively. A ferromagnetic coupling, and thus a common alignment of the magnetizations of Fe and Ni, results in an equal algebraic sign of the corresponding L_2 and L_3 edges of the XMCD spectra. In contrast, an antiferromagnetic coupling gives rise to an opposite sign of the corresponding edges reflecting the anti-aligned orientation of the individual magnetizations. Analogously, the shape of element-selective hysteresis loops of Fe and Ni will show the same magnetization reversal in the case of a ferromagnetic coupling and an opposite magnetization reversal of both elements if the coupling is antiferromagnetic.

The identification of the easy axis of the magnetization \mathbf{M} requires sequent measurements at different polar angles θ . For an in-plane magnetized film there will be no dichroism at normal incidence of the x-rays ($\mathbf{k} \parallel \mathbf{n}$). The polar-angular dependent XMCD intensities of a perpendicularly magnetized film follow the law:

$$I(\theta) = I_{\perp} \cos(\theta) \quad (2.7)$$

where I_{\perp} denotes the XMCD intensity for $\mathbf{k} \parallel \mathbf{n}$. In the case of a canted magnetization the components M_{\perp} and M_{\parallel} have to be measured in order to determine the polar angle α of \mathbf{M} from $\tan(\alpha) = \frac{M_{\parallel}}{M_{\perp}}$. However, a grazing angle $\theta = 90^\circ$ is not possible but $\theta = 80^\circ$ can be used. In this case the canting angle α is determined by²:

$$\alpha = \arctan\left(\frac{I_{\parallel} - I_{\perp} \cos(\theta)}{I_{\perp} \sin(\theta)}\right) \quad (2.8)$$

where I_{\parallel} denotes the XMCD intensity measured at a grazing angle of $\theta = 80^\circ$. It should be noted that the correction of saturation effects becomes all-important at large angles θ . Alternatively, the absorption spectra can be measured by successively increasing θ from 0° to 80° and thus determining the angle, for which the XMCD signal is largest, indicating the direction of the magnetization.

²The details are given in the appendix A.6.

2.3 SQUID magnetometry

This chapter is restricted to a short introduction to the principles of operation of a radio frequency (rf)-SQUID. A detailed description of the fundamental physics of SQUIDS is given e. g. in [155]. The determination of the magnetization from the detected magnetic stray field is elucidated in section 2.3.2.

An rf-SQUID consists of a superconducting loop containing one weak link, i. e. a Josephson junction [156]. dc-SQUIDS which operate at a constant bias current have two Josephson junctions as described for example in [155]. A SQUID yields an output voltage signal which is a periodic function of the flux Φ penetrating the superconducting loop. By means of the critical temperature T_c , below which the material becomes superconducting, SQUIDS are further divided into two types: conventional low- T_c ($T_c < 10$ K) and high- T_c ($T_c > 10$ K) SQUIDS. While Niobium ($T_c = 9.25$ K) is a common material for low- T_c -SQUIDS, which must be cooled with liquid helium (lHe), high- T_c -SQUIDS are nowadays fabricated from $\text{YBa}_2\text{Cu}_3\text{O}_{7-x}$ (YBCO, $T_c = 93$ K) where the use of liquid nitrogen (lN₂) is sufficient to maintain $T < T_c$ [39,157]. The main advantage of the use of lN₂ is the lower cost and the easier handling compared to lHe. Due to their high sensitivity SQUIDS have found various applications, e. g. in the fields of non-destructive testing [158], magnetic microscopy [159], geophysics [160] and magnetocardiology [161].

2.3.1 Operation of an rf-SQUID

The electrical properties of the Josephson junction which is a thin insulating layer are determined by the two Josephson equations. The tunnel current I through the ideal barrier is limited by the critical current I_c which is given by the dc-Josephson equation:

$$I = I_c \sin \delta \quad (2.9)$$

where the relative phase $\delta = \Phi_1 - \Phi_2$ is determined by the phases Φ_i on the two sides of the junction. The associated superconducting order parameter is $\Psi = \Psi_0 e^{i\Phi_i}$, and $|\Psi|^2$ equals the density of the Cooper-pairs. The ac-Josephson equation yields the voltage V across the ideal junction:

$$V = \frac{\hbar}{2e} \left(\frac{d\delta}{dt} \right) \quad (2.10)$$

In Fig. 2.8 (a) the inductive coupling of an rf-SQUID to the electronics is sketched. The real junction is illustrated by the equivalent circuit of the ideal, noise free junction, its physical capacitance and a resistor in a parallel connection, which accurately models the electrical properties of the SQUID [158].

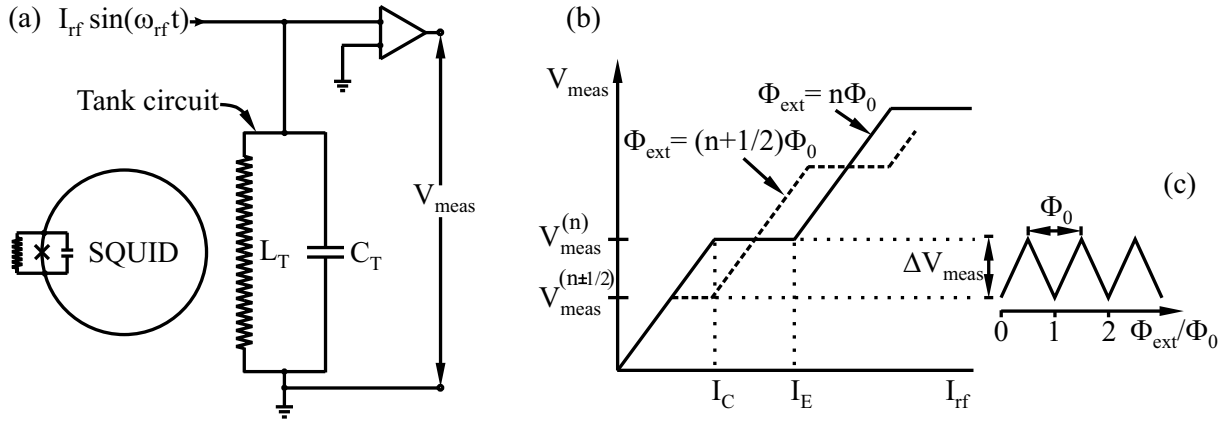


Figure 2.8: (a) Schematic of an rf-SQUID loop. The Josephson junction is marked by “x”, and the loop is inductively coupled to an rf-tank circuit. The junction is shunted by a resistor, and its physical capacitance is shown as well. (b) Voltage V_{meas} drop at the tank circuit versus the bias current I_{rf} for the quantum states $\Phi_{ext} = n\Phi_0$ and $\Phi_{ext} = (n + \frac{1}{2})\Phi_0$. (c) Voltage-to-flux transfer function of the rf-SQUID. (After [163]).

According to the Bohr-Sommerfeld quantization constraint [162] a superconducting loop will contain flux only in multiples of the flux quantum, i. e. $n\Phi_0$, where n is any integer. A change in the flux Φ_{ext} applied to the SQUID will cause currents to oppose that change, resulting in a phase shift across the junction, which according to Eq. (2.10) gives rise to a voltage. The typical step function of the measured voltage V_{meas} versus the rf-current I_{rf} is depicted in Fig. 2.8 (b). V_{meas} increases linearly with I_{rf} until the current I_s , which is induced by the tank circuit reaches the critical current I_C . At this point a flux quantum jump occurs in the SQUID, and V_{meas} stays constant until the dissipation caused by the normal-conducting junction is compensated by $I_{rf} = I_E$ again [163]. The voltage-to-flux transfer function reveals a typical triangular shape as demonstrated in Fig. 2.8 (c).

2.3.2 Determination of magnetic moments from the stray field

The magnetic stray field of a thin film can be calculated by integrating elementary magnetic dipoles over the film area. A magnetic dipole $d\mathbf{m}$ in a distance \mathbf{R} causes a field $d\mathbf{B}$, which is given by [2]:

$$d\mathbf{B} = \frac{\mu_0}{4\pi} \frac{(3 \mathbf{n} \cdot d\mathbf{m}) \mathbf{n} - d\mathbf{m}}{R^3} \quad (2.11)$$

where $\mathbf{n} = \mathbf{R}/R$ is a unit vector. Eq. (2.11) is based on the assumption that only magnetic dipoles contribute to the stray field, which is justified since the stray field is detected in a distance of approximately 5 mm. In this distance quadrupole- and higher order contributions are negligible since they vanish with higher powers of R^{-n} ($n = 5, 7, \dots$).

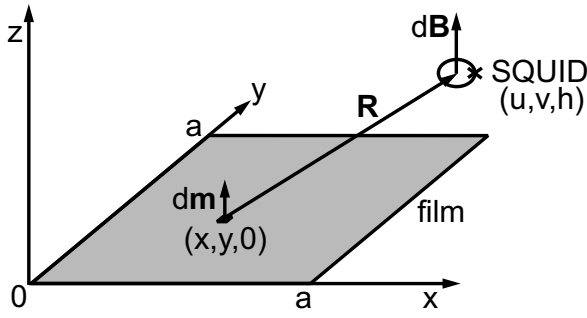


Figure 2.9: Coordinates and vectors used to calculate the stray field integrals.

For an in-plane magnetized square-shaped ultrathin film in the single domain state the z -component of the stray field after integration of Eq. (2.11) reads [164]:

$$B_z^{tot}(u, v, h) = \frac{3\mu_0}{4\pi} M d h \int_{-a/2}^{a/2} \int_{-a/2}^{a/2} \frac{u-x}{R^5} dx dy \quad (2.12)$$

where a is the width of the film, M the magnetization, d the film thickness, h the distance in which the stray field is detected and $\mathbf{R} = (u-x, v-y, h)$. The coordinates and vectors used to calculate the stray field integrals are given in Fig. 2.9.

The magnetic dipoles are assumed to have only an x -component m , i. e. $d\mathbf{m} = (m, 0, 0)$, and they are located at the position $(x, y, 0)$ in the film plane. All contributions to the magnetization are projected onto the x -axis which is the easy axis of the film. The detection of the stray field along the x -direction in a constant distance h and in a centered position ($v = 0$) yields the field distribution of $B_z(u, v, h)$ shown in Fig. 2.10 (a). The position and the shape of the two peaks are affected by h and a as discussed elsewhere [39,165], whereas their peak-to-peak value is determined by h , d and M . Since the magnetization is the only unknown parameter, the value of M can be derived from applying Eq. (2.12) with M as a fit parameter to a SQUID measurement. Knowing the crystal structure of the film and the inter- and intralayer spacing of the atoms, the total magnetic moment per atom can be obtained.

For a perpendicularly magnetized ultrathin film where $d\mathbf{m} = (0, 0, m)$ Eq. (2.12) changes to:

$$B_z^{tot}(u, v, h) = \frac{\mu_0}{4\pi} M d \int_{-a/2}^{a/2} \int_{-a/2}^{a/2} \frac{3h^2}{R^5} - \frac{1}{R^3} dx dy \quad (2.13)$$

An exemplary calculation of the stray field distribution according to Eq. (2.13) for an out-of-plane magnetized 3 ML Fe film is demonstrated in Fig. 2.10 (b). The numerical solutions for Eq. (2.12) and Eq. (2.13) can be found in [39]. In conclusion, the decrease of the distance h from 6 mm to 4 mm enhances the signal by a factor of ≈ 3 . This indicates that the smallest possible distance is required in order to achieve the maximum signal-to-noise ratio of a ferromagnetic monolayer. Since the equations 2.12 and 2.13 are based on a homogeneously

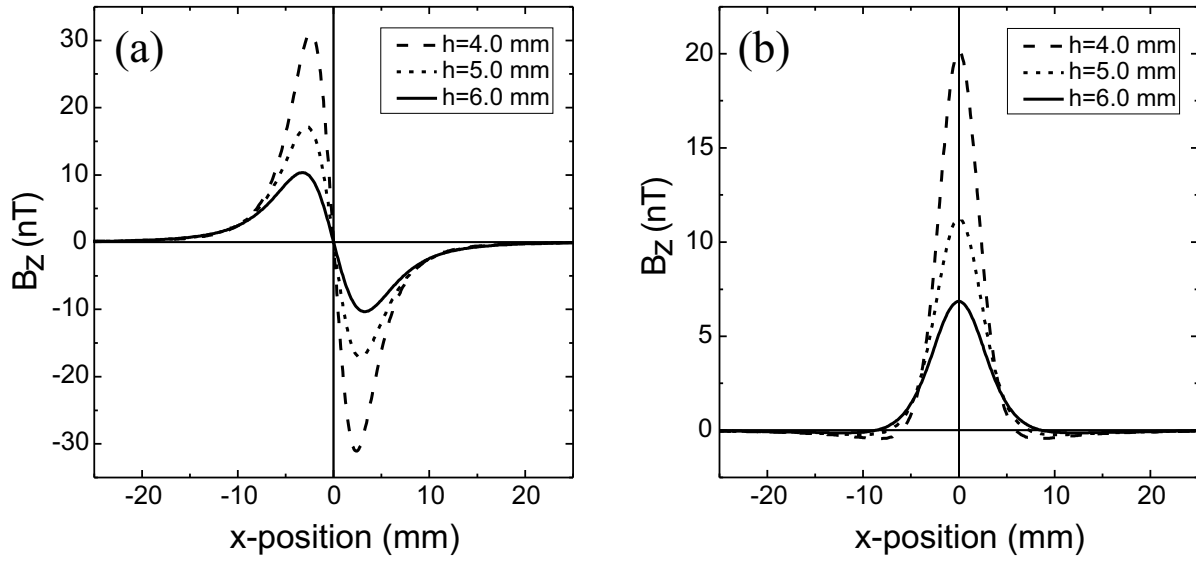


Figure 2.10: Calculated stray field distribution of a homogeneously magnetized rectangular-shaped ultrathin Fe film of 3 mm width and a magnetization of 1740 kA/m for different distances h . The calculation (a) according to Eq. (2.12) corresponds to an 11 ML in-plane magnetized Fe film, and (b) shows the calculation according to Eq. (2.13) for a 3 ML perpendicularly magnetized Fe film.

magnetized perfectly rectangular sample, only the stray field component B_z of *in situ* grown rectangular-shaped films can be simulated. Possible deviations of the measured stray field distribution from the calculation may arise from closure domains at the edges of the film, which are not considered in the above theory.

3 Substrate preparation and ultrathin film growth

The growth of Ni, Fe and Fe/Ni films on Cu(100) and their investigations by SPLEEM, XMCD and SQUID, respectively, have been performed in three different UHV-chambers. In all three cases cylindrical Cu(100) single crystals of 2 mm thickness were used. The diameter of the substrates was 10 mm for the SPLEEM and XMCD measurements and 5 mm for the SQUID experiments. Additionally, a square-shaped GaAs(001) crystal served as a substrate for Fe monolayers during the SQUID measurements. In this chapter the preparation of the substrates and the growth of the $3d$ transition metal films is described.

3.1 Preparation of the Cu(100) and GaAs(001) substrates

A carefully developed substrate cleaning procedure was used to prepare the Cu(100) single crystals for the SPLEEM experiments. It was found to be effective to suppress possible bunching of atomic steps. Suppression of step bunching in substrate surfaces is an important issue in magnetic microstructure research, because even in otherwise highly perfect epitaxial ultrathin films, substrate step bunches can easily act as pinning sites for magnetic domain walls and thus influence the magnetic properties of the sample. Before each experiment, the Cu(100) crystal was prepared by 12 hours of Ar^+ -ion sputtering, using a low current density of approximately $0.1 \mu\text{A}/\text{cm}^2$ and an ion energy in the range of 1.5 – 3 keV. In order to heal up the imperfection and the roughness of the surface caused by the Ar^+ -ion bombardment, the crystal was automatically flash annealed to about 1000 K in 10-minute intervals during sputtering. A previous investigation on the effects of ion bombardment and thermal treatment on the topography of Cu(001) surfaces revealed, that the average size of terraces is determined by the annealing temperature and not by the ion energy. The largest average size of terraces was found for the highest temperature (900 K) [166]. After this preparation schedule, no surface contamination was detectable using a single-pass cylindrical mirror Auger electron spectrometer (CMA). Imaging the bare Cu(100) substrate in the LEEM mode, we confirmed that the resulting surface had atomically flat terraces separated by mostly monoatomic steps. A typical prepared Cu(100) surface

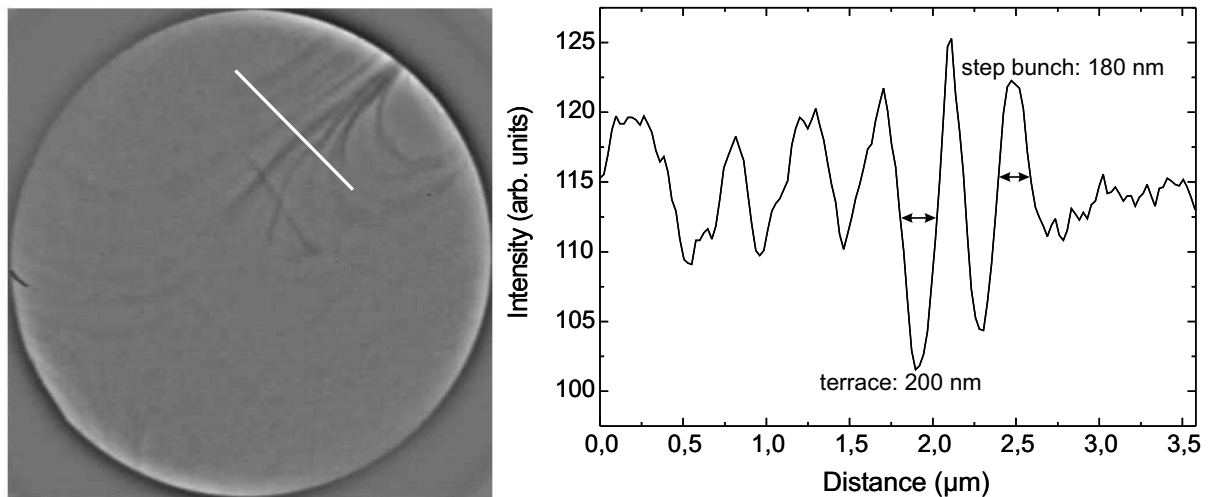


Figure 3.1: Left: LEEM image of the sputtered and annealed Cu(100) crystal surface taken at an energy of the electrons of 9.5 eV. The dark lines are monoatomic step edges and step bunches separating different terraces. The field of view is 10 μm . Right: Profile plot along the white line in the LEEM image. The average terrace width is ≈ 200 nm.

is depicted in the left image of Fig. 3.1, which shows Cu-step edges as dark lines by means of LEEM. A profile scan (right) across the white line in the left image reveals an average width of the Cu-terraces of ≈ 200 nm. Note, that the energy of the electrons was optimized for magnetic contrast of Ni, which occurs at 9.5 eV, and which may not be optimum to image structural features like Cu-step edges with highest contrast. Consequently, it cannot be ruled out that there are steps of atomic height –between the step bunches– which are not resolved. These would reduce the average width of the terraces.

Prior to the film growth for the XMCD measurements the cleanliness of the sputtered and annealed Cu(100) crystal was checked by x-ray absorption spectroscopy (XAS). The Cu(100) surface was cleaned until no contamination was detected in the x-ray absorption spectra, which otherwise reveal residual contaminations element-selectively. In the chamber, where the XMCD measurements have been performed, no Auger electron spectrometer was available.

The cleanliness of the Cu(100) and GaAs(001) substrates, on which Fe monolayers have been grown for the SQUID measurements, was checked by Auger electron spectroscopy. The cycles of sputtering and annealing were repeated until no residual contaminations of oxygen, carbon, carbon oxide or ferromagnetic materials from previous evaporations were detected by the CMA. A typical Auger spectrum of the bare Cu(100) crystal is shown in Fig. 3.2. The peaks in the spectrum are clearly identified as peaks originating from copper. No oxygen ($E = 510$ eV) is detected.

In order to prepare the surface of the GaAs(001) crystal we followed the procedure described in Refs. [167,168], i.e. cycles of Ar^+ -ion sputtering ($E = 0.5 - 1$ keV) and annealing

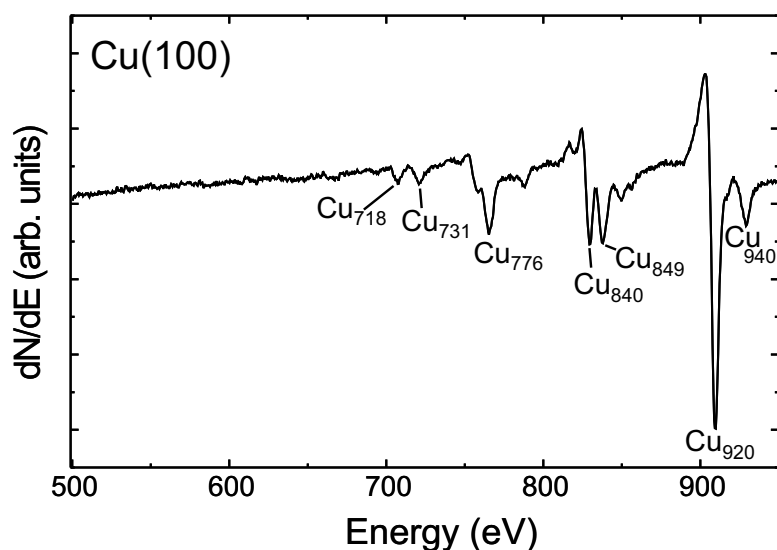


Figure 3.2: Auger spectrum of the bare Cu(100) crystal. No oxygen ($E = 510$ eV) is detected.

(873 K), and a subsequent annealing at 873 K for 12 hours.

3.2 Growth of ultrathin Ni, Fe and Fe/Ni films on Cu(100) and GaAs(001)

Ni films were deposited *in situ* with the Cu(100) substrate held at either 100 K or 300 K. The evaporator target was a high purity rod of 2 mm diameter, which was brought to sublimation temperature by direct electron beam heating inside a water-cooled evaporator. The base pressure during SPLEEM measurements was 2×10^{-8} Pa; the maximum pressure during evaporation reached 4×10^{-8} Pa. The Ni evaporator has been calibrated before by growing a Ni/Cu(100) film at 300 K. The oscillation of the sum $I^\uparrow + I^\downarrow$ of the average LEEM intensities as a function of the deposition time was used to observe the layer-by-layer growth of Ni/Cu(100) and to determine the layer thickness during the film growth as described elsewhere [169]. Since LEEM imaging of crystalline surfaces is based upon diffraction, and since the sum of the intensities $I^\uparrow + I^\downarrow$ contains only diffraction information and no magnetic information, the well-known diffraction intensity oscillations [170] correspond to periodic nucleation, growth and completion of atomic monolayers during epitaxial growth. This oscillation is shown in Fig. 3.3. The distance between two maxima yields the Ni deposition rate, which was typically around 0.4 ML/min. The reduced amplitude of each following maximum (minimum) is attributed to roughness effects, which increase with the increasing number of atomic layers and have already been investigated [171, 172]. The oscillation disappears after 3 ML Ni in Fig. 3.3, which indicates a change of the layer-by-layer growth. Scanning tunnelling microscopy (STM) measurements showed a layer-by-layer growth of Ni/Cu(001) up to 5 ML, followed by a growth of pyramids with their ≈ 6 nm wide basis parallel to the $\langle 110 \rangle$ directions. The STM images of a 9 ML Ni/Cu(001) revealed

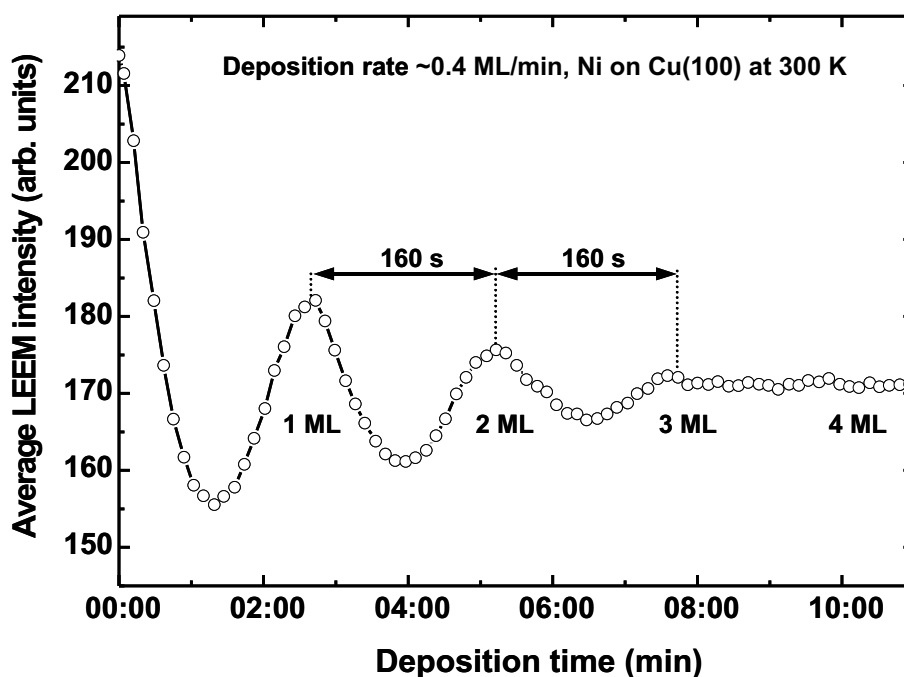


Figure 3.3: Film thickness calibration by the oscillation of the integrated LEEM intensity during the Ni deposition at 300 K. The maxima indicate full atomic Ni layers, and their distance determines the deposition rate equal to ≈ 0.4 ML/min. Each point corresponds to the sum of two \uparrow - and \downarrow -LEEM images.

3–4 unfinished layers [173]. Films grown at 100 K show a reduced amplitude and a faster decay of the intensity oscillation indicating a higher degree of roughness (not shown here). Since Ni/Cu(100) grows pseudomorphically up to thicknesses of about 15 ML [82,174], yielding a Ni(100) surface with the Cu lattice constant, Fe is expected to grow in a similar fct-like distorted structure on this Ni surface as on the blank Cu(100) surface. Fe films¹ have been grown on Ni/Cu(100) films with a deposition rate of typically 0.1 ML/min. This deposition rate, which is four times lower than that used for the 7 – 11 ML Ni/Cu(100) films, was chosen in order to precisely increase the Fe thickness near the SRT.

During the *in situ* XMCD investigation the thickness of Ni and Fe layers on Cu(100) was determined from the absorption spectra by using the edge-jump ratio J_R , which is the signal-to-background ratio at the L_3 absorption edge. It is a precise measure for the number of emitted Auger electrons. From the calibration curve given in Ref. [154], in which J_R is plotted versus the layer thickness measured by a quartz micro balance, the layer thickness can be determined within an error of 0.25 ML for thicknesses below 3 ML. In the saturation range of the curve, i. e. around 20 ML thickness, the error becomes approximately 15%.

¹The Fe evaporator was calibrated in the same way as the Ni evaporator, i. e. by the LEEM intensity oscillation at 300 K.

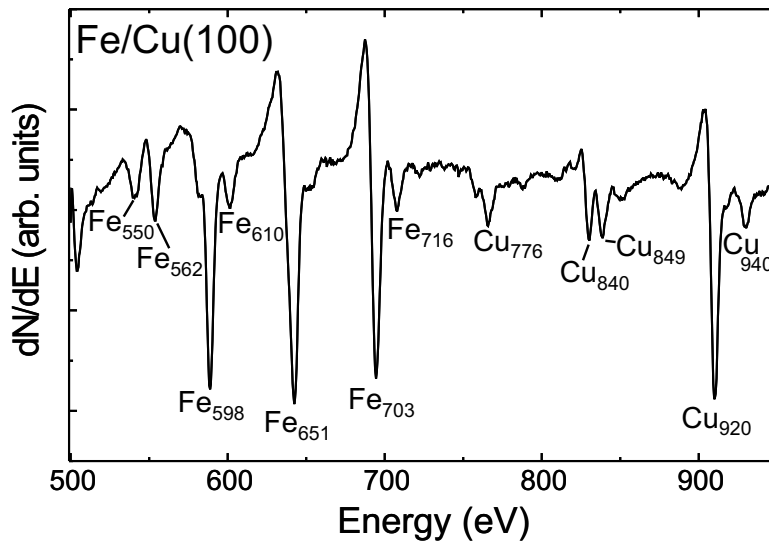


Figure 3.4: Auger spectrum of an Fe/Cu(100) film. From this spectrum the Fe thickness is determined by the calibration curve shown in the appendix A.5 in Fig. A.7 to be 4 ML.

For the purpose of controlled Fe film growth for SQUID measurements a careful thickness calibration of the Fe evaporator was performed. Therefore, Auger electron spectra of various Fe layer thicknesses on Cu(100) were taken. By the determination of the peak-to-peak signals of the Auger spectra of Cu at 920 eV and Fe at 651 eV and assigning the intensity ratios $I_{\text{Cu}920}/I_{\text{Fe}651}$ to the different Fe layer thicknesses of the respective ratios from Ref. [175], a calibration curve of the Fe evaporator has been established. In Ref. [175] Auger spectra have been recorded at various Fe layer thicknesses, which have been determined by a quartz micro balance. The calibration curve is depicted in the appendix A.5 in Fig. A.7 and yields the correlation between the ratio of the Auger peak intensity and the Fe layer thickness and time of evaporation, respectively. From this curve the thickness of the Fe/Cu(100) film, whose CMA spectrum is displayed in Fig. 3.4, is determined to be 4 ML. The error of this thickness determination is estimated to be on the order of 20%. Unlike the CMA spectrum of the bare Cu(100) surface after cycles of cleaning (Fig. 3.2), the CMA spectrum of the 4 ML Fe/Cu(100) film clearly reveals traces of oxygen, which is indicated by the peak at an energy of 510 eV in Fig. 3.4. Comparing the low energy electron diffraction (LEED) images of the bare Cu(100) crystal and the Fe/Cu(100) film confirms the existence of oxygen atoms at the Fe surface. This

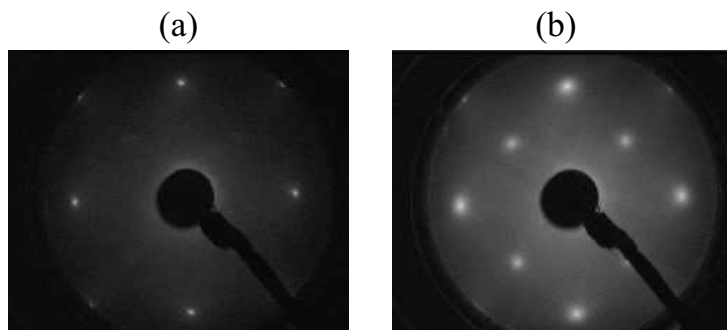


Figure 3.5: (a) LEED image of the bare Cu(100) crystal. (b) Crystallographic structure of a 4 ML Fe/Cu(100) film showing an oxygen superstructure. Both images have been taken at an energy of the electrons of 122 eV.

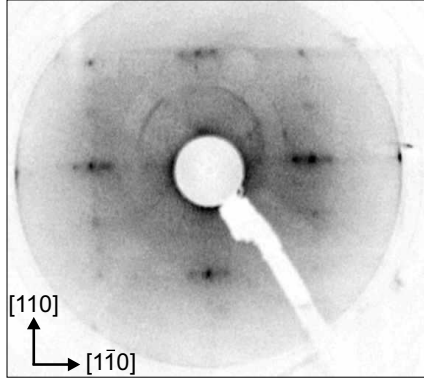


Figure 3.6: LEED image of the bare GaAs(001) substrate taken at an energy of the electrons of 127 eV at 300 K. The $[1\bar{1}0]$ direction is parallel to the easy axis of the magnetization and parallel to the scan direction x during SQUID measurements.

is illustrated in Fig. 3.5. The Cu(100) surface (a) imaged at an energy of the electrons of 122 eV shows sharp 1×1 LEED reflexes and a low background intensity, which is indicative for a low roughness. Higher degrees of roughness would lead to a diffuse scattering.

At the same energy of the electrons the Fe/Cu(100) film reveals additional spots originating from the oxygen atoms forming a 2×2 superstructure. Moreover, the LEED pattern is more diffuse and the background intensity is higher as compared with the pattern of the bare substrate surface. This implies that the roughness of the Fe surface is much higher than the surface of the substrate. The existence of oxygen on the film and the rise in pressure up to 1×10^{-7} Pa during the evaporation indicates, that the Fe evaporator was not sufficiently degassed.

In preparation for SQUID measurements of ultrathin Fe/GaAs(001) films, square-shaped Fe films of an area of $3 \times 3 \text{ mm}^2$ were grown on the cleaned GaAs(001) substrate using an aperture plate (see section 4.4). The distance between the crystal surface and the aperture was kept at a minimum distance below ≈ 0.5 mm, in order to evaporate films of sharp rectangular shape. This is important, since the simulation function of the magnetic stray field (section 2.3.2) is based on a perfectly rectangular thin film. Deviations from the rectangular shape will otherwise add errors in the determination of the magnetization.

Bcc Fe is known to grow epitaxial on GaAs(100) ‘with the film crystallographic axes coincident with those of the substrate’ [176]. At least between 5 ML and 30 ML Fe/GaAs(100) films exhibit a uniaxial in-plane magnetic anisotropy along the $[0\bar{1}1]$ direction, which dominates over the fourfold bulk anisotropy along the $[001]$ and $[010]$ direction, respectively [177]. The resulting easy in-plane direction of the magnetization was found to be parallel to the $[0\bar{1}1]$ axis. In Fig. 3.6 the LEEM image of the bare GaAs(001) substrate taken at an energy of the electrons of 127 eV is shown. The $[1\bar{1}0]$ direction is parallel to the easy axis of the magnetization and parallel to the scan direction x during the SQUID measurements. By comparing the LEED images taken at different energies of the electrons, a 4×6 reconstructed surface is revealed as was proposed by Xue *et al.* [178] on the basis of STM studies of GaAs(001).

4 Design of the UHV-SQUID system

One aim of this PhD-thesis was the setup of an ultrahigh vacuum (UHV)-chamber for ultrathin magnetic film analysis comprising a SQUID-magnetometer to determine the magnetization of a sample on an absolute scale. In this chapter the construction of the UHV-system and the design and calibration of the SQUID is described. Magnetic, structural and chemical investigations are exemplarily demonstrated for ultrathin Fe films grown on a Cu(100) and a GaAs(001) single crystals, respectively. First SQUID measurements are presented confirming the functionality of the system. The UHV-setup offers the opportunity to perform SQUID and ferromagnetic resonance (FMR) [40] measurements on the *same* sample for the first time.

4.1 Construction of the UHV chamber

The UHV-chamber (welded by the company VTS Schwarz [179]) is designed on the basis of a sphere of 150 mm radius. All main flanges are focussed on the center of the sphere. The principle axes x , y , z are used as follows:

- x -axis: sample manipulation; glass finger for FMR measurements (magneto-optical Kerr effect (MOKE) possible).
- y -axis: Low energy electron diffraction (LEED) for structural investigation and Auger electron spectroscopy (AES) for chemical analysis and film thickness determination.
- z -axis: sample preparation by electron beam evaporation from below and SQUID magnetometry from above.

Moreover, the following devices are incorporated in the UHV-chamber:

- Sputter gun for sample cleaning with Ar^+ -ions.
- Quadrupol mass spectrometer for residual gas analysis.
- Rotatable aperture plate used during evaporation to create thin films of an area of 3×3 mm².
- Plasma gun for controlled reactive gas exposure (O, H, N atoms and ions).

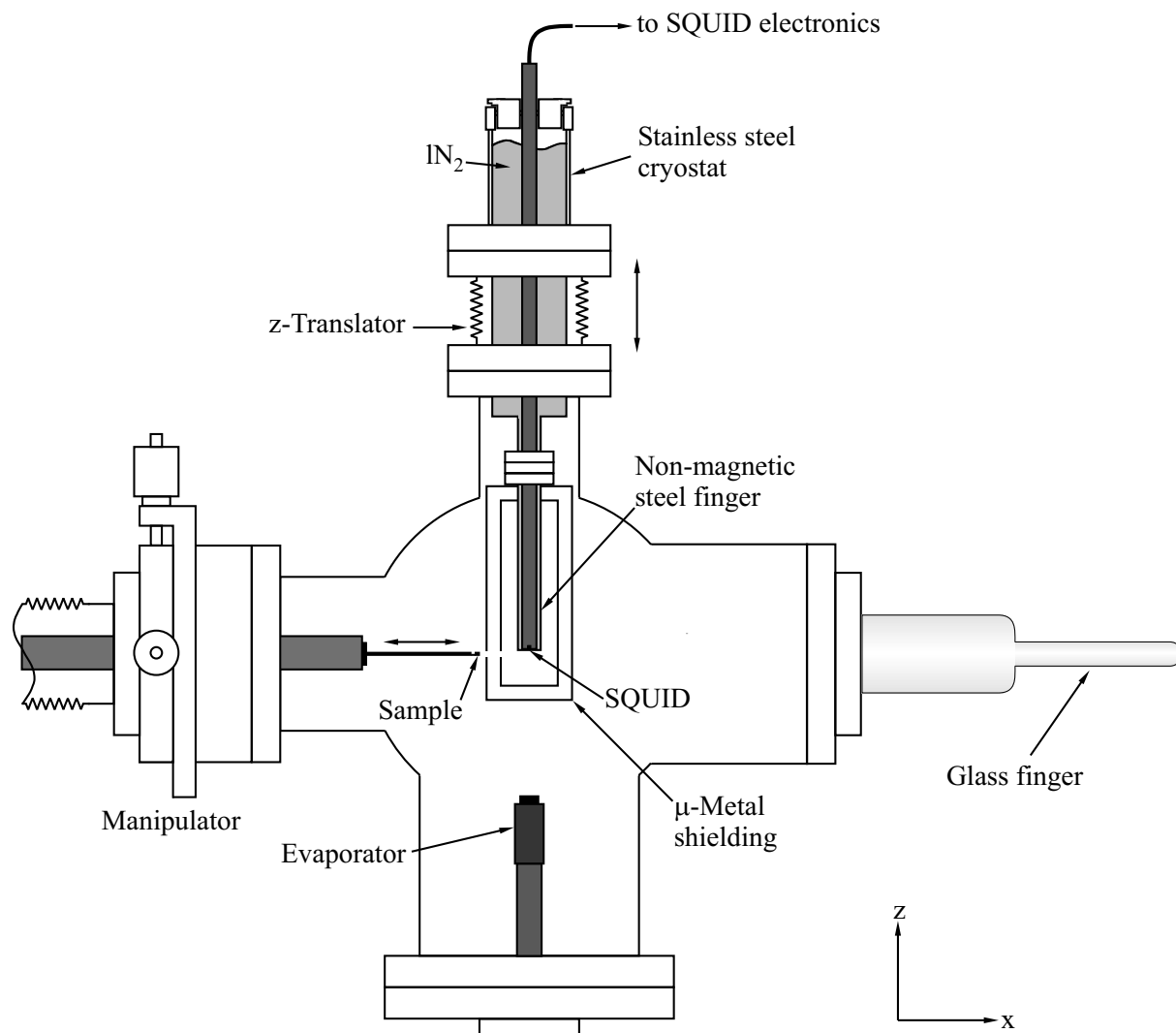


Figure 4.1: UHV-SQUID setup. Square-shaped ferromagnetic films of $3 \times 3 \text{ mm}^2$ can be evaporated by means of an aperture plate. Before SQUID measurements the sample is magnetized in the tip of the glass finger by an external field along the x - or the z -axis, then the SQUID setup including the LN_2 -cryostat and the double wall μ -metal screening is vertically transferred to the center of the chamber. At a distance of $\approx 4 \text{ mm}$ the sample is moved laterally to the SQUID in order to measure its magnetic stray field. The LEED optics and the cylindrical mirror analyzer for structural characterization and Auger-spectroscopy, respectively, are directed along the y -axis through the center of the spherical chamber (not shown).

- Rotary vane pump, turbo molecular pump (250 l) and ion getter pump (300 l) and Titanium sublimation pump (TSP).
- Longauge for UHV pressure measurement.
- One main viewport (DN 63 CF) and several smaller ones (DN 38 CF, DN 16 CF).

The complete list of the flange positions and a technical drawing of the chamber is given in the appendix (table A.3 and Fig. A.1). A simplified cross section through the x - z -plane of the

UHV-chamber is shown in Fig. 4.1. An ultrathin film sample, e. g. Fe/Cu(100), which has been grown by electron beam evaporation is transferred to the tip of the glass finger where an external field is applied in order to magnetize the sample to a single domain out-of-plane or in-plane state. At a distance of ≈ 4 mm the sample is then moved laterally to the SQUID which resides in a μ -metal shielded, liquid nitrogen (LN_2) filled non-magnetic metal dewar. From the detected magnetic stray field as described in chapter 2.3.2 the magnetization of the thin film is determined on an absolute scale. The base pressure is on the order of 2×10^{-8} Pa.

4.2 The SQUID sensor

The high- T_c rf-SQUID sensor M900 used in this work is a standard sensor of the JSQ company [180]. It is made out of YBCO deposited on a SrTiO_3 substrate with the Josephson junction fabricated by pattern induced grain boundaries. The technical data of the sensor are listed in the appendix (table A.4). The rod which incorporates the SQUID has been custom-made, in order to suit the dimensions of the finger of the metal cryostat. A drawing of its dimensions can be found in the appendix A.4 (a).

4.3 Cryostat and magnetic shielding

The UHV-compatible LN_2 -cryostat is mounted vertically to the chamber and consists of two parts: the upper part accounting for $\approx 90\%$ of the volume and the non-magnetic metal finger mounted thereunder. In order to minimize the thickness of the bottom of the cryostat a non-magnetic sheeting of 0.5 mm was used for the finger tip. The SQUID sensor is kept *ex situ* under LN_2 in close vicinity to the bottom resulting in a distance to the sample of ≈ 4 mm. As demonstrated in Fig. 2.10 a reduction of the distance between SQUID and sample tremendously increases the detected signal.

Both the cryostat and the magnetic shielding stand temperatures in the range of 77 K (LN_2 -cooling) to 500 K during the baking procedure. The SQUID, however, is removed before baking the system and is warmed up with dry air, since the sensor stands neither temperatures above 350 K nor water, which condensates on the SQUID rod after the use in LN_2 if the rod is not warmed up.

The cryostat is manufactured of a single stainless steel tube of 0.3 mm wall thickness, which is thermally isolated by the ultrahigh vacuum within the chamber. In order to avoid mechanical vibrations the thin-walled tube is supported by an outer stainless steel tube of 2 mm thickness, which simultaneously acts as a radiation shield. Lateral oscillations are inhibited, whereas an axial expansion during baking and contraction under LN_2 is possible. The support tube is welded on a DN CF 63-flange and welded to the inner tube via a metal ring of 1 mm, which reduces

the thermal conduction to the chamber. Additionally, the cryostat is encapsulated by a closely matching Polyoxymethylene cap at the feed opening, which prevents the vessel from icing up during the utilization of liquid nitrogen. At the bottom of the inner tube a DN 16 CF-flange is welded to which the non-magnetic metal finger is mounted. The dimensions of the cryostat are given in Fig. A.4 (b) of the appendix. In order to shield the cryostat finger against magnetic fields it is surrounded by a double wall μ -metal cylinder. The accurate dimensions of this construction are depicted in Fig. A.3.

4.4 The sample holder

The sample holder is solely fabricated of non-magnetic materials in order to allow for detecting only the stray field of the ferromagnetic film grown on the Cu- or GaAs-single crystal. The holder is made of one piece of oxygen-free copper (OFHC) for the purpose of optimum thermal conduction during cooling with liquid helium. Annealing of the sample is achieved via resistive heating using a W-wire of 0.3 mm thickness, which is plugged through two bores within the crystal. Since the sample is transferred horizontally during SQUID measurements the crystal has to be adequately stabilized mechanically to suppress vibrations of the W-wire. To impede an overheating of the whole sample holder during annealing up to 900 K ceramic tubes of 0.8 mm² connect the crystal with the holder in a distance of 3 mm, which simultaneously fix the substrate. Moreover, ceramic tubes of different sizes are used to isolate the non-magnetic *Pallaplat*¹ thermocouple, which is used for temperature control, and the electrical wiring as depicted in Fig. 4.2. In order to use the sample holder as an electric conductor it is isolated

¹The *Pallaplat* 32/40 thermocouple consists of 95% Pt 5% Rh / 52% Au 46% Pd 2% Pt.

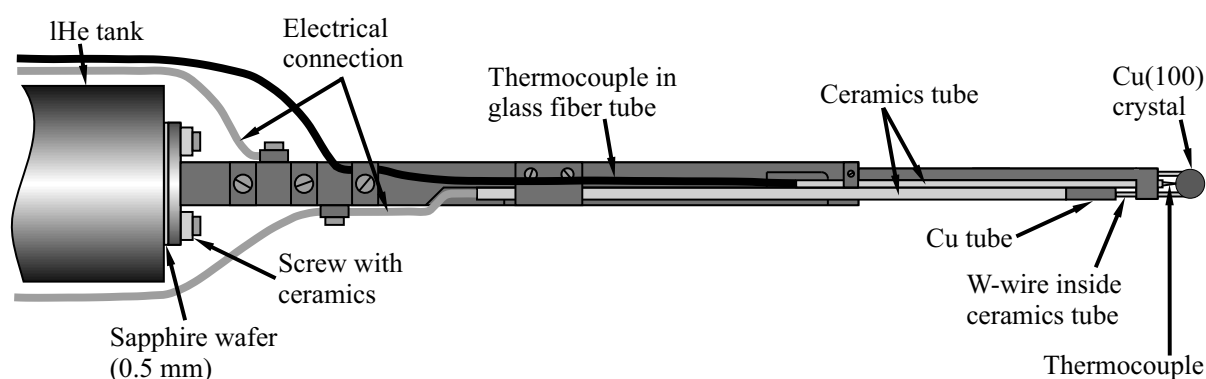


Figure 4.2: Top view of the non-magnetic sample holder made of oxygen-free copper, which is connected to the IHe-cooled manipulator via a sapphire plate. The substrate is held by a tungsten wire of 0.3 mm thickness for resistive heating, guided by two ceramic tubes of 0.8 mm outer diameter (gray), which stabilize the crystal (dark gray). The sample holder and the electrical connections are isolated from ground potential via a sapphire wafer of 0.5 mm thickness.

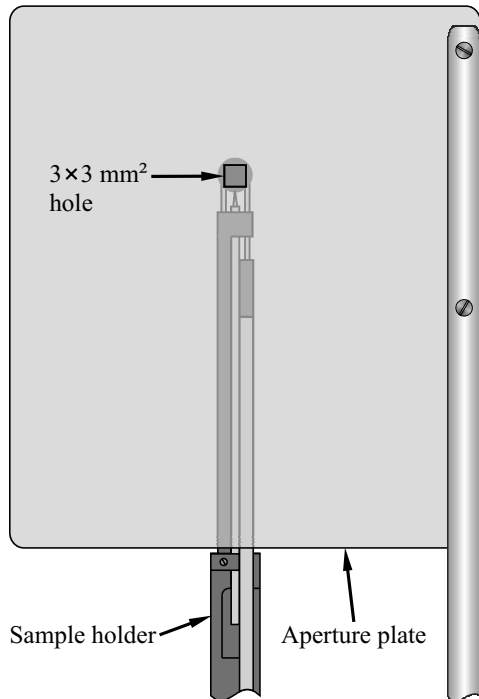


Figure 4.3: By means of the aperture plate ferromagnetic films of $3 \times 3 \text{ mm}^2$ size are grown on the single crystal substrate. The dimensions of the aperture plate are chosen, such that the whole part of the sample holder, which enters the magnetic shielding, is covered during evaporation. This ensures that the stray field measured by SQUID exclusively originates from the grown film. After evaporation the aperture can be rotated off its position.

from the manipulator, which is on ground potential, by a sapphire wafer which ensures a good thermal conduction during cooling. One end of the W-wire is directly screwed to the sample holder by a molybdenum slug, while the other end is connected to a Cu-wire by a Cu-tube crimping the ends of the wires.

In order to evaporate an ultrathin magnetic film of rectangular shape² onto the single crystal substrate, an aperture plate with a square-shaped hole of $3 \times 3 \text{ mm}^2$ is used as shown in Fig. 4.3. Keeping the distance between the substrate surface and the aperture plate below $\approx 0.5 \text{ mm}$, an ultrathin film is evaporated through the hole onto the substrate. The distance between the evaporator and the substrate is 130 mm , therefore the film is of the same size as the hole of the aperture. Fig. 4.3 also shows that the whole part of the sample holder, which enters the μ -metal shielding, is covered by the aperture plate³ during the evaporation. This is necessary in order to protect the holder from contamination by ferromagnetic materials. Thus, it is ensured that the stray field measured by SQUID exclusively originates from the grown film.

4.5 Calibration of the SQUID

The magnetic flux which crosses the area of the SQUID loop is detected, and it is converted by the electronics into an output voltage proportional to the magnetic field perpendicular to the loop. A determination of the magnetic field component on an absolute scale, however, requires

²Only the stray field component B_z of rectangular films can be simulated by the Eqs. (2.12) and (2.13).

³The width and the length of the aperture plate are 66 mm and 75 mm , respectively.

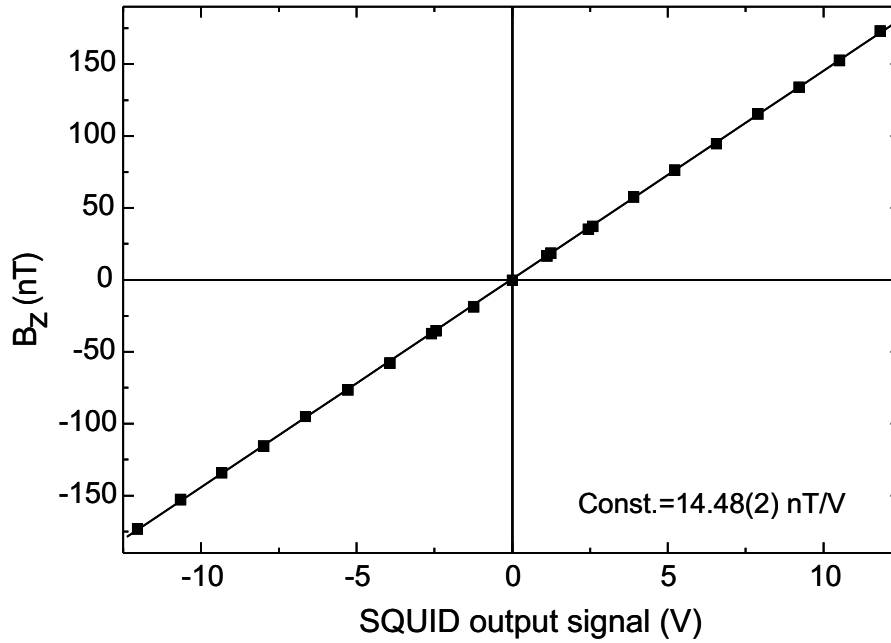


Figure 4.4: Calibration of the SQUID sensor signal by means of a small coil. The calibration factor yields 14.48(2) nT/V.

a calibration of the SQUID. The SQUID has a factory adjusted field-to-flux ratio setting of $9.3 \text{ nT}/\Phi_0$. The transfer coefficient of the electronics was adjusted to a high voltage-to-flux ratio of $0.64(1) \text{ V}/\Phi_0$ by means of an oscilloscope, using the triangle pattern in the test mode of the SQUID. Both settings in combination yield the desired field-to-voltage ratio $14.5(2) \text{ nT/V}$. A much more precise method, which is necessary in order to determine the magnetic moments per atom of a single monolayer of a ferromagnetic material, is the calibration by the magnetic field of a small current conducting loop. Since the SQUID is a $100 \mu\text{m} \times 100 \mu\text{m}$ ring in the center of the sensor head, a small calibration coil ($r = 6.5 \text{ mm}$) of two turns is sufficient to create an almost homogeneous magnetic field in the SQUID. Within an *ex situ* setup described elsewhere [181], which consists of a non-magnetic cryostat and a double μ -metal shielding, a high-precision current in the μA -range was applied to a Cu-coil around the SQUID sensor. The sensor resided in the center of the coil, which had a radius of $r = 6.75 \text{ mm}$ and two turns n . The resulting current (I) depending magnetic field B at the site of the SQUID is given by:

$$B = \mu_0 I \frac{n}{2r} \quad (4.1)$$

with $\mu_0 = 1.2566 \times 10^{-6} \text{ VsA}^{-1}\text{m}^{-1}$ and yields for the used coil $B = 0.186(7) \cdot \text{nT}/\mu\text{A}$. The calibration factor arising from this method is given by the slope of the linear fit in Fig.4.4, which is $14.48(2) \text{ nT/V}$ in excellent agreement with the previous determination but with higher accuracy.

4.6 Data acquisition

The magnetized sample is moved laterally below the SQUID sensor as sketched in Fig. 4.1 by the use of a motor-driven manipulator. In order to minimize the vibrations the motor is driven continuously. The setting parameters like the measuring velocity, the number and length of single scans and the data acquisition are controlled by the same computer program. By means of an AD-DA transformer card the output voltage of the SQUID is assigned to the actual motor position. Since the SQUID signal is proportional to the perpendicular component of the sample's stray field according to the calibration curve shown in Fig. 4.4 the stray field distribution as a function of the x -position is obtained. A detailed description of the operation of the program and the performance of the measurements can be found in the appendix A.3.

4.7 Measurements of the stray field of a 12.5 ML Fe/GaAs(001) film

In order to test the UHV-SQUID magnetometer, an ultrathin Fe film of 12.5 ML thickness was grown on a GaAs(001) single crystal surface. The Fe layer thickness was determined by using a quartz micro balance. The expected layer thickness based on the previously determined calibration curve of the Fe evaporator (see Fig. A.7) was 10 ML. Since Fe was evaporated on a semiconductor substrate, a thickness determination via Auger electron spectroscopy as described for the case of Fe/Cu(100) in section 3.2 was not possible.

Before the stray field measurements our sample was in-plane magnetized by an external magnetic field of ≈ 8 kA/m along the x -direction, which is the scan direction (see Fig. 4.1) and parallel to the $[0\bar{1}1]$ axis of the crystal. The easy axis of the magnetization is parallel to the scan direction. In Fig. 4.5 three different SQUID measurements of the 12.5 ML Fe/GaAs(001) film are superposed. The stray field component B_z (nT)⁴ is shown versus the x -position (mm). No data smoothing has been performed. The inset in the figure reveals an average noise of ≈ 0.4 nT. Within this noise the measurements are reproducible. The peak-to-peak signal is about 20 nT, so that the resulting signal-to-noise ratio is about 50 : 1. The limiting signal-to-noise ratio is assumed to be 3 : 1. Moreover, the measured signal scales linearly with respect to the film thickness and the magnetization. Therefore, the sensitivity limit is ≈ 0.6 ML of Fe in the present configuration of the UHV-SQUID system. However, as the asymmetric shape of the stray field distribution reveals, there are still some problems with the setup, since in the ideal case (see section 2.3.2) a homogeneously magnetized film should give rise to a symmetric curve. The sources of error are discussed in the following, and they have to be solved in order to determine the magnetization of an ultrathin film on an absolute scale in future experiments. The

⁴The SQUID output voltage is converted into nT by the calibration coefficient.

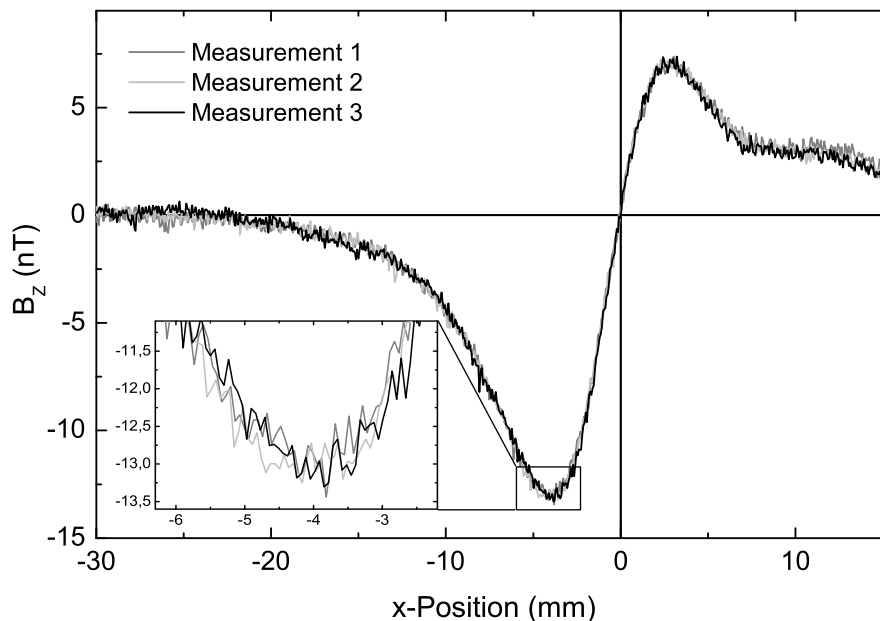


Figure 4.5: Measured stray field component B_z of a 12.5 ML Fe/GaAs(001) film, which was in-plane magnetized along the x -direction. The three different measurements at 300 K are reproducible within an average noise level of 0.4 nT. The signal-to-noise ratio is about 50:1. The asymmetric shape of the curves is attributed to both a tilt of the sample and a ferromagnetic signal originating from the sample holder.

sample holder, which is composed of non-magnetic materials only, obviously contains traces of ferromagnetic substances. This is indicated by the shoulder on the right hand side of the stray field curve, which is unlikely to originate from the Fe film. Therefore, a measurement of the sample holder and the blank substrate is indispensable. The main source of the asymmetric shape of the curves, however, is attributed to a tilt of the sample with respect to the z -axis of the UHV system (see Fig. 4.1). This tilt causes a linear variation of the distance between the SQUID and the sample during the scanning process, which was shown in section 2.3.2 to strongly influence the measured signal.

In conclusion, with the present calibrated UHV-SQUID setup the stray field distribution $B_z(x)$ of an in-plane magnetized ultrathin film can be reproducibly detected on an absolute scale with a high signal-to-noise ratio. In order to determine the magnetization from simulations of the measured stray field, however, further improvements of the system have to be done.

5 Magnetic domains

As stated in section 1.2.2 ultrathin Ni/Cu(100) films are magnetized in-plane between 5 ML and 9 ML at room temperature. In section 5.1 the formation of in-plane magnetized domains is studied in detail. The internal structure of a Néel wall is analyzed, and the wall profile is compared with theoretical calculations. In section 5.2 the domain evolution of ultrathin Fe/Cu(100) as a function of the thickness is discussed. This evolution is compared with the formation of magnetic domains of Fe grown on a perpendicularly magnetized Ni/Cu(100) film in section 5.3.

5.1 5 to 8 ML Ni on Cu(100)

5.1.1 Comparison of domains at 100 K and 300 K

At 300 K the onset of ferromagnetic order was found to occur around 5 ML Ni/Cu(100) in agreement with the well-established phasediagram [33,85] shown in Fig. 1.7. Below 5 ML the Ni film is in the paramagnetic state, since the Curie-temperature T_C , below which the magnetic moments order ferromagnetically, decreases with decreasing film thickness. In this thickness regime no in-plane or out-of-plane magnetic contrast (MC) was observed by SPLEEM. Around 5 ML Ni the Curie-temperature has reached 300 K, and the ferromagnetic order within the film plane is revealed by the appearance of magnetic contrast in the SPLEEM image. At the same thickness no MC was detected for the perpendicular component of the magnetization, indicat-

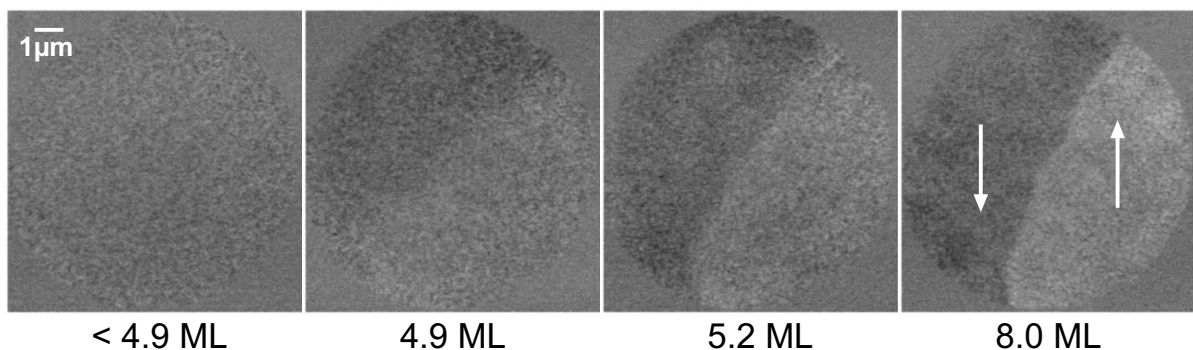


Figure 5.1: Onset of ferromagnetic order within the film plane around 5 ML Ni on Cu(100) and increasing magnetic contrast up to 8 ML Ni at 300 K. The arrows indicate the direction of the magnetization. No magnetization component perpendicular to the film plane was detected. The field of view is 10 μm .

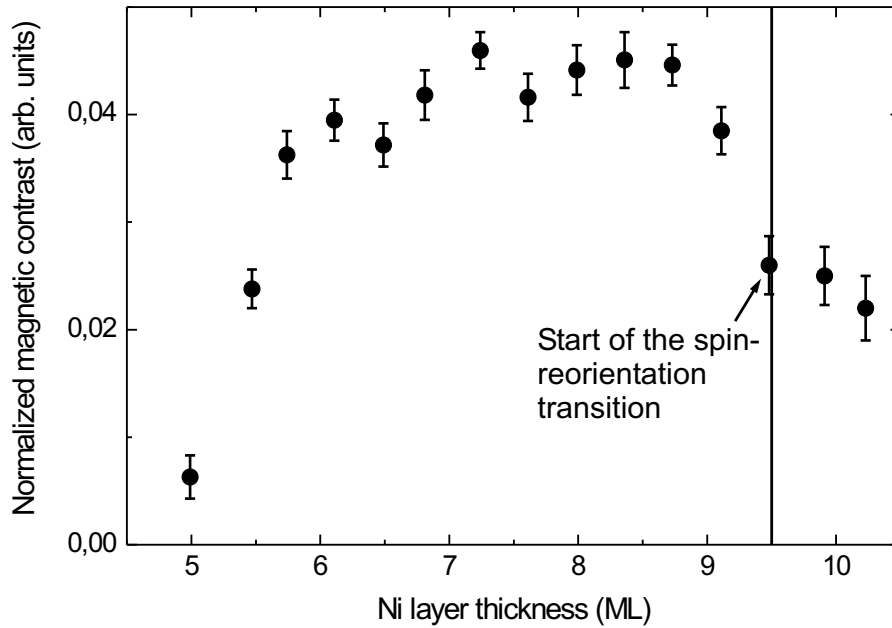


Figure 5.2: Normalized magnetic contrast of the in-plane magnetized domains of Ni/Cu(100) as a function of the Ni layer thickness. The MC increases monotonically up to about 8.5 ML Ni/Cu(100). With the start of the spin-reorientation transition at 9.5 ML the MC decreases.

ing that the magnetization was oriented parallel to the surface of the film. This is depicted in Fig. 5.1. Interestingly, no formation of smaller magnetic domains at the onset of the ferromagnetic order like in ultrathin Fe/Cu(100) (section 5.2) was observed, when the film thickness was increased in 0.1-ML steps across the critical thickness (about 4.9 ML) for ferromagnetism at 300 K. The position and the structure of the domain wall remained unchanged during subsequent deposition of additional Ni up to a thickness of 8 ML. For a film grown at 100 K the onset of ferromagnetic order was observed at lower thickness in agreement with the magnetic phasediagram of Ni/Cu(100).

As the Ni/Cu(100) film grows, the magnetic contrast increases monotonically up to about 8.5 ML Ni/Cu(100) due to the increasing number of magnetic moments contributing to the magnetization of the sample. This is demonstrated in Fig. 5.2. However, only up to 7 ML Ni the expected linear increase of the MC according to $MC \propto \mathbf{P} \cdot \mathbf{M}$ is observed. Between 7.5 and 8.5 ML the MC can also be regarded as constant within error bars, and it drops around 9 ML as the spin-reorientation transition starts (see section 6.1). The opposite orientation of the magnetization in the two adjacent domains in Fig. 5.1, which are separated by a 180° -Néel wall, is indicated by the white arrows in the image and will be discussed in the next section in detail.

Scanning over a $2 \times 2 \text{ mm}^2$ area of the surface of many in-plane magnetized Ni/Cu(100)

films of thicknesses between 4 and 8 ML the average domain size was found to be several $10\ \mu\text{m}$, substantially larger than the $10\text{-}\mu\text{m}$ maximum field of view. No statistically significant difference between the domain sizes and shapes of room temperature (RT)-grown and RT-measured films, RT-grown films measured at 100 K (low temperature, LT) and LT-grown and LT-measured films was found. In Fig. 5.3 an example of a 4.8 ML RT-grown Ni/Cu(100) measured *in situ* at 100 K is shown. For maximum contrast the polarization \mathbf{P} of the electron beam was rotated within the film plane. For \mathbf{P} perpendicular to the film plane no MC was observed, confirming the in-plane orientation of \mathbf{M} . This microscopic observation of in-plane magnetization is in good agreement with earlier findings [85]. To confirm that the SPLEEM images of the domain boundaries are representative of typical configurations, domain walls were traced over extended distances. In Fig. 5.3 the imaged area (circles) was moved in several steps to trace the domain wall. The correct alignment of the magnetic images was unambiguously verified by comparing surface step patterns in the corresponding LEEM images, which are demonstrated next to the SPLEEM images. Close inspection of the “spin-up” and “spin-down” LEEM topographic images and comparison with the corresponding magnetic images reveals no correlation between the topography of the Ni film and its magnetic domain structure. No evidence for domain wall pinning at atomic step bands was found. Comparing the images of Figs. 5.1 and 5.3 one observes a difference in the smoothness of the domain walls but no change in the domain size. The increased wall roughness of the film measured at 100 K (Fig. 5.3) is attributed to two effects: (a) when cooling from 300 K to 100 K at a base pressure of 1.5×10^{-8} Pa trace amounts of residual gases like CO and CO₂ may adsorb, which reduce the total magnetic anisotropy in the 5 ML regime considerably and (b) the formation of a zigzag domain wall which is not completely resolved. Such domain walls are known to originate from “head-on” 180° -domain walls [182], in which the magnetization vectors of the adjacent domains point to each other in an antiparallel alignment. These domain walls develop a zigzag shape in order to reduce the magnetic charge density. A straight wall would have the strongest charge concentration [17]. The SPLEEM apparatus, however, does not provide the high resolution (<5 nm) to resolve fine details of the domain wall structure as for example spin-polarized scanning tunnelling microscopy (SP-STM) techniques do (see e. g. [131]).

The systematic investigation of the domain wall width as a function of the Ni thickness at 300 K reveals a decrease in width from the onset of MC with increasing layer thickness up to 8 ML as shown in Fig. 5.4. The width of a 180° wall is theoretically given by $w_{180^\circ} = 2\sqrt{A/K_2^{\text{eff}}}$ [17], (see section 1.3.2). The error bars in Fig. 5.4 arise from the noise of each domain profile extracted from the SPLEEM images. Each profile consisting of the average of 50 parallel profile lines was taken at the same part of the domain wall as indicated in the inset of Fig. 5.4. The solid line in the figure is a guide to the eye. The domain wall width is also plotted versus the reciprocal thickness in the inset of the figure. The decrease of the width of the domain wall

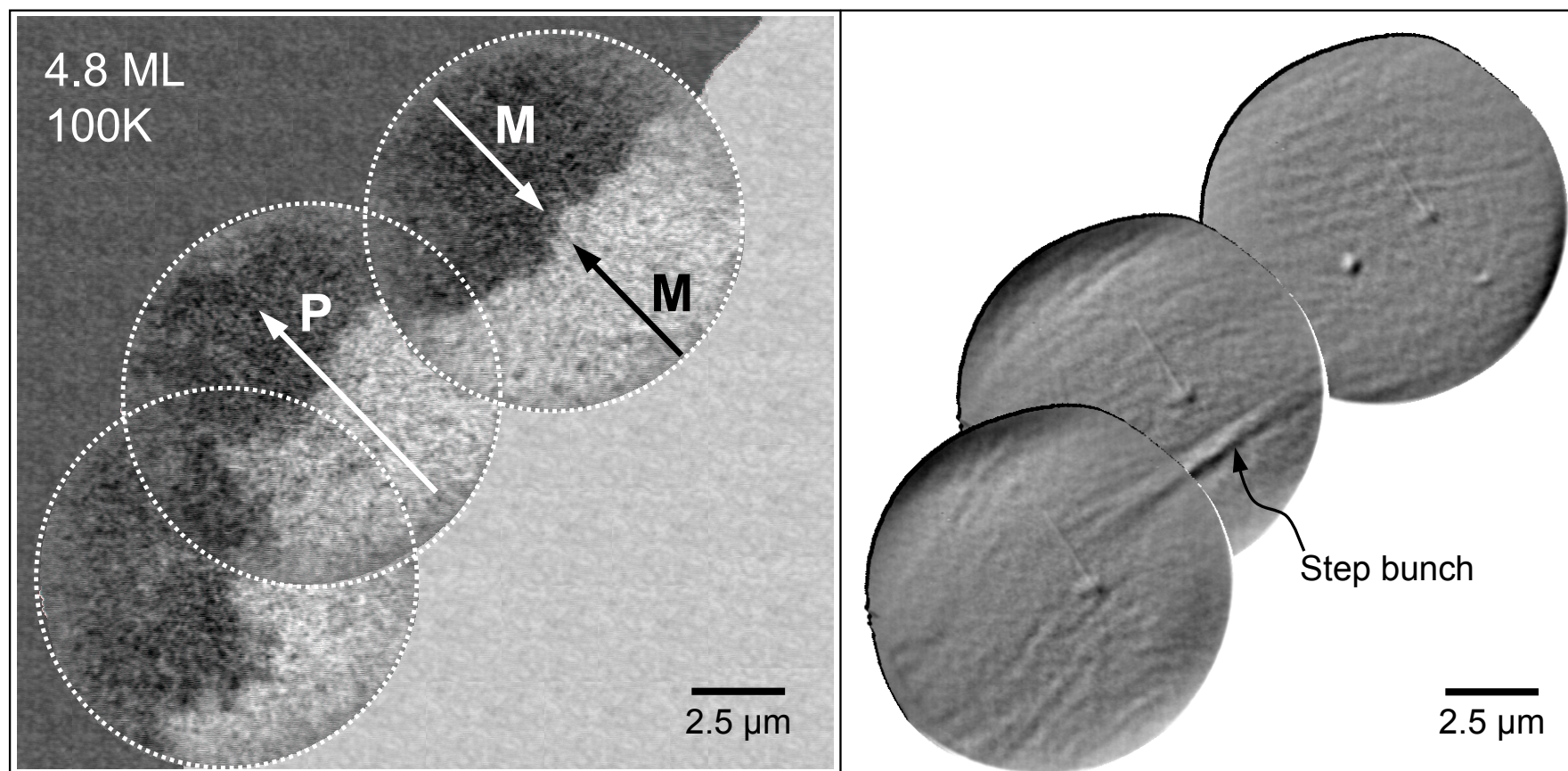


Figure 5.3: Left: Three SPLEEM images with $10\text{-}\mu\text{m}$ field of view (circles) tracing a domain wall of a 4.8 ML Ni film prepared at 300 K and measured at 100 K. The domains have several $10\ \mu\text{m}$ extension. The zigzag wall structure originates from a “head-on” domain configuration (see text). Right: With the aid of the three corresponding LEEM images the correct alignment of the domain images is found by exploiting topographic features like the marked step bunch. No preferred direction or pinning of the domain wall with respect to the step edges was found.

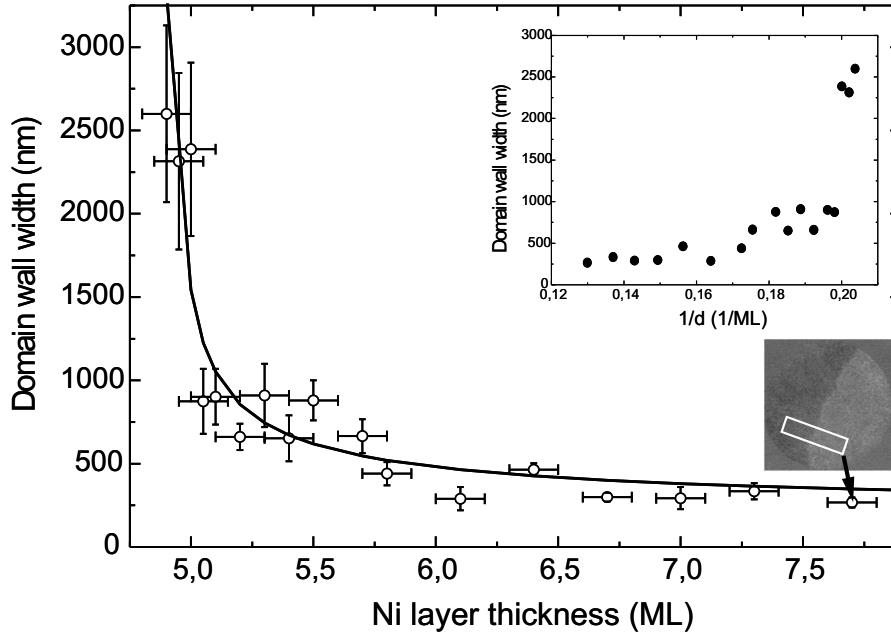


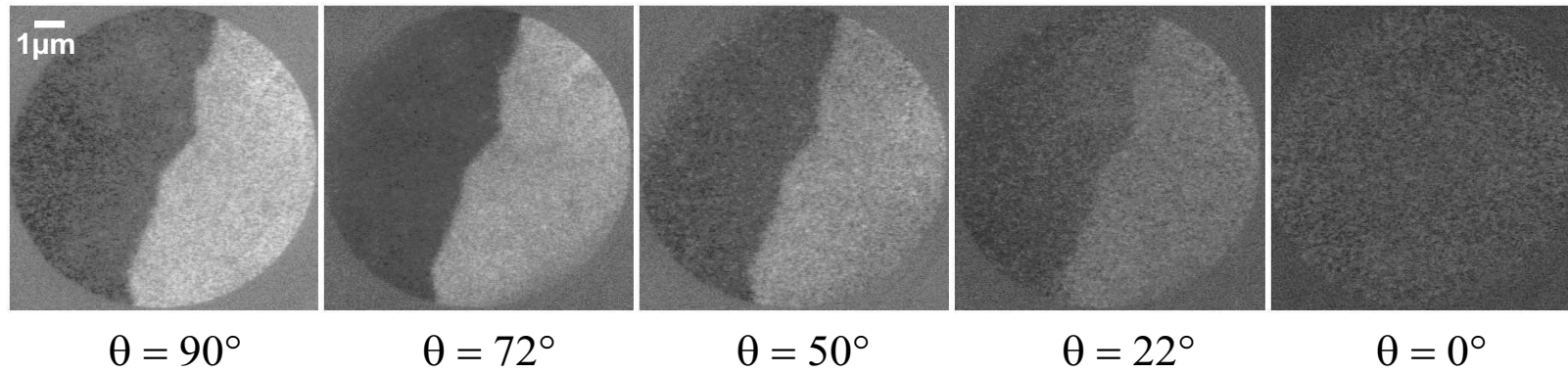
Figure 5.4: Width of the domain wall of in-plane magnetized ultrathin Ni/Cu(100) films as a function of the thickness at 300 K. The expected decrease in wall width with increasing film thickness d is due to the decrease of the surface anisotropy contribution $2K_2^S/d$. The solid line is a guide to the eye. The inset shows the width of the wall versus the reciprocal thickness.

with increasing Ni layer thickness can be understood in terms of an increase of the effective anisotropy constant $K_2^{\text{eff}} = K_2^V + 2K_2^S/d - K_d$. Since $2K_2^S/d$ is negative and large at small thicknesses, K_2^{eff} is small around 5 ML, where the domain formation sets in, leading to an extended width of the domain wall according to $w_{180^\circ} = 2\sqrt{A/K_2^{\text{eff}}}$. As the thickness of the Ni layer increases, the surface contribution $2K_2^S/d$ to K_2^{eff} decreases. Hence, the resulting increase of K_2^{eff} causes a narrowing of the domain wall. Applying $w_{180^\circ} = 2\sqrt{A/K_2^{\text{eff}}}$ as a fit function to the experimental data fails, if the previously determined anisotropy contributions $K_d = 7.5 \mu\text{eV/atom}$ [9], $2K_2^S = -166 \mu\text{eV/atom}$ [83] and $K_2^V = 30 \mu\text{eV/atom}$ [37] to K_2^{eff} are used. The calculated widths of the domain wall are more than one order of magnitude too small, indicating that the assumed K_2^{eff} is too large, or that the theoretical approach is not valid for systems, like the tetragonally distorted ultrathin Ni/Cu(100) films. In order to obtain a better understanding of the Néel walls of in-plane magnetized Ni/Cu(100) films, the domain wall of a film of 8 ML thickness was analyzed in detail.

5.1.2 Analysis of a domain wall of an 8 ML Ni/Cu(100) film

For the following discussion of magnetization and electron spin-polarization directions, spherical coordinates are used. The polar angle is denoted as θ , which is measured against the surface normal ($\theta = 0^\circ$). The azimuthal angle Φ is measured in the counter-clockwise direction, and

Variation of the polar angle of \mathbf{P} :



Variation of the azimuthal angle of \mathbf{P} :

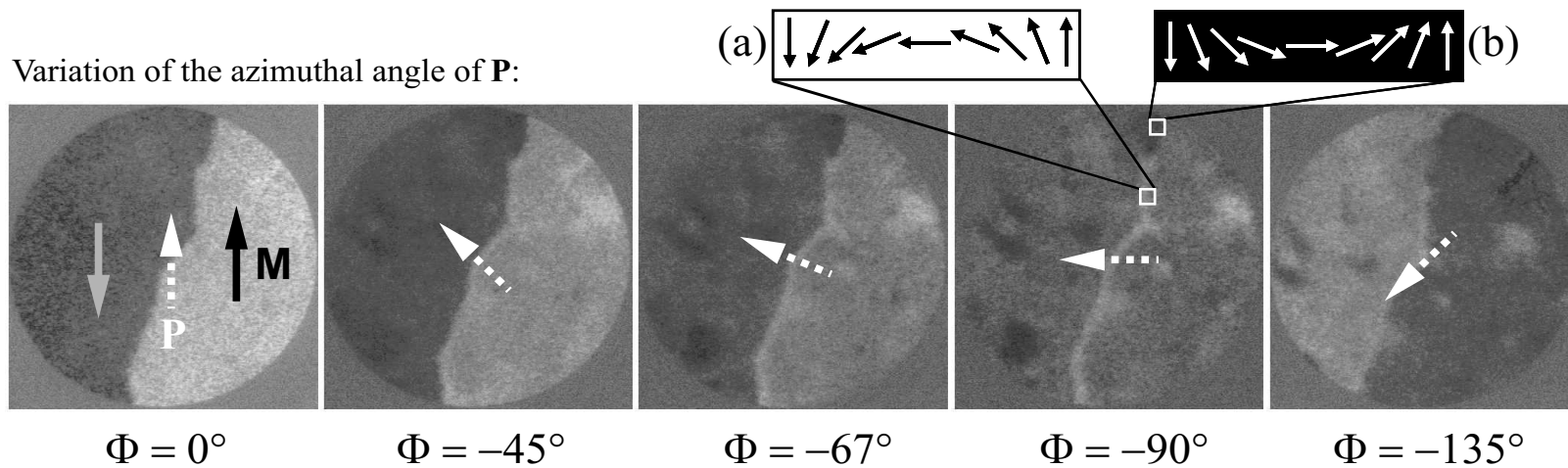


Figure 5.5: SPLEEM images of an 8 ML Ni/Cu(100) film at 300 K as a function of the polar angle θ (top) and azimuthal angle Φ (bottom) of the polarization \mathbf{P} of the electron beam (white dashed arrow). Top: Sharp magnetic contrast with \mathbf{P} oriented in the film plane (left), no MC with \mathbf{P} normal to the surface (right), i. e. the Ni film is fully in-plane magnetized. Bottom: The MC disappears at $\Phi = -90^\circ$, i. e. the magnetization in the domains is oriented as indicated by the arrows in the left image. Two chiralities exist in the Néel wall, as shown in the image ($\Phi = -90^\circ$).

$\Phi = 0^\circ$ corresponds to the “12 o’clock” orientation in the SPLEEM images.

The structure of the domain wall of the 8 ML Ni/Cu(100) film imaged in Fig. 5.1 was analyzed in greater detail as shown in Fig. 5.5. Initially, while keeping the azimuthal angle fixed at $\Phi = 0^\circ$, the polar angle θ of the electron beam polarization was varied in steps from $\theta = 90^\circ$ (\mathbf{P} in-plane) to $\theta = 0^\circ$ (\mathbf{P} along the surface normal). Diminishing contrast in this series confirms the absence of out-of-plane magnetization components, i. e. the local magnetization vectors lie in the surface plane in both domains. Then, the polar alignment of the illumination beam polarization was fixed at $\theta = 90^\circ$ (\mathbf{P} in-plane) and the azimuthal polarization orientation was swept through an angle of $\Phi = -135^\circ$. The magnetic contrast between the domains can be seen to decrease in this series: it finally vanishes when \mathbf{P} is perpendicular to the magnetization vectors of the two domains. The absence of magnetic contrast between the two domains for the alignment $\Phi = -90^\circ$ confirms that the two domains are anti-aligned and are thus separated by a 180° domain wall. In all but the $\Phi = 0^\circ$ direction of \mathbf{P} , additional contrast can be discerned in the region of the domain wall. Most clearly at $\Phi = -90^\circ$, a large section of the domain appears brighter and a shorter segment near the top of the image appears dark. Consequently, the domain wall has Néel structure, in which the magnetization reorientation between the two anti-aligned domains takes place within the film plane. In a Bloch wall, in which the magnetization rotates in a plane normal to the film surface, no MC would occur in the image at $\Phi = -90^\circ$. The fact that different sections of the observed wall show opposite magnetic contrast is consistent with the expectation that Néel walls must occur in two degenerate chiralities, as indicated schematically in the figure.

To confirm this interpretation the average line profile across the 180° wall of the SPLEEM image at $\Phi = -90^\circ$ of Fig. 5.5 (lower panel) is depicted in Fig. 5.6. The profile, consisting of the average of about 50 parallel profile lines, shows the typical shape of a Néel wall consisting of a narrow core and two long tails as discussed in reference [17]. The gray curve in the figure is a fit according to Eq. (5.2), which is based on continuum micromagnetic theory [17] and was recently applied to fit Bloch wall profiles [183]. The solid gray curve adequately describes the core of the Néel wall, yielding a width of $w_{\text{core}} \approx 400$ nm. However, this function fails in the elongated tail region of the Néel wall (dashed curve). Numerical computations yield that in the tail the direction cosine $\alpha(x)$ between the magnetization vector in the wall and the x -axis, which is assumed to be perpendicular to the easy axis of the uniaxial anisotropy of the film, decrease with the distance x from the wall center according to a logarithmic law [184,185]. The magnetic stray field originating in the tail region is shown to be responsible for the logarithmic variation. A complex analytic solution of the Néel wall shape is presented by Riedel et al. [99] which is beyond the scope of this work. For the sake of simplicity Eq. (5.3) is used to fit the tail region showing an appropriate description of the logarithmic tail of the domain wall, which is given by the black solid curve in the Fig. 5.6.

The total description of the Néel wall profile is given by Eq. (5.1), which sums up the functions for the core and the tail.

$$y(x) = y_{core}(x) + y_{tail}(x) \quad (5.1)$$

$$y_{core}(x) = y_0 + y_1 \sin\left(\arcsin\left[\tanh\left(\frac{x - x_0}{w/2}\right)\right] + \frac{\pi}{2}\right), \quad (5.2)$$

$$-0.237 \mu m < x < 0.237 \mu m$$

$$y_{tail}(x) = y_{core}(x) + \ln|x|, \quad (5.3)$$

$$x > 0.237 \mu m \quad \wedge \quad x < -0.237 \mu m$$

The offset $y_0 = -141.5$ and the factor $y_1 = -6.5$ are used to fit the profile of the domain wall. Since the ordinate in Fig. 5.6 corresponds to the grey scale values determined from the SPLEEM image, there is no strict physical meaning in the values of y_0 and y_1 . The fit function Eq. (5.1) rather demonstrates, that the *shape* of the Néel wall profile can be described taking a logarithmic behavior of the extended tails into account, whereas the approach for Bloch walls (Eq. (5.2)) alone is not sufficient to fit the whole Néel wall profile.

Using the equation for the width of a 180° -domain wall $w_{180^\circ} = 2\sqrt{A/K_2^{\text{eff}}}$ with the exchange constant $A = 0.75 \times 10^{-11}$ J/m, which is the average of values given for Ni films with 157 to 250 nm thickness [186], an effective anisotropy parameter $K_2^{\text{eff}} = K_2 - K_d = 0.9 \times 10^3$ J/m³ is derived. The parameter K_2^{eff} , which includes shape (K_d) and second-order magnetocrystalline anisotropy (K_2), is about one order of magnitude smaller than the experimental determined K_2^{eff} of an 8 ML Ni film on Cu(001) at 300 K [33,85]. Such a difference by orders of magnitude was also observed for Co monolayers on Cu(100) [187], where a Néel wall width of about 500 nm and 300 nm was measured for films of 5.5 ML and 9 ML thickness. One should note here, that a calculation of the Néel wall width of “negative anisotropy materials” favoring $\langle 111 \rangle$ directions like Ni should be corrected by taking magnetostriction effects into account, yielding a wall width $w = 6.5..7.2\sqrt{A/K_2^{\text{eff}}}$ (p. 234 of Ref. [17]) in better agreement with the experimental observations. Note, that in the SPLEEM images of the 8 ML Ni/Cu(100) film shown in Fig. 5.5 ($\Phi = -90^\circ$, lower panel) dark and bright areas within the domains appear, indicating that the magnetization there has a different in-plane orientation than the surrounding domains. Such features have also been observed in the vicinity of the spin-reorientation transition, which starts around 9.5 ML Ni. Near the SRT the effective anisotropy is known to become very small ($< 10^2$ J/m³) [84,85], and the small K_2^{eff} derived at 8 ML Ni may be explained within this framework. To quantitatively check the theoretical predicted shape and width of domain walls in magnetic monolayers one needs accurate knowledge of the magnetic anisotropy K_2^{eff} and the exchange constant A , which turns out not to be available in many systems. For example,

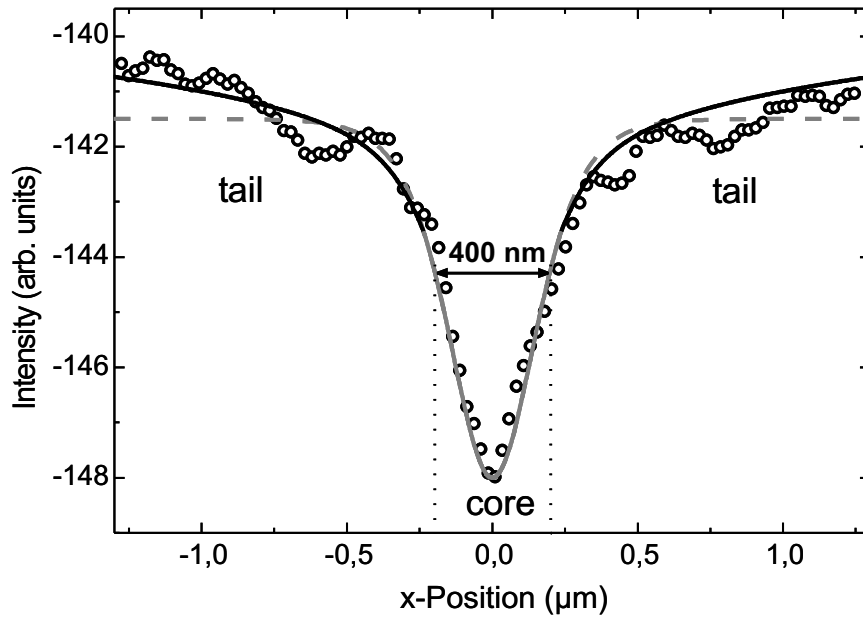


Figure 5.6: Profile of the white imaged Néel wall of the 8 ML Ni/Cu(100) film discussed in Fig. 5.5 (bottom). The gray curve is a fit according to equation 5.2. It describes adequately the 400 nm wide core of the domain wall, but it fails to fit the extended logarithmic tails of the Néel wall, which is described by equation 5.3 (black curves).

to obtain a quantitative agreement between the experimentally measured wall width of in-plane magnetized 1 ML Fe/W(110) [188] and the calculated one according to $w = 2\sqrt{A/K_2^{\text{eff}}}$, the exchange constant A had to be assumed one order of magnitude smaller than the bulk value and K_2^{eff} turned out to be more than two orders of magnitude larger than typical values of Fe films.

5.2 Evolution of magnetic stripe domains in Fe/Cu(100) films

The magnetic domains of Fe/Cu(100) ultrathin films have been observed during the film growth to investigate their evolution on a blank Cu(100) surface. The measurements have been performed at a deposition rate of 0.1 ML/min at 300 K and by using an energy of the electrons of 4.4 eV, which was optimized before, hence, to obtain the highest MC for Fe domains. Below 2.2 ML Fe no magnetic contrast was observed, which confirms that the film is in the paramagnetic state. In agreement with previous SPLEEM studies on Fe/Cu(100) films [38,169] the onset of magnetic contrast occurs around 2.2 ML Fe/Cu(100) at room temperature by the formation of anti-aligned narrow stripe domains with a perpendicularly oriented magnetization within regions of about $1 \mu\text{m} \times 1 \mu\text{m}$ lateral size. As the Fe layer thickness is increased, both the MC

and the area in which stripe domains are formed increase within an Fe thickness interval of 0.04 ML while the stripe width remains constant. Fig. 5.7 shows the evolution of domains as a function of Fe layer thickness. At 2.22 ML the highest density of 6 stripe domains per micrometer is observed, which yields an average stripe width of 165 nm. The stripe domains run parallel to the Cu step edges and their length exceeds the field of view of the microscope which is 7 μm . Man et al. [38] observed a meandering multi domain state in the 2 ML Fe thickness range rather than ordered stripe domains. Imaging the clean Cu surface by LEEM, round step edges with no preferential direction separated by terraces of some 100 nm were observed. In contrast to their findings the stripe domains observed in this work are clearly pinned to the parallel oriented Cu steps which are separated by only 100 – 200 nm wide terraces. Upon increasing the Fe layer thickness up to about 2.4 ML the direction of the magnetization in dark (bright) colored stripe domains, confined by adjacent bright (dark) colored stripe domains of opposite orientation of the magnetization is reversed spontaneously. This results in a formation of broader dark and bright imaged stripe domains as depicted in Fig. 5.7 (f)-(h). The maximum domain width of about 5 μm is found around 3 ML Fe/Cu(100) at room temperature [12]. Above 3 ML the domains start to form smaller stripe domains again in the vicinity of the structural transition from fct to fcc, which occurs around 3.6 ML at 300 K and is accompanied by a transition to a phase of a ferromagnetic “live layer” (not shown here).

The occurrence of magnetic contrast in Fe/Cu(100) as a function of the thickness is a consequence of the thickness dependent T_C which increases with increasing film thickness. Around 2.2 ML Fe/Cu(100) T_C reaches room temperature and ferromagnetic order sets in. Since Fe has a positive surface anisotropy, which favors an orientation of the magnetization normal to the surface and which leads to an increase of K_2 with decreasing film thickness d according to $K_2 = K_2^V + 2K_2^S/d$, the domains are perpendicularly magnetized at low thicknesses. For a 4 ML Fe/Cu(100) film the surface anisotropy $2K_2^S$ and the volume anisotropy K_2^V were determined to equal $2K_2^S = 120 \mu\text{eV/atom}$ and $K_2^V = 78 \mu\text{eV/atom}$, resulting in a total $K_2 = 108 \mu\text{eV/atom}$ at a reduced temperature $T/T_C = 0.54$ [189]. At 2.2 ML Fe K_2 is only slightly larger than the long-range dipole-dipole-interaction, which favors an in-plane orientation of the magnetization. In order to reduce the dipolar stray field energy, a domain pattern of up and down magnetized narrow stripe domains is formed at the onset of ferromagnetism. This reduction of the stray field energy, however, competes against the increase of the domain wall energy. The sinusoidal domain profile depicted in Fig. 5.8 (a) is derived from the SPLEEM image of Fig. 5.7 (e) and reflects a ratio $\delta = \frac{w}{a} = 1$ of the domain wall width w to the domain width a . In agreement with the theory stated in chapter 1.3.3 this ratio corresponds to the minimum value of the dimensionless quantity $f = f_{min} = \frac{K_2^S}{\frac{1}{2}\mu_0 M_0^2 a_0 c} \approx 1$, for which domains occur in ultrathin films. The domain configuration becomes energetically stable as f increases from f_{min} . Thus, the evolution of broader stripe domains, i. e. the degradation of domain walls, between 2.2 ML and

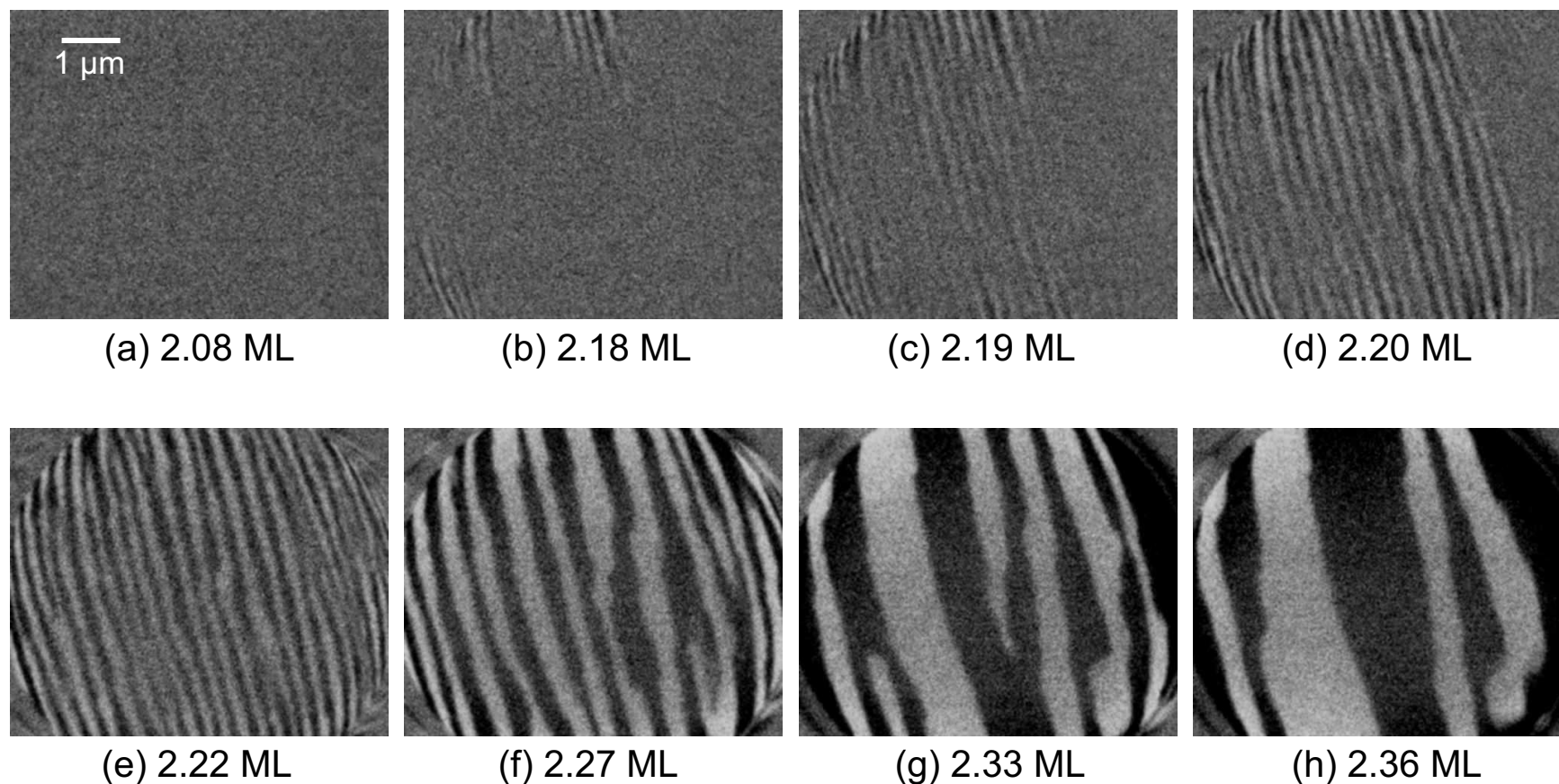


Figure 5.7: Evolution of magnetic domains of an ultrathin Fe/Cu(100) film as a function of the Fe layer thickness at 300 K. The component of the magnetization normal to the surface is imaged at an energy of the electrons of 4.4 eV. Below 2 ML the Fe film is in the paramagnetic state. At 2.2 ML Fe (b) ferromagnetic order starts by the formation of narrow, perpendicularly magnetized stripe domains. With increasing Fe layer thickness the magnetic contrast increases and the narrow stripe domains form broader domains.

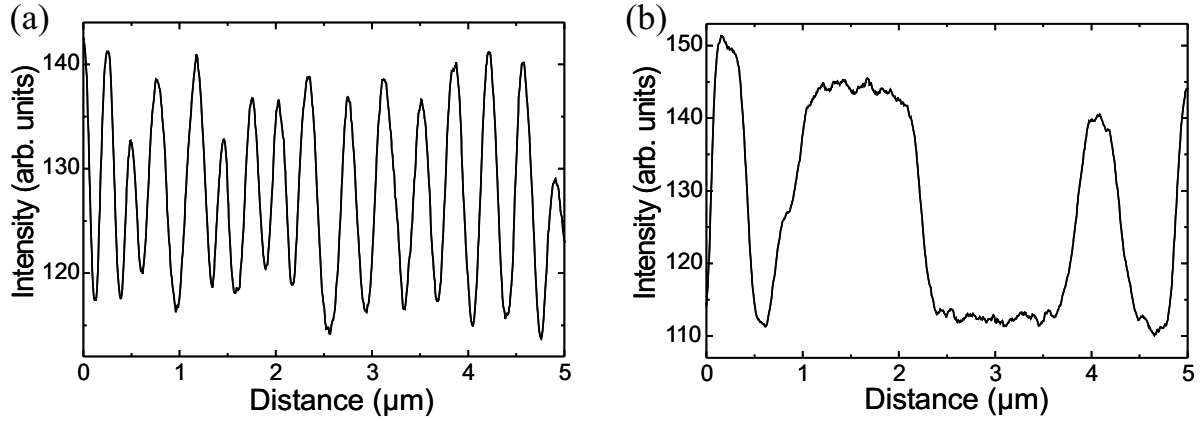


Figure 5.8: Profiles of perpendicularly magnetized stripe domains of Fe/Cu(100). (a) The profile is derived from the SPLEEM image of a 2.2 ML film shown in Fig. 5.7 (e). The average domain width is 165 nm. The sinusoidal shape reflects the equal size of domains and the separating walls and yields in agreement with theory $f = f_{min}$ (see chapter 1.3.3) for which domains occur. (b) Typical domain widths of a 2.4 ML film imaged in Fig. 5.7 (h) are 500 nm to 1500 nm.

3 ML Fe as illustrated in Fig. 5.8 (b) must be interpreted in terms of an increased K_2 , indicating that in this low thickness range the proportionality $K_2 \propto \frac{1}{d}$ is obviously not valid. The domain wall energy per unit length, which is given by $\gamma = 4d\sqrt{A|K_2^{eff}|}$ [16], increases with increasing layer thickness d , and hence the number of domain walls is reduced. Earlier investigations of this thin film system showed again a breakup of smaller stripe domains as the Fe layer thickness is increased from 3 ML to 4 ML [12,38,169]. Here, the increase of d reduces K_2 and the multi domain state becomes energetically favorable, before K_2 becomes smaller than the shape anisotropy. This leads to a reorientation of the magnetization into the film plane around 6 ML Fe/Cu(100) grown at low temperatures [29,190].

5.3 Fe monolayers on 7 to 11 ML Ni/Cu(100)

In the previous section Fe layers were grown on a non-magnetic Cu(100) surface and the evolution of narrow stripe domains at the onset of ferromagnetism has been observed. In this section it will be demonstrated how magnetic domains evolve as Fe layers are grown on out-of-plane magnetized Ni(100) surfaces with the Cu in-plane lattice constant.

In the following chapters, again polar coordinates are used to characterize magnetization and electron spin-polarization directions, as introduced in section 5.1.2. The azimuthal angle Φ , however, is now measured against the Cu step direction as indicated in the respective figures.

5.3.1 Out-of-plane magnetized domains (0 to 2.5 ML Fe)

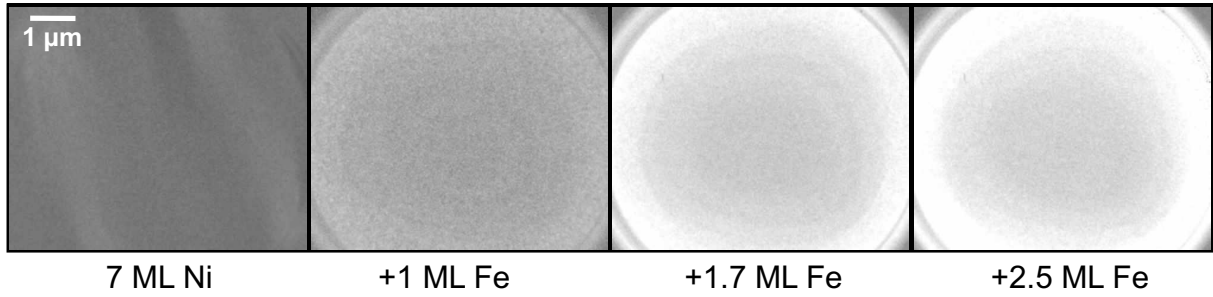
Fe layers up to 2.5 ML thickness were grown on out-of-plane magnetized Ni/Cu(100) films of 7 ML, 7.5 ML and 11 ML thickness. In this thickness range Ni films are still tetragonally distorted adopting the Cu in-plane lattice constant [82]. The size of the Ni domains vary between 1 μm and 6 μm , which is considerably smaller than the in-plane magnetized Ni domains at lower thicknesses which had been observed in section 5.1 to be several 10 μm . Three different Ni underlayers are discussed:

1. Ni films around 7 ML, which reveal an out-of-plane canted magnetization states with a canting angle of $20^\circ - 30^\circ$ against the surface normal.
2. Ni films around 7.5 ML, which are fully perpendicularly magnetized but still in the vicinity of the spin-reorientation transition thickness.
3. Ni films of 11 ML, which are perpendicularly magnetized and well above the SRT thickness.

The canted magnetization in 7 ML Ni/Cu(100) films yields only a weak magnetic contrast of the magnetization component normal to the surface. This is due to the small magnetic moment of Ni ($0.62 \mu_B$) and the fact that only the component perpendicular to the film plane contributes to the signal $MC \propto \mathbf{P} \cdot \mathbf{M}$. However, the parallel alignment of the domain walls of the 7 ML Ni/Cu(100), which is the orientation of the Cu atomic step edges, can be faintly seen in Fig. 5.9. As less than 1 ML Fe is deposited onto the Ni/Cu(100) film, the domain pattern of the pure Ni film changes into a state of out-of-plane magnetized domains, which are much larger than the field of view, i. e. 7 μm . The magnetic contrast of the SPLEEM images increases as a consequence of the increased number of magnetic moments as the Fe layer grows up to 2.5 ML.

The perpendicularly magnetized domains of the 11 ML Ni/Cu(100) give rise to a strong MC, which shows that the domain walls are pinned along the substrate step edges, as compared to the topographic LEEM image in Fig. 5.10. Upon depositing Fe on top of the Ni film, again, the MC increases but the original domain pattern of the Ni film is broadened by only 20% as demonstrated in Fig. 5.9 (b). No significantly greater broadening of the original domain pattern of 11 ML Ni/Cu(100) films was observed as Fe layers were deposited up to the critical thickness, at which the spin-reorientation transition takes place. The strong domain wall pinning at the regularly aligned Cu step edges, which emerge in the LEEM image of Fig. 5.10, obviously impede the linear domain expansion in ultrathin films with large perpendicular anisotropy as found by Allenspach *et al.* [105] in Co/Au(111), or as determined by the earlier theory of Kittel [18]. There, the domain growth was found to increase with the square root of the film thickness. The domain wall width of the Ni/Cu(100) film of $w_{\text{Ni}} = 130 \pm 10 \text{ nm}$ increases by 15% to $w_{\text{Fe-Ni}} = 150 \pm 10 \text{ nm}$ by the deposition of Fe layers up to 2.3 ML. This leads to a reduction of

(a) Fe on 7 ML Ni/Cu(100)



(b) Fe on 11 ML Ni/Cu(100)

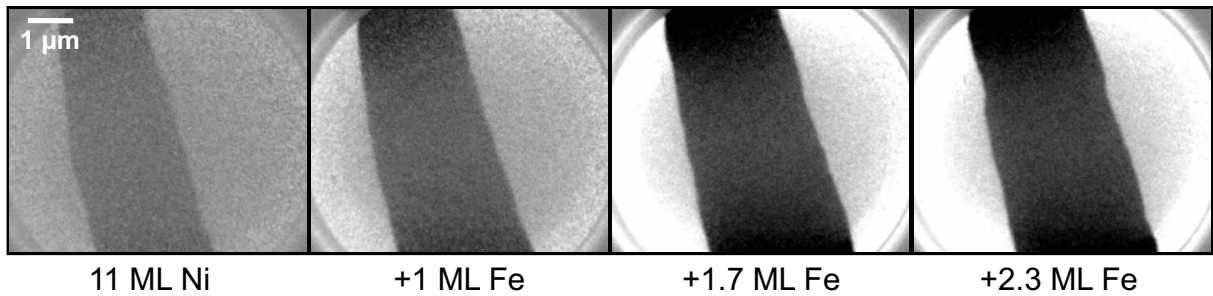


Figure 5.9: Evolution and size of magnetic domains of ultrathin Fe layers on out-of-plane magnetized Ni/Cu(100) films. The perpendicular component of the magnetization of the 7 ML Ni/Cu(100) is weak, deposition of Fe enlarges the domain size over the field of view ($7 \mu\text{m}$) and increases the magnetization dramatically (a). The magnetic contrast of the 11 ML Ni is stronger compared to 7 ML Ni and the original width of the dark imaged domain increases by only 20% (b).

the effective anisotropy K_2^{eff} including the shape anisotropy according to $w_{180^\circ} = 2\sqrt{A/K_2^{\text{eff}}}$ by 25%.

The completely perpendicularly magnetized 7.5 ML Ni/Cu(100) film reveals a domain pattern of wide stripe domains of irregular width in the range of $0.5 \mu\text{m}$ to more than $3 \mu\text{m}$. These stripe domains are confined by domain boundaries, which are pinned at the substrate step edges as shown in Fig. 5.10. With increasing Fe layer thickness d the number of domain walls is reduced due to the enhanced wall energy given by $\gamma \propto d\sqrt{A|K_2^{\text{eff}}|}$. No major change of the domain wall width $w_{Ni} = 210 \pm 10 \text{ nm}$ of the Ni film is found during Fe deposition, indicating that K_2^{eff} does not change significantly. Up to approximately 0.5 ML Fe the residual domain walls keep pinned in their original direction, as the domain size grows beyond the $7 \mu\text{m}$ -field of view of the SPLEEM. As the Fe thickness exceeds 0.6 ML, parts of the walls detach from the pinning site. At 0.8 ML Fe the whole domain wall within the field of view has rotated counter clockwise by -30° degrees away from the initial orientation into the [011] direction, which is confirmed by the LEED image, which shows the cubic lattice structure of the bare Cu(100) crystal. Compared to the 11 ML Ni/Cu(100) the conclusion is, that the larger perpendicular

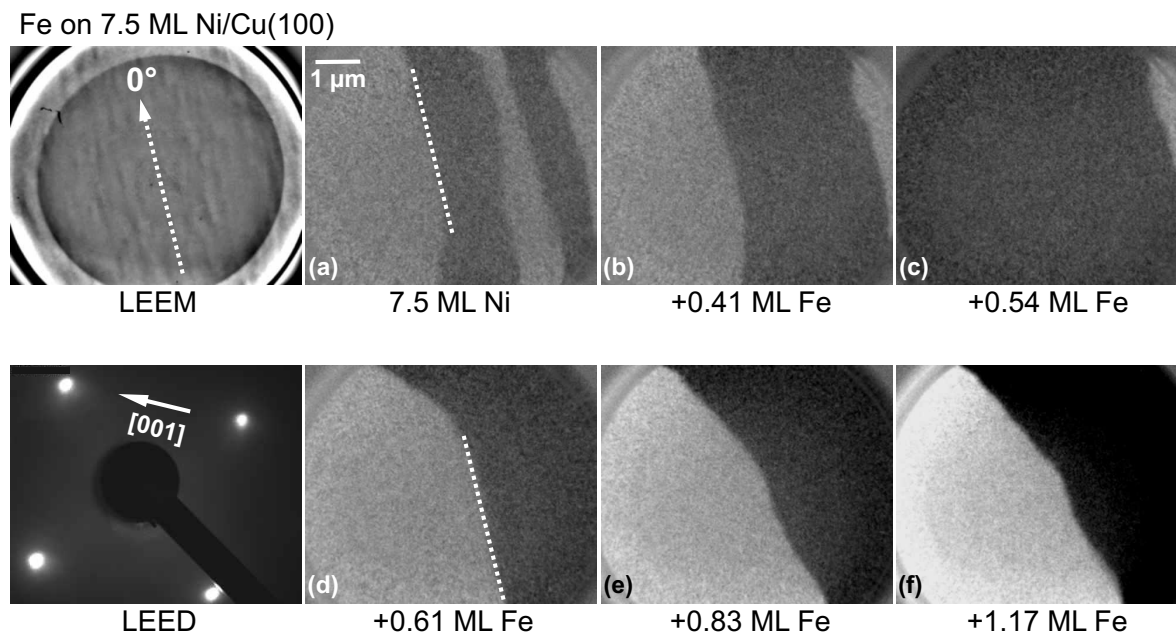


Figure 5.10: Perpendicularly magnetized stripe domains of a 7.5 ML Ni/Cu(100) film have a width of 0.5-3 μm and are pinned along the Cu atomic step edges, as indicated by the white dotted line (a). Addition of 0.5 ML Fe causes a formation of larger domains (b)-(c). At an Fe amount of more than 0.6 ML the domain wall pinning is lifted, and an orientation of the wall without correlation to the topography but along [011] takes place, (d)-(f). Note, that the sample has been moved to a different position in (d).

anisotropy of the Ni underlayer must be responsible for the strong domain wall pinning. The thinner Ni film has a lower effective anisotropy, since the film thickness is still close to the spin-reorientation thickness, where the value of K_2^{eff} becomes small. The larger width of the domain walls found for Fe layers grown on 7.5 ML Ni/Cu(100) compared to bilayers based on 11 ML Ni/Cu(100) is also attributed to the lower anisotropy. Obviously, the pinning of the narrower domain walls is stronger than that of the wider ones. Note, that the wall rotation in the 7.5 ML Ni film is accompanied by the occurrence of slight in-plane contrast, which indicates that the magnetization is tilted against the surface normal. Such spin canting below 1 ML Fe is observed in all studied Fe/Ni bilayers on Cu(100). Due to the increased shape anisotropy and the change of the surface anisotropy, as Fe atoms are adsorbed at the surface, the perpendicular anisotropy of the Ni layer is reduced leading to a canted orientation of the magnetization of the bilayer system.

The identification of the type of domain walls in perpendicularly magnetized Ni/Cu(100) and Fe/Ni/Cu(100) ultrathin films with low Fe coverage turned out to be difficult. Although the magnetization reorientation mechanism is different in Bloch and Néel walls –as discussed in section 1.3– the magnetization in the core of both walls lies parallel to the surface and should give rise to magnetic contrast of the walls in one direction of the electron beam polarization \mathbf{P} within the film plane. However, no magnetic contrast of the domain walls within the film plane

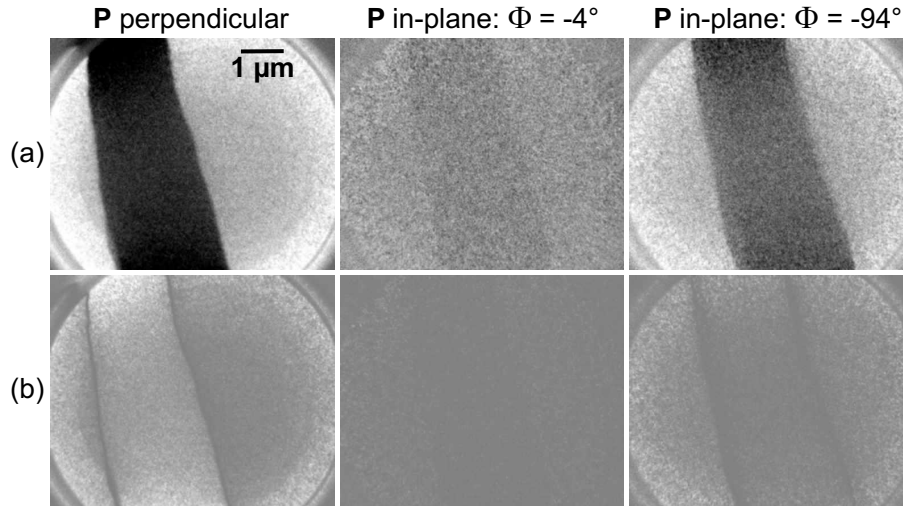


Figure 5.11: (a) Original SPLEEM images of an $\text{Fe}_{0.7}/\text{Ni}_{11}/\text{Cu}(100)$ at three different orientations of the beam polarization \mathbf{P} and (b) the corresponding modified images, in which areas are accented which do *not* show any magnetic contrast in the SPLEEM images above. Only in the images with \mathbf{P} perpendicular to the surface and \mathbf{P} along $\Phi = -94^\circ$ in-plane the domain walls are visible in (b), indicating that the magnetic moments do *not* point into these directions but along the domain wall. The walls are Bloch walls.

of $\text{Ni}/\text{Cu}(100)$ and $\text{Fe}/\text{Ni}/\text{Cu}(100)$ films with an Fe layer thickness below 1.75 ML is observed. Weak MC of the walls occurs for the first time at 1.75 ML Fe in the SPLEEM images taken at $\Phi = -4^\circ$, and no MC in the walls is detected at $\Phi = -94^\circ$. In the Fe thickness range of 1.75 ML to 2.5 ML magnetic contrast occurs in the domain walls of the images detecting the in-plane component of the magnetization along the domain walls ($\Phi = -4^\circ$ orientation), but no in-plane MC within the walls is found perpendicular to this direction ($\Phi = -94^\circ$ orientation of \mathbf{P}). In Fig. 5.11 (a) original SPLEEM images of an $\text{Fe}_{0.7}/\text{Ni}_{11}/\text{Cu}(100)$ film at three different orientations of \mathbf{P} and the corresponding modified images (b), in which areas are accented which do *not* show any magnetic contrast in the SPLEEM images above (i. e. the domain walls and the background outside the circular field of view) are presented. Only in the modified images (b) with \mathbf{P} perpendicular to the surface and \mathbf{P} oriented in-plane along $\Phi = -94^\circ$ the domain walls are visible, which indicates that the magnetization does *not* point into these directions. No dark lines are seen in the image with \mathbf{P} oriented in-plane along $\Phi = -4^\circ$ (b), which indicates that the magnetization in the wall must be aligned parallel to the wall. Since in this Fe thickness range the film is out-of-plane magnetized with a polar angle of $\theta \approx 15^\circ$, these domain walls are identified as Bloch walls. In Fig. 5.12 the in-plane component of the canted magnetization pointing along the Bloch wall is imaged. Interestingly, the chirality of both walls changes as the Fe thickness is increased from 1.75 ML to 2.5 ML, where the domain splitting indicates the beginning of the spin-reorientation transition. As will be discussed in chapter 6 the Bloch walls turn into Néel walls during the SRT.

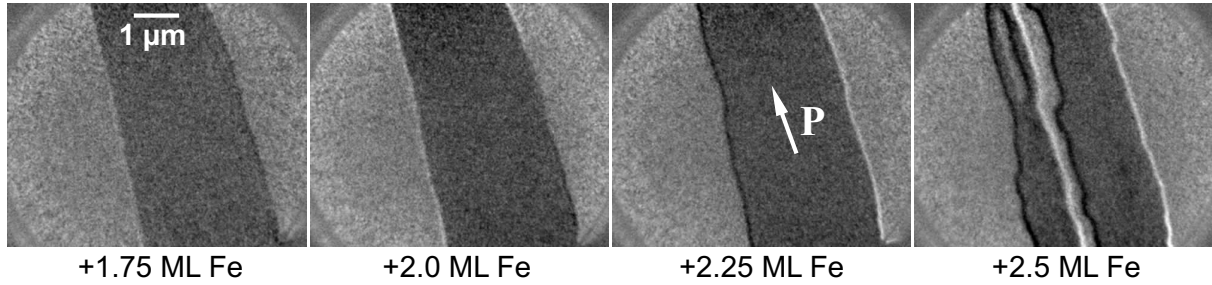


Figure 5.12: Evolution of Bloch walls of an $\text{Fe}_x/\text{Ni}_{11}/\text{Cu}(100)$ film as a function of the Fe layer thickness x . Imaged is the magnetization component pointing into $\Phi = -4^\circ$ within the film plane as indicated by the white arrow and **P**. At 1.75 ML Fe magnetic contrast occurs in the domain wall and increases up to 2.5 ML Fe. Interestingly, the chirality of both walls changes from 1.75 to 2.25 ML Fe coverage. No magnetization component of the wall within the film plane is observed at $\Phi = -94^\circ$ (perpendicular to the wall) below 2.5 ML Fe, indicating the sense of magnetization reorientation of a Bloch wall.

It remains unclear why there is no in-plane MC of the domain walls of the 11 ML Ni/Cu(100) film. One might argue that the perpendicular anisotropy of the film is so large that according to $w = 2\sqrt{A/K_{\text{eff}}}$ the wall width w becomes too small to be resolved. Using the anisotropy constants $K_{2,\text{Ni}}^V$ and $K_{2,\text{Ni}-\text{Cu}}^S$ from table 6.3 and $K_{2,\text{Ni}-\text{vac}}^S = -159 \mu\text{eV/atom}$ from [83] and $7.5 \mu\text{eV/atom}$ [9] for the shape anisotropy yields a domain wall width of ≈ 30 nm. This result could indeed mean that the wall is too narrow to be resolved, since it is close to the best resolution of 10 nm of the SPLEEM. However, the measurement of the wall width of the domains in the images with **P** normal to the surface yields ≈ 130 nm, which is in clear contradiction to the calculated width. The idea to extrapolate the wall width, derived from the images with **P** oriented in-plane along $\Phi = -4^\circ$ and $\Phi = -94^\circ$, from 2.5 ML Fe down to 0 ML Fe, in order to determine the wall width of the 11 ML Ni/Cu(100) film also did not confirm a wall width around 30 nm. Furthermore, the wall width in the images with **P** oriented in-plane do not show a monotonic dependence as a function of the Fe thickness, but they remain rather constant at 130 nm within an error of ± 10 nm. This confirms the width measured in the domain image probing the normal magnetization component of 11 ML Ni/Cu(100). A vanishing domain wall MC in the film plane may be due to the small magnetic moment of Ni. It shall be noted, that even the expected in-plane magnetic contrast of films in the thickness range of 5 to 7 ML was not detected on the used Cu(100). A theoretical explanation that the wall is a vortex wall with a Néel cap, in which the in-plane projection of magnetic moments pairwise compensated each other and thus yield a net magnetic moment near zero within the wall, is rather improbable, since such vortex walls are more likely to appear in thicker films, e. g. 100 nm Permalloy [17].

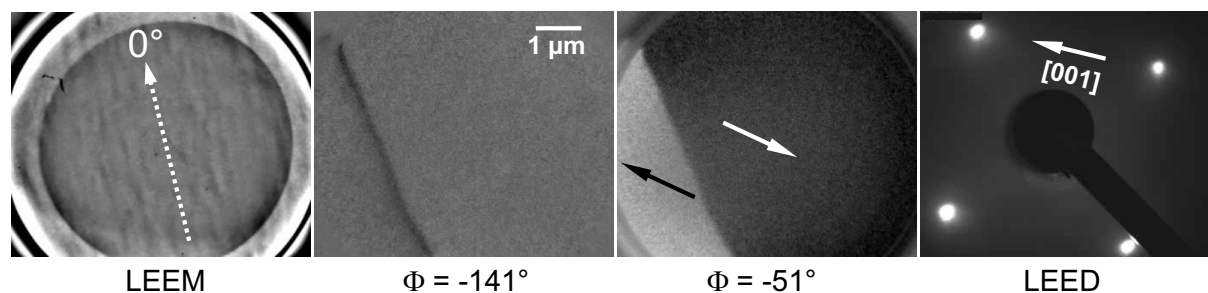


Figure 5.13: In-plane magnetized $\text{Fe}_{2.8}/\text{Ni}_{7.5}/\text{Cu}(100)$ film at 300 K. At $\Phi = -141^\circ$ the magnetic contrast vanishes and the Néel wall is revealed by dark contrast. The arrows indicate the direction of the magnetization, which is collinear to the [001] crystallographic axis, as confirmed by the LEED image taken at an energy of the electrons of 150 eV.

5.3.2 In-plane magnetized domains (> 2.8 ML Fe)

Fe/Ni bilayers on Cu(100) with Fe cap layers above 3 ML are magnetized in the film plane for all Ni layer thicknesses studied (1.5 ML to 11 ML). The domain size is found to be on the order of $10 \mu\text{m}$. The magnetization direction with respect to the crystallographic axes was checked by low energy electron diffraction. In agreement with the expectation for the easy axis of the magnetization of Fe films grown on Cu(100), which is [001], the easy axis of the $\text{Fe}_{2.8}/\text{Ni}_{7.5}/\text{Cu}(100)$ film is collinear to the [001] crystal axis. It should be noted that the LEED system was installed after the measurement, and only for this measurement the crystallographic orientation of the Cu(100) substrate was determined. Fig. 5.13 illustrates the determination of the magnetization direction in the film plane. With the electron beam polarization directed in the plane ($\theta = 90^\circ$) the azimuthal angle Φ was varied until the magnetic contrast in both domains vanished at $\Phi = -141^\circ$. Since $MC \propto \mathbf{P} \cdot \mathbf{M}$ the easy direction is collinear to the orientation $\Phi = -51^\circ$. The magnetization vectors within the two domains are anti-aligned as indicated by the arrows, and they are parallel to the [001] direction, which is confirmed by the LEED pattern taken at an energy of the electrons of 150 eV. The domain wall, however, seems to be pinned although it does not exactly run parallel to the Cu atomic steps as shown in Fig. 5.10. The width of the domain wall is $215 \pm 10 \text{ nm}$, which is the same as measured for the perpendicularly magnetized underlayer with and without Fe cap layers up to 2.25 ML. From the dark MC of the domain wall at $\Phi = -141^\circ$ in Fig. 5.13 it is clear, that the magnetization within the wall rotates in the film plane, which is characteristic for a Néel wall.

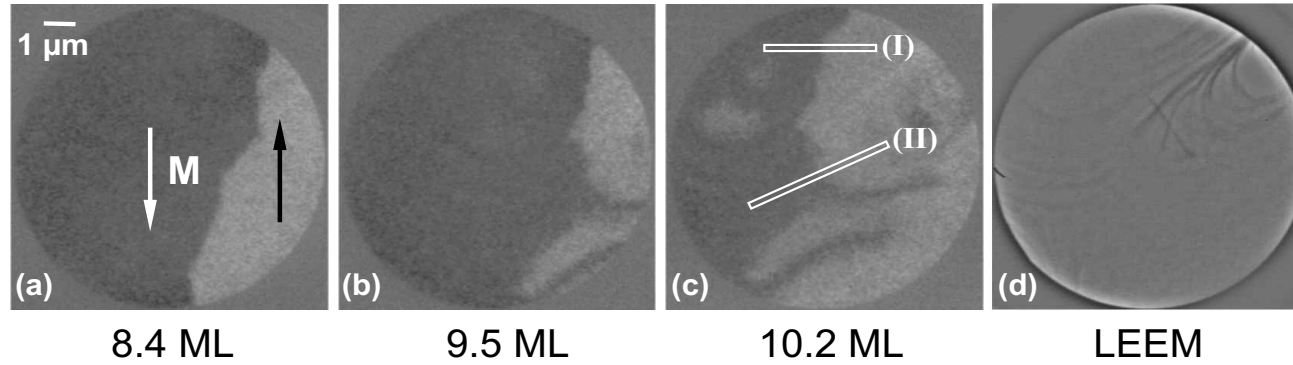
6 Magnetic domains near the spin-reorientation transition

The modification of magnetic domains and domain walls at the continuous spiral-like spin-reorientation transition of ultrathin Ni/Cu(100) films at 300 K as a function of film thickness is discussed in section 6.1. In section 6.2 the reorientation of the magnetization of Fe/Ni bilayers on Cu(100) from the out-of-plane direction to an in-plane direction is analyzed as a function of the Fe layers thickness at room temperature. The orientation of the individual magnetizations of the Fe and the Ni layer is determined element-selectively as a function of the thickness. Finally, the change of the effective magnetic anisotropy and the value of the magnetic moments at the Fe-Ni interface is discussed.

6.1 Continuous reorientation of the magnetization in Ni/Cu(100) films

The formation of in-plane magnetized domains in the thickness range of 5 ML to 8 ML Ni/Cu(100) has already been discussed in section 5.1. It was found that the domain structure remains unchanged for Ni thicknesses below 9.5 ML. Around 9.5 ML a spontaneous modification of the domain wall is observed, whereby about $0.5 \mu\text{m}$ wide protrusions of approximately $6 \mu\text{m}$ length, along with a reduced magnetic contrast, are formed perpendicular to the domain wall as shown in Fig. 6.1 (b). These features correspond to an elongation of the domain wall within the $10 \mu\text{m}$ -field of view of 180%. The reduced MC indicates a change of the magnetization direction within the protrusions. Moreover, smaller domains of inverse magnetic contrast emerge within the still existing and large in-plane magnetized original domains. This also corresponds to an elongation of domain boundaries, which can be understood in terms of the lowered domain wall energy density per unit length γ due to the reduced effective anisotropy at the spin-reorientation transition according to $\gamma = d\sqrt{A K_2^{\text{eff}}}$, d being the film thickness. The reduction of the effective anisotropy is correlated with a domain wall broadening according to $w = 2\sqrt{A/K_2^{\text{eff}}}$. A typical example is shown in Fig. 6.2 by two domain wall profiles obtained from the two line scans (I) and (II) in image (c) of Fig. 6.1. While the width of the domain wall measured at (I) is comparable to the typical wall width of fully in-plane magnetized ultrathin

In-plane magnetization component ($\theta=90^\circ$, $\Phi=0^\circ$):



10.2 ML Ni/Cu(100) after 20 minutes:

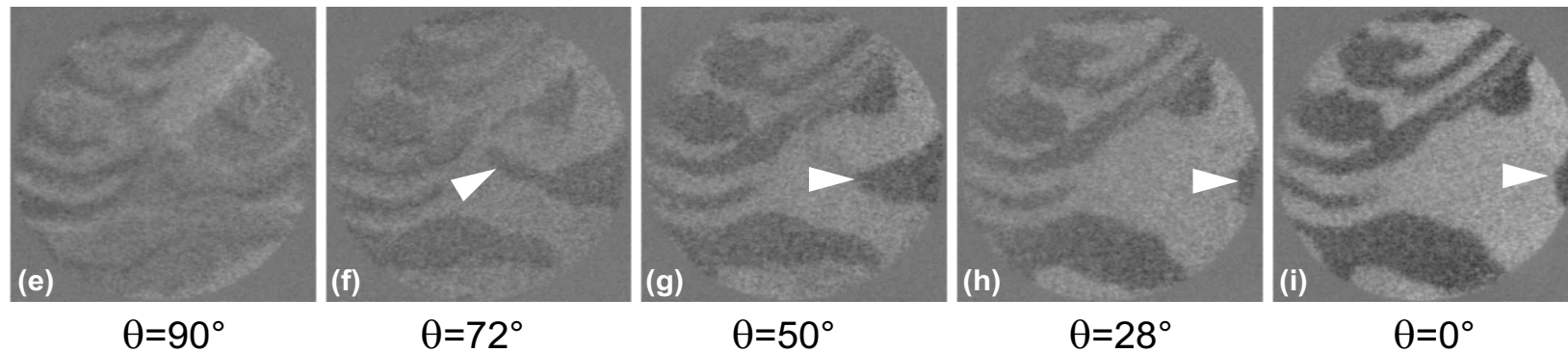


Figure 6.1: Spin-reorientation transition of Ni/Cu(100) at 300 K as a function of the thickness. The domain wall of the 8.4 ML in-plane magnetized Ni film (a) spontaneously forms elongated protrusions normal to the wall as the SRT thickness of $d_c = 9.5$ ML is reached (b). At 10.2 ML smaller domains of a reversed magnetization direction appear within the original domains (c). The domain wall in (c) was centered manually, and the profiles (I) and (II) are shown in Fig. 6.2. 20 min after film deposition. The 10.2 ML Ni film reveals a multi domain pattern with the magnetizations canting in an orientation close to the surface normal as indicated by polar angular investigations (e)-(i).

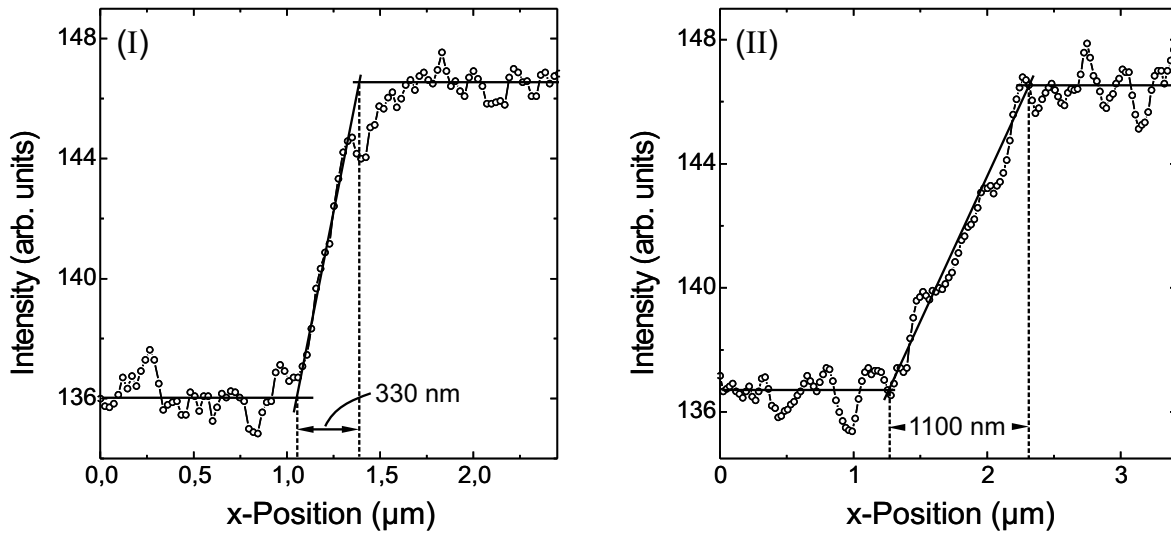


Figure 6.2: Domain wall profiles taken at the sites (I) and (II) of the domain image (c) in Fig. 6.1 of a 10.2 ML Ni/Cu(100) film at the SRT. While the width of the upper part of the domain wall (I) is still comparable to the typical wall width of fully in-plane magnetized ultrathin Ni/Cu(100) films (300 – 400 nm), the width of the wall segment (II), in close vicinity to the wall protrusion, is increased by $\approx 300\%$ due to the lowered effective anisotropy at the SRT according to $w = 2\sqrt{A/K_2^{\text{eff}}}$.

Ni/Cu(100) films (300 – 400 nm), the width of the wall segment (II), which is located in close vicinity to the wall protrusion, is increased by $\approx 300\%$. Similar results are obtained for wall segments of the elongated protrusion and also for the smaller domains with inverse magnetic contrast (bright areas). Here, the width of the walls ranges from 500 nm to more than 1200 nm. The determination of the exact domain wall width, however, is more difficult here since the signal to noise ratio decreases, due to the decrease of MC in these areas.

The time evolution of the domain configuration of the 10.2 ML Ni/Cu(100) film was checked by polar angular investigations 20 minutes after completion of the film growth. Fig. 6.1 (e) demonstrates that a meandering domain pattern with a low magnetic contrast of the in-plane component of the magnetization \mathbf{M} has formed. As the polar angle of the polarization \mathbf{P} was successively lowered to $\theta = 0^\circ$, where \mathbf{P} is aligned perpendicular to the surface, the MC increased, which is shown in Fig. 6.1 (e)-(i). The strongest MC in (i) indicates that the component of \mathbf{M} perpendicular to the surface is largest, which means that \mathbf{M} is oriented largely parallel to the surface normal. The reduction in size of the dark imaged domain at the right hand side of the SPLEEM images (see arrow) is not an angular dependent effect, but it corresponds to an increase in size of the respective surrounding out-of-plane magnetized domain as a function of time. This was checked by subsequently increasing the polar angle of \mathbf{P} back to $\theta = 90^\circ$. It was found (not shown here), that the meandering domain structure further developed to larger domains as a function of time. After 60 minutes waiting time at a base pressure of 2×10^{-8}

Pa, which corresponds to a gas exposure of 0.54 Langmuir, the orientation of \mathbf{M} of the 10.2 ML Ni/Cu(100) film was perpendicular to the film surface. This indicates the completion of the spin-reorientation transition. The adsorption of O and CO at the Ni surface is known to reduce the surface anisotropy and therefore shifts the SRT to lower thickness values [83,96,97]. We would like to emphasize, that although the SRT as a function of the Ni layer thickness was not completed at 10.2 ML, as confirmed by the existence of a magnetization component within the film plane (Fig. 6.1 (c) and (e)), the magnetization vector further on rotates completely out-of-plane. This is due to the fact that the surface anisotropy $2K_2^S$ is reduced, such that the positive volume anisotropy K_2^V becomes the dominant contribution to the total anisotropy.

In order to determine the orientation of the magnetization during the SRT, angular dependent domain imaging has been performed. Therefore, the perpendicular and two orthogonal in-plane directions of \mathbf{M} have been probed. The results of these additional measurements, which have been done by C. Klein and A. K. Schmid [191] recently, are depicted in Fig. 6.3. No perpendicular component of \mathbf{M} is detected in the thickness range 5 – 9 ML (a_1). The analysis of the clear magnetic contrast in the $\Phi = -162^\circ$ in-plane orientation of \mathbf{P} and the weak inverse MC in the $\Phi = -72^\circ$ in-plane orientation reveals, that the magnetization vector is aligned along the $\Phi = -176^\circ \pm 5^\circ$ within the film plane. Comparing this direction of \mathbf{M} with the LEEM and the LEED images presented at the bottom of Fig. 6.3 indicates, that the easy axis of the magnetization is collinear to the parallel alignment of the Cu step edges which do not run along the $\langle 011 \rangle$ directions, which are known to be low energy step directions on Cu surface vicinal to [100], Ref. [192]. Moreover, $\langle 011 \rangle$ is known to be the easy in-plane orientation for Ni/Cu(100). This means, that the in-plane easy axis of the magnetization of ultrathin Ni/Cu(100) films is predominantly determined by a step induced uniaxial anisotropy if many steps are aligned parallel. In the present case this step induced anisotropy overcomes the magnetocrystalline anisotropy along $\langle 011 \rangle$. In previous studies on the influence of parallel Cu step edges on the easy in-plane direction of the magnetization in Ni/Cu(001) it was shown, that the step induced anisotropy in films grown on Cu(001) crystals with miscuts of $<1^\circ$ [10] and 2.5° [90] orients the magnetization parallel to the steps.

At the start of the SRT around 9.3 ML a breakup into a state of micrometer-sized domains of irregularly shaped protrusions and isolated areas of a changed orientation of the magnetization with respect to the surrounding domain takes place. At the same time the magnetization rotates out of the film plane by an angle $\theta = 23^\circ \pm 5^\circ$ with respect to the sample's normal within the bright domain in (a_2). This angle is determined from the magnetic contrast of the three SPLEEM images at 9.3 ML. Here, both in-plane directions of \mathbf{P} yield a similar MC within the domain, which has formed in the upper left of the images, indicating that the in-plane component of \mathbf{M} has changed (b_3, b_4). The deviation in the domain shape of the images showing the in-plane component of \mathbf{M} (b_3, b_4) from the domain pattern in (a_2), i. e. the perpendicular component,

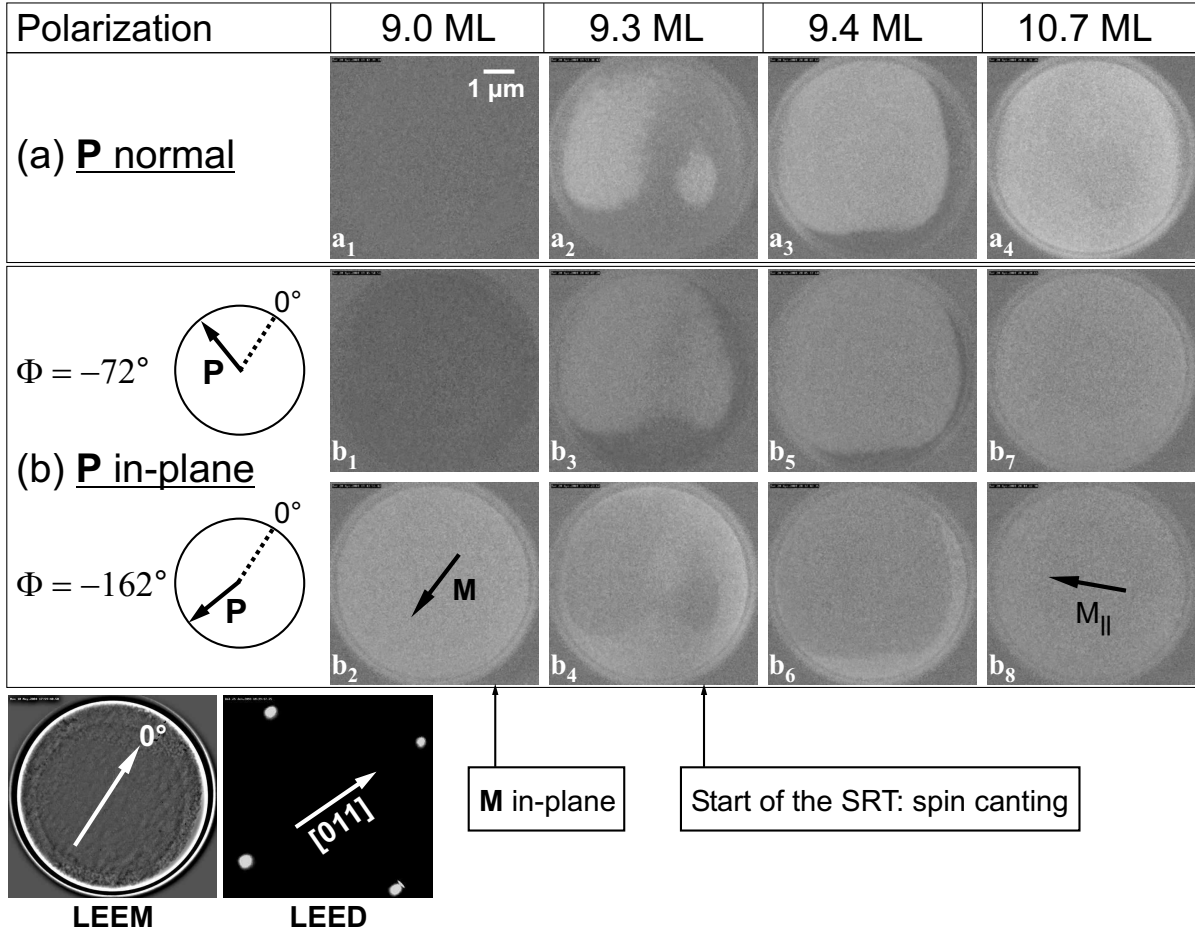


Figure 6.3: Spin canting at the SRT of Ni/Cu(100) as a function of the thickness at 300 K. At 9.0 ML the magnetization lies in the film plane pointing into the $\Phi = -176^\circ$ direction (a_1, b_1, b_2), which is rather parallel to the Cu step edges than parallel to the [011] direction, as indicated by the LEED image (taken at 150 eV). The continuous SRT takes place via the formation of micrometer-sized domains of irregular shape (a_2, b_3, b_4). At 10.7 ML an out-of-plane magnetized domain larger than the field of view ($7 \mu\text{m}$) has formed. The canted magnetization vector at 10.7 ML is characterized by the polar angle $\theta \approx 23^\circ$ and the azimuthal angle $\Phi \approx -113^\circ$.

is due to the domain evolution process, since the images could not be imaged at the same time. However, the canting of the magnetization is clearly visible in the image series at 9.3 ML Ni/Cu(100). As the Ni layer thickness is further increased up to 10.7 ML, the canting angle θ remains almost constant, while the domain size increases beyond the field of view ($7 \mu\text{m}$) where the in-plane component of \mathbf{M} has rotated to $\Phi = -113^\circ \pm 5^\circ$. Finally, the magnetization is perpendicular to the surface, as the Ni thickness exceeds 11 ML (not shown). In conclusion, the rotation of the in-plane component of \mathbf{M} proceeds from a parallel alignment to the steps to an orientation perpendicular to the steps. The superposition of this rotation and the reorientation of the magnetization toward the surface normal results in a *spiral-like* motion of \mathbf{M} during the SRT. Such spiral-like SRT was also observed by Dhesi *et al.* [90] and Jähnke *et al.* [10].

6.2 Spin-reorientation transition of Fe/Ni bilayers on Cu(100)

The magnetic domain microstructure of 0 to 3 ML of Fe on 7 and 11 ML Ni/Cu(100) films was studied by SPLEEM at 300 K. As described in chapter 5.3.1 the two Ni underlayers vary in their anisotropy due to the different layer thickness. The 7 ML Ni/Cu(100) film was in a canted magnetization state, whereas the 11 ML Ni/Cu(100) film was perpendicularly magnetized due to the large positive volume anisotropy. However, qualitatively, the spin-reorientation transition was found to be similar for Fe/Ni bilayers fabricated on a 7 ML and an 11 ML Ni underlayer. In both cases we have observed a continuous spiral-like SRT, accompanied by a stripe domain state. In section 6.2.1 the ferromagnetic coupling between the Fe and Ni layer is investigated by means of angular dependent XMCD measurements. The nature of the continuous SRT in Fe/Ni/Cu(100) films is discussed in detail in the following sections, including the role of magnetic moments at the Fe/Ni interface determined by XMCD.

6.2.1 Coupling between Fe and Ni layers

SPLEEM is not an element-selective technique. The magnetic contrast of Fe/Ni bilayers on Cu(100) arises from the magnetization of both the Fe and the Ni layer, since below an energy of the electrons of 10 eV, the penetration depth of the spin-polarized beam may be several nanometers. No domains or domain walls of different magnetic contrast are observed, which would otherwise indicate a different position of domains or their magnetization orientation in the Ni underlayer with respect to the Fe layer. Thus, there is evidence for a strong ferromagnetic coupling between the Ni and the Fe layer. In order to confirm this coupling, angular dependent element-specific XMCD measurements have been performed. The orientation of the magnetization of both layers was found to be parallel in the whole thickness range studied, indicating a ferromagnetic coupling of out-of-plane and in-plane magnetized Fe/Ni bilayers. Since the helicity of the x-rays was kept constant at $\sigma = -1$, and the magnetization was switched by 180° to obtain the two individual (Fe, Ni) XMCD spectra, a ferromagnetic coupling is revealed, if the algebraic sign of the intensities equals, as obtained from the L_2 (L_3) edges of the spectra for Fe and Ni, respectively. An inverse sign would otherwise identify an antiferromagnetic coupling. Fig. 6.4 typically shows the ferromagnetic coupling of an $\text{Fe}_4/\text{Ni}_{17}/\text{Cu}(100)$ film as obtained from XMCD spectra.

The analysis of the angular dependence of the data, which have been corrected in respect of saturation effects, is consistent with the expected $\cos\theta$ -law [153]. This indicates that the bilayer is perpendicularly magnetized, and it does not reveal a canted magnetization. At an Fe thickness of 6.5 ML the magnetization of the bilayer has rotated into the film plane. The parallel alignment of the magnetizations within the plane of the Ni and the Fe layer is demonstrated

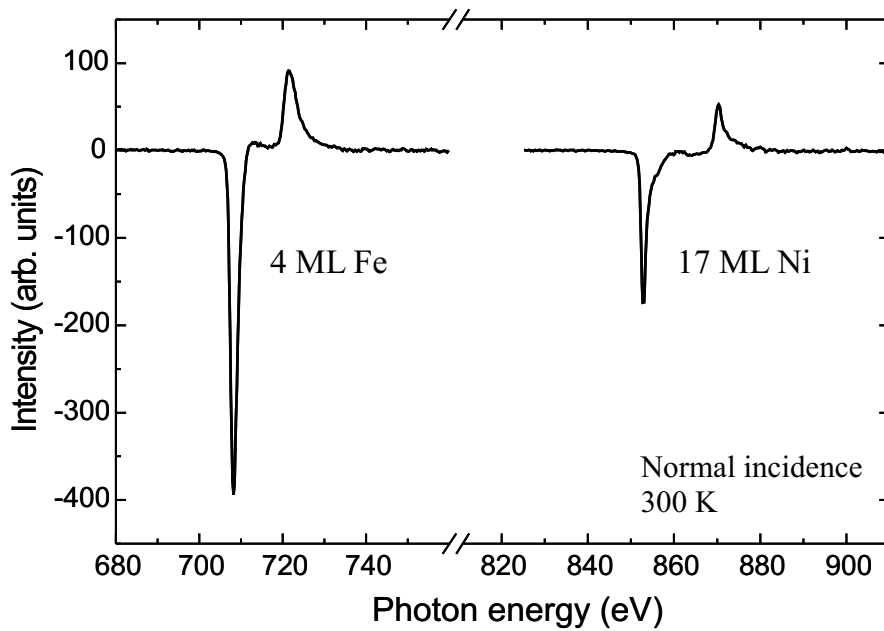


Figure 6.4: Element-selective XMCD signals of a perpendicularly magnetized $\text{Fe}_4/\text{Ni}_{17}/\text{Cu}(100)$ film at the Fe and Ni $L_{2,3}$ edges at normal photon incidence ($\theta = 0^\circ$). The equal sign of the intensities at the corresponding L -edges of Fe and Ni reveals the ferromagnetic coupling between both layers.

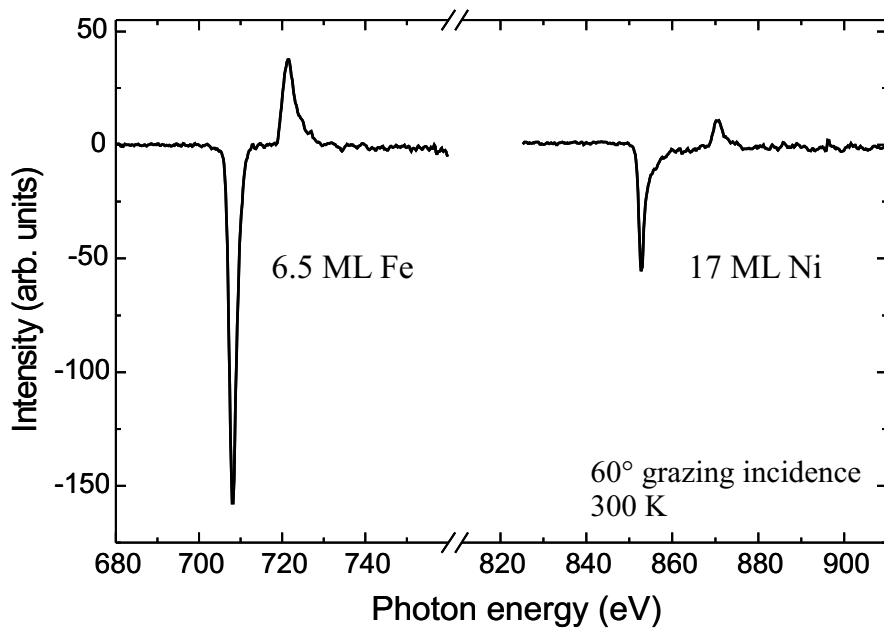


Figure 6.5: Element-selective XMCD signals of an in-plane magnetized $\text{Fe}_{6.5}/\text{Ni}_{17}/\text{Cu}(100)$ film at the Fe and Ni $L_{2,3}$ edges at a grazing photon incidence of $\theta = 60^\circ$ with respect to the sample's normal. The equal sign of the intensities at the corresponding L -edges of Fe and Ni indicates the ferromagnetic coupling between both layers.

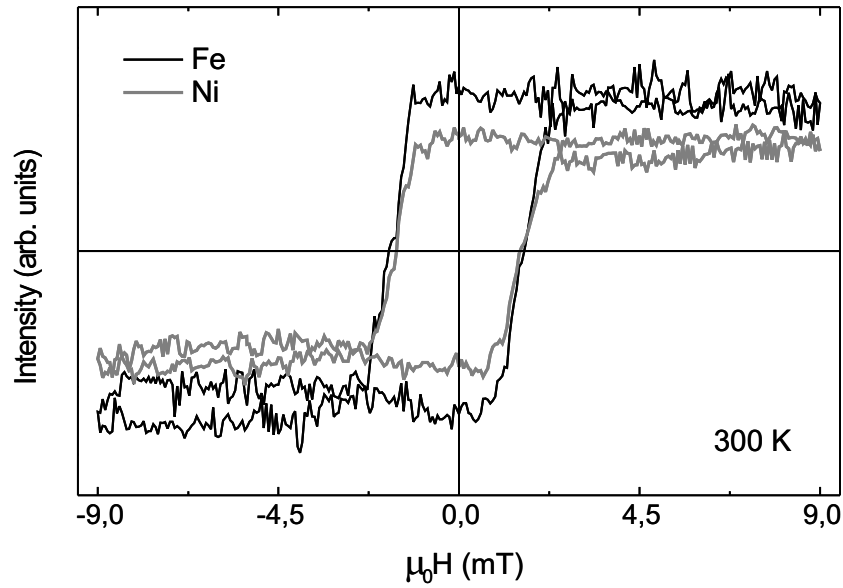


Figure 6.6: Element-selective hysteresis loops taken at the L_3 edges of Fe and Ni of an $\text{Fe}_{17}/\text{Ni}_{17}/\text{Cu}(100)$ film at a grazing angle of incidence of $\theta = 80^\circ$. Both loops show the same magnetization switching as the external field is reversed indicating the ferromagnetic coupling. The rectangular shape exhibits the easy axes of the magnetization lying in the plane, and the equal coercive field (± 1.6 mT) confirms the strong coupling. The data are smoothed and have been corrected in respect of a linear background signal.

in Fig. 6.5, which shows the XMCD spectra at a grazing angle of $\theta = 60^\circ$ with respect to the sample's normal. No dichroism was observed at normal incidence. Again, the negative (positive) intensity values at the L_3 (L_2) edges of Fe and Ni, respectively, confirm the ferromagnetic coupling in the bilayer. Moreover, the coupling was determined, by recording element-specific hysteresis loops. At a grazing angle of $\theta = 80^\circ$ the reflected x-ray was detected by a photodiode, which gives rise to an output voltage proportional to the magnetization. The energy of the x-ray was set to 708 eV and 852 eV, respectively, which corresponds to the L_3 edges of Fe and Ni. Magnetic fields up to ± 9 mT¹ were applied in-plane during the magnetization reversal, using a water-cooled pair of Helmholtz coils. Both hysteresis loops, which have been smoothed and corrected by subtracting a linear background signal, are depicted in Fig. 6.6. Despite the electronic noise of the measurements the hysteresis loops for Fe and Ni clearly show the same magnetization switching as the external field is reversed. The almost rectangular shape of both loops indicates that the easy axis of the magnetization lies in the film plane. A strong ferromagnetic coupling between both layers is revealed by the equal coercive field of 1.6 mT.

¹The magnetic field is here given in the SI unit Tesla of the magnetic induction $\mu_0 H$

6.2.2 Magnetic moments per Fe and Ni atom

Exploiting the element-selectivity of the XMCD method the magnetic moments per Fe and Ni atom have been determined for out-of-plane magnetized Fe/Ni bilayers as a function of the Fe layer thickness at 300 K. This was done in order to study the effect of alloying at the Fe/Ni interface on the magnetic moments per atom. The results for Ni and Fe are listed in table 6.1 and 6.2, respectively. The orbital magnetic moment μ_L and the spin magnetic moment μ_S are derived following the approach of [154]. Since the number of $3d$ -holes n_h enters the equations to determine μ_L and μ_S (see section 2.2.1), a difficulty arises at the Fe/Ni interface, where the number of holes for Ni and Fe will change with the degree of intermixing which is not known. Recent calculations of the individual density of states (DOS) of Fe and Ni in variously composed Fe-Ni alloys [193] revealed, that the number of $3d$ -holes in the minority band of Fe increases drastically with increasing Fe amount due to a broadening of the DOS above the Fermi level. The same effect –but much less pronounced– is found for the majority band. The inverse behavior is calculated for Ni: a narrowing of the DOS leads to a reduction of n_h^{Ni} . Experimentally, the number of holes can be deduced from the alloy-dependent change of the integrated isotropic absorption spectra (half-sum spectra), which are proportional to n_h . The detailed analysis of the area of the normalized isotropic absorption spectra of Ni reveals a linear decrease with increasing Fe layer thickness (not shown here). Based on the above mentioned theoretical findings we attribute this decrease to a reduction of $3d$ -holes of Ni and not due to an absorption effect by the Fe cap layers. The validity of this assumption is confirmed by the increasing value of the integrated half-sum spectra of Fe with increasing Fe layer thickness. For the 17 ML Ni/Cu(100) film $n_h^{\text{Ni}} = 1.5$ has been used, which is in close agreement to theoretical values [151,194] and was found experimentally for a 23 ML Ni/Cu(100) [195]. From the linear decrease of the Ni L_3 edge of the isotropic spectra versus the Fe layer thickness the number of Ni $3d$ holes is determined to be $n_h^{\text{Ni}} = 1.36$ for the $\text{Fe}_1/\text{Ni}_{17}$ film and $n_h^{\text{Ni}} = 1.23$ for the $\text{Fe}_4/\text{Ni}_{17}$ film. According to the decrease of n_h^{Ni} the respective residual number of holes have been added to $n_h^{\text{Fe}} = 3.4$ which is the number of $3d$ -holes of Fe taken from Ref. [196].

The magnetic moments of Ni in Fe/Ni/Cu(100) films of various Fe thicknesses listed in table 6.1 can be considered as constant and in reasonable agreement with previous measurements of a 15 ML Ni/Cu(100) film [197] within the error bar of $\pm 0.05 \mu_B$. Since from XMCD the averaged element-selective moment of a film is obtained and the changes of moments at the interface contribute to the moment of the whole film of 17 ML thickness, only minor changes of the total moment may be expected. The ratios μ_L/μ_S , however, are larger than determined generally for Ni/Cu(100) films in that thickness range. It should be noted that the relatively large error bar arises from the average of only two measurements. To obtain more reliable data five spectra should be averaged.

By considering the magnetic moments of 1 ML and 4 ML Fe of the same Fe/Ni bilayer,

Table 6.1: Magnetic moments per Ni atom of an $\text{Fe}_x/\text{Ni}_{17}/\text{Cu}(100)$ film as a function of the Fe layer thickness x .

Fe thickness (ML)	$\mu_L(\mu_B)$	$\mu_S(\mu_B)$	$\mu_{tot}(\mu_B)$	$\frac{\mu_L}{\mu_S}$
0	0.13	0.60	0.73	0.22
1.0	0.12	0.60	0.72	0.21
4.0	0.12	0.65	0.77	0.18
15 ML Ni/Cu(100) [197]	0.08	0.61	0.69	0.13

Table 6.2: Magnetic moments per Fe atom of an $\text{Fe}_x/\text{Ni}_{17}/\text{Cu}(100)$ film as a function of the Fe layer thickness x .

Fe thickness (ML)	$\mu_L(\mu_B)$	$\mu_S(\mu_B)$	$\mu_{tot}(\mu_B)$	$\frac{\mu_L}{\mu_S}$
1.0	0.22	1.47	1.68	0.15
4.0	0.28	2.05	2.36	0.14
3.8 ML Fe/Cu(100) [198]	0.25	3.46	3.71	0.07

good agreement is found for the orbital magnetic moment with previous measurements of a 3.8 ML Fe/Cu(100) film [198]. The spin magnetic moment of 1 ML Fe is determined to be 30% smaller than the bulk value of bcc Fe. In order to clarify if the spin moment of 1 ML Fe is reduced, measurements at low temperatures are required which have not been performed. On the other hand the Fe monolayer is deposited on perpendicularly magnetized Ni, which due to the direct exchange interaction stabilizes the magnetic moments of Fe against thermal fluctuations and should yield a magnetic moment of Fe near the low temperature value. The formation of an Fe-Ni alloy leads to an average magnetic moment of $\approx 1.6 \mu_B$ of the alloy according to the Slater-Pauling curve, if an $\text{Fe}_{0.5}\text{Ni}_{0.5}$ alloy with fcc structure is assumed at the interface as discussed in section 1.1.2. The individual magnetic moments per Fe and Ni atom, which correspond to that average value, have been determined by neutron diffraction experiments to be $\mu^{\text{Ni}} \approx 0.7 \mu_B$ and $\mu^{\text{Fe}} \approx 2.5 \mu_B$ [46] which in the case of Fe is contradictory to our measurement.

The total magnetic moment of 4 ML Fe on 17 ML Ni/Cu(100) is determined to be $2.36 \pm 0.05 \mu_B$. In order to obtain the contribution of the three additional Fe layers of the 4 ML film compared to the monoatomic Fe layer at the Fe-Ni interface, the following approach is considered. Assuming an $\text{Fe}_{0.5}\text{Ni}_{0.5}$ alloy at the interface, three different Fe layers contribute to the measured moment of Fe: the Fe interface layer with a magnetic moment equal to that of 1 ML Fe on Ni/Cu(100) and full coordination number, the interior double layer and the surface layer with a reduced coordination number. The average magnetic moment μ of the three topmost

layers is then given by $\frac{1}{4} \times 1.68 \mu_B + \frac{3}{4} \times \mu \mu_B = 2.36 \mu_B$, which reveals $\mu = 2.59 \mu_B$. This value indicates a high-spin state of Fe and gives strong evidence for the fct or fcc structure. Moreover, this result becomes important in terms of interpreting the SRT, which is discussed in the following sections in detail, since a high-spin state of Fe gives rise to a large shape anisotropy that favors an in-plane orientation of the magnetization.

6.2.3 Continuous SRT as a function of the Fe layer thickness

The spin-reorientation transition of Fe/Ni bilayers on Cu(100) has been investigated as a function of the Fe layer thickness in the range of 0 to 3 ML Fe at room temperature. At first, the magnetization state of an 11 ML Ni/Cu(100) film was magnetically characterized by SPLEEM, by probing the three components of the magnetization. The perpendicular orientation of the magnetization of the 11 ML Ni/Cu(100) film was confirmed by imaging the magnetic domain structure of the film in the perpendicular and in several in-plane orientations of the electron beam polarization \mathbf{P} as shown in Fig. 6.7 (“0 ML Fe”). The magnetic domain pattern of the Ni film consists of stripes of several micrometers width with a perpendicularly up and down oriented magnetization ([100] direction) as depicted in (a_1) . No in-plane magnetization components were found in this pure Ni film. Typically, the two images in the left most column (“0 ML Fe”) in Fig. 6.7 (b) were acquired with a spin-polarization oriented along two orthogonal in-plane directions at $\Phi = -4^\circ$ and $\Phi = -94^\circ$. The absence of magnetic contrast in these images confirms that there is no spin canting in the Ni/Cu(100) film of 11 ML thickness. Upon Fe deposition on top of the Ni/Cu(100) film, the modification of both the domain pattern and the magnetization direction is demonstrated by the sequence of images illustrated in Fig. 6.7. The deposition of less than 1 ML Fe results in an increase of the magnetic contrast along the perpendicular direction and a slight broadening of the Ni domain pattern as described in section 5.3.1. Upon further Fe deposition the out-of-plane MC (Fig. 6.7 (a)) increases up to 2.5 ML Fe. Here, the onset of the formation of narrower domains is observed, which corresponds to the start of the SRT. As the Fe layer thickness is further increased, the large out-of-plane domains breakup into ≈ 180 nm wide stripe domains. The correlation of the shape of the magnetic domains with the topography of the Cu crystal is revealed by the LEEM image of the bare Cu surface, which is shown in the lower left of Fig. 6.7. The domain walls of the stripe domains are obviously aligned parallel to the Cu atomic steps. A typical profile of the stripe domain pattern at the maximum number of stripes, i. e. at 2.6 ML Fe, is depicted in Fig. 6.8. Mostly cosine-shaped profiles of the stripe domains similar to that of 2.2 ML Fe/Cu(100) are revealed. In contrast to the calculated perpendicular orientation of the magnetization within the stripe domain pattern of cosine-like profile by Jensen *et al.*, the magnetization is canted within the narrow stripe domains. The different amplitudes in the figure indicate different canting angles of the magnetization within the respective stripe domains.

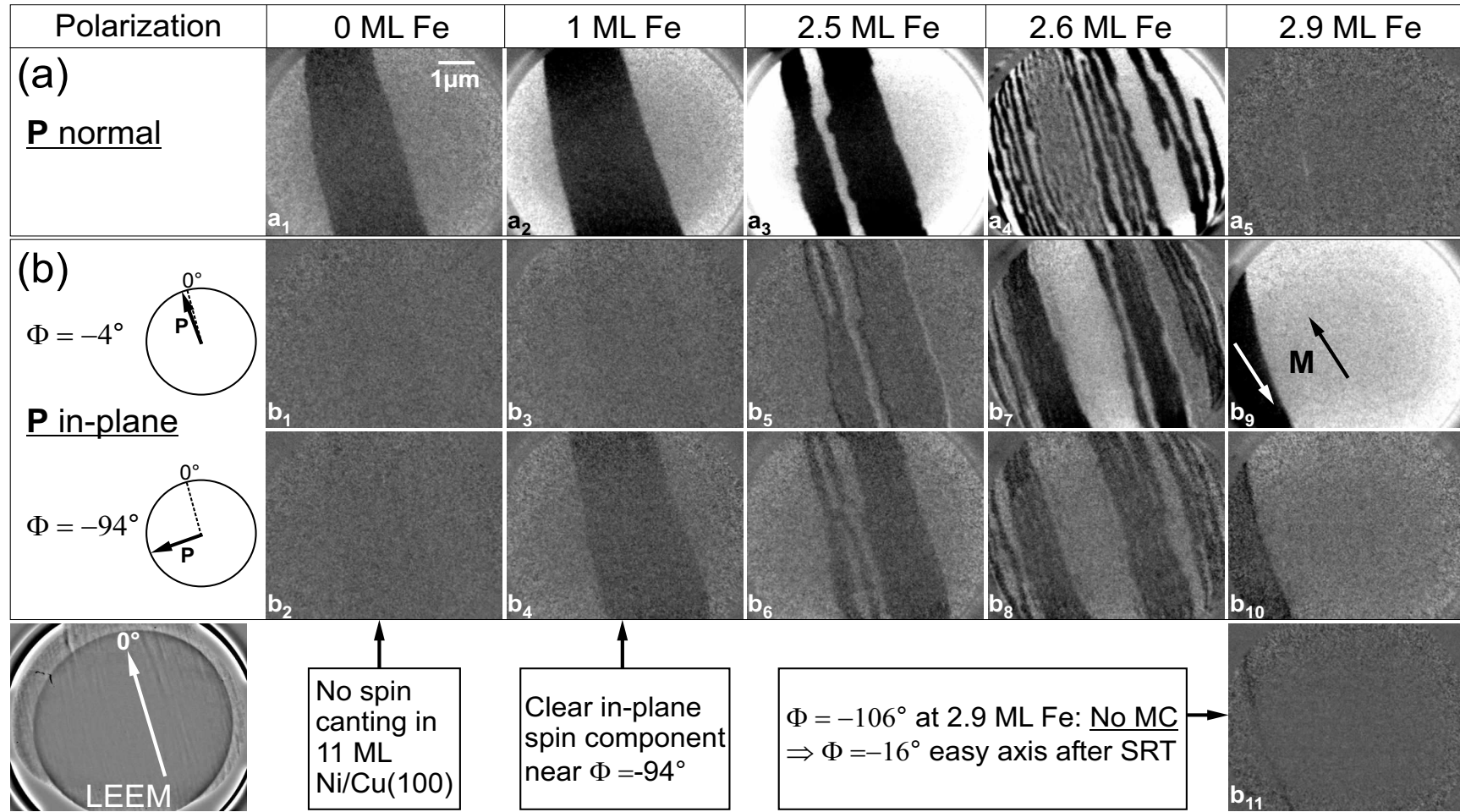


Figure 6.7: Spin-reorientation transition of an $\text{Fe}_x/\text{Ni}_{11}$ bilayer on $\text{Cu}(100)$ at 300 K as a function of the Fe layer thickness ($x = 0 - 2.9$ ML). The SRT takes place by a continuous spin rotation, a breakup of domains into stripe domains parallel to the Cu step edges and a reformation to large in-plane magnetized domains at 2.9 ML Fe, where the out-of-plane magnetic contrast has vanished (a_5). For details see text.

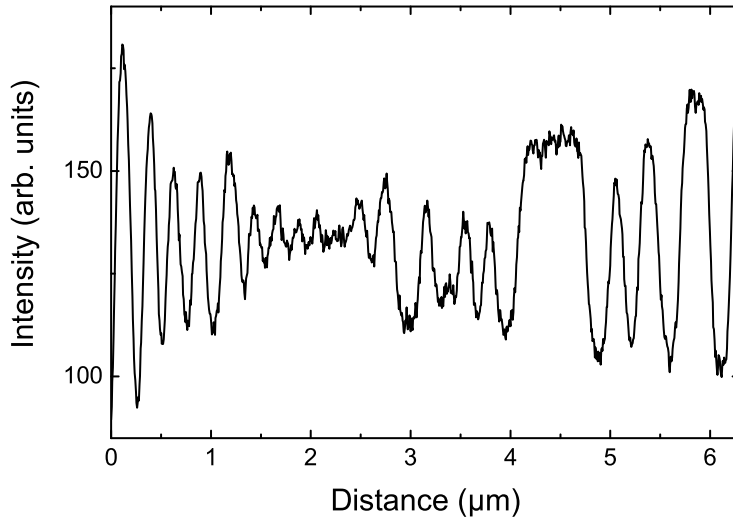


Figure 6.8: Profile of the stripe domain pattern of an $\text{Fe}_{2.6}/\text{Ni}_{11}/\text{Cu}(100)$ film probing the magnetization component perpendicular to the film surface. The different amplitudes are due to different canting angles of the magnetization within the respective stripes.

Finally, the MC in perpendicular orientation vanishes at 2.9 ML Fe. This proves that the magnetization is now completely oriented in the film plane. Unlike this finding, a perpendicular orientation of the magnetization was reported for Fe coverages up to 11 ML on 15 ML Ni/Cu(100) by O'Brien *et al.* using XMCD [25]. Thereby, around 4 ML Fe a transformation from the fct to the fcc structure of Fe occurred, and the small detected perpendicularly oriented magnetization of the Fe film was attributed to the Fe layer at the Fe/Ni interface. An in-plane oriented magnetization was found by these authors for an Fe film thickness larger than 11 ML, i. e. a similar behavior as observed for Fe/Cu(100) films.

In order to determine the easy axis of the in-plane magnetized domains at 2.9 ML Fe, the electron beam polarization \mathbf{P} was rotated, until the MC between the domains vanished. Since the MC vanishes at $\Phi = -106^\circ$ (see b_{11}), the magnetization orientation within the domains lies perpendicular to this angle, i. e., the magnetization within the domains is parallel and antiparallel at an angle of $\Phi = -16^\circ$ with respect to the step edges, as indicated by the arrows in the image (b_9). No magnetization orientation at 90° with respect to this direction was found, as one might have expected for a cubic system. The image contrast at $\Phi = -106^\circ$ vanishes and reveals a 300 nm wide Néel wall, which is visible by the line of darker contrast on the left hand side of this image (b_{11}). Within this wall, the magnetization rotates in the film plane. In the core of the wall the magnetic moments are aligned perpendicular to the easy axis of the domains. A Bloch wall would not cause any magnetic contrast in the middle of the wall for the given \mathbf{P} . Since there was no technique available to verify the crystal orientation in the SPLEEM setup at that time, we can only make the following reasonable assumption about the relation of the domain pattern to the crystallographic direction. It is known that the magnetization \mathbf{M} of Ni/Cu(100) films favors the [011] in-plane direction in the thickness range above 6 ML [33], whereas in

Fe/Cu(100) \mathbf{M} favors a [001] in-plane direction with a much larger in-plane anisotropy than for Ni/Cu(100). Therefore, in the coupled Fe/Ni/Cu(100) system the [001] direction most likely is the easy axis. It should be noted, that for one single series of SPLEEM images, which were taken on Fe/Ni films grown on a different Cu(100) crystal a LEED investigation exists. The comparison of the easy axis of the magnetization determined from the domain image of an Fe_{2.8}/Ni_{7.5}/Cu(100) film with the corresponding LEED image (Fig. 5.13) confirms the easy axis of the bilayer system to be [001]. As stated already in section 5.3.2, the LEED system was installed after the measurement. However, the crystal orientation was imaged with the Cu(100) substrate being in the same position as for the previously reported domain images. As shown above, the $\Phi = -16^\circ$ direction is the easy axis of the magnetization of the Fe_{2.9}/Ni₁₁/Cu(100) film, which according to our interpretation is thus parallel to the [001] crystallographic axis of the bilayer. Based on these reasonable assumptions regarding the orientation of the used crystal, the step edges, which are seen in the LEEM image of Fig. 6.7, have no certain orientation to a crystallographic axis. This indicates that the preferential direction caused by cutting the crystal to a Cu(100) surface has a lower energy than the [011], which is known to be a low energy step direction on Cu surfaces vicinal to [100] (Refs. [90,192]). Note, that the in-plane components M_{\parallel}^{\uparrow} and $M_{\parallel}^{\downarrow}$ of the canted and oppositely oriented domains could not be detected by second harmonic generation [10] or x-ray magnetic circular dichroism [90], since these techniques average over large areas.

The breakup into stripe domains is also observed for the two in-plane directions (Fig.6.7 (b)), which unambiguously shows that the magnetization of the bilayer is canted within the stripes. The canting angle θ with respect to the film normal increases with Fe coverage as seen by the increase of the MC in the series of images on top in Fig. 6.7 (a). Hence, the reorientation of the magnetization from perpendicular to in-plane with increasing Fe layer thickness occurs via a breakup of the original domain pattern and *simultaneously*, by a continuous rotation of \mathbf{M} within the individual domains.

Interestingly, at a coverage of 1 ML Fe, a magnetic contrast appears also for the polarization vector \mathbf{P} at $\Phi = -94^\circ$ as shown in Fig. 6.7 (b) (see b_4). There is nearly no MC for 1 ML Fe if \mathbf{P} is set to $\Phi = -4^\circ$, which is perpendicular to \mathbf{P} in the above described image. At larger coverages of Fe the contrast becomes much stronger for \mathbf{P} along $\Phi = -4^\circ$ but stays constant for \mathbf{P} along $\Phi = -94^\circ$, at least within the error bar of $\pm 5^\circ$, which arise from the uncertainty in determining the angle Φ from the SPLEEM images. The analysis of the grayscale images (normalized to their background, which is the area around the circular field of view) reveals that the easy axis of the magnetization M_{\parallel} is at $\Phi = -90^\circ$ (perpendicular to the Cu step edges) for 1 ML Fe on 11 ML Ni. For 2.9 ML Fe the easy axis is at $\Phi = -16^\circ$, i. e. along [001]. The in-plane component of \mathbf{M} rotates from “perpendicular to the steps” into the [001] direction by crossing the SRT. This in-plane rotation was observed for both Ni thicknesses. Since the steps do not run

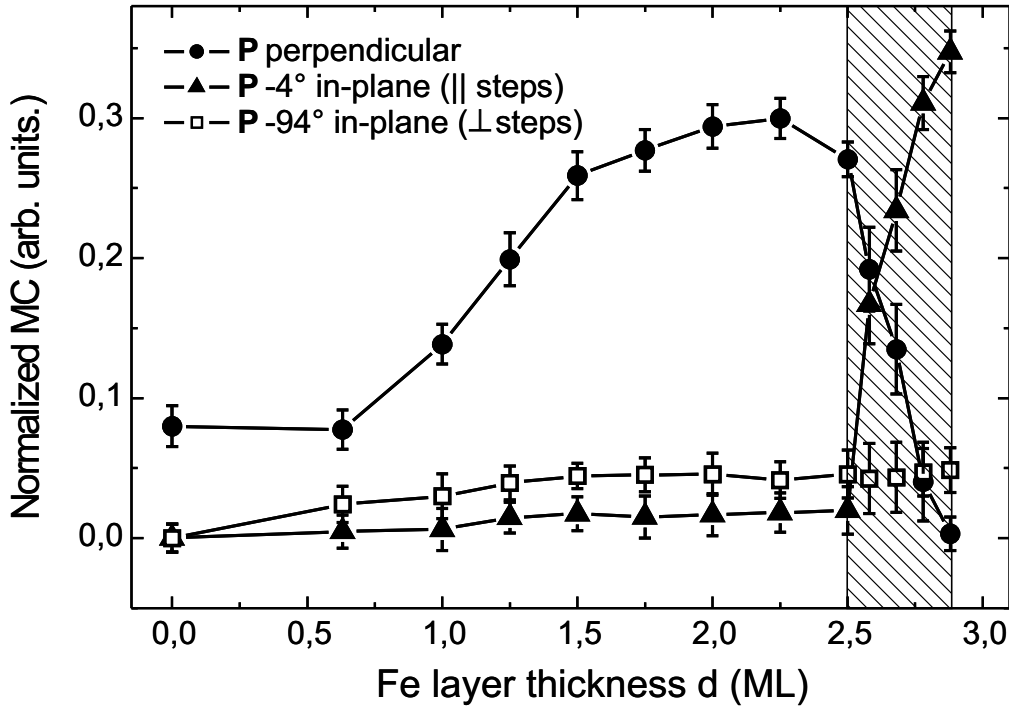


Figure 6.9: Angular dependent normalized magnetic contrast versus the Fe layer thickness x of an $\text{Fe}_x/\text{Ni}_{11}/\text{Cu}(100)$ film at 300 K. The hatched area demonstrates the interval of the SRT. Below 2.5 ML Fe the perpendicular component of the magnetization \mathbf{M} increases ($-\bullet-$) while the two in-plane components stay almost constant. The in-plane components are much smaller and point into directions of $\Phi = -4^\circ$ ($-\blacktriangle-$) and $\Phi = -94^\circ$ ($-\square-$) with respect to the Cu step edges. Note that the in-plane MC perpendicular to the steps ($-\square-$) occurs around 0.6 ML Fe before a component of \mathbf{M} parallel to the steps is established. During the SRT the magnetization direction switches from out-of-plane to in-plane, while the in-plane component rotates from normal to almost parallel to the steps.

parallel to a crystallographic axis, the “perpendicular to the steps” orientation of the in-plane component of \mathbf{M} has to be interpreted in terms of a step-induced anisotropy perpendicular to the steps. The in-plane component of the canted magnetization of the 7 ML Ni/Cu(100) *without* the Fe top layer showed the same orientation perpendicular to the Cu step edges. This indicates that the in-plane preferential direction “perpendicular to the steps” is not due to the Fe layer, but it originates either directly from the Cu steps or from an interplay between the magnetic anisotropy, induced by the step edges and the bulk magnetoelastic contribution of the Ni film. The latter favors an easy axis perpendicular to the surface and, thus, at least to some degree also perpendicular to the step edges. At larger Fe thicknesses, the in-plane anisotropy of Fe dominates, which then favors the [001] direction.

Fig. 6.9 shows the magnetic contrast, normalized to the background grayscale, as obtained from the individual domain images taken at three different directions of \mathbf{P} (see Fig. 6.7) as a

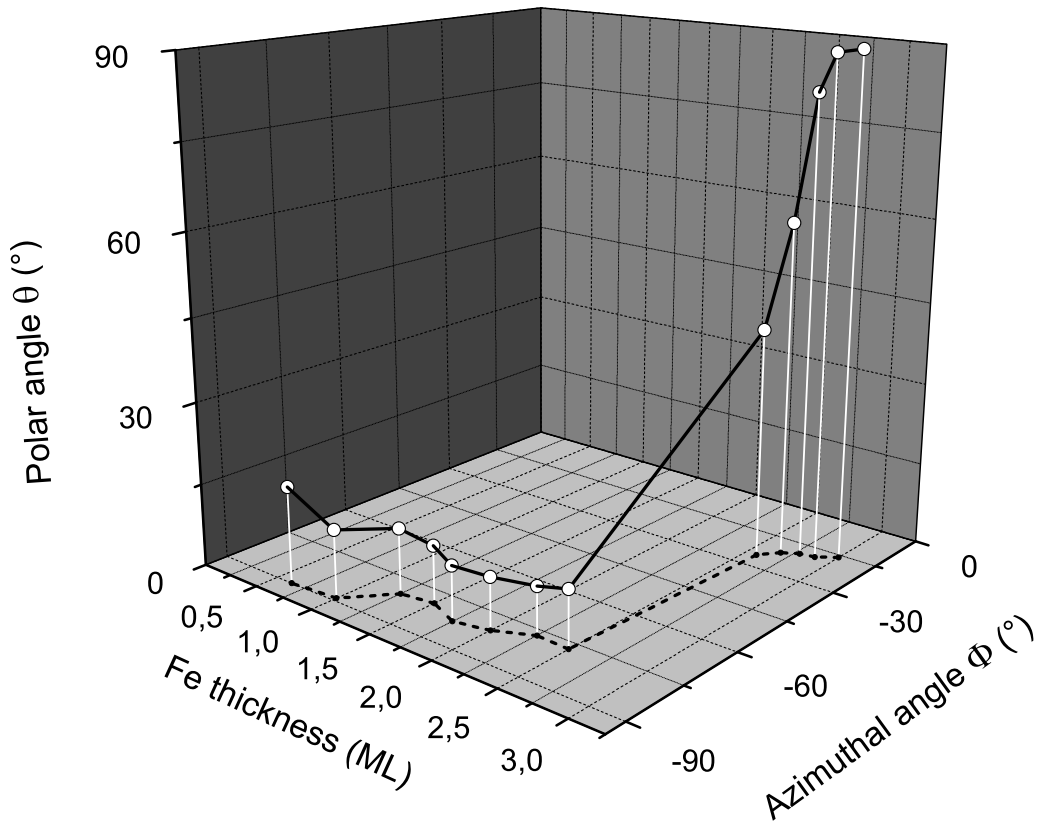


Figure 6.10: 3D-plot of the angular dependence of the magnetization direction versus the Fe layer thickness x of an $\text{Fe}_x/\text{Ni}_{11}/\text{Cu}(100)$ film at the spin-reorientation transition at 300 K. θ is the angle between the surface normal and the easy axis of the in-plane component of the magnetization. It is derived from a series of SPLEEM images, which are partly shown in Fig. 6.7. Φ is the azimuthal angle measured counter-clockwise against the direction of the substrate steps (see Fig. 6.7).

function of the Fe layer thickness. The in-plane contrast obtained for $\Phi = -4^\circ$ remains small and constant up to 2.5 ML Fe, where it sharply increases upon reaching the SRT. At around 0.6 ML Fe, a small MC occurs for the $\Phi = -94^\circ$ direction, which then stays constant within error limits up to 2.9 ML Fe. The behavior of the perpendicular component may be divided into 4 thickness ranges: Below 0.6 ML Fe, the MC is constant, followed by two intervals, where the MC strongly (0.6 – 1.5 ML Fe) and weakly (1.5 – 2.25 ML Fe) increases. Finally, a rather strong drop to zero of the MC is observed within the SRT interval from 2.5 to 2.9 ML Fe.

The observed plateau in the perpendicular MC below 0.6 ML Fe can be explained as resulting from two effects, namely from a reduced magnetic moment per Fe atom on the Ni surface, and from the canting of the magnetization. Obviously, the expected increase of the MC following the increasing number of Fe magnetic moments is here compensated by a respective reduction of the perpendicular magnetization component due to the canting angle of $\theta \approx 17^\circ$ found for the case of $\Phi = -94^\circ$. This canting angle reduces the normal component of \mathbf{M} by

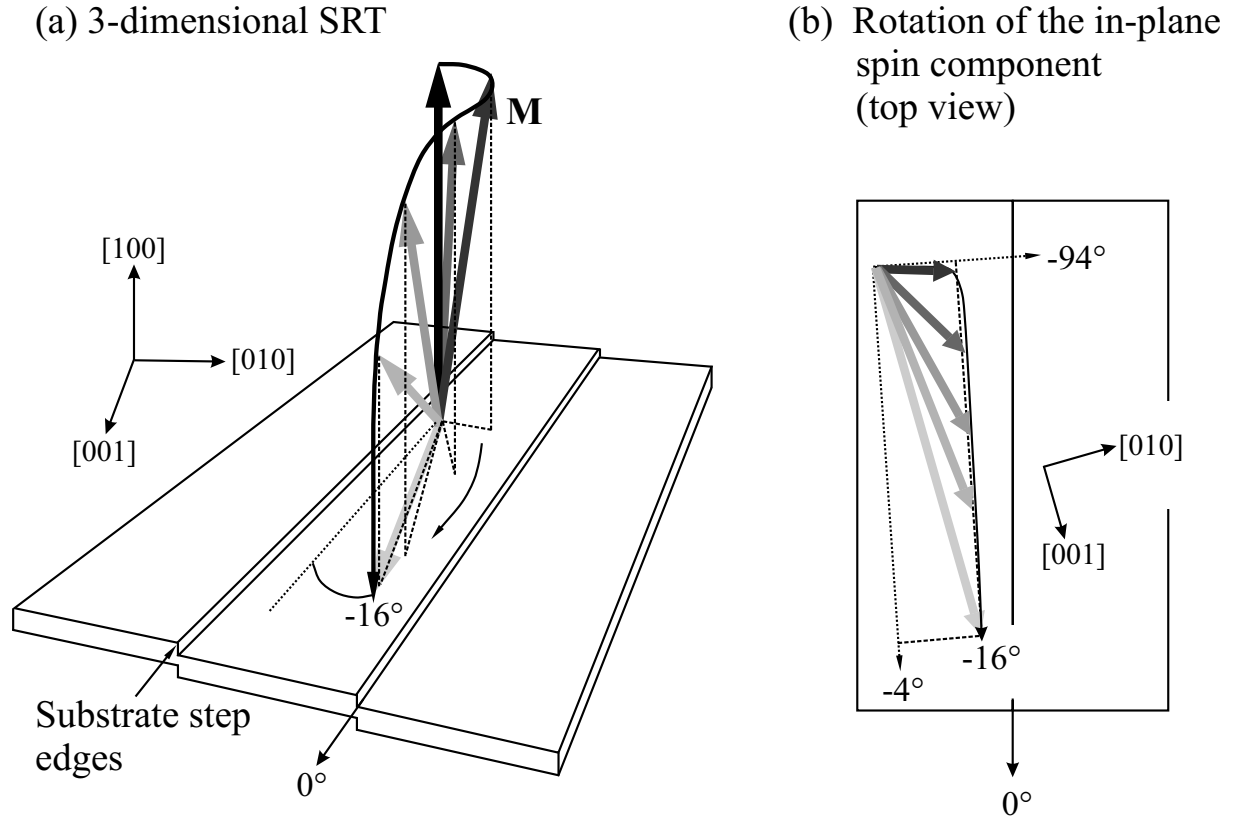


Figure 6.11: Model of the spiral-like motion of the magnetization vector of Fe/Ni/Cu(100) films during the spin-reorientation transition. The perpendicular magnetization M spontaneously tilts off the [100] direction with the in-plane component normal to the Cu step edges at the beginning of the SRT and rotates into the [001] in-plane direction at the end of the SRT (a). The brightness of the magnetization vectors scales with increasing Fe layer thickness. The accompanied rotation of the in-plane component of M is sketched in (b).

$\approx 4.4\%$, which exactly compensates the increase of the average magnetic moment within error bars. One might also speculate that at the Fe layer of 0.6 ML the Fe atoms do not carry their usual bulk magnetic moment, but that the Fe moment is reduced within the Fe/Ni interface due to alloy formation. If one assumes the bulk magnetic moments of $2.2 \mu_B$ and $0.62 \mu_B$ per Fe and Ni atom, respectively, the average moment of the Fe/Ni bilayer would increase by 13%. In order to compensate for the according increase in magnetic contrast, a canting angle of $\approx 30^\circ$ would be required, which almost doubles the measured canting angle. On the other hand, from the measured canting angle of 17° , a magnetic moment of $\approx 1.1 \mu_B$ is obtained for Fe, which is unrealistic at first glance. However, the angle θ as obtained from SPLEEM images inhibits an uncertainty of $\pm 5^\circ$, such that the magnetic moment as obtained in the case of weak MC is just a rough estimate. On the other hand, element-specific XMCD measurements (section 6.2.2) reveal, that the magnetic moment of 1 ML Fe on 17 ML Ni/Cu(100) is indeed reduced to a value of $\approx 1.7 \mu_B$ at 300 K, which supports the reduced Fe moment derived from the domain images.

Fig. 6.10 shows (in a 3-dimensional plot) the superposition of the polar angle θ , measured between the surface normal and the easy axis of the in-plane component of \mathbf{M} , and the azimuthal angle Φ , both as a function of the Fe layer thickness. Below 2.5 ML Fe the polar angle remains at $\theta = 13^\circ \pm 5^\circ$, whereas the azimuthal angle changes from “perpendicular to the steps” ($\Phi = -90^\circ$) to $\Phi \approx -77^\circ \pm 5^\circ$. At 2.5 ML Fe the SRT starts with a breakup of the original domains, and both the polar and the azimuthal angle vary drastically. The in-plane component of \mathbf{M} performs a rotation of $\Phi \approx 50^\circ$ within a range of the Fe thickness of less than 0.1 ML. Within the same interval, θ increases by almost 40° . A further rotation of $\Delta\theta \approx 40^\circ$ occurs for the Fe thickness ranging from 2.6 to 2.9 ML. Here, Φ further changes by only $\approx 6^\circ$, such that the magnetization is finally oriented parallel to the [001] easy direction.

The spiral-like SRT that is discovered at least qualitatively by the series of domain images is additionally illustrated in Fig. 6.11 (a) as a three dimensional sketch, which shows the superposition of the spin-reorientation from out-of-plane to in-plane. The top view (Fig. 6.11 (b)) shows the rotation of only the in-plane component, starting from “perpendicular to the Cu step edges” to the easy axis of the magnetization, which is the [001] direction. In order to comply with the information obtained from the series of domain images, in our model of the SRT the projection of \mathbf{M} onto the $\Phi = -94^\circ$ direction is kept constant, as shown in Fig. 6.7 (b). Thus, in Fig. 6.11 the arrowheads of the in-plane magnetization vectors follow a slight curve, which then allows for an equal projection onto the $\Phi = -94^\circ$ direction. This, then nicely explains the unchanged magnetic contrast as measured in that orientation.

6.2.4 Determination of the Fe-Ni interface magnetic anisotropy from the critical Fe layer thickness

The domain images at 300 K unambiguously reveal that the reorientation of the magnetization is a continuous one. To describe the nature of a continuous SRT, the magnetic anisotropy constants of second and fourth-order have to be included in the consideration [3]. First of all, the orientation of the magnetization of the Fe/Ni bilayer is determined by the delicate balance between the intrinsic magnetic anisotropy energy (MAE) and the shape anisotropy. As stated before in section 1.2.1 the shape anisotropy always favors an in-plane orientation of \mathbf{M} , whereas the intrinsic MAE may either favor an in-plane or a perpendicular orientation of \mathbf{M} , which is expressed in terms of the ratio of the respective anisotropy constants. The observed SRT from an out-of-plane to an in-plane direction occurs, when the shape anisotropy dominates over the magnetocrystalline anisotropy upon the increase of the Fe layer thickness. The easy axis of the magnetization is determined by the minimum of the free energy density F per unit area, which in

the case of the tetragonal bilayer system Fe/Ni on Cu(100) includes the following contributions:

$$\begin{aligned}
 F = & \left(\frac{1}{2} \mu_0 M_{Ni}^2 - K_{2,Ni}^V \right) \cos^2 \theta d_{Ni} + \left(\frac{1}{2} \mu_0 M_{Fe}^2 - K_{2,Fe}^V \right) \cos^2 \theta d_{Fe} - K_2^{S,\text{eff}} \cos^2 \theta - \\
 & - \frac{1}{2} K_{4\perp}^{\text{eff}} \cos^4 \theta - \frac{1}{8} K_{4\parallel}^{\text{eff}} (3 + \cos 4\Phi) \sin^4 \theta - J \mathbf{M}_{Ni} \cdot \mathbf{M}_{Fe}
 \end{aligned} \quad (6.1)$$

where $K_2^{S,\text{eff}} = K_{2,Ni-Cu}^S + K_{2,Fe-Ni}^S + K_{2,Fe-vac}^S$ and

$K_i^{\text{eff}} = K_{i,Ni}^V d_{Ni} + K_{i,Fe}^V d_{Fe} + K_{i,Ni-Cu}^S + K_{i,Fe-Ni}^S + K_{i,Fe-vac}^S$ with $i = 4\perp, 4\parallel$. θ is the polar angle with respect to the [100] direction, Φ is the azimuthal angle measured against the easy [001] in-plane direction of the system. J is the ferromagnetic coupling constant between the magnetizations M_{Ni} and M_{Fe} of Ni and Fe, which are always aligned parallel as shown by the XMCD measurements in section 6.2.1. K_2 , $K_{4\perp}$ and $K_{4\parallel}$ are the second- and the fourth-order perpendicular and in-plane terms of the MAE. K^V denotes the volume contribution and K^S the various surface- and interface anisotropies as given by the lower index. If $K_{4\perp} = K_{4\parallel} = 0$, no tilted orientation of the magnetization is possible. Hence, if K_2 changes, a *discontinuous* reversal of the magnetization is expected [22]. Since we observe both an out-of-plane spin-canting as well as a continuous rotation of the magnetization, the second-order contributions to the MAE alone are not sufficient to account for this behavior. Thus, a fourth-order contribution needs to be included within the analysis. However, the reorientation interval of 0.4 ML Fe is rather small, i. e. the K_4 values are also small. For this reason the K_4 values are neglected in the further analysis. Only if $K_4 \gg K_2$, the difference between the critical thicknesses d_{c1} and d_{c2} , which denote for the onset and the end of the SRT, becomes significant. It should be noted, though, that SPLEEM is a suitable technique, in order to reveal even such a small difference between the lower and the upper critical thickness, which then makes it feasible to determine the true nature of this transition. In the following approximation we consider the 0.4 ML interval as a discontinuous reversal of \mathbf{M} at a mean value $d_{c,Fe} = 2.7$ ML .

In our simplified model, the sum of the shape anisotropy and the crystalline anisotropy contributions vanishes at $d_{c,Fe}$:

$$\begin{aligned}
 \left(\frac{1}{2} \mu_0 M_{Ni}^2 - K_{2,Ni}^V \right) d_{Ni} + \left(\frac{1}{2} \mu_0 M_{Fe}^2 - K_{2,Fe}^V \right) d_{Fe} - K_{2,Ni-Cu}^S - K_{2,Fe-Ni}^S - \\
 - K_{2,Fe-vac}^S = 0.
 \end{aligned} \quad (6.2)$$

For the following discussion of the question, which of the various contributions plays the major role for the observed SRT, we consider two scenarios. In the first case, a sharp interface between the Fe and Ni layer is assumed and the volume, interface and surface contributions for Fe and Ni layers on Cu(100) are taken from the literature (table 6.3). The shape anisotropy of the bilayer structure here increases from $7.5 \mu\text{eV/atom}$ [9] to $32 \mu\text{eV/atom}$ (averaged for the bilayer) by the deposition of Fe, due to the 3.5 times larger bulk magnetic moment of the Fe atoms ($2.22 \mu_B$) as compared to the Ni atoms ($0.62 \mu_B$). Using these values together with the literature values of

Table 6.3: Anisotropy constants of Ni/Cu(100) and Fe/Cu(100) at 300 K.

Anisotropy constant	Energy ($\mu\text{eV}/\text{atom}$)	Reference
$K_{2,\text{Ni}}^V$	30	[37]
$K_{2,\text{Fe}}^V$	77.7	[199]
$K_{2,\text{Ni-Cu}}^S$	-59	[83]
$K_{2,\text{Fe-vac}}^V$	64	[31]

the anisotropy constants listed in table 6.3, one realizes, that the sum of these quantities is zero, only, if an interface anisotropy $K_{2,\text{Fe-Ni}}^S = -93 \mu\text{eV}/\text{atom}$ is present. Thus, a *large negative interface anisotropy* is needed to explain the critical thickness of 2.7 ± 0.2 ML for the SRT. Note, that in the case of Fe/Cu(100), where no Fe-Ni interface is present, the magnetization of 3 ML Fe grown at 300 K is oriented perpendicular to the surface [169].

In a second but more realistic approach we consider intermixing within the interface, which then may result in an $\text{Fe}_{0.5}\text{Ni}_{0.5}$ alloy spanning over two monolayers. According to the Slater-Pauling curve, the average magnetic moment per atom in these two layers is $\approx 1.6 \mu_B$. Recalculation of the shape anisotropy of the Fe/Ni bilayer with a 2 ML thick alloyed interface region, but keeping constant the number of deposited Fe and Ni atoms, and assuming an enhanced magnetic moment of the 1.7 ML thick toplayer of $2.7 \mu_B$, yields an increase of the shape anisotropy by only about 15%. Thus, we can conclude that the increase of the shape anisotropy as a function of the Fe thickness is not sufficient to force the direction of the magnetization of the bilayer into the film plane below a thickness of 3 ML Fe. A relatively large Fe-Ni interface anisotropy needs to be taken into account to explain the critical Fe thickness at which the SRT occurs.

Determination of an effective fourth-order anisotropy constant

The SPLEEM images prove that the SRT is a continuous one over a *small* thickness interval. As mentioned above, the value of K_4 is therefore expected to be small. The analysis of the polar angle θ as a function of the Fe layer thickness allows for a rough estimation of the effective anisotropy coefficient K_4^{eff} , which represents the average of the fourth-order contributions of the entire bilayer. In Fig. 6.12 the polar angle is displayed as a function of the Fe thickness within an interval of 2.25 ML to 3.0 ML. The solid line is a fit based on the minimization of the free energy density per unit area given by Eq. (6.1) with respect to θ . For simplicity, a cubic lattice is assumed, i. e. $K_{4\perp} = K_{4\parallel} = K_4^{\text{eff}}$. The unit of K_4^{eff} is “energy per volume” due to the separation $K_4^{\text{eff}} = K_4^{V,\text{eff}} + K_4^{S,\text{eff}}/d$. In a strict sense the Fe and the Ni layers contribute to both $K_4^{V,\text{eff}}$ and $K_4^{S,\text{eff}}/d$. However, measurements by ferromagnetic resonance (FMR) yield values of K_4^V for Ni/Cu(001) that are more than three times smaller than the K_4^S constants [22].

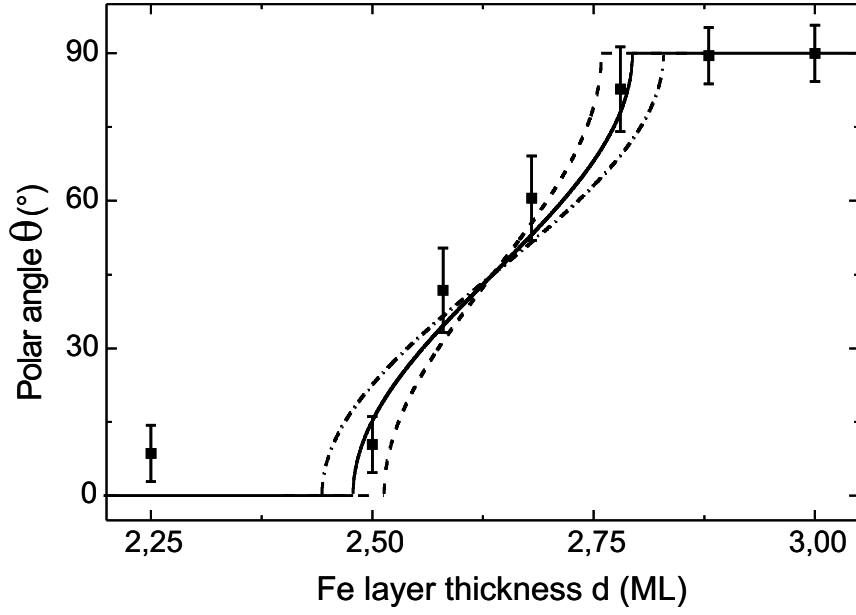


Figure 6.12: Angular dependence of the magnetization direction versus the Fe layer thickness x of an $\text{Fe}_x/\text{Ni}_{11}/\text{Cu}(100)$ film at the spin-reorientation transition at 300 K. θ is the angle between the surface normal and the magnetization vector, which is derived from a series of domain images which in part is depicted in Fig. 6.7. The curves represents the fits according to Eq. (6.4). For details see text.

Moreover, due to the small layer thickness of Fe the volume contribution to $K_4^{V,\text{eff}}$ from the Fe layer is regarded as negligible. Hence, $K_4^{V,\text{eff}}$ is neglected in the following, i. e. K_4^{eff} will be treated as a pure surface/interface contribution of the bilayer.

Minimization of the free energy density per unit area (Eq. 6.1) for the case $K_{4\perp} = K_{4\parallel} = K_4^{\text{eff}}$ and $\Phi = 0$, yields $\theta = 0^\circ$ and $\theta = 90^\circ$, which correspond to the orientation of the magnetization before and after the SRT, respectively, and:

$$\cos^2 \theta = \frac{\left(\left(\frac{1}{2} \mu_0 M_{\text{Ni}}^2 - K_{2,\text{Ni}}^V \right) d_{\text{Ni}} + \left(\frac{1}{2} \mu_0 M_{\text{Fe}}^2 - K_{2,\text{Fe}}^V \right) d_{\text{Fe}} - K_{2,\text{Ni-Cu}}^S - K_{2,\text{Fe-Ni}}^S - K_{2,\text{Fe-vac}}^S + K_4^{\text{eff}} \right)}{2K_4^{\text{eff}}}. \quad (6.3)$$

within the reorientation interval. The solid, dashed and dashed-dotted lines in Fig. 6.12 are given by

$$\theta = \arccos \sqrt{\frac{\left(\left(\frac{1}{2} \mu_0 M_{\text{Ni}}^2 - K_{2,\text{Ni}}^V \right) d_{\text{Ni}} + \left(\frac{1}{2} \mu_0 M_{\text{Fe}}^2 - K_{2,\text{Fe}}^V \right) d_{\text{Fe}} - K_{2,\text{Ni-Cu}}^S - K_{2,\text{Fe-Ni}}^S - K_{2,\text{Fe-vac}}^S + K_4^{\text{eff}} \right)}{2K_4^{\text{eff}}}}. \quad (6.4)$$

for different values of K_4^{eff} . The error bars in Fig. 6.12 identify the individual inaccuracy in the determination of the polar angle from each domain image. Error bars range from $\pm 5^\circ$ for the large out-of-plane and in-plane domains with reasonable magnetic contrast to $\pm 8^\circ$ for the

case of stripe domains. The fit yields an interval of less than 0.3 ML for the width of the spin-reorientation transition.

In order to determine K_4^{eff} from this fit, the anisotropy constants of Ni/Cu(100) and Fe/Cu(100) from table 6.3 were used. A saturation magnetization of Fe of 1820 kA/m, which is $\approx 4.5\%$ enhanced with respect to the literature value for bulk bcc Fe, was taken to account for the increased average magnetic moment found by XMCD measurements for an Fe coverage of 4 ML. Since $K_{2,Fe-Ni}^S = -93 \mu\text{eV/atom}$ was determined, provided that $K_4^{\text{eff}} = 0$, i. e. assuming a discontinuous SRT at 2.7 ML Fe, both $K_{2,Fe-Ni}^S$ and K_4^{eff} were varied. The fit, which is given by the solid line in Fig. 6.12, yields $K_{2,Fe-Ni}^S = -68 \mu\text{eV/atom}$ and $K_4^{\text{eff}} = -10.7 \mu\text{eV/atom}$. The value for K_4^{eff} is of reasonable magnitude compared to the second-order coefficients. Although the error of the determined K_4^{eff} is expected to be too large to make the value of K_4^{eff} comparable to anisotropy constants determined by other methods like FMR, the existence of a non-zero K_4^{eff} is all-important to fit the data points in Fig. 6.12, which correspond to canted magnetization vectors. For comparison, another two fits are shown in the figure, which yield $K_4^{\text{eff}} = -13.0 \mu\text{eV/atom}$ (dashed line) and $K_4^{\text{eff}} = -8.3 \mu\text{eV/atom}$ (dashed-dotted line) for the same value of $K_{2,Fe-Ni}^S$. Note also that K_4^{eff} is negative in all three cases. This means, that also the numerator in the square root of Eq. (6.4) must be negative in the Fe thickness range from 2.5 to 2.9 ML, such that the radicand remains positive. Thus, according to $\tilde{K}_2 = K_2 - \frac{1}{2}\mu_0 M^2$, (see Fig. 1.4), \tilde{K}_2 must be positive for the Fe/Ni bilayer system. Then, the SRT takes place in the fourth quadrant of the anisotropy diagram (Fig. (1.4)), for which theory [4,11] predicts a canted magnetization in agreement with our results. Interestingly, the breakup of the large domains into stripe domains of a cosine-like profile, which is theoretically predicted to occur in the *second* quadrant at positive K_4 and negative \tilde{K}_2 values, is *simultaneously* observed during the reorientation process.

6.2.5 Domain wall evolution near the SRT

The same reorientation behavior of the magnetization is found for Fe/Ni bilayers, when Fe is deposited on an 11 ML Ni/Cu(100) underlayer and a 7 ML Ni/Cu(100) underlayer. The latter one is in a state of a canted magnetization with the in-plane component of the magnetization oriented perpendicular to the Cu step edges. Again, there is no magnetic contrast detected in the $\Phi = -4^\circ$ polarization orientation for Fe coverages below 1 ML but in the $\Phi = -94^\circ$ direction. The MC remains nearly constant in the $\Phi = -94^\circ$ direction, whereas the MC in the $\Phi = -4^\circ$ direction increases only weakly up to an Fe coverage of 2.5 ML, followed by a dramatic increase just at the thickness, where the domains break up into stripes. The orientation of the magnetization within the in-plane domains after crossing the SRT is again directed along [001], confirming a similar spiral-like magnetization reorientation as it was found for the bilayer with 11 ML Ni. Fig. 6.13 shows a domain wall of the Fe_x/Ni_7 bilayer imaged with \mathbf{P} oriented

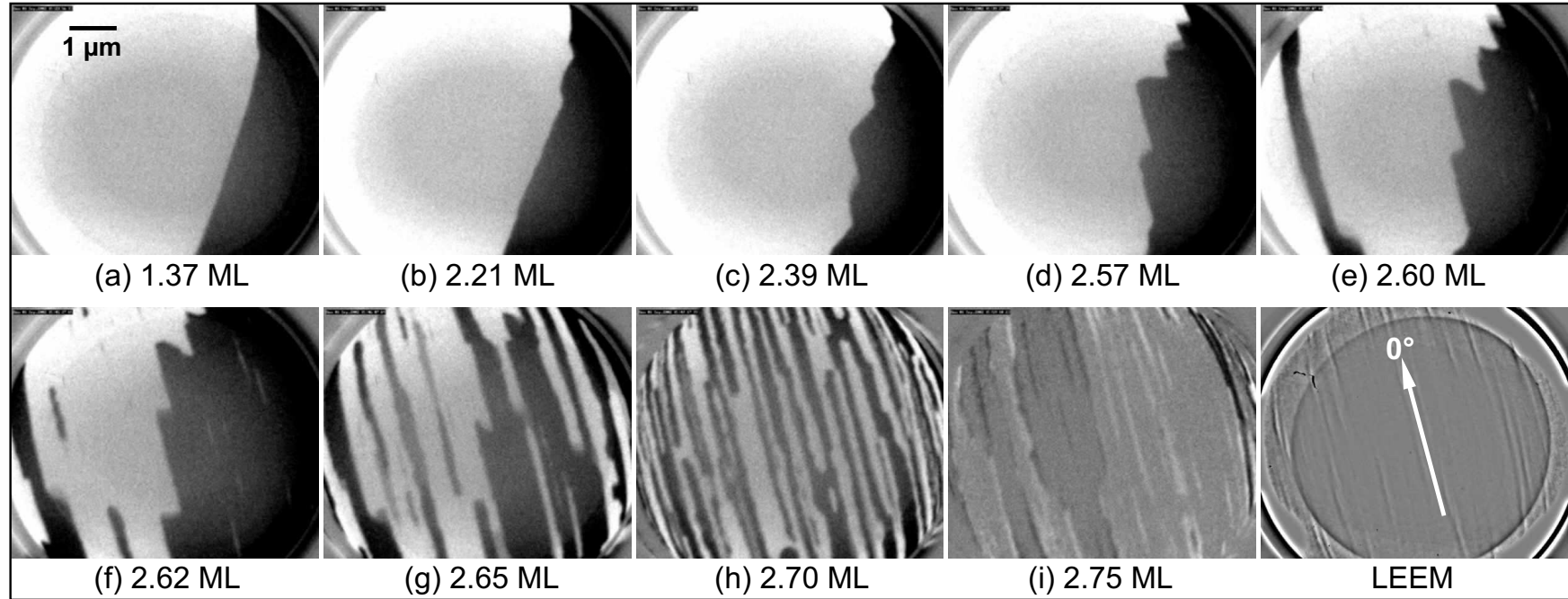


Figure 6.13: Domain wall evolution as a function of the Fe layer thickness (a)-(i) on a 7 ML Ni/Cu(100) film at 300 K imaged with the polarization \mathbf{P} of the electron beam directed normal to the surface. Stripe domains evolve from the original straight domain wall. The stripe domains are parallel to the Cu atomic step edges (0°), which is confirmed by the LEEM image of the bare Cu(100) surface. The low magnetic contrast in (i) indicates that the magnetization has almost completely rotated into the film plane.

perpendicular to the surface as a function of Fe deposition. The direction of the wall segment was found to have no correlation with topographic features, as can be seen by comparing the magnetic SPLEEM images with the LEEM image of the bare Cu crystal surface. At about 1.4 ML Fe the observed domain wall is almost straight, but it is not pinned to the substrate. Note also, that there is just one domain wall within the $7\ \mu\text{m}$ -field of view (Fig. 6.13 (a)). Both latter facts indicate, that the domain wall energy must be relatively high. As the Fe layer thickness increases, the domain wall starts to extend by forming protrusions, similar to that of the domain wall at the SRT of Ni/Cu(100). Here, however, the domain wall starts to adjust to the substrate step edges by forming rectangular protrusions with one side running parallel to the direction of the Cu atomic steps (6.13 (b)-(c)). Obviously, lowering of the effective anisotropy due to the Fe deposition is responsible for the elongation of the domain wall, following a reduced wall energy according to $\gamma \propto d\sqrt{A K_2^{\text{eff}}}$. The alignment of wall segments with the step edges further minimizes the wall energy. Finally, this process evolves into a stripe domain pattern along the step direction (6.13 (e)). At about 2.6 ML Fe (6.13 (c)) stripe domains along the steps also appear spontaneously somewhere within the domains. The average stripe domain width at the maximum number of stripes around 2.7 ML Fe is about 180 nm, which is comparable to the wall width measured for 2.2 ML Fe/Cu(100).

The detailed analysis of domain walls in out-of-plane magnetized Fe/Ni bilayers has shown that the walls are Bloch walls (section 5.3.1), whereas in in-plane magnetized Fe/Ni bilayers the walls are of Néel type (section 5.3.2). Obviously, there is a transition from Bloch type to Néel type domain walls during the SRT from out-of-plane to in-plane. In Fig. 6.14 such a transition is typically demonstrated for an $\text{Fe}_x/\text{Ni}_7/\text{Cu}(100)$ film as a function of the Fe layer thickness x . At the start of the SRT at 2.6 ML Fe, the black and white MC of the domain walls in the image with \mathbf{P} directed along the $\Phi = -4^\circ$ in-plane direction (a_1) and the zero MC perpendicular to that direction in the film plane (b_1) clearly shows, that the walls are Bloch walls. At the breakup into a multi stripe domain pattern at 2.7 ML Fe most of the domain walls are in a transition state between the Bloch and the Néel mode, which is indicated by the SPLEEM images (a_2), (b_2) and their corresponding modified images (a_3), (b_3), where areas of zero MC are enhanced. In these two images the domain walls are identified from both orientations of \mathbf{P} , which confirms that the magnetization within the wall consists of both in-plane components. The domain images probing the component of \mathbf{M} normal to the surface (not shown) confirm that the magnetization within the walls rotates in the plane. The white and black arrows in the images indicate the identical features. A close inspection of these spots reveals, that a few wall segments are still in the Bloch mode, whereas others are already in the Néel mode.

After completion of the SRT at 2.8 ML Fe, all domain walls are Néel walls (Fig. 6.14 (a_4), (b_4)), i. e. the orientation of the magnetization within the wall has rotated by 90° within the plane into the Néel wall mode during the SRT. The slight shift of the walls in (a_4), (b_4) is due to

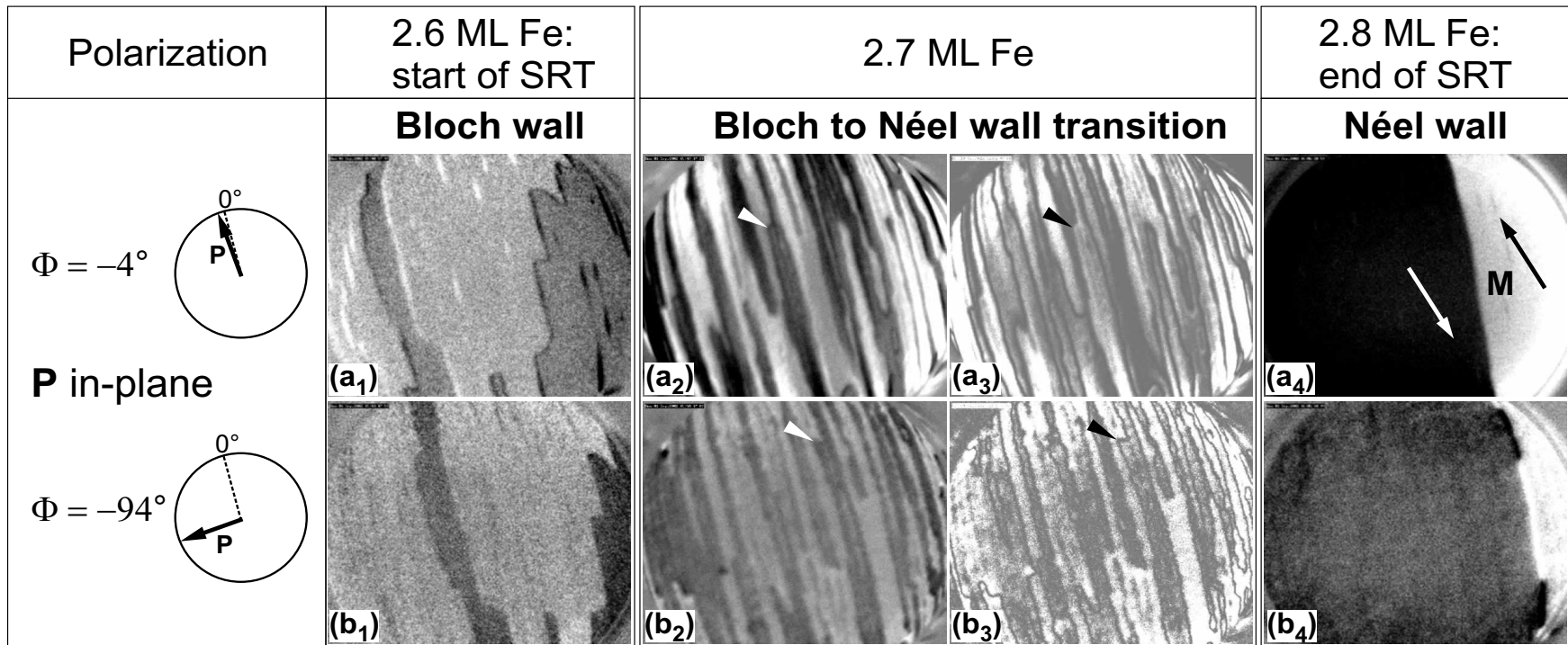


Figure 6.14: Bloch to Néel wall transition of an $\text{Fe}_x/\text{Ni}_7/\text{Cu}(100)$ film as a function of the Fe layer thickness x during the SRT at 300 K. Left: After the start of the SRT at 2.6 ML Fe the black domain wall is identified as a Bloch wall with the magnetization rotating collinear to the $\Phi = -4^\circ$ direction (a_1 , no MC of the wall in b_1). At the breakup into stripe domains (2.7 ML Fe) most of the domain walls are in a transition state between the Bloch and Néel mode, which is indicated by the SPLM images (a_2), (b_2) and their corresponding modified images (a_3), (b_3), where areas of zero MC are enhanced. The domain walls are revealed in both orientations of \mathbf{P} , confirming that the magnetization in the wall has both in-plane components. The white and black arrows show the same feature. Right: At the end of the SRT the domains are in-plane magnetized. The orientation of the magnetization within the wall has rotated by 90° within the plane into the Néel wall mode (a_4 , b_4). The shift of the wall is due to a misalignment between the polarization directions.

a misalignment between the polarization directions. The direction of the magnetization within the domains was determined from an image, where \mathbf{P} was oriented in-plane at $\Phi = -106^\circ$ away from the direction of the step edges, in which the MC between the domains vanishes. Consequently, $\Phi = -16^\circ$, i. e. the [001] direction, is the easy axis of the magnetization like in the Fe/Ni bilayer with 11 ML Ni.

6.2.6 SRT of $\text{Fe}_x/\text{Ni}_{1.5}/\text{Cu}(100)$

In contrast to the investigations of the SRT of Fe/Ni bilayers containing a Ni/Cu(100) film, which exhibits an out-of-plane magnetization, the domain formation at the SRT of Fe grown on 1.5 ML Ni/Cu(100) is presented in the following. According to the magnetic phase diagram shown in Fig. 1.7, 1.5 ML Ni on Cu(100) is in the paramagnetic state at room temperature. This is confirmed by the domain images, which do not reveal any magnetic contrast perpendicular or parallel to the surface (not shown). Upon Fe deposition on top of the Ni film the formation of $\approx 1 - 2 \mu\text{m}$ wide stripe domains occur at 1.35 ML Fe. Both a perpendicular and an in-plane component of the magnetization within the domains is detected, which is depicted in Fig. 6.15 and indicates a canted magnetization. The canting angle with respect to the surface normal derived from the SPLEEM images is $\theta \approx 30^\circ$. Two clear differences of the domain formation at the onset of ferromagnetism at 300 K of the Fe/Ni/Cu(100) film as compared to the Fe/Cu(100) film, which was previously grown on the same substrate can be pointed out: (i) the domain width is considerably larger and (ii) the magnetization is canted as domains occur in the Fe/Ni bilayer. Firstly, the high density of perpendicularly magnetized stripe domains of Fe/Cu(100) at 2.2 ML was explained by the reduction of the stray field energy, which is large due to the large magnetic moment of Fe. Furthermore, the ratio of the magnetocrystalline anisotropy to the shape anisotropy near unity characterized the pure cosine-like domain profile (section 5.2). In the bilayer system only 1.35 ML Fe and 1.5 ML Ni, which are most likely alloyed, contribute to the magnetic stray field. The individual magnetic moments of Fe and Ni near an $\text{Fe}_{0.5}\text{Ni}_{0.5}$ alloy have been determined to reach values of $2.5 \mu_B$ and $0.7 \mu_B$ [46], respectively, which yields a thickness-weighted average magnetic moment of about $1.6 \mu_B$ in agreement with the Slater-Pauling curve. On the other hand high-spin states of tetragonally distorted Fe monolayers on Cu(100) with moments up to $3.55 \mu_B$ have been reported [198]. Consequently, the stray field energy of the considered bilayer is smaller than that of the Fe/Cu(100) film of 2.2 ML thickness and can be reduced by a smaller number of larger domains. Secondly, the canted magnetization, which is found in all Fe/Ni/Cu(100) films studied in this work, indicates that the Fe-Ni interface anisotropy is negative and thus shifts the anisotropy balance in favor of an in-plane orientation of the magnetization. Eventually, the ratio of the reduced perpendicular anisotropy to the small shape anisotropy of the $\text{Fe}_{1.35}/\text{Ni}_{1.5}/\text{Cu}(100)$ must be larger than that of Fe/Cu(100) in order to stabilize the observed broad stripe domains.

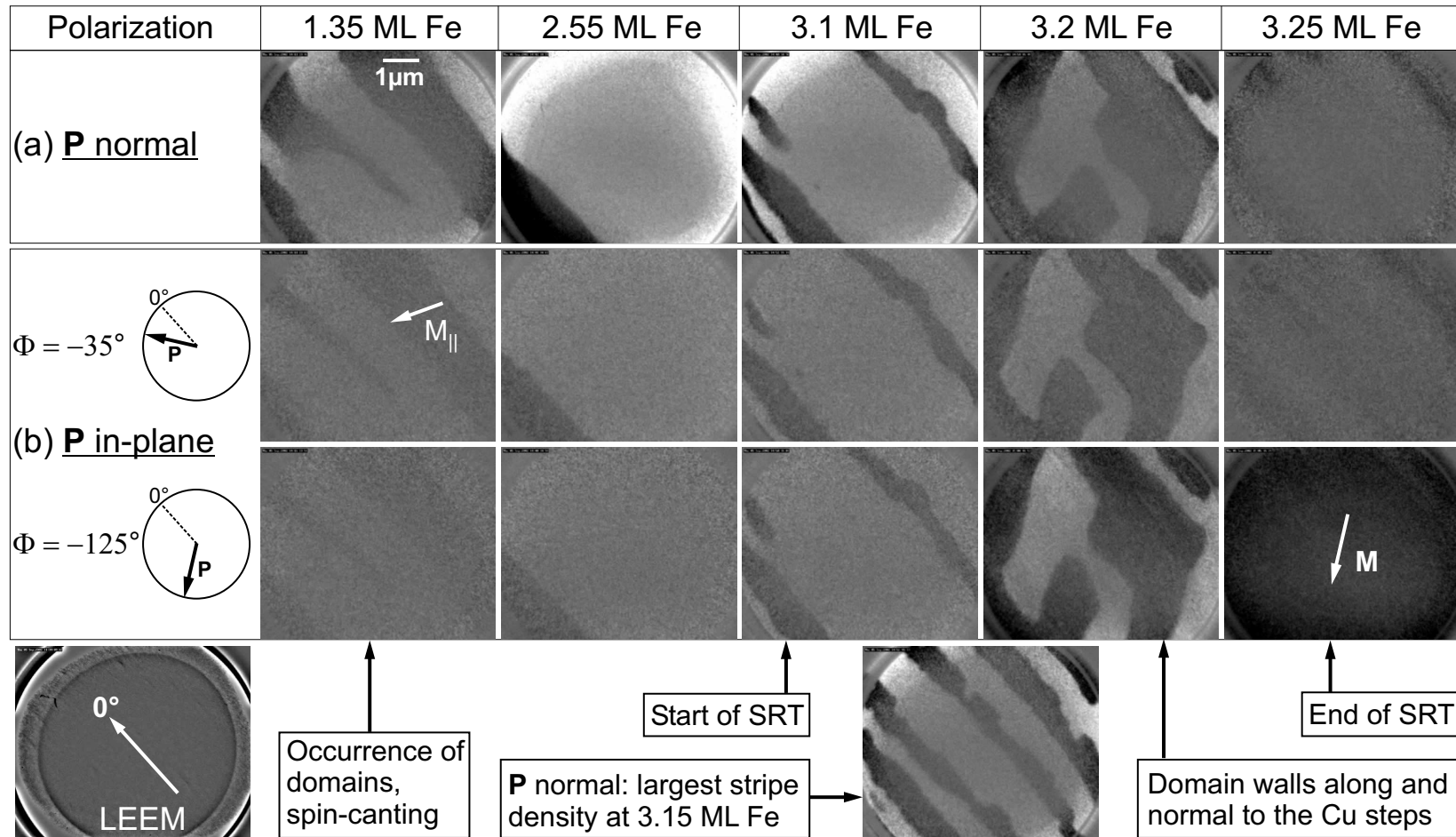


Figure 6.15: Domain formation of an $\text{Fe}_x/\text{Ni}_{1.5}/\text{Cu}(100)$ film at the SRT. At 1.35 ML Fe 1 – 2 μm wide magnetic stripe domains, aligned with the Cu step edges, occur, in which the magnetization is canted. The domains laterally expand up to 3.1 ML Fe, where the SRT starts via a breakup into ≈ 750 nm wide stripes. A domain pattern with domain walls oriented both parallel and perpendicular to the Cu steps forms as the magnetization continuously rotates into the film plane.

As the Fe thickness grows further the domains become larger in agreement with the observation of Fe on thicker Ni/Cu(100) films and previous findings [105,106]. The size of the domains reaches its maximum of more than $7 \mu\text{m}$ around 3 ML Fe. Also in Fe/Cu(100) films the largest domains form around 3 ML, but the average width is on the order of only $2 \mu\text{m}$. At 3.1 ML Fe the SRT of the bilayer starts via a disintegration into a stripe domain pattern. As compared to the stripe formation observed for Fe monolayers on 7 ML and 11 ML Ni two differences arise: (i) the critical thickness for the breakup into stripe domains is shifted to a larger Fe thickness by 0.6 ML and (ii) the width of the stripe domains at the highest density of stripes is $\approx 750 \text{ nm}$ for the $\text{Fe}_{1.35}/\text{Ni}_{1.5}/\text{Cu}(100)$ film, which is more than four times larger. This finding may again be attributed to the smaller magnetic stray field of the bilayer due to the minor Ni layer thickness. Besides the quantitative differences, as compared to bilayers containing thicker Ni layers (sections 6.2.3-6.2.5) the formation of domains up to the stripe pattern are qualitatively similar in both systems. However, a unique domain pattern of the $\text{Fe}_{1.35}/\text{Ni}_{1.5}/\text{Cu}(100)$ film is observed at 3.2 ML Fe, as the in-plane component of the magnetization starts to rotate towards the $\Phi = -125^\circ$ direction where the domain size increases again. These domains are separated by domain boundaries running partially along and almost perpendicular to the substrate step edges, respectively, and thus forming rectangular corners. No such behavior was found in other Fe/Ni bilayers. At the end of the SRT at 3.25 ML Fe the magnetization lies in the film plane with its easy axis parallel to the $\Phi = -125^\circ$ direction, which is confirmed by the vanishing contrast in the domain images, which detect the perpendicular and the in-plane component with \mathbf{P} along the $\Phi = -35^\circ$ direction in Fig. 6.15. The thickness interval of the SRT is about 0.15 ML Fe, which is less than half the value found for bilayers with thicker Ni layers. Despite this small value the magnetization reorientation is unambiguously demonstrated to be a transition of second order by the spin canting within the domains. The smaller reorientation interval must be interpreted in terms of smaller anisotropy contributions of second and fourth order. In particular the volume part of the magnetocrystalline anisotropy of Ni is considered to be negligible due to the small amount of Ni.

In the present case neither at the start nor at the end of the SRT the in-plane component of the magnetization coincides with the Cu step direction. In summary, a spiral-like continuous SRT is found in $\text{Fe}_{1.35}/\text{Ni}_{1.5}/\text{Cu}(100)$ films, which is in qualitative agreement with the other Fe/Ni films studied in this work. However, the SRT starts at an increased Fe thickness and a unique domain pattern is revealed compared to the other bilayer systems. The differences of the domain formation of ultrathin Fe layers grown on Cu(100) have been elaborated, which emphasize the strong influence of alloying at the Ni/Fe interface.

7 Conclusion

In the present work the spin-reorientation transition of ultrathin $\text{Ni}_x/\text{Cu}(100)$ and $\text{Fe}_y/\text{Ni}/\text{Cu}(100)$ films was investigated as a function of the layer thickness x and y , respectively, at 300 K in UHV. One aim of this thesis was the clarification of the question, whether the SRT of $\text{Ni}/\text{Cu}(100)$ represents a phase transition of first or second order. Another aim was the characterization of the SRT of Fe/Ni bilayers on $\text{Cu}(100)$, whose individual layers – $\text{Fe}/\text{Cu}(100)$ and $\text{Ni}/\text{Cu}(100)$ – exhibit an opposite SRT. By imaging the magnetic domain microstructure during the film growth by means of spin-polarized low energy electron microscopy (SPLEEM), it was shown that the SRT of ultrathin $\text{Ni}/\text{Cu}(100)$ films is a transition of second order, i. e. the magnetization reorients *continuously* within the large domains. In the Fe/Ni bilayers both a *continuous* reorientation of the magnetization and a simultaneous breakup of the large domains into *stripe domains* was observed. For both thin film systems the change of the magnetization direction during the SRT with respect to the orientation of the Cu substrate step edges was measured. The size of the domains and the width and the type of domain walls was determined. In the following the results for the studied systems are summarized separately.

In $\text{Ni}/\text{Cu}(100)$ films the ferromagnetic order at 300 K sets in around 5 ML, in agreement with previous experiments. The size of the in-plane magnetized domains is typically on the order of some 10 μm without a systematic correlation of the domain walls to the step edges of the Cu substrate. The large size of these domains, compared to the ≈ 165 nm wide stripe domains at the onset of the ferromagnetic order in $\text{Fe}/\text{Cu}(100)$ films at 2.2 ML, is due to the in-plane orientation of the magnetization of ultrathin $\text{Ni}/\text{Cu}(100)$ films. Whereas Fe monolayers have a perpendicular magnetic anisotropy, and their magnetic stray field energy is minimized by a stripe domain state, the magnetization and thus the stray field of the $\text{Ni}/\text{Cu}(100)$ film lies in the plane, i. e. in the orientation where the stray field energy is minimum. In-plane magnetized Ni films are observed in the thickness range of 5 – 9 ML. The domain walls, which separate antiparallel magnetized domains, are 180° -Néel walls. These show the typical profiles of Néel walls, consisting of a core with two symmetrically extended logarithmic tails. For an 8 ML $\text{Ni}/\text{Cu}(100)$ film such a profile yields a wall width of ≈ 400 nm. No systematic differences in the domain structure of Ni films grown and measured at 300 K and Ni films grown and measured at 100 K were found. At the beginning of the SRT at 300 K, which takes place around 9.5 ML $\text{Ni}/\text{Cu}(100)$, an *elongation* of the original domain walls and spontaneously, reversely

magnetized areas ($>1 \times 1 \mu\text{m}^2$) occurred within the large domains. These observations are due to the decrease of the domain wall energy density, which originates from a decreased effective anisotropy at the SRT. The observed *broadening* of the domain walls is also a result of the decreased effective anisotropy. The SRT proceeds *continuously* from an in-plane oriented magnetization to an orientation of the magnetization perpendicular to the film surface with increasing Ni layer thickness. Canted magnetization vectors within the domains are unambiguously verified by imaging the three components of the magnetization. The reorientation of the magnetization takes place via a *spiral-like* motion from the orientation of the magnetization parallel to the Cu step edges to the orientation perpendicular to the steps and perpendicular to the surface.

In Fe/Ni/Cu(100) films the orientation of the individual magnetizations of the Fe and the Ni layer was determined by XMCD and element-specific hysteresis loops as a function of the Fe layer thickness at 300 K. These measurements show, that the individual magnetizations are aligned parallel to each other during the SRT, thus indicating a ferromagnetic coupling between the Fe and the Ni film. The determination of the magnetic moments per Fe and Ni atom in perpendicularly magnetized Fe/Ni/Cu(100) films by means of XMCD at 300 K yields a reduced magnetic moment per Fe atom of $\approx 1.7 \mu_{\text{B}}$ for 1 ML Fe at the Fe-Ni-interface. In 4 ML Fe on Ni/Cu(100) a high-spin state of Fe according to the Slater-Pauling curve was found. This finding implies that the Fe layers grow in the face-centered-cubic structure up to at least 4 ML on the Ni surface. The SRT takes place from an orientation of the magnetization perpendicular to the surface for uncovered Ni/Cu(100) films (7-11 ML) to an orientation of the magnetization parallel to the surface by a *spiral-like* motion with increasing Fe coverage. In this reorientation process the in-plane component of the magnetization rotates from “perpendicular to the substrate steps” towards “parallel to the steps”. *Simultaneously* to this motion, the domains break up into approx. 180 nm wide *stripe domains* within the interval of the magnetization reorientation (2.5 – 2.9 ML Fe). The stripe domains are aligned parallel to the Cu step edges, and the magnetization is found to *continuously* rotate within the stripes. The easy in-plane axis of the magnetization of the coupled bilayer system is the [001] direction, which also is the easy axis in bulk Fe. A straight domain wall with a random orientation to the Cu steps was observed to form rectangular protrusions at the start of the SRT. These elongated wall segments were found to turn toward the step edges, where they remained pinned until the stripe domain pattern was formed with increasing Fe layer thickness. At the maximum density of stripe domains a Bloch to Néel wall transition occurs within a narrow thickness interval of about 0.1 ML Fe.

From the average critical Fe layer thickness of the SRT, i. e. under the assumption of a *discontinuous* reorientation transition, the Fe-Ni interface anisotropy is determined to be $-93 \mu\text{eV/atom}$, by using literature values for the volume, the surface and the shape anisotropy contributions of the individual Fe and Ni layers grown on a Cu(100) surface. It was shown, that the

increase of the shape anisotropy of the Fe/Ni/Cu(100) film by the increase of the Fe coverage, alone, is not sufficient to explain the observed SRT. In fact, the Fe-Ni interface anisotropy provides a decisive contribution to the reorientation of the magnetization into the film plane. Taking the *continuous* reorientation of the magnetization into account, a negative effective fourth-order anisotropy constant K_4^{eff} of the bilayer system is determined from the Fe thickness dependence of the tilt angle of the magnetization. At the same time the sum of the anisotropy contributions of second order yields $K_2 - K_d > 0$. In agreement with theoretically developed stability diagrams of the easy axis of the magnetization in the anisotropy space (K_4 vs. $K_2 - K_d$), this finding characterizes the observed canted magnetization during the SRT. However, the simultaneously observed breakup of the large domains into stripe domains of a cosine-like profile is not predicted by theory.

Finally, the SRT of Fe layers grown on 1.5 ML Ni/Cu(100), which is paramagnetic at 300 K, is investigated. Clear deviations of the domain pattern as compared to those of ultrathin Fe/Cu(100) films were found. The most important results are itemized in the following. (i) The onset of the ferromagnetic order in Fe/Ni_{1.5}/Cu(100) occurs at a lower Fe layer thickness (≈ 1.35 ML as compared to ≈ 2.2 ML Fe/Cu(100)), and broader stripe domains occurred in the Fe/Ni bilayer due to the smaller magnetic stray field. (ii) A canted magnetization is observed in the Fe/Ni film at the occurrence of domains due to the negative Fe-Ni interface anisotropy. Qualitatively, the SRT takes place as observed for Fe layers on perpendicularly magnetized Ni/Cu(100) films, however, the critical Fe thickness of the SRT is increased by ≈ 0.6 ML. The average width of the stripe domains of ≈ 750 nm at the SRT is more than four times larger than those of Fe layers grown on perpendicularly magnetized Ni/Cu(100) films. This broadening of the domains is attributed to the smaller magnetic stray field of the bilayer due to the minor Ni layer thickness. Despite the very narrow width of the SRT interval of only 0.15 ML Fe, the domain images unambiguously show a *continuous* reorientation of the magnetization into the film plane, i. e. a second-order SRT. No correlation of the magnetization direction with the substrate step edges at the start and at the end of the SRT was found in this system.

The UHV-SQUID magnetometer, which has been built up in the framework of this thesis and offers the possibility to determine the absolute value of the magnetization of an ultrathin film *in situ*, was presented. First measurements of an Fe/GaAs(100) film were shown. The design of the UHV-chamber allows for measurements of the *same* sample by SQUID magnetometry and ferromagnetic resonance for the first time.

A Appendix

A.1 Conversion of properties and units

In the literature various units are used for the energy and the magnetic properties. In table A.1 the conversion of energy units is given. For the purpose of converting surface and volume anisotropy energy densities table A.2 can be utilized. The units of the most important magnetic properties can be converted as follows:

$$\text{Magnetic field strength : } H[\text{Oe}] \cdot 79.58 = H[\text{A/m}]$$

$$\text{Magnetic flux density: } B[\text{G}] \cdot 10^{-4} = B[\text{T}]$$

$$\text{Magnetization: } 4\pi M[\text{G}] \cdot 79.58 = M[\text{A/m}] \text{ or } M[\text{G}] = M[\text{kA/m}]$$

Table A.1: Conversion of energy units.

	J	erg	eV
1 J	1	10^7	$6.242 \cdot 10^{18}$
1 erg	10^{-7}	1	$6.242 \cdot 10^{11}$
1 eV	$1.602 \cdot 10^{-19}$	$1.602 \cdot 10^{-12}$	1

Table A.2: Lattice constants, surface and volume density of atoms and proportionality constants for the conversion of erg cm^{-2} (1 mJ m^{-2}) and 10^6 erg cm^{-3} (10^5 J m^{-3}) to $\mu\text{eV/atom}$.

	Lattice constant (nm)	Atoms cm^{-2}	1 erg cm^{-2} multiplied by	Atom cm^{-3}	10^6 erg cm^{-3} multiplied by
fcc Ni(100)	0.352	$1.61 \cdot 10^{15}$	$386 \mu\text{eV/atom}$	$9.17 \cdot 10^{22}$	$6.83 \mu\text{eV/atom}$
fct Ni(Fe) /Cu(100)	0.361	$1.78 \cdot 10^{15}$	$350 \mu\text{eV/atom}$	$9.03 \cdot 10^{22}$	$6.91 \mu\text{eV/atom}$
fcc Fe(100)	0.359	$1.55 \cdot 10^{15}$	$403 \mu\text{eV/atom}$	$8.65 \cdot 10^{22}$	$7.22 \mu\text{eV/atom}$
bcc Fe(100)	0.286	$1.21 \cdot 10^{15}$	$515 \mu\text{eV/atom}$	$8.46 \cdot 10^{22}$	$7.38 \mu\text{eV/atom}$

A.2 Drawings of the UHV-components

In table A.3 the position of the flanges of the UHV-chamber and the respective applications are listed. The flanges are numbered and can be found in the different views of the UHV-chamber shown in Fig. A.1. In the following drawings of the sample holder, the μ -metal shielding, the SQUID holder and the UHV-cryostat are presented with their dimensions.

Table A.3: Construction of the UHV-chamber: positions of the flanges and the respective applications.

No. of flange	Type	Application	Azimuthal angle (°)	Polar angle (°)	Length (mm)	Tube \varnothing_i (mm)	Shift (mm)
1	DN 100 CF	CMA	90	90	381	104	-
2	DN 100 CF	Manipulator	180	90	228	100	-
3	DN 160 CF	LEED	270	90	224	150	-
4	DN 100 CF	Glass finger	0	90	262	150	-
5	DN 63 CF	SQUID	-	0	180	66	-
6	DN 160 CF	Pumps	240	90	160	146	z=-180
7	DN 63 CF	Plasmasource	135	145	252	66	-
8	DN 160 CF	Evaporators	-	180	302	150	-
9	DN 16 CF	View port	0	35	150	16	-
10	DN 40 CF	View port	-	0	133	38	x=174
11	DN 16 CF	Spare	90	72	110	16	x=174
12	DN 16 CF	Spare	270	72	110	16	x=174
13	DN 16 CF	Spare	90	40	110	16	x=174
14	DN 16 CF	Spare	270	40	110	16	x=174
15	DN 40 CF	Ion gauge	90	90	117	38	x=-170
16	DN 63 CF	View port	160	50	176	66	-
17	DN 40 CF	Sputter gun	225	45	140	38	-
18	DN 40 CF	View port	270	60	131	38	x=110
19	DN 40 CF	View port	90	90	135	38	z=-94
20	DN 40 CF	QMS	45	40	184	38	-
21	DN 16 CF	View port	45	100	164	16	-
22	DN 16 CF	View port	225	100	164	16	-
23	DN 16 CF	Spare	270	90	113	16	x=132
24	DN 16 CF	Aperture plate	90	90	113	16	x=-94
25	DN 16 CF	View port	90	40	140	16	-

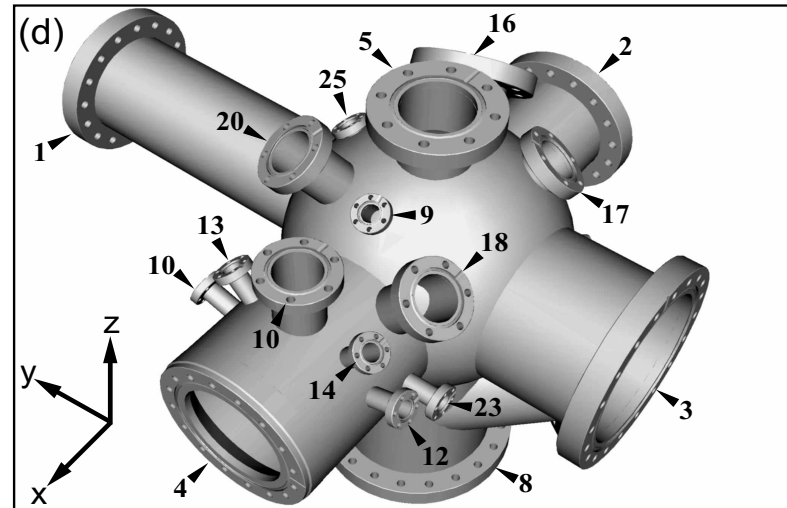
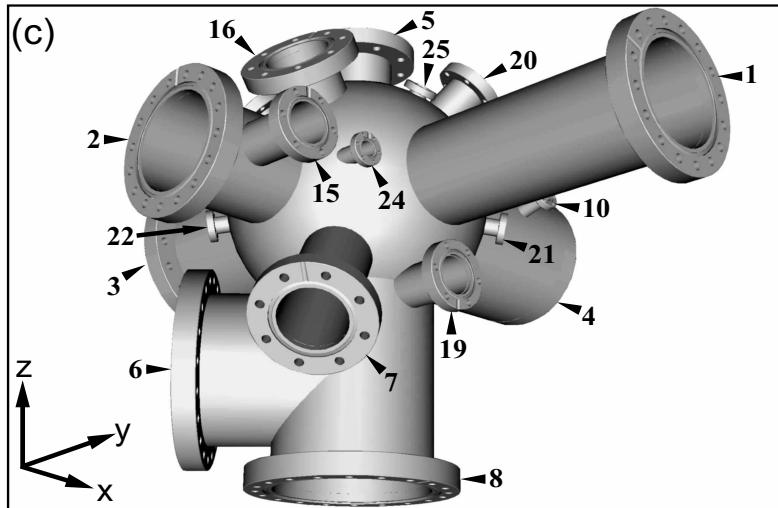
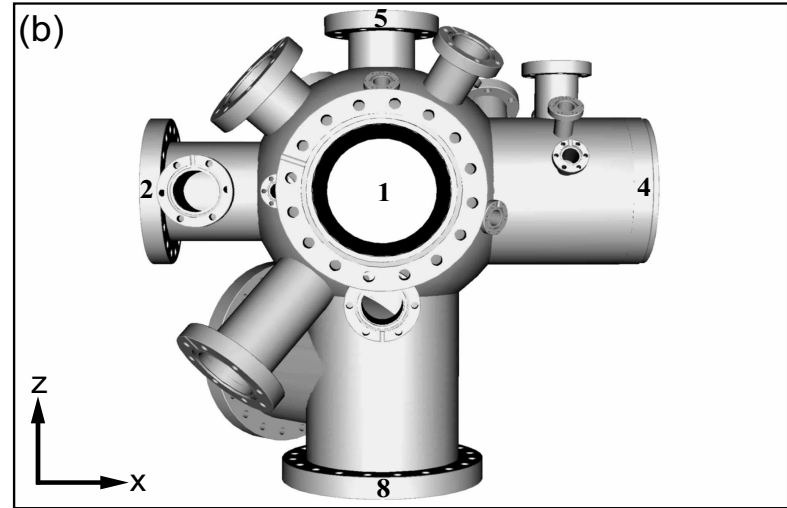
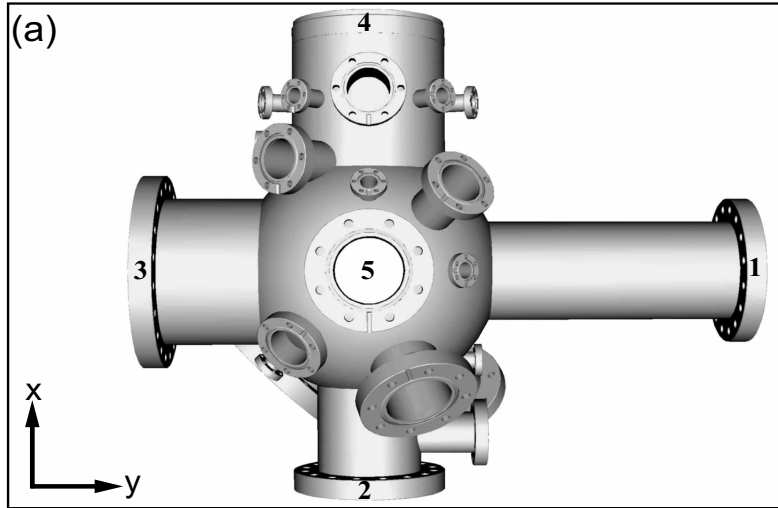


Figure A.1: Different views of the UHV-chamber: (a) top view , side view (b) and two 3D-views (c,d). The dimensions and angles of the numbered flanges and their applications are described in table A.3.

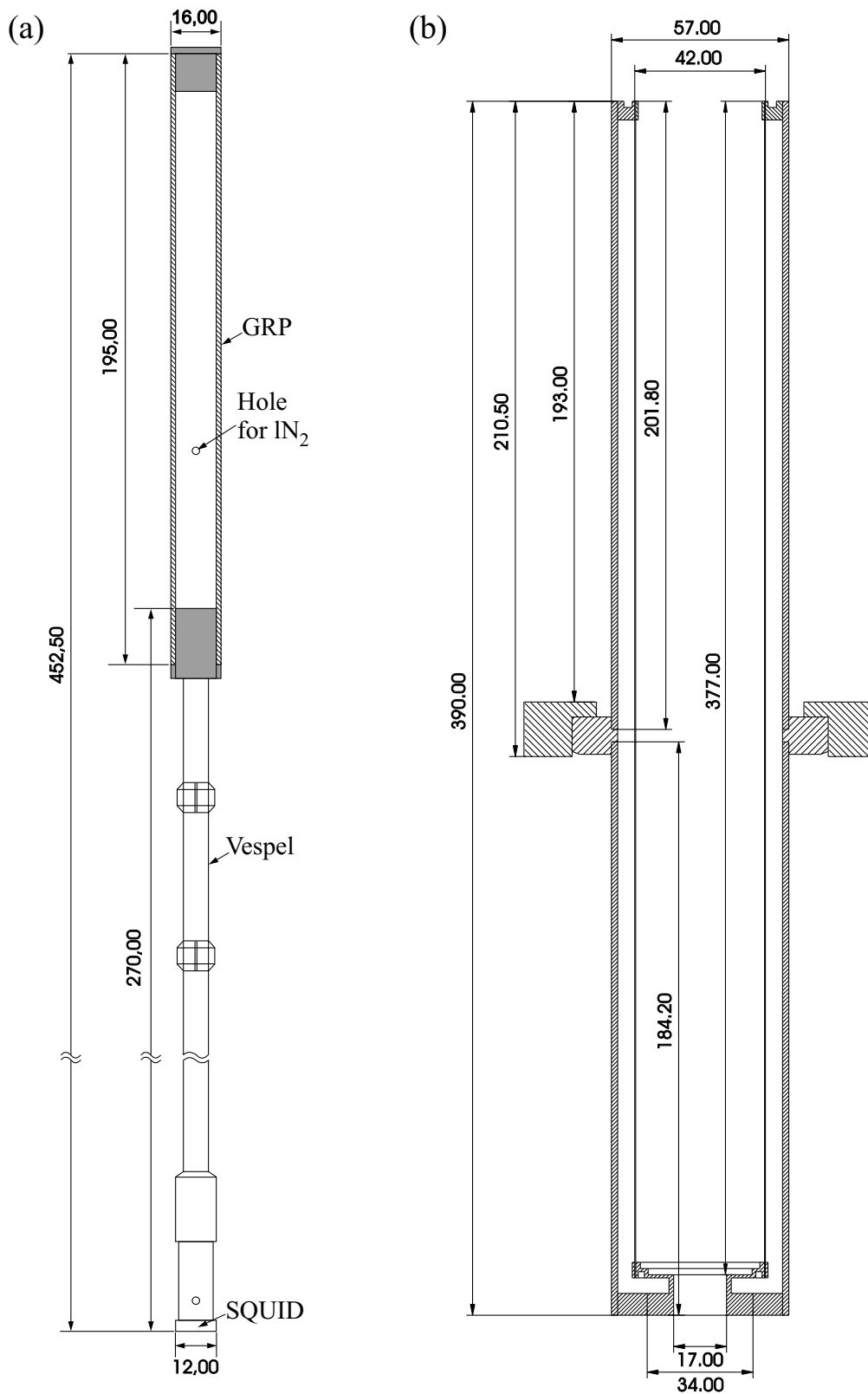


Figure A.4: (a) Dimensions in mm of the SQUID holder made of a *Vespel* rod, which is connected to a tube of glass fiber reinforced plastic (GRP). (b) Dimensions in mm of the cryostat mounted on a DN 63 CF flange.

A.3 Motor control and data acquisition program

The main program controls the two stepper motors which transfer and rotate the manipulator, in order to position the sample with respect to the desired application. It was developed by F. Römer and is based on *LabView 6.1*. Due to its voluminous structure the wiring diagram has not been printed here. With the control panel shown in Fig. A.5 the sample position can directly be approached by setting the angle of rotation θ and the transfer distance x . Once the angle θ is calibrated to the position of the respective application, the sample can be moved at the push of a button in the upper left corner of the control panel. Alternatively, θ can be adjusted by the large turning knob on the left hand side or the input field below it. The current

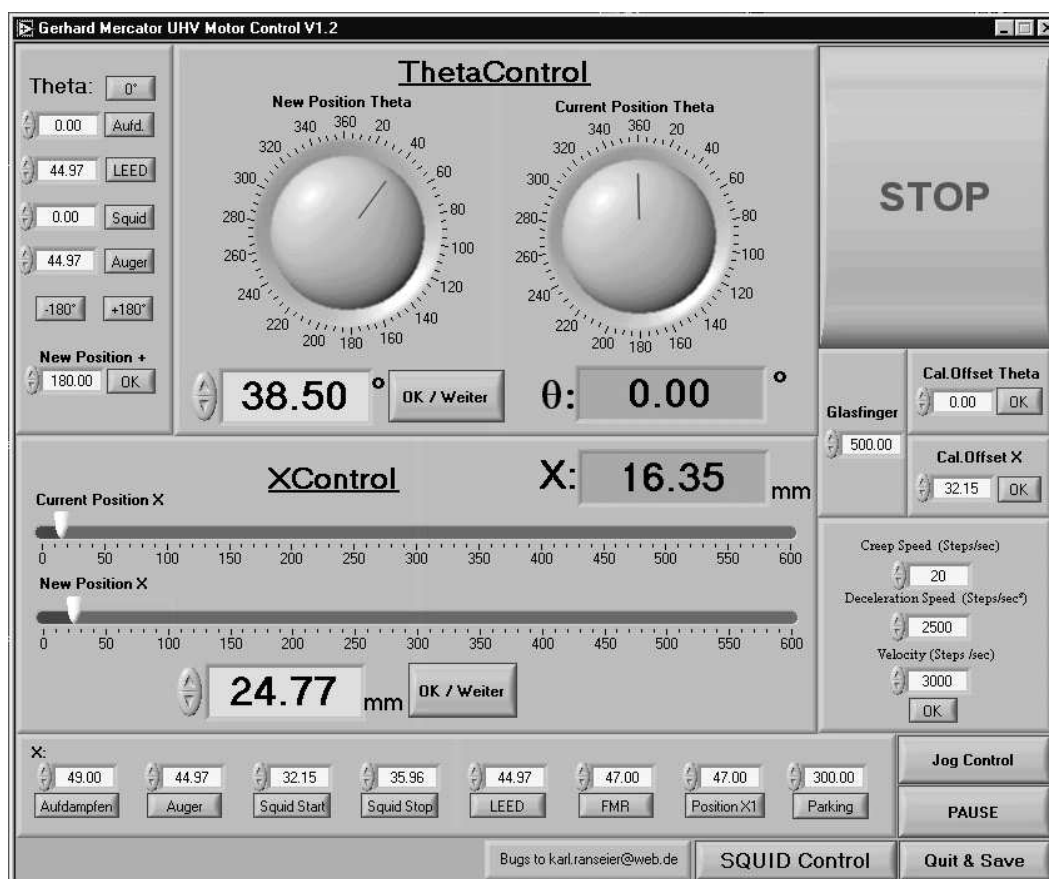


Figure A.5: Control panel of the main program, which allows for specific sample manipulation. Rotation and horizontal translation are governed and displayed by the turning knobs and the control slides, respectively. Sample positions for the various investigation techniques can be individually calibrated, saved and retrieved. The button “SQUID Control” grants access to the SQUID data acquisition program displayed in Fig. A.6.

angle is then displayed by the large turning knob on the right hand side and the output field below it. Analogously, the new horizontal x -position can be either set by the control slide or the input field in the middle of the panel. Again, a previously performed calibration of the x -position allows for a quick approach of the desired device. The current x -position is displayed by the upper control slide and the output field above it. Moreover, on the lower right hand side different modi of the velocity for the movement of the manipulator can be chosen. If the button *Jog Control* is pushed the manipulator can be operated by remote control. For SQUID measurements a subprogram can be started by pushing the button *SQUID Control* at the bottom of the main control panel. The SQUID control panel is depicted in Fig. A.6. It is divided into the graph, which displays the SQUID output voltage –proportional to the stray field component B_z of the sample– versus the x -position, and the fields for setting the parameters. The stray field distribution can be observed either during or after (*Liveshow OFF*) the measurement. Having chosen the direction of movement along the x -axis by the lever below the graph, measurements are started by the accordingly labelled knob on the right hand side and can be saved either manually or automatically (*Autosave ON*). Before a measurement the data acquisition can be specified by choosing the number of output values to be averaged per measuring point (*Scans*

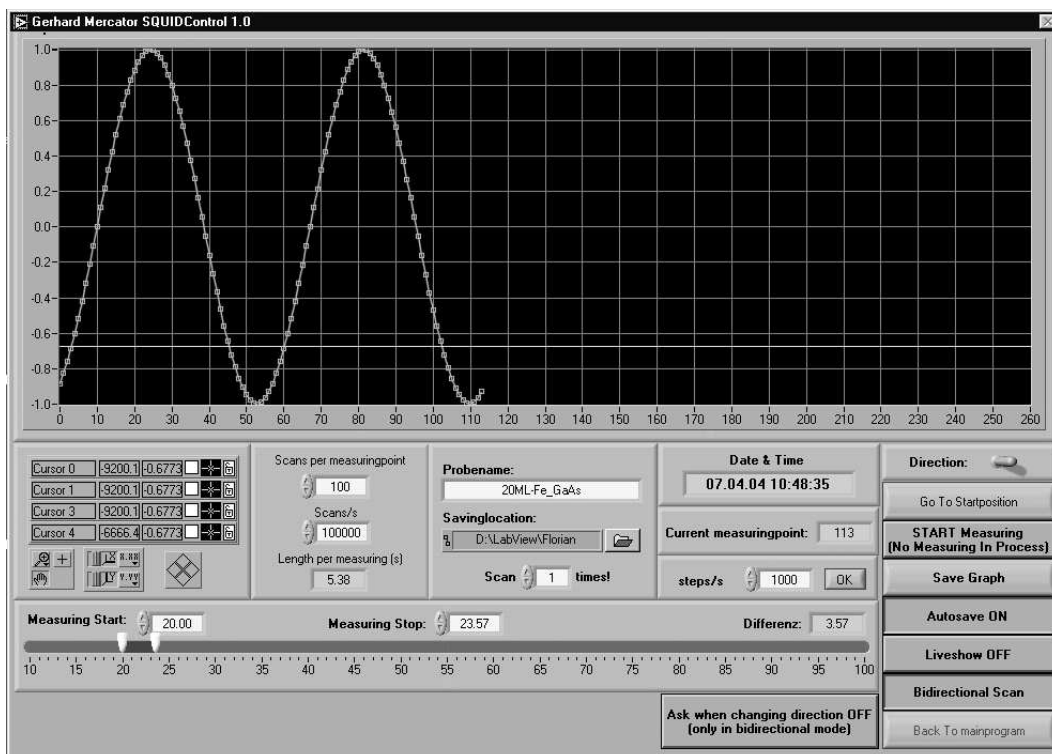


Figure A.6: Control panel of the program, which allows for SQUID data acquisition. An x - y -chart displays the SQUID signal versus the x -position (here a test pattern is shown). Start and end position of the scan as well as the velocity, the direction, the number of repetitions and file name of the measurement can be chosen. In the auto-save mode every scan is saved automatically.

per measuring point). Furthermore, the data acquisition per second (*Scan/s*) at the input unit can be defined, which in combination with the scans per measuring point determines the total duration of acquisition per point. The total period of one measurement is output in the field *Length of measuring (s)*, which is determined by the totally covered distance adjusted by the control slide at the bottom and the velocity of the motor.

A.4 Technical data of the SQUID sensor

Table A.4: Technical details of the SQUID. From [200].

Manufacturer	Jülicher SQUID GmbH
Washer	$\varnothing = 3.5 \text{ mm}$
SQUID-Loop	$100 \times 100 \mu\text{m}^2$
Inductance	260 pH
Tank circuit	Lumped element
Resonance frequency	861 MHz
Coupling (rf absorption)	-26 dB
Quality factor	340
SQUID signal amplitude	$0.5 \text{ V}_{\text{pp}}$
Resolution	$<1 \text{ pT}/\sqrt{\text{Hz}}$
Transfer coefficient	$0.64(1) \text{ V}/\Phi_0$
Intrinsic calibration	$9.3 \text{ nT}/\Phi_0$

A.5 Calibration of the Fe evaporator

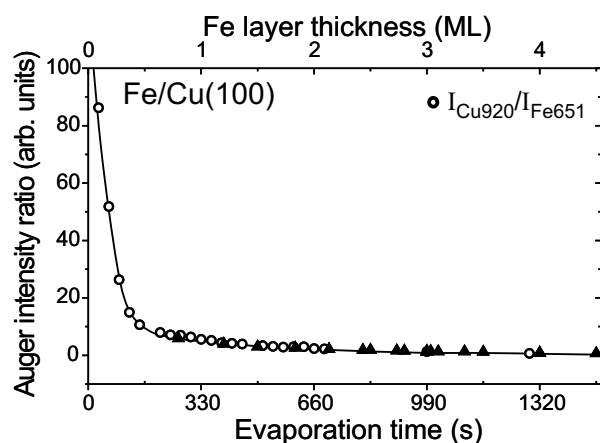


Figure A.7: Calibration of the Fe evaporator by the ratio of the Auger peak intensities Cu_{920} and Fe_{651} of various Fe/Cu(100) spectra as a function of the evaporation time and the corresponding Fe layer thickness (circles). The triangles represent earlier measurements [175]. The curve is a guide to the eye.

A.6 Determination of the canting angle from XMCD measurements

The relevant lengths shown in Fig. A.8 are given by:

$$\overline{OW} = M_{\parallel} \sin(\theta) \quad (\text{A.1})$$

$$\overline{OV} = M_{\parallel} \cos(\theta) \quad (\text{A.2})$$

$$\overline{OZ} = \frac{M_{\parallel}}{\cos(\theta)} \quad (\text{A.3})$$

θ being the angle of incidence of the x-ray beam. By using the theorem on intersecting lines, x from Fig. A.8 is given by:

$$x = (\overline{OZ} - M_{\perp}) \times \frac{\overline{OW}}{\overline{OZ} - \overline{OV}} \quad (\text{A.4})$$

The canting angle α of the magnetization is defined by:

$$\tan(\alpha) = \frac{x}{M_{\perp}} \quad (\text{A.5})$$

$$(\text{A.6})$$

The computation yields:

$$\alpha = \arctan\left(\frac{M_{\parallel} - M_{\perp} \cos(\theta)}{M_{\perp} \sin(\theta)}\right) \quad (\text{A.7})$$

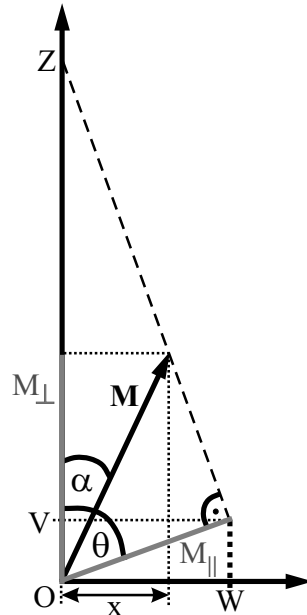


Figure A.8: Determination of the canting angle α of the magnetization \mathbf{M} by using the theorem on intersecting lines. M_{\perp} and M_{\parallel} are the projections of \mathbf{M} onto the directions of the incident x-ray, whereas x is the true in-plane component of \mathbf{M} .

Since the measured XMCD intensities I_{\perp} and I_{\parallel} are proportional to the respective components of \mathbf{M} , the canting angle of the magnetization can be obtained from:

$$\alpha = \arctan\left(\frac{I_{\parallel} - I_{\perp} \cos(\theta)}{I_{\perp} \sin(\theta)}\right) \quad (\text{A.8})$$

List of Figures

1.1	Slater-Pauling curve for an Fe-Ni alloy	7
1.2	Local magnetic moments on Fe and Ni sites for an Fe-Ni alloy	8
1.3	Local intermixing at the Fe/Ni interface assuming fcc growth	9
1.4	Stability diagram of the easy axis of the magnetization	11
1.5	Different types of spin-reorientation transitions	12
1.6	Magnetic phase diagram of Fe/Cu(100) as a function of the film thickness	16
1.7	Magnetic phase diagram of Ni/Cu(001) as a function of the film thickness	18
1.8	Equilibrium number of magnetic moments within a domain wall of a bulk-like Fe/Cu(100) film	22
1.9	Rotation of the magnetization within a Bloch and a Néel wall	23
1.10	Cross section through a Bloch and a Néel wall in thin films	24
1.11	Zigzag-shaped charged domain wall between two domains meeting “head-on”	25
1.12	Profile of a perpendicularly magnetized stripe domain state of a monolayer	26
1.13	Magnetic phase diagram of a thin film at $T = 0$ in the $(K_2 - K_4)$ plane	27
2.1	Band structure of Co and the asymmetry oscillation as a function of the electron energy	30
2.2	Schematic arrangement of the spin manipulator of the SPLEEM	31
2.3	Electron optical schematic diagram of the SPLEEM	32
2.4	Sketch of the detection system of the SPLEEM	33
2.5	Mechanisms of the LEEM phase contrast	34
2.6	Spin-selective excitation from the spin-orbit split $2p_{3/2,1/2}$ core shell to the exchange split $3d$ band	38
2.7	Isotropic absorption and XMCD spectra and the corresponding integrals of Fe ₄ /Ni ₁₇ /Cu(100)	40
2.8	Schematic of an rf-SQUID loop and the V-I-characteristics	43
2.9	Coordinates and vectors used to calculate the stray field integrals	44
2.10	Calculated stray field distribution of an in-plane and an out-of-plane magnetized Fe film	45

3.1	LEEM image of the bare Cu(100) surface and the corresponding step edge profile	48
3.2	Auger spectrum of the bare Cu(100) crystal	49
3.3	Oscillation of the average LEEM intensity versus time during Ni deposition . .	50
3.4	Auger spectrum of a 4 ML Fe/Cu(100) film	51
3.5	LEED images of the bare Cu(100) crystal and a 4 ML Fe/Cu(100) film	51
3.6	LEED image of the bare GaAs(001) substrate	52
4.1	UHV-SQUID setup.	54
4.2	Construction and electrical connections of the sample holder	56
4.3	Evaporation of ferromagnetic films of $3 \times 3 \text{ mm}^2$ by means of an aperture plate	57
4.4	Calibration of the SQUID sensor signal by means of a small coil	58
4.5	Measured stray field component B_z of a 12.5 ML Fe/GaAs(001) film	60
5.1	Onset of ferromagnetic order within the plane of a Ni/Cu(100) film at 300 K . .	61
5.2	Magnetic contrast versus the Ni layer thickness	62
5.3	Large “head-on” domains in 4.8 ML Ni/Cu(100) at 100 K	64
5.4	Domain wall width of in-plane magnetized Ni/Cu(100) versus the thickness . .	65
5.5	Angular dependent investigation of magnetic domains of an 8 ML Ni/Cu(100) film at 300 K	66
5.6	Néel wall profile of an 8 ML Ni/Cu(100) film	69
5.7	Evolution of magnetic domains of an ultrathin Fe/Cu(100) film as a function of the thickness	71
5.8	Profiles of perpendicularly magnetized stripe domains of Fe/Cu(100) films . . .	72
5.9	Evolution and size of out-of-plane magnetized domains of two different Fe/Ni/Cu(100) films	74
5.10	Broadening of perpendicularly magnetized domains of 7.5 ML Ni/Cu(100) upon Fe deposition	75
5.11	Imaging of Bloch walls of an $\text{Fe}_{0.7}/\text{Ni}_{11}/\text{Cu}(100)$ film	76
5.12	Evolution of Bloch walls of an $\text{Fe}_x/\text{Ni}_{11}/\text{Cu}(100)$ film as a function of the Fe layer thickness	77
5.13	In-plane magnetized $\text{Fe}_{2.8}/\text{Ni}_{7.5}/\text{Cu}(100)$ film at 300 K	78
6.1	Spin-reorientation transition of Ni/Cu(100) at 300 K as a function of the thickness	80
6.2	Domain wall profiles of a 10.2 ML Ni/Cu(100) film at the SRT	81
6.3	Spin canting at the SRT of Ni/Cu(100) as a function of the thickness at 300 K .	83
6.4	XMCD spectra of a perpendicularly magnetized $\text{Fe}_4/\text{Ni}_{17}/\text{Cu}(100)$ film at the Fe and Ni $L_{2,3}$ edges at normal photon incidence	85
6.5	XMCD spectra of an in-plane magnetized $\text{Fe}_{6.5}/\text{Ni}_{17}/\text{Cu}(100)$ film at the Fe and Ni $L_{2,3}$ edges at a grazing photon incidence of $\theta = 60^\circ$	85

6.6	Element-selective hysteresis loops taken at the L_3 edges of Fe and Ni of an $\text{Fe}_{17}/\text{Ni}_{17}/\text{Cu}(100)$ film	86
6.7	Continuous spin-reorientation transition of an $\text{Fe}_x/\text{Ni}_{11}/\text{Cu}(100)$ film as a function of the Fe thickness	90
6.8	Profile of the stripe domain pattern of an $\text{Fe}_{2.6}/\text{Ni}_{11}/\text{Cu}(100)$ film	91
6.9	Angular dependent magnetic contrast of $\text{Fe}_x/\text{Ni}_{11}/\text{Cu}(100)$ as a function of the Fe layer thickness	93
6.10	3D-plot of the angular dependence of the magnetization direction versus the Fe thickness of an $\text{Fe}_x/\text{Ni}_{11}/\text{Cu}(100)$ film	94
6.11	Model of the spiral-like SRT of Fe/Ni/Cu(100) films during the SRT	95
6.12	Angular dependence of the magnetization direction of an $\text{Fe}_x/\text{Ni}_{11}/\text{Cu}(100)$ film during the SRT	99
6.13	Domain wall evolution of an $\text{Fe}_x/\text{Ni}_7/\text{Cu}(100)$ film as a function of the Fe thickness	101
6.14	Bloch to Néel wall transition of an $\text{Fe}_x/\text{Ni}_7/\text{Cu}(100)$ film at the SRT	103
6.15	Domain formation of an $\text{Fe}_x/\text{Ni}_{1.5}/\text{Cu}(100)$ film at the SRT	105
A.1	Different views of the UHV-chamber	113
A.2	Dimensions and different views of the sample holder	114
A.3	Dimensions of the cryostat finger and the μ -metal screening	114
A.4	Dimensions of the SQUID holder	115
A.5	Control panel of the main program	116
A.6	Control panel of the program for SQUID data acquisition	117
A.7	Calibration of the Fe evaporator	118
A.8	Determination of the canting angle of the magnetization.	119

List of Tables

2.1	Domain imaging methods	35
6.1	Magnetic moments per Ni atom of an $\text{Fe}_x/\text{Ni}_{17}/\text{Cu}(100)$ film as a function of the Fe layer thickness x	88
6.2	Magnetic moments per Fe atom of an $\text{Fe}_x/\text{Ni}_{17}/\text{Cu}(100)$ film as a function of the Fe layer thickness x	88
6.3	Anisotropy constants of Ni/Cu(100) and Fe/Cu(100) at 300 K	98
A.1	Conversion of energy units	111
A.2	Lattice constants, surface and volume density of atoms and conversion constants	111
A.3	Construction of the UHV-chamber: positions and angles of the flanges	112
A.4	Technical details of the SQUID	118

References

- [1] U. Gradmann, *Magnetism in ultrathin transition metal films*, in: *Handbook of Magnetic Materials*, ed. K. H. J. Buschow, Vol. 7, p. 1–96, Elsevier Science Publishers, Amsterdam (1993)
- [2] J. A. C. Bland and B. Heinrich, eds., *Ultrathin magnetic structures I*, Springer-Verlag Berlin (1994)
- [3] H. Fritzsche, J. Kohlhepp, H. J. Elmers and U. Gradmann, *Phys. Rev. B* **49**, 15665 (1994)
- [4] Y. Millev and J. Kirschner, *Phys. Rev. B* **54**, 4137 (1996)
- [5] A. Hucht and K. D. Usadel, *J. Mag. Mag. Mater.* **198-199**, 493 (1999)
- [6] K. D. Usadel and A. Hucht, *Phys. Rev. B* **66**, 024419 (2002)
- [7] W. L. O'Brien and B. P. Tonner, *Phys. Rev. B* **49**, 15370 (1994)
- [8] M. Farle, W. Platow, A. N. Anisimov, P. Pouloupoulos and K. Baberschke, *Phys. Rev. B* **56**, 5100 (1997)
- [9] R. Vollmer, Th. Gutjahr-Löser and J. Kirschner, *Phys. Rev. B* **60**, 6277 (1999)
- [10] V. Jähnke, J. Gütde and E. Matthias, *J. Mag. Mag. Mater.* **237**, 69 (2001)
- [11] P. J. Jensen and K. H. Bennemann, *Phys. Rev. B* **52**, 16012 (1995)
- [12] A. Vaterlaus, C. Stamm, U. Meier, M. G. Pini, P. Politi and D. Pescia, *Phys. Rev. Lett.* **84**, 2247 (2000)
- [13] H. F. Ding, S. Pütter, H. P. Oepen and J. Kirschner, *Phys. Rev. B* **63**, 134425 (2001)
- [14] E. Y. Vedmedenko, H. P. Oepen and J. Kirschner, *Phys. Rev. B* **66**, 214401 (2002)
- [15] S. Chikazumi, *Physics of Magnetism*, Wiley, New York (1964)
- [16] S. Chikazumi, *Physics of Ferromagnetism*, Oxford Univ. Press (1999)

- [17] A. Hubert and R. Schäfer, *Magnetic Domains*, Springer Verlag, Berlin (1998)
- [18] C. Kittel, *Phys. Rev.* **70**, 965 (1946)
- [19] Zhu-Pei Shi, *J. Phys.: Condens. Matter* **4**, L191 (1992)
- [20] K. Grzelakowski, T. Duden, E. Bauer, H. Poppa and S. Chiang, *IEEE Trans. Magn.* **30**, 4500 (1994)
- [21] T. Duden and E. Bauer, *J. Electron Microscopy* **47**, 379 (1998)
- [22] M. Farle, B. Mirwald-Schulz, A. N. Anisimov, W. Platow and K. Baberschke, *Phys. Rev. B* **55**, 3708 (1997)
- [23] W. L. O'Brien, T. Droubay and B. P. Tonner, *Phys. Rev. B* **54**, 9297 (1996)
- [24] U. Bovensiepen, H. J. Choi and Z. Q. Qiu, *Phys. Rev. B* **61**, 3235 (1999)
- [25] W. L. O'Brien and B. P. Tonner, *Phys. Rev. B* **52**, 15332 (1995)
- [26] X. Liu and M. Wuttig, *Phys. Rev. B* **64**, 104408 (2001)
- [27] D. P. Pappas, K.-P. Kämper and H. Hopster, *Phys. Rev. Lett.* **64**, 3179 (1990)
- [28] R. Allenspach and A. Bischof, *Phys. Rev. Lett.* **69**, 3385 (1992)
- [29] Dongqi Li, M. Freitag, J. Pearson, Z. Q. Qiu and S. D. Bader, *Phys. Rev. Lett.* **72**, 3112 (1994)
- [30] R. H. Madsen, A. N. Koveshnikov, C. Harwell, R. Hall, R. L. Stockbauer and L. Kurtz, *J. Appl. Phys.* **85**, 6211 (1999)
- [31] J. Shen, A. K. Swan and J. F. Wendelken, *Appl. Phys. Lett.* **75**, 2987 (1999)
- [32] J. P. Pierce, J. Shen and R. Wu, *Phys. Rev. B* **65**, 132408 (2002)
- [33] M. Farle, *Rep. Prog. Phys.* **61**, 755 (1998)
- [34] B. Schirmer and M. Wuttig, *Phys. Rev. B* **60**, 12945 (1999)
- [35] X. Liu, B. Schirmer and M. Wuttig, *Phys. Rev. B* **65**, 224413 (2002)
- [36] R. Thamankar, A. Ostrokhova and F. O. Schumann, *Phys. Rev. B* **66**, 134414 (2002)
- [37] B. Schulz and K. Baberschke, *Phys. Rev. B* **50**, 13467 (1994)
- [38] K. L. Man, M. S. Altman and H. Poppa, *Surf. Sci.* **480**, 163 (2001)

-
- [39] A. Ney, *A new design of an UHV-High- T_c -SQUID magnetometer: Absolute determination of magnetic moments of 3d-transition metal films*, PhD Thesis, Freie Universität Berlin (2001)
- [40] S. Vonsovskij, *Ferromagnetic resonance: The phenomenon of resonant absorption of a high-frequency magnetic field in ferromagnetic substances*, Pergamon Press (1966)
- [41] P. Bruno, *Phys. Rev. B* **39**, 865 (1989)
- [42] R. M. Bozorth, *Ferromagnetism*, Van Nostrand, New York (1951)
- [43] B. Heinrich, S. T. Purcell, J. R. Dutcher, K. B. Urquhart, J. F. Cochran and A. S. Arrott, *Phys. Rev. B* **38**, 12879 (1988)
- [44] B. Heinrich and J. A. C. Bland, eds., *Ultrathin magnetic structures II*, Springer-Verlag Berlin (1994)
- [45] S. S. P. Parkin, N. More and K. P. Roche, *Phys. Rev. Lett.* **64**, 2304 (1990)
- [46] R. C. O'Handley, *Modern Magnetic Materials: Principles and Applications*, Wiley, New York (2000)
- [47] W. Pepperhoff and M. Acet, *Constitution and magnetism of iron and its alloys*, Springer-Verlag, Berlin (2001)
- [48] I. A. Abrikosov, O. Eriksson, P. Söderlind, H. L. Skriver and B. Johansson, *Phys. Rev. B* **51**, 1058 (1995)
- [49] G. Dumpich, J. Kästner, U. Kirschbaum, H. Mühlbauer, J. Liang, Th. Lübeck and E. F. Wassermann, *Phys. Rev. B* **46**, 9258 (1991)
- [50] E. F. Wassermann, *Ferromagnetic materials* ed. K. H. J. Buschow and E. P. Wohlfarth, Vol. 5, North Holland, Amsterdam (1990)
- [51] P. Luches, G. C. Gazzadi, A. di Bona, L. Marassi, L. Pasquali, S. Valeri and S. Nannarone, *Surf. Sci.* **419**, 207 (1999)
- [52] L. Néel, *J. Phys. Radium* **15**, 225 (1954)
- [53] K. S. Cheung, R. J. Harrison and S. Yip, *J. Appl. Phys.* **71**, 4009 (1992)
- [54] A. Kirilyuk, J. Giergiel, J. Shen, M. Straub and J. Kirschner, *Phys. Rev. B* **54**, 1050 (1996)
- [55] D. Peterka, A. Enders, G. Haas and K. Kern, *Phys. Rev. B* **66**, 104411 (2002)

- [56] C. Liu, E. R. Moog and S. D. Bader, *J. Appl. Phys.* **64**, 5325 (1988)
- [57] J. Thomassen, F. May, B. Feldmann, M. Wuttig and H. Ibach, *Phys. Rev. Lett.* **69**, 3831 (1992)
- [58] J. Giergiel, J. Shen, J. Woltersdorf, A. Kirilyuk and J. Kirschner, *Phys. Rev. B* **52**, 8528 (1995)
- [59] M. Zharnikov, A. Dittschar, W. Kuch, C. M. Schneider and J. Kirschner, *J. Mag. Mag. Mater.* **174**, 40 (1997)
- [60] A. Biedermann, R. Tscheließnig, M. Schmid and P. Varga, *Phys. Rev. Lett.* **87**, 086103 (2001)
- [61] D. Spišák and J. Hafner, *Phys. Rev. Lett.* **88**, 056101 (2002)
- [62] S. Müller, P. Bayer, C. Reischl, K. Heinz, B. Feldmann, H. Zillgen and M. Wuttig, *Phys. Rev. Lett.* **74**, 765 (1995)
- [63] M. Straub, R. Vollmer and J. Kirschner, *Phys. Rev. Lett.* **77**, 743 (1996)
- [64] V. L. Moruzzi, P. M. Marcus, K. Schwarz and P. Mohn, *Phys. Rev. B* **34**, 1784 (1986)
- [65] A. Biedermann, M. Schmid and P. Varga, *Phys. Rev. Lett.* **86**, 464 (2001)
- [66] R. D. Ellerbrock, A. Fuest, A. Schatz, W. Keune and R. A. Brand, *Phys. Rev. Lett.* **74**, 3053 (1995)
- [67] W. A. A. Macedo and W. Keune, *Phys. Rev. Lett.* **61**, 475 (1988)
- [68] V. Popescu, H. Ebert, L. Szunyogh, P. Weinberger and M. Donath, *Phys. Rev. B* **61**, 15241 (2000)
- [69] K. Amemiya, S. Kitagawa, D. Matsumura, T. Yokoyama and T. Ohta, *J. Phys.: Condens. Matter* **15**, S561 (2003)
- [70] L. Li, A. Kida, M. Ohnishi and M. Matsui, *Surf. Sci.* **493**, 120 (2001)
- [71] E. Mentz, *UHV-Kerr-Mikroskopie und STM an dünnen Eisen- und Nickelfilmen auf Cu(100)*, PhD Thesis, Freie Universität Berlin (1997)
- [72] D. E. Fowler and J. V. Barth, *Phys. Rev. B* **53**, 5563 (1996)
- [73] J. P. Pierce, M. A. Torija, J. Shen and E. W. Plummer, *Phys. Rev. B* **64**, 224409 (2001)
- [74] D. P. Pappas, *J. Vac. Sci. Technol. B* **14**, 3203 (1996)

-
- [75] H. B. Callen and E. R. Callen, *J. Phys. Chem. Solids* **27**, 1271 (1966)
- [76] A. Kashuba and V. L. Pokrovsky, *Phys. Rev. Lett.* **70**, 3155 (1993)
- [77] R. Vollmer and J. Kirschner, *Phys. Rev. B* **61**, 4146 (2000)
- [78] C. Liu, E. R. Moog and S. D. Bader, *Phys. Rev. Lett.* **60**, 2422 (1988)
- [79] Y. Zhao, J. Ye, C. L. Gao, B. Ma and Q. Y. Jin, *J. Appl. Phys.* **94**, 5100 (2003)
- [80] M. A. Torija, J. P. Pierce J. Shen, *Phys. Rev. B* **63**, 092404 (2001)
- [81] H. Jenniches, J. Shen, Ch. V. Mohan, S. Sundar Manoharam, J. Barthel, P. Ohresser, M. Klaua and J. Kirschner, *Phys. Rev. B* **59**, 1196 (1999)
- [82] W. Platow, U. Bovensiepen, P. Pouloupoulos, M. Farle, K. Baberschke, L. Hammer, S. Walter, S. Müller and K. Heinz, *Phys. Rev. B* **59**, 12641 (1999)
- [83] J. Lindner, P. Pouloupoulos, R. Nünthel, E. Kosubek, H. Wende and K. Baberschke, *Surf. Sci.* **523**, L65 (2002)
- [84] K. Baberschke, *Appl. Phys. A: Mater. Sci. Process* **62**, 417 (1996)
- [85] K. Baberschke and M. Farle, *J. Appl. Phys.* **81**, 5038 (1997)
- [86] J. Henk, A. M. Niklasson and B. Johansson, *Phys. Rev. B* **59**, 9332 (1999)
- [87] S. Z. Wu, G. J. Mankey, F. Huang and R. F. Willis, *J. Appl. Phys.* **76**, 6434 (1994)
- [88] M. Farle, W. Platow, A. N. Anisimov, B. Schulz and K. Baberschke, *J. Mag. Mag. Mater.* **165**, 74 (1997)
- [89] M. Zheng, J. Shen, P. Ohresser, C. V. Mohan, M. Klaua, J. Barthel and J. Kirschner, *J. Appl. Phys.* **85**, 5060 (1999)
- [90] S. S. Dhesi, H. A. Dürr and G. van der Laan, *Phys. Rev. B* **59**, 8408 (1999)
- [91] A. B. Shick, Y. N. Gornostyrev and A. J. Freeman, *Phys. Rev. B* **60**, 3029 (1999)
- [92] S. Z. Wu, G. J. Mankey and R. F. Willis, *J. Vac. Sci. Technol. A* **13**, 1497 (1995)
- [93] R. Nünthel, *Wachstum und Magnetismus dünner 3d Metalle auf Cu-Substraten – Einfluß von O als Surfactant*, PhD Thesis, Freie Universität Berlin (2003)
- [94] W. L. O'Brien and B. P. Tonner, *J. Appl. Phys.* **79**, 5623 (1996)

- [95] H. M. Hwang, J. C. Park, D. G. You, H. S. Park, K. Jeong and J. Lee, *J. Appl. Phys.* **93**, 7625 (2003)
- [96] S. van Dijken, R. Vollmer, B. Poelsema and J. Kirschner, *J. Mag. Mag. Mater.* **210**, 316 (2000)
- [97] R. Nünthel, T. Gleitsmann, P. Pouloupoulos, A. Scherz, J. Lindner, E. Kosubek, Ch. Litwinski, Z. Li, H. Wende, K. Baberschke, S. Stolbov and T. S. Rahman, *Surf. Sci.* **531**, 53 (2003)
- [98] M. Redjdal, A. Kakay, M. F. Ruane and F. B. Humphrey, *IEEE Trans. Magn.* **38**, 2471 (2002)
- [99] H. Riedel and A. Seeger, *Phys. Stat. Sol. (B)* **46**, 377 (1971)
- [100] H. J. Williams and R. C. Sherwood, *J. Appl. Phys.* **28**, 548 (1957)
- [101] L. A. Finzi and J. A. Hartmann, *IEEE Trans. Magn.* **4**, 662 (1968)
- [102] M. Gronau, H. Goeke, D. Schüffler and S. Sprenger, *IEEE Trans. Magn.* **19**, 653 (1983)
- [103] B. K. Middleton, M. Aziz, M. Wdowin and J. J. Miles, *IEEE Trans. Magn.* **34**, 2339 (1998)
- [104] B. K. Middleton, J. J. Miles and R. H. Noyau, *IEEE Trans. Magn.* **24**, 3099 (1988)
- [105] R. Allenspach, M. Stampanoni and A. Bischof, *Phys. Rev. Lett.* **65**, 3344 (1990)
- [106] Zhu-Pei Shi, *J. Phys.: Condens. Matter* **4**, L191 (1992)
- [107] G. Meyer, *In situ Abbildung magnetischer Domänen in dünnen Filmen mit magnetooptischer Rasternahfeldmikroskopie*, PhD Thesis, Freie Universität Berlin (2003)
- [108] Y. Yafet and E. M. Gyorgy, *Phys. Rev. B* **38**, 9145 (1988)
- [109] P. Jensen, *privat communication* (2004)
- [110] National Center of Electron Microscopy, <http://ncem.lbl.gov> (2004)
- [111] Th. Duden and E. Bauer, *Surf. Rev. Lett.* **5**, 1213 (1998)
- [112] E. Bauer, T. Duden, H. Pinkvos, H. Poppa and K. Wurm, *J. Magn. Magn. Mater.* **156**, 1 (1996)
- [113] E. Bauer, *Rep. Prog. Phys.* **57**, 895 (1994)

-
- [114] M. S. Altman, W. F. Chung and C. H. Liu, *Surf. Rev. Lett.* **5**, 1129 (1998)
- [115] R. Zdyb and E. Bauer, *Surf. Rev. Lett.* **9**, 1485 (2002)
- [116] D. T. Pierce and F. Meier, *Phys. Rev. B* **13**, 5484 (1976)
- [117] D. T. Pierce, R. J. Celotta, G. C. Wang, W. N. Unertl, A. Galejs, C. E. Kuyatt and S. R. Mielczarek, *Rev. Sci. Instrum.* **51**, 478 (1980)
- [118] P. A. Hayes, D. H. Yu and J. F. Williams, *Rev. Sci. Instrum.* **68**, 1708 (1997)
- [119] P. S. Farago, *The polarization of electron beams and the measurement of the g-factor anomaly of free electrons*, in: *Adv. Electronics Electr. Phys.*, Vol. 21, p. 1, ed. L. Marton, Academic Press, New York (1965)
- [120] K. Grzelakowski and E. Bauer, *Rev. Sci. Instrum.* **67**, 742 (1996)
- [121] R. J. Phaneuf and A. K. Schmid, *Physics Today* **50** (March 2003)
- [122] T. Duden and E. Bauer, *Rev. Sci. Instrum.* **66**, 2861 (1995)
- [123] H. J. Williams, F. G. Foster and E. A. Wood, *Phys. Rev.* **82**, 119 (1951)
- [124] C. A. Fowler, Jr. and E. M. Fryer, *Phys. Rev.* **104**, 552 (1956)
- [125] W. Rave and A. Hubert, *IEEE Trans. Magn.* **26**, 2813 (1990)
- [126] G. L. Houze, Jr., *J. Appl. Phys.* **38**, 1089 (1967)
- [127] A. Bauer, *Far-field and near-field magneto-optical microscopy of ultrathin films*, Prof. Diss., Freie Universität Berlin (2000)
- [128] Ch. Stamm, F. Marty, A. Vaterlaus, V. Weich, S. Egger, U. Maier, U. Ramsperger, H. Fuhrmann and D. Pescia, *Science* **282**, 449 (1998)
- [129] O. Schmidt, M. Bauer, C. Wiemann, R. Porath, M. Scharfe, O. Andreyev, G. Schönhense and M. Aeschlimann, *Appl. Phys. B* **74**, 223 (2002)
- [130] A. K. Schmid, *private communication* (2004)
- [131] H. Yang, A. R. Smith, M. Prikhodko and W. R. L. Lambrecht, *Phys. Rev. Lett.* **89**, 226101 (2002)
- [132] K. Koike and K. Hayakawa, *Jpn. J. Appl. Phys., Part 2* **23**, L187 (1984)
- [133] M. R. Scheinfein, J. Unguris, R. J. Celotta and D. T. Pierce, *Phys. Rev. Lett.* **65**, 668 (1989)

- [134] T. Kohashi, H. Matsuyama and K. Koike, *Rev. Sci. Instr.* **66**, 5537 (1995)
- [135] H. P. Oepen, G. Steierl and J. Kirschner, *J. Vac. Sci. Technol.* **20**, 2535 (2002)
- [136] J. Lohau, A. Carl, S. Kirsch and E. F. Wassermann, *Appl. Phys. Lett.* **78**, 2020 (2001)
- [137] Th. Kebe and A. Carl, *J. Appl. Phys.* **95**, 775 (2004)
- [138] H. J. Hug, B. Stiefel, P. J. A. van Schendel, A. Moser, R. Hofer, S. Martin, H.-J. Güntherodt, S. Porthun, L. Abelmann, J. C. Lodder, G. Bochi and R. C. O'Handley, *J. Appl. Phys.* **83**, 5609 (1998)
- [139] P. J. A. van Schendel, H. J. Hug, B. Stiefel, S. Martin and H.-J. Güntherodt, *J. Appl. Phys.* **88**, 435 (2000)
- [140] M. R. Freemann and B. C. Choi, *Science* **294**, 1484 (2001)
- [141] J. Vogel, W. Kuch, M. Bonfim, J. Camareo, Y. Pennec, F. Offi, K. Fukumoto, J. Kirschner, A. Fontaine and S. Pizzini, *Appl. Phys. Lett.* **82**, 2299 (2003)
- [142] W. Wulfhekel and J. Kirschner, *Appl. Phys. Lett.* **75**, 1944 (1999)
- [143] O. Pietzsch, A. Kubetzka, M. Bode and R. Wiesendanger, *Phys. Rev. Lett.* **84** (2000)
- [144] A. Kubetzka, M. Bode, O. Pietzsch and R. Wiesendanger, *Phys. Rev. Lett.* **88**, 057201 (2002)
- [145] H. Poppa, E. D. Tober and A. K. Schmid, *J. Appl. Phys.* **91**, 6932 (2002)
- [146] J. Stöhr, *J. Mag. Mag. Mater.* **200**, 470 (1999)
- [147] T. Nawrath, H. Fritzsche, F. Klose, J. Nowikow and H. Maletta, *Phys. Rev. B* **60**, 9525 (1999)
- [148] D. P. Pappas, G. A. Prinz and M. B. Ketchen, *Appl. Phys. Lett.* **65**, 3401 (1994)
- [149] B. T. Thole, P. Carra, F. Sette and G. van der Laan, *Phys. Rev. Lett.* **68**, 1943 (1992)
- [150] P. Carra, B. T. Thole, M. Altarelli and X. Wang, *Phys. Rev. Lett.* **70**, 694 (1993)
- [151] R. Wu and A. J. Freeman, *Phys. Rev. Lett.* **73**, 1994 (1994)
- [152] R. Wu, D. Wang and A. J. Freeman, *Phys. Rev. Lett.* **71**, 3581 (1993)
- [153] J. Hunter Dunn, D. Arvanitis, N. Mårtensson, M. Tischer, F. May, M. Russo and K. Baberschke, *J. Phys.: Condens. Matter.* **7**, 1111 (1995)

-
- [154] D. Arvanitis, M. Tischer, J. Hunter Dunn, F. May, N. Mårtensson and K. Baberschke, *Experimental determination of orbital and spin moments from MCXD on 3d metal overlayers*, in: *Lecture notes in physics: Spin-orbit-influenced spectroscopies of magnetic solids*, eds. H. Ebert and G. Schütz, p. 145, Springer-Verlag (1995)
- [155] H. Weinstock, *SQUID Sensors: Fundamentals, Fabrication and Applications*, Kluwer (1996)
- [156] B. D. Josephson, *Phys. Lett.* **1**, 251 (1962)
- [157] W. Buckel, *Supraleitung : Grundlagen und Anwendungen*, Wiley-VCH, Weinheim, 5. Ed. (1994)
- [158] W. G. Jenks, S. S. H. Sadeghi and J. P. Wikswo, Jr., *J. Phys. D: Appl. Phys.* **30**, 293 (1997)
- [159] J. R. Kirtley, C. C Tsuei, K. A. Moler, V. G. Kogan, J. R. Clem, and A. J. Turberfield, *Appl. Phys. Lett.* **74**, 4011 (1999)
- [160] A. Chwala, R. Stolz, J. Ramos, V. Schultze, H.-G. Meyer and D. Kretzschmar, *Supercond. Sci. Technol.* **12**, 1036 (1999)
- [161] Y. Tavrín, Y. Zhang, M. Mück, A. I. Braginski and C. Heiden, *Appl. Phys. Lett.* **62**, 1824 (1993)
- [162] C. Gerthsen and H. Vogel, *Physik*, Springer-Verlag, 17. Ed. (1993)
- [163] Jülicher SQUID GmbH, The JSQ-tutorial for users of rf-SQUIDs, Technical report, Forschungszentrum Jülich (2001)
- [164] O. Snigirev, K. E. Andreev, A. M. Tishin, S. A. Gudoshnikov and J. Bohr, *Phys. Rev. B* **55**, 14429 (1997)
- [165] R. Ramchal, *Aufbau und Inbetriebnahme eines Hochtemperatur-SQUID-Magnetometers und -Gradiometers*, Diplomathesis, Technische Universität Braunschweig, unpublished (2001)
- [166] M. Ritter, M. Stindtman, M. Farle and K. Baberschke, *Surf. Sci.* **348**, 243 (1996)
- [167] M. Doi, B. Roldán Cuenya, W. Keune, T. Schmitte, A. Nefedov, H. Zabel, D. Spoddig, R. Meckenstock and J. Pelzl, *J. Mag. Mag. Mater.* **240**, 407 (2002)
- [168] R. Moosbühler, F. Bensch, M. Dumm and G. Bayreuther, *J. Appl. Phys.* **91**, 8757 (2002)

- [169] K. L. Man, W. L. Ling, S. Y. Paik, H. Poppa, M. S. Altman and Z. Q. Qiu, *Phys. Rev. B* **65**, 024409 (2001)
- [170] C. M. Schneider, A. K. Schmid, P. Schuster, H. P. Oepen and J. Kirschner, in: *Magnetism and Structure in Systems of Reduced Dimensions*, ed. R. F. C. Ferrow *et al.*, p. 453–466, Plenum Press, New York (1993)
- [171] P. Pouloupoulos, J. Lindner, M. Farle and K. Baberschke, *Surf. Sci.* **437**, 277 (1999)
- [172] J. Shen, J. Giergiel, and J. Kirschner, *Phys. Rev. B* **52**, 8454 (1995)
- [173] J. Lindner, *Ferromagnetische Resonanz an ultradünnen magnetischen Einfach- und Mehrfachlagen der 3d-Übergangsmetalle - Statik und Dynamik*, PhD Thesis, Freie Universität Berlin (2002)
- [174] K. Heinz, S. Müller and L. Hammer, *J. Phys.: Condens. Matter* **11**, 9437 (1999)
- [175] J. Lindner, private communication (2004)
- [176] E. Kneedler, P. M. Thibado, B. T. Jonker, B. R. Bennett, B. V. Shanabrook, R. J. Wagner and L. J. Whitman, *J. Vac. Sci. Technol. B* **14**, 3193 (1996)
- [177] J. J. Krebs, B. T. Jonker and G. A. Prinz, *J. Appl. Phys.* **61**, 2596 (1987)
- [178] Q. Xue, T. Hashizume, J. M. Zhou, T. Sakata, T. Ohno and T. Sakurai, *Phys. Rev. Lett.* **74**, 3177 (1995)
- [179] VTS J. Schwarz GmbH, Carl-Maria-von-Weber-Strasse, D-76437 Rastatt, <http://www.vts-gmbh.de>, custom-made UHV-chamber (2003)
- [180] Jülicher SQUID GmbH, Lankenstrasse 29, D-52428 Juelich, Germany, <http://www.jsquid.com>, SQUID magnetometer model M900 (2003)
- [181] R. Ramchal, A. K. Schmid, M. Farle and H. Poppa, *Phys. Rev. B* **68**, 054418 (2003)
- [182] V. I. Nikitenko, V. S. Gornakov, A. J. Shapiro, R. D. Shull, Kai Liu, S. M. Zhou and C. L. Chien, *Phys. Rev. Lett.* **84**, 765 (2000)
- [183] M. Bode, A. Kubetzka, S. Heinze, O. Pietzsch, R. Wiesendanger, M. Heide, X. Nie, G. Bihlmayer and S. Blügel, *J. Phys.: Condens. Matter* **15**, 679 (2003)
- [184] A. Holz and A. Hubert, *Z. Angew. Phys.* **26**, 145 (1969)
- [185] R. Kirchner and W. Döring, *J. Appl. Phys.* **39**, 855 (1968)

-
- [186] H. P. J. Wijn, *Condensed Matter*, Vol. 19 of *Group III, Pt. G*, Springer-Verlag, Berlin (1988)
- [187] A. Berger and H. P. Oepen, *Phys. Rev. B* **45**, 12596 (1992)
- [188] M. Pratzner, H. J. Elmers, M. Bode, O. Pietzsch, A. Kubetzka and R. Wiesendanger, *Phys. Rev. Lett.* **87**, 127201 (2001)
- [189] W. Platow, A. N. Anisimov, M. Farle and K. Baberschke, *Phys. Stat. Sol.* **173**, 145 (1999)
- [190] X. Liu, A. Berger and M. Wuttig, *Phys. Rev. B* **63**, 144407 (2001)
- [191] C. Klein and A. K. Schmid, Additional SPLEEM measurements on the SRT of Ni/Cu(100) at the LBNL, Berkeley, USA, (May 2004)
- [192] S. Dieluweit, H. Ibach, M. Giesen and T. L. Einstein, *Phys. Rev. B* **67**, 121410 (2003)
- [193] P. Entel, H. C. Herper, E. Hoffmann, G. Nepecks, E. F. Wassermann, M. Acet, V. Crisan and H. Akai, *Philosophical Magazine B* **80**, 141 (2000)
- [194] P. Söderlind, O. Eriksson, B. Johansson, R. C. Albers and A. M. Boring, *Phys. Rev. B* **45**, 12911 (1992)
- [195] F. May, M. Tischer, D. Arvanitis, M. Russo, J. Hunter Dunn, H. Henneken, H. Wende, R. Chauvistre, N. Mårtensson and K. Baberschke, *Phys. Rev. B* **53**, 1076 (1996)
- [196] C. T. Chen, Y. U. Idzerda, H.-J. Lin, N. V. Smith, G. Meigs, E. Chaban, G. H. Ho, E. Pellegrin and F. Sette, *Phys. Rev. Lett.* **75**, 152 (1995)
- [197] F. Wilhelm, *Magnetic properties of ultrathin films, coupled trilayers and 3d/5d multilayers studied by x-ray magnetic circular dichroism*, PhD Thesis, Freie Universität Berlin (2000)
- [198] J. Hunter Dunn, D. Arvanitis and N. Mårtensson, *Phys. Rev. B* **54**, R11157 (1996)
- [199] W. Platow, M. Farle and K. Baberschke, *Europhys. Lett.* **43**, 713 (1998)
- [200] Jülicher SQUID GmbH, SQUID magnetometer data sheet, Technical report (2003)

Publications and contributions to conferences

I. Articles

1. M. Spasova, U. Wiedwald, R. Ramchal, M. Farle, M. Jergel, E. Majkova, S. Luby, R. Senderak
Magnetization and magnetic anisotropy of Co/W multilayers
457 Phys. Stat. Sol. B - Basic Research **225**, 449 (2001)
2. M. Spasova, U. Wiedwald, R. Ramchal, M. Farle, M. Hilgendorff, M. Giersig
Magnetic properties of arrays of interacting Co nanocrystals
J. Magn. Magn. Mater. **240**, 40 (2002)
3. R. Ramchal, A. K. Schmid, M. Farle, H. Poppa
Magnetic domains and domain wall structure in Ni/Cu(001) films imaged by spin-polarized low energy electron microscopy
Phys. Rev. B **68**, 054418 (2003)
4. R. Ramchal, A. K. Schmid, M. Farle, H. Poppa
Spiral-like continuous Spin-Reorientation Transition of Fe/Ni bilayers on Cu(100)
Phys. Rev. B **69**, 214401 (2004)
5. R. Ramchal, C. Klein, A. K. Schmid, M. Farle, H. Poppa
Step-induced spiral-like Spin-Reorientation Transition of ultrathin Ni/Cu(100) films in preparation

II. Talks

1. R. Ramchal, A. K. Schmid, M. Farle, H. Poppa
Domänenbeobachtung am Spin-Reorientierungsübergang von ultradiinnen Ni/Cu(100)-Filmen mittels SPLEEM
Frühjahrstagung der Deutschen Physikalischen Gesellschaft, (Regensburg, 2002)

2. R. Ramchal, A. K. Schmid, M. Farle, H. Poppa
Domänenbeobachtung am Spin-Reorientierungsübergang von ultradünnen Ni- und Fe/Ni-/Filmen auf Cu(100) mittels SPLEEM
Workshop “Struktur und Magnetismus ultradünner Metallfilme 5”, (Chandolin, Switzerland, 2003)
3. R. Ramchal, A. K. Schmid, M. Farle, H. Poppa
Domänenbeobachtung am Spin-Reorientierungsübergang von ultradünnen Fe/Ni/Cu(100)-Filmen mittels SPLEEM
Frühjahrstagung der Deutschen Physikalischen Gesellschaft, (Dresden, 2003)
4. R. Ramchal, A. K. Schmid, M. Farle, H. Poppa
Imaging the magnetic microstructure of ultrathin Fe/Ni/Cu(100) films at the spin-reorientation transition by SPLEEM
XVIII. International Colloquium on Magnetic Films and Surfaces, (Madrid, 2003)

III. Posters

1. M. Spasova, U. Wiedwald, E. L. Bizdoaca, R. Ramchal, M. Farle, M. Hilgendorff, M. Giersig
Magnetic properties of magnetophoretically deposited Co nanocrystals
Symposium on Magnetic Multilayers (Aachen, 2001)
2. M. Spasova, U. Wiedwald, E. L. Bizdoaca, R. Ramchal, M. Farle, M. Hilgendorff, M. Giersig
Magnetic properties of magnetophoretically deposited Co nanocrystals
Joint Summer Workshop on Mesomagnetism (Santorini, Greece, 2001)
3. R. Ramchal, A. K. Schmid, M. Farle, H. Poppa
Observation of magnetic domains of ultrathin Ni/Cu(100) films by SPLEEM
281. WE Heraeus Seminar “Spin-Orbit Interaction and Local Structure in Magnetic Systems with Reduced Dimensions”, (Wandlitz, 2002)
4. R. Ramchal, A. K. Schmid, M. Farle, H. Poppa
Magnetic domain wall structure of Ni/Cu(100) and the Spin-Reorientation Transition of Fe/Ni/Cu(100) thin films imaged by SPLEEM
International Workshop X “Magnetic Heterostructures”, (Bochum, 2002)
5. R. Ramchal, A. K. Schmid, M. Farle, H. Poppa
Magnetic domain structure of Ni/Cu(100) and the Spin-Reorientation Transition of

Fe/Ni/Cu(100) thin films imaged by SPLEEM

International Symposium on Structure and Dynamics of Heterogeneous systems, (Duisburg, 2003)

6. R. Ramchal, A. K. Schmid, M. Farle, H. Poppa

Magnetic domain imaging at the Spin-Reorientation Transition of ultrathin Ni and Fe/Ni films on Cu(100) by SPLEEM

30. Edgar Lüscher Seminar, (Serneus, Switzerland, 2004)

Acknowledgment

I want to thank all those who contributed to the success of this work. Especially in a PhD thesis, which is partially based on the construction of a new equipment the support of technicians and workshop members is of great value. First of all I express my gratitude to **Prof. Dr. M. Farle** for giving me the opportunity to start the doctorate in his group. He promoted this work with valuable discussions and followed the progress of the UHV-SQUID magnetometer with continuous interest and helpful comments.

Moreover, my thanks go to:

Prof. Dr. H. Poppa for giving me the chance to benefit from the collaboration with his group in Berkeley.

Dr. A. K. Schmid for introducing me into the low energy electron microscopy. Without him SPLEEM measurements would not have been possible! It was a great time in Berkeley.

Priv.-Doz. Dr. A. Carl for valuable explanations and details about the nature of magnetic domains and for proofreading of this thesis.

Prof. Dr. M. Acet for helpful discussions about the physics of Fe-Ni alloys.

Dr. M. Spasova for fruitful discussions and for helping to perform the XMCD measurements.

Dr. M. Ulmeanu for assisting with the performance of the XMCD measurements.

Prof. Dr. D. Arvanitis, Dr. A. Fraile-Rodríguez, Dr. A. Preobrajensky, Dr. J. Hunter Dunn and **Dr. A. Hahlin** for assistance and hints during the XMCD measurements.

Dr. C. Klein for performing additional SPLEEM measurements.

Dr. J. Lindner for beneficial discussions and proofreading of this thesis.

Dr. A. Hucht for adjuvant theoretical comments on the nature of SRTs.

Dr. P. J. Jensen for helpful theoretical discussions about the role of domain formation near the SRT.

T. Kebe and **K. Zakeri Lori** for their constant assistance during the built-up and testing of the UHV-equipment.

D. Schädel for the construction of all the small and big tools and devices. Without him the UHV-equipment would not have been built-up in time.

U. Wiedwald for profitable discussions about XMCD and magnetism in general.

H. Zähres for his valuable suggestions and numerous discussions about electronics.

C. Raeder for assisting during the built-up of the UHV-setup.

A. Scherz and **M. Bernien** for helpful remarks and the correction of x-ray absorption spectra.

Dr. habil. M. Bode for valuable information about domain walls.

K. Lenz and **A. Ney** for helpful discussions about problems concerning SQUID magnetometry.

Dr. T. Duden for helping to solve technical problems concerning the SPLEEM instrument.

Dr. H. Ding for helping to clarify the sense of rotation of the electron polarization in the SPLEEM.

F. Römer for writing the SQUID data acquisition and control program.

C. Antoniak and **A. Schlachter** for proofreading of this thesis.

O. Bendix for helpful algebraic hints.

M. Vennemann for retrieving important measuring data after a hard disc crash.

JSQ for technical assistance and helpful hints to improve the SQUID system.

Deutscher Akademischer Austauschdienst who supported the SPLEEM measurements in Berkeley.

My parents who supported and helped me all the time during my studies.

Daniela for her encouragement and the beautiful time we had so far.

Zusammenfassung

In der vorliegenden Arbeit wurde der Spinreorientierungsübergang von ultradünnen $\text{Ni}_x/\text{Cu}(100)$ - und $\text{Fe}_y/\text{Ni}/\text{Cu}(100)$ -Filmen als Funktion der Schichtdicke x bzw. y bei 300 K im UHV untersucht. Ein Ziel dieser Arbeit war die Klärung der Frage, ob es sich bei dem SRT von $\text{Ni}/\text{Cu}(100)$ um einen Phasenübergang erster oder zweiter Ordnung handelt. Ein weiteres Ziel war die Charakterisierung des SRT von Fe/Ni -Zweischichtsystemen auf $\text{Cu}(100)$, deren Einzelschichten – $\text{Fe}/\text{Cu}(100)$ und $\text{Ni}/\text{Cu}(100)$ – einen entgegengesetzten SRT zeigen. Über die Abbildung der magnetischen Domänenstruktur während des Filmwachstums mittels SPLEEM wurde gezeigt, dass der SRT von $\text{Ni}/\text{Cu}(100)$ ein Übergang *zweiter* Ordnung ist, bei dem sich die Magnetisierung *kontinuierlich* innerhalb der großen Domänen dreht. In den Fe/Ni -Doppellagen wurde neben einer *kontinuierlichen* Reorientierung der Magnetisierung ein gleichzeitiges Aufbrechen der großen Domänen in *Streifendomänen* beobachtet. Für beide Dünnschichtsysteme wurde die Änderung der Magnetisierungsrichtung in Bezug auf die Orientierung der atomaren Stufenkanten des Cu -Substrats während des SRT gemessen, sowie die Größe der Domänen und die Breite und der Typ der Domänenwände bestimmt. Im folgenden werden die Ergebnisse für die untersuchten Systeme im einzelnen zusammengefasst.

In $\text{Ni}/\text{Cu}(100)$ -Filmen setzt die ferromagnetische Ordnung bei 300 K in Übereinstimmung mit früheren Experimenten bei etwa 5 ML ein. Die in der Filmebene magnetisierten Domänen haben eine typische Ausdehnung von einigen $10 \mu\text{m}$ ohne systematische Korrelation der Domänenwände zu den Stufenkanten des Substrats. Die großen Abmessungen dieser Domänen, im Vergleich zu den 165 nm breiten Streifendomänen beim Einsetzen der ferromagnetischen Ordnung in $\text{Fe}/\text{Cu}(100)$ -Filmen von 2.2 ML Schichtdicke, ist auf die parallel zur Oberfläche ausgerichtete Magnetisierung von ultradünnen $\text{Ni}/\text{Cu}(100)$ -Filmen zurückzuführen. Während in Fe -Monolagen aufgrund der großen senkrechten magnetischen Anisotropie die Streufeldenergie durch einen Streifendomänenzustand minimiert wird, liegt die Magnetisierung und damit das Streufeld des Ni -Films in der Ebene, in der die Streufeldenergie minimal ist. In der Ebene magnetisierte Ni -Filme werden im Schichtdickenbereich von 5 – 9 ML beobachtet. Die Domänenwände, die antiparallel magnetisierte Domänen trennen, sind 180° -Néel-Wände. Diese zeigen ein für Néel-Wände typisches Wandprofil bestehend aus einem Kernbereich und zwei symmetrisch dazu ausgedehnten logarithmischen Randbereichen. Für einen 8 ML $\text{Ni}/\text{Cu}(100)$ -Film liefert ein solches Profil eine typische Wandbreite von 400 nm. Es wurden keine systemati-

schen Unterschiede in der Domänenstruktur von Ni-Filmen gefunden, die bei Raumtemperatur hergestellt und gemessen wurden zu denen, die bei 100 K hergestellt und gemessen wurden. Am Anfang des SRT, der bei etwa 9.5 ML Ni stattfindet, tritt eine *Verlängerung* der bereits vorhandenen Domänenwände neben spontan ummagnetisierten Bereichen ($>1 \times 1 \mu\text{m}^2$) innerhalb der großen Domänen auf. Diese Beobachtungen sind auf die Erniedrigung der Domänenwandenergie infolge der verminderten effektiven magnetische Anisotropie am SRT zurückzuführen. Die beobachtete *Verbreiterung* der Domänenwände ist ebenfalls eine Folge der verminderten effektiven Anisotropie. Der SRT erfolgt kontinuierlich von einer Orientierung der Magnetisierung parallel zur Filmebene zu einer Orientierung der Magnetisierung senkrecht zur Filmebene mit zunehmender Ni-Schichtdicke. Über Minuten stabile verkippte Magnetisierungsvektoren innerhalb der Domänen werden eindeutig über die Abbildung der drei Magnetisierungskomponenten nachgewiesen. Die Reorientierung der Magnetisierung erfolgt über eine *spiralförmige* Bewegung von der Orientierung der Magnetisierung parallel zu den Cu-Stufen zu der Orientierung senkrecht zu den Stufen und senkrecht zur Filmoberfläche.

In Fe/Ni/Cu(100)-Filmen wurde die Orientierung der Magnetisierung der Fe- und der Ni-Schicht während des SRT als Funktion der Fe-Schichtdicke bei 300 K mittels XMCD und aus elementspezifischen Magnetisierungskurven für beide Schichten separat bestimmt. Diese Messungen zeigen, dass beide Magnetisierungen während des SRT parallel ausgerichtet sind, die Kopplung zwischen den Einzellagen also ferromagnetisch ist. Die Bestimmung der magnetischen Momente pro Fe- bzw. Ni-Atom in senkrecht magnetisierten Fe/Ni-Filmen mittels XMCD bei 300 K liefert ein reduziertes magnetisches Moment von $\approx 1.7 \mu_B$ für 1 ML Fe an der Fe-Ni-Grenzschicht. In 4 ML Fe auf Ni/Cu(100) wurde ein “high-spin”-Zustand des Fe gemäß der Slater-Pauling-Kurve gefunden. Dies lässt auf ein Wachstum der Fe-Schicht in der kubisch-flächenzentrierten Struktur bis mindestens 4 ML schliessen. Der SRT erfolgt von einer senkrecht zur Filmoberfläche orientierten Magnetisierung für unbedeckte Ni/Cu(100)-Filme (7 – 11 ML) zu einer Ausrichtung parallel zur Oberfläche mit zunehmender Fe-Bedeckung in einer *spiralförmigen* Bewegung. Dabei rotiert die in der Ebene liegende Magnetisierungskomponente von “senkrecht zu den Substratstufen” in Richtung “parallel zu den Stufen”. In dem Reorientierungsintervall (2.5 – 2.9 ML Fe) findet *gleichzeitig* ein Aufbrechen der Domänen in circa 180 nm breite *Streifendomänen* statt, die entlang der Cu-Stufen verlaufen und in denen die Magnetisierung *kontinuierlich* in die Filmebene reorientiert. Die leichte Richtung der Magnetisierung des gekoppelten Zweischichtsystems in der Ebene ist die [001] Richtung, die auch die leichte Richtung im Fe-Volumenmaterial ist. Bei einer Domänenwand, die vor dem SRT keine Korrelation zu den Substratstufen zeigte, wurde am Anfang des SRT die Anhaftung einzelner Wandsegmente an den Substratstufen (*domain wall pinning*) nachgewiesen, aus denen sich mit zunehmender Fe-Schichtdicke Streifendomänen bildeten. Am Maximum der Streifendichte findet ein Übergang von Bloch-Wänden zu Néel-Wänden in einem sehr schmalen

Schichtdickenbereich von etwa 0.1 ML Fe statt.

Aus der mittleren kritischen Fe-Schichtdicke des SRT, d. h. unter der Annahme eines diskontinuierlichen Übergangs, ergibt sich eine Fe-Ni-Grenzflächenanisotropie von $K_{2,Fe-Ni}^S = -93 \mu\text{eV/Atom}$ unter Verwendung der Literaturwerte für Volumen-, Oberflächen- und Formanisotropien der Einzellagen Fe/Cu(100) und Ni/Cu(100). Es wurde gezeigt, dass die Erhöhung der Formanisotropie des Fe/Ni/Cu(100)-Films durch die zunehmende Fe-Bedeckung allein für den SRT bei der kritischen Fe-Schichtdicke nicht ausreicht, sondern dass die Grenzflächenanisotropie einen entscheidenden Beitrag zur Reorientierung der Magnetisierung liefert. In einer Erweiterung des obigen Modells, die der kontinuierlichen Rotation der Magnetisierung Rechnung trägt, wird aus dem Fe-Schichtdicken abhängigen Neigungswinkel der Magnetisierung eine für das Zweilagensystem negative effektive Anisotropiekonstante K_4^{eff} bestimmt, während die Summe der Anisotropiekonstanten zweiter Ordnung positiv ist. In Übereinstimmung mit theoretisch entwickelten Stabilitätsdiagrammen der leichten Magnetisierungsrichtung im Anisotropieraum (K_4 vs. $K_2 - K_d$) wird dadurch die beobachtete verkippte Magnetisierung während des SRT charakterisiert. Das gleichzeitig beobachtete Aufbrechen der großen Domänen in Streifendomänen mit kosinusförmigem Profil wird durch die Theorie nicht vorausgesagt.

Abschliessend wurde der SRT von Fe-Lagen auf einem 1.5 ML Ni/Cu(100)-Film untersucht, der bei 300 K paramagnetisch ist. Hier zeigten sich deutliche Abweichungen zu der Domänenstruktur von Fe/Cu(100)-Filmen. Die wichtigsten Ergebnisse sind (i) ein Einsetzen der ferromagnetischen Ordnung bei kleineren Fe-Schichtdicken (1.35 ML) mit einem breiteren Streifendomänenmuster aufgrund des geringeren Streufeldes und (ii) "Spin-canting" beim Auftreten der Domänen infolge der negativen Grenzflächenanisotropie. Qualitativ verläuft der SRT wie bei Fe-Schichten auf senkrecht magnetisierten Ni/Cu(100)-Filmen, die kritische Fe-Schichtdicke für den SRT liegt jedoch 0.6 ML höher. Die mittlere Streifenbreite der Domänen am SRT ist mit ca. 750 nm mehr als viermal so gross und wird auf das geringere magnetische Streufeld aufgrund der wesentlich dünneren Ni-Schicht zurückgeführt. Trotz der geringen Breite des SRT-Intervalls von nur 0.15 ML Fe zeigen die Domänenabbildungen eindeutig eine *kontinuierliche* Reorientierung der Magnetisierung in die Filmebene, also einen SRT zweiter Ordnung. Eine Korrelation der Magnetisierungsrichtung mit den Substratstufen am Anfang und am Ende des SRT wurde in diesem System nicht gefunden.

Das im Rahmen dieser Arbeit aufgebaute UHV-SQUID-Magnetometer, mit dem die Magnetisierung eines ultradünnen Films *in situ* bestimmt werden kann, wurde vorgestellt. Erste Messungen an einem Fe/GaAs(100)-Film wurden präsentiert. Die Konstruktion der UHV-Kammer erlaubt erstmalig Messungen *derselben* Probe mittels SQUID-Magnetometrie und ferromagnetischer Resonanz.